Zusammenfassung

Die Tjörnes Fracture Zone (TFZ) ist eine Transformzone im Nordatlantik, welche die Nördliche Vulkanzone Islands vom Kolbeinseyrücken trent. Aktiver Vulkanismus, Hydrothermalismus und starke Erdbebenaktivität kennzeichnen die Region. Mit einem gemeinsamen geowissenschaftlichen Programm bestehend aus Reflexionsseismik, gasgeochemischen Messungen, U-Boot-Tauchgängen und Gesteinsprobenahmen der oberen 5 m wurde versucht, die Dynamik des Gebiets zu erkunden. Im ersten Teil dieser Arbeit wird daher eine Methode entwickelt um die lithologischen Parameter aus Gesteinsproben und physikalischen Eigenschaften, die in der Seismik vermessen wurden, miteinander in Einklang zu bringen. Der zweite Teil gibt schließlich eine Übersicht über verschiedenste Beobachtungen im Meßgebiet und stellt ein Modell für die Entwicklung der TFZ am Beispiel der Skjalfandi Bucht vor.

Die neue Methode verwendet die typischen Auswertungen von Amplitude Variation with Angle (AVA) Methoden, um die seismische Reflektivität in physikalische Gesteinseigenschaften umzurechnen und so die Meeresbodenlithologie zu erkennen. Da die Korrelation zwischen Reflektivität und physikalischen Eigenschaften nicht eindeutig ist, ist es empfehlenswert, die Fehler bei der Reflektivitätsaufnahme möglichst klein zu halten. Das geschieht klassischerweise durch technische Regelungen während der Aufnahme, wird hier jedoch durch eine statistische Mittelung der Kurven durch eine Selbst-Organisierende Karte (SOM) bzw. ein Kohonen-Netzwerk verbessert. Das Kohonen-Netzwerk ist ein nicht-überwachtes neuronales Netzwerk, das auf die Clusteranalyse spezialisiert ist. Ferner wird der unabhöngige Parameter Rauhigkeit, der aus Powerspektren der Meeresbodenreflektion errechnet wird, als zusätzliche Meeresbodeneigenschaft eingeführt, um die Ergebnisse der charakteristischen Kurven aus der Clusteranalyse zu verifizieren. Mit diesen Ergebnissen wird schließlich eine geologische Karter der TFZ entwickelt.

Die dynamischen Kräfte im submarinen Teil der TFZ werden in der Tiefe durch die Scherung entlang des Grimseylineament hervorgerufen. Diese Bewegung öffnet Klüfte im Gestein, die durch aufsteigendes Magma von einer flachen Krusten-Mantelgrenze gefüllt werden. Diese Krusten-Mantelgrenze bei ca. 16 km steht im Kontakt mit Konvektionszellen des Meerwassers, die von den aufsteigenden Magmen angetrieben werden. In Bereichen um Kolbeinsey und Grimsey, in der B-Werte von Mikrobebenverteilungen Magmaansammlungen im Untergrund andeuten, führt dies sehr wahrscheinlich zu Vulkanismus. $^{3}He/^{4}He$-Verhältnissen deuten auf eine stark ausdünnende Kruste zwischen Island und der ozeanischen Kruste hin. Sedimente wurde mithilfe der Reflexionsseismik noch in einer Tiefe von ca. 350-400 m erkannt. Diese Sedimentvorkommen werden durch thermogene Anteile in Kohlenwasserstoffen des Grimsey-Hydrothermalfeldes (GHF) untermauert, die nur in Gegenden auftreten, in denen mindestens 30 m Sedimente angetroffen wurden. Die Häufigkeitsverteilungen der einzelnen Kohlenwasserstoffkettenlängen weist zudem auf eine weitere Kohlenwasserstoffquelle, sogenannte Fischer-Tropsch-Reaktionen. Diese Reaktionen werden wahrscheinlich durch mafische bis ultramafische Pikrite, Laven der Theistareykirspalten, katalysiert, welche ihre untermeerische Fortsetzung im Manareyjarrücken nördlich der Tjörneshalbinsel finden.

Abstract

The Tjörnes Fracture Zone (TFZ) is a transform zone in the North Atlantic separating the Northern Volcanic Zone (NVZ) of Iceland from Kolbeinsey Ridge. The area exposes active volcanism and hydrothermalism and is subject to strong earthquakes. A reflection seismic survey has been conducted. It was complimented by gasgeochemical measurements, submersible diving and geological sampling of the seafloor. During the first part of the thesis a method is developped to detect the lithology from physical properties calculated from the acquired seismic data. The second part compares the results of the new method with the other observations and unravels the geological setting of the TFZ, in particular in Skjalfandi Bay.

The new method makes use of typical amplitude variation with angle (AVA) evaluations to connect reflectivity information to physical properties of rocks as density (ρ) and seismic velocities (v_p, v_s) and, thus, to lithology of the seafloor. Since the correlation between reflectivity and physical properties can be ambiguous, it is recommendable to establish relevant reflectivity trends before. Classical seafloor reflectivity methods tried to establish these trends by technical means. The present approach uses statistical averaging of the trends in a Self-Organizing Map (SOM) or Kohonen network, which is a neural network specialized on cluster analysis. The further physical parameter of roughness which is derived from power spectra ratios of the seismic reflections is an independent parameter discussed to improve the interpretation of the statistical classe. By comparing the results to stratigraphic and geological investigations it is possible to verify the information, so that finally a geological map (of surface lithology) is derived.

The dynamic forces acting in the offshore part of the TFZ are caused by the movement of the deep subsurface along the Grimsey Lineament. The shear movement opens up void spaces in the subsurface which are filled by magmatic fluids from shallow mantle reservoirs. This drives geothermal phenomena from submarine hydrothermalism to volcanism. The supply of magma and aqueous solutions reaches down to the base of the crust at ~16 km beneath Grimsey. B-value distributions of microquakes in the TFZ imply magma accumulations in the shallow subsurface (<10 km) just southeast of Grimsey. This thin crust - getting thinner to the north - is confirmed by $^3He/^4He$ isotope ratios. Reflection seismic stratigraphy and seafloor lithology indicate sediments up to a depth of ~350-400 m in Skjalfandi Bay. This is confirmed by thermogenic components in the isotopic composition of hydrocarbons, which are confined to zones of thick sedimentation (>30 m).

The frequency of the various hydrocarbon chains points to an additional origin of the gases, a Fischer-Tropsch reaction catalyzed by ultramafic rocks, i.e. probably rocks related to the picrites of the Theistareykir fissure zones. The Manareyjar Ridge spreading in the submarine part north of Tjörnes Peninsula may consequently represent the prolongation of the Theistareykir fissures offshore. A further source of volcanism appears to be a sill-dike complex between Kolbeinsey Island and the submarine hill called Hóll.

Index

Have a look at her. Wobbling around as if she had underestimated the effect of that last whisky in the restaurant at the end of the universe. She is still spinning around, staring at the stars, cooling her turbulent heart. Not that any of her brothers or sisters would care. She is a noble kind of wandering star keeping her shell clean of asteroids and hiding most of her scars and pocks beneath an aqueous solution thick as vaseline. Sometimes old wounds and pocks break open and wash away the miniature life forms roaming where they are not expected to. Not that she would care about those stupid symbionts and parasites. Red-eyed as her big brother or entangled in clouds of paraphernalia as her sister they wouldn´t even notice a giant turtle and four megasized elephants on top. It´s a rather lonely life living in blue. So why not spend your time quaking and shaking ? A revolution every year ? And, in between, let your smoke go up in bubbles and blow a ring of fire !

„A world like that which exists only because the gods enjoy a joke must be a place where magic would want to stay alive and it did...“ (T. Pratchett, Equal Rites)

History

A review

1. History - a review

"All did that, men and animals, earth,
rocks, trees and all ores; as you will
have seen, these things weep if they are
leaving frost for to come into warmth."
(Snorri Sturluson, Edda)

1.1. The original descriptions up to 1900

It might sound far reaching to start off a geoscientific thesis with the settlement of Iceland by the vikings. On the other hand it is exactly at this time that geoscience makes its first steps into these barren lands. Unfortunate vikings like Kolbein Sigmundarson leave their trace in the naming of an island (Landnámabok and Svarfdæla Saga, ca. 1200) - Kolbeinsey (Iceland´s northernmost point at 67, 19) - which today imprints its name on the arctic part of the Mid Atlantic Ridge north of Iceland, Kolbeinsey Ridge. A wise man in his time, Snorri Godi, chieftain of the western district of Iceland, is frequently claimed to be one of the first geologists on Iceland. After discussing whether to adopt christianity in a meeting of the Althing - the icelandic council - at Thingvellir in 1000 AD, a volcano erupted in the surroundings. While many Icelandic people claim that it is no wonder that the old gods should be angered, the chieftain asks quite rationally: "*What angered the gods when the lava flowed which we now stand on ?" (Gudjonsson, 1999*) The decision to adopt christianity was settled and it is obvious that his contemporaries must have known about the evolution of basaltic rocks from lava to be able to evaluate the argument. This takes place hundreds of years before neptunists of central Europe discuss the possibility that basalt columns might be derived from water (Schmincke, 2000).
History forgets about the wet and icy spot in the Atlantic for some hundred years. Europe prefers to call the „bewitched“ icelandic volcanoes the "gate to hell", but the few Icelanders learn to cope with the natural forces. As seamen they stick to the fringes of their island, because most of the interior of the island does not supply fertile grounds. Thus the offshore structures are welcome spots for settlement and the realm of friendly territories soon spreads out from the Faroe Islands to Greenland and Newfundland in Canada.

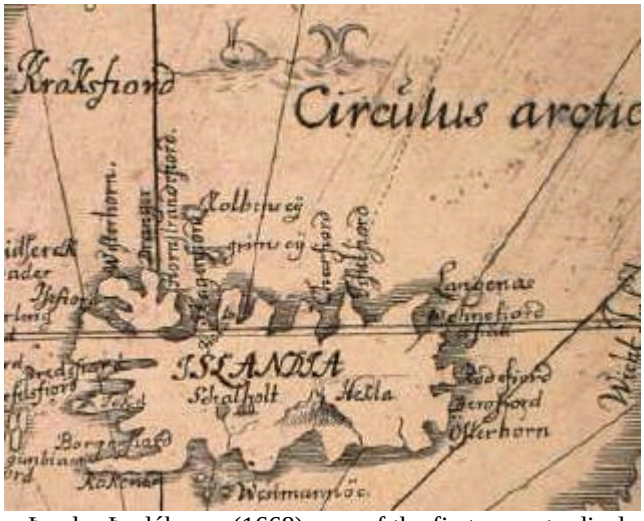

Figure 1: Map of Iceland by Þordur Þorláksson (1668), one of the first maps to display the island of Kolbeinsey.

The main part of the population settles in the north of Iceland only after christianity is introduced, when abbeys are built along the shores. To and fro some words of mouth reach Skálholt, the seat of the Bishop, from them, but most of them are incredible to the ears of the Bishop and besides a short note of Bishop .... : „"(...) *he ran fast from somewhere in the northern land to tell that new land was coming up somewhere to the north of Grimsey* (...)" (Annals of the People of Iceland), it needs a

rumour among dutch sailors to spread the word of an offshore volcanic eruption in 1378:

„ "(...) *there were seven islands northeast of Langanes, the largest of which was called Kolbeinsey... There is now a great mystery about the islands, since men cannot find them, although it is said that the crew of a Dutch vessel once approached them and saw the smoke of nine farms. They were intending to sail closer and examine the island more carefully when a figure appeared on the tip of a headland, waving something in their direction, and immediately they were enveloped in pitch black fog and lost sight of the island and never found it again.*" (Arnárson, 1960)

Langanes is the northern cape of the island of Grimsey and the seven islands are probably all parts of Kolbeinsey. Although only one rocky island remains till today, it is known from measurements of 1616 that Kolbeinsey has been crumbling away since the last ice age and temporarily split up into several parts (Saemundsson and Hjartarson, 1994). The pitch black fog is probably the sign of the volcanic eruption, that took part near Kolbeinsey in 1378, the exact position remains unclear, but there are hints for young volcanism in dredged rocks in the Tjörnes Fracture Zone (TFZ) (McMaster et al., 1977).

Those rumours keep strangers from the north of Iceland and enable an illegal trade with the dutch people in an icelandic territory occupied and monopolized by the danish government. Kolbeinsey Island cannot be found on a danish map until the 16th century. Thus, Icelanders use the dutch ships as escape routes from starvation, induced by the trade monopoly of the danish government and the warm climate of the year 1000 coming to an end, from the relatively unguarded eastern and northern shores (described in "The Iceland Bell", Laxness, 1979).

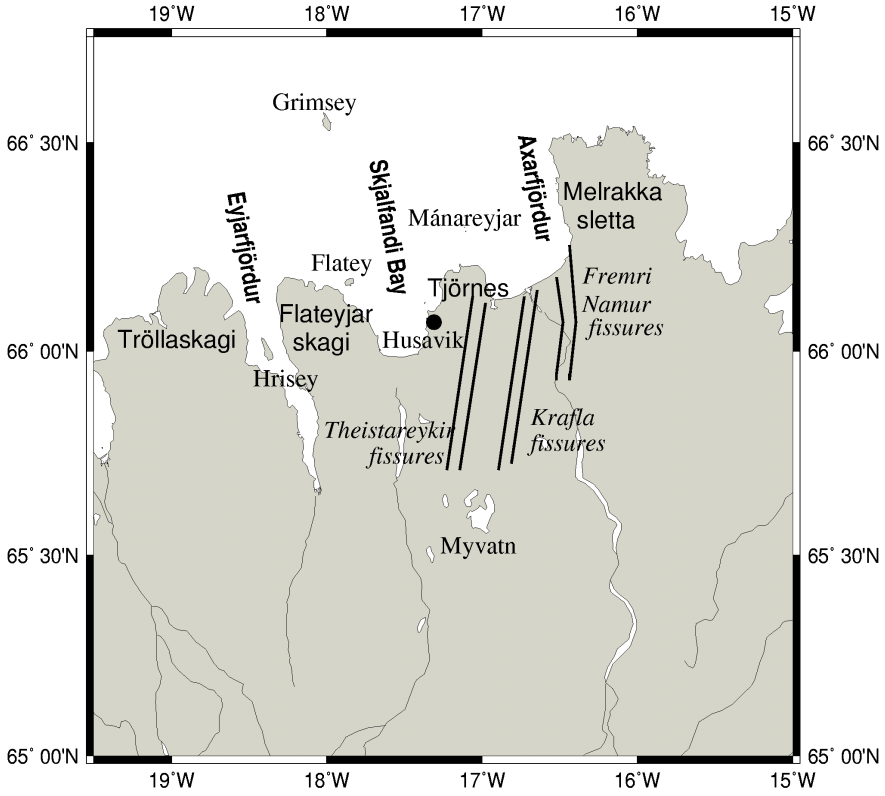

Figure 2: Map of northern Iceland, the peninsulas Tröllaskagi, Flateyjarskagi, Tjörnes and Melrakkasletta are marked as well as the main offshore regions Eyjarfjördur, Skjalfandi Bay and Axarfjördur, the islands Grimsey, Mánareyjar skerries Lagey and Haey, and Hrisey, the town of Husavik, lake Myvatn and the main fissure zones Theistareykir, Krafla and Fremri-Namur.

In 1724 the Myvatn Eldar (Moskito Water Fires) eruption starts off at the Krafla fissures (fig.2), a

reason to stay away from North Iceland, but 5 years of permament lava production allow for a lot of observations even in a society that is not as mobile as ours today. They are later on published as an edited version by Thoroddsen (1925). The geologists of that time are more interested in the age of the world and the flora and fauna of ages long gone, so the 17th century and 18th century are dedicated to the fossils of the Tjörnes Peninsula, the only major fossil outcrop in Iceland (fig.2) north of the town of Husavik (Strauch, 1963). Pliocene rocks deposited in a marine environment are situated on the hangigng wall of a steeply dipping right-lateral strike-slip fault, where the foot wall is entirely made up of tertiary flood basalts, the Husavik-Fault (fig.3).
In 1783 the big Laki eruption in southern Iceland delivers a chilly summer in most of Europe. Many beautiful sunsets can be observed due to the dust particles of the volcanic plume spreading in the atmosphere. They are stored in the paintings of contemporary artists. The king of Denmark thinks about evacuating the whole of Iceland, but that never happens. Rather the Europeans turn away from the Iceland and consequently, the big event is origin for a quiescence period in talk about minor eruptions in Iceland.

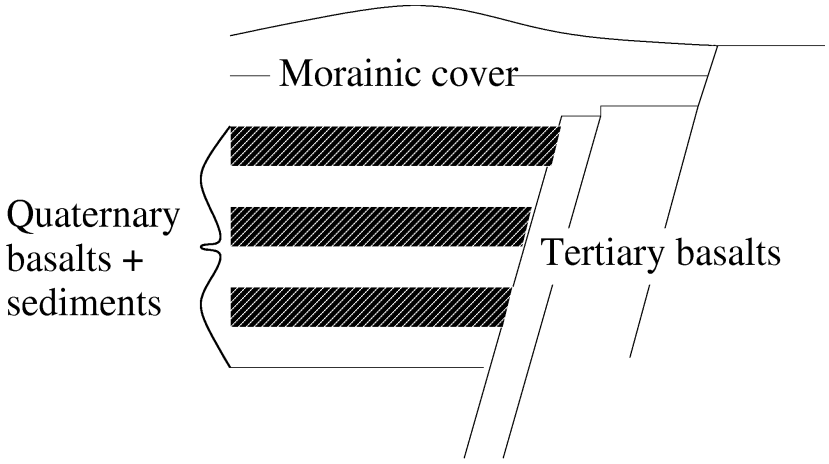

Figure 3: Schematic section of the Husavik Fault (modified after Saemundsson, 1974).

At the end of the 19th century, the field investigations of Thorwaldur Thorodssen (1855-1921) give the first modern outline of Iceland´s geology (Hansen, 1985). At about the same time seismological observations are introduced in Iceland. The north is recognized as a location of frequent earthquakes. Since volcanism remains more than a possibility, some easily identifiable earthquakes occur from 1868 and 1869 just north of the Tjörnes Peninsula (Vedurstofa, 1999). The cause is probably a volcanic fissure eruption in the TFZ. The Mánareyjar Eldar (Moonriver Islands Fires) eruption lights the nightsky near the islands Lagey and Haey (Strauch, 1963) north of the Tjörnes peninsula (Fig. 2), showing fiery outbursts and dark clouds (Thoroddsen, 1925). The location near the Mánareyjar (fig.2) remains unclear, because the eruption leaves no subaerial volcanic edifice like Surtsey in 1963. Only 4 years later a first major earthquake sequence (magnitude M=6.3) is recorded on the Husavik-Fault (Rögnvaldsson, 1998; Tryggvason, 1959).

1.2. Modern science in the 20th century

In the beginning of the 20th century, desaster strikes in northern Iceland. A major earthquake (magnitude M=6.3) destroys the fishing village of Dalvik in 1934 (Tryggvason, 1973), not far north from Akureyri and causes great damage to property throughout Iceland´s north. In the years following world war II, the TFZ is first defined, roughly as the area between Krafla and Kolbeinsey (Ward, 1971), along which epicenters are distributed (Tryggvason, 1959). Interest in the TFZ leads to inevtisgations on the island of Grimsey (fig.2). It is found to consist of southwest-dipping basalts

with intercalated conglomeratic sediment and hyaloclastite suggesting glacial conditions at the time of formation (Saemundsson, 1974). The island of Kolbeinsey is also found to be created during glacial times inferred from its structure as a table mountain and the palagonite formations sampled there (Sigurdsson and Brown, 1970). Since massive erosion is still taking place on the rocky icelandic outpost (Saemundsson and Hjartarson, 1994), its formation must be quite young and is attributed to the last ice age. The lineations of fractures and jointing are observed to be N25°E, i.e. subparallel to Kolbeinsey Ridge.

The emergence of the theory of plate tectonics sees the TFZ redefined as a 120-150 km wide transform fault running at 67° oblique to the Mid Atlantic Ridge (MAR) (Sykes, 1967) and connecting the southern part of Kolbeinsey Ridge in the Kolbeinsey area with the northermost part of Iceland´s "axial rifting zone" (Saemundsson, 1974) along the Tjörnes-Mánareyjar ridge. Transform faults striking at 60° in relation to the rifting zone are common on the MAR (Macdonald, 1986), but more than 100 km width is much wider than usual.

The 75 km wide seismogenic belt which served as the basic definition of the TFZ (Tryggvason, 1959) is recognized to find its surface expression in the Husavik-Flatey Fault (HFF) near the large fossiliferous deposits north of Husavik striking through the island of Flatey. A relative bathymetric low marks the continuation offshore along a gravity expression that is meant to be a sediment filled graben (Palmason, 1974).

The main north-south trending systems are layed out by Saemundsson (1974) as the Axarfjördur, Skjalfandi Trough and Eyjarfjördur (fig.2) separated by the Manareyjar Ridge extending 40 km from the northernmost point of Tjörnes Peninsula. McMaster et al. (1977) attribute these north-south trending features to en echelon movement due to the shear forces in the TFZ. They find passive rifting patterns in Skjalfandi Trough and a „structural-volcanic discontinuity“ at 66°40´N in Eyjarfjördur which is understood as the southernmost end of Kolbeinsey Ridge. The WNW trending strike-slip fault of Tryggvason (1973) is doubted. Sediment depth in the Eyjarfördur discontinuity from their line drawings can be observed as 0.13 s in terms of two-way traveltime (TWT). The prolongation of their proposed active rifting axis from the Iceland towards the offshore parts shifts from the Tjörnes peninsula to Axarfjördur which is covered by 0.1 s TWT of sediments (McMaster et al., 1977).

The discussion is focussed on the main plate boundary at that time. While the Husavik-Fault seems to be a good candidate, it cannot explain the complex geology north of it and it fails to explain the large earthquake in Dalvik to the south. The history of the spreading axis however seems to be reasonably explained by a shift from Grimseyjargrunn to Axarfjördur about 1 Ma ago. This spreading axis movement in the north is interpreted as a hint on an eastward shift of the whole icelandic spreading zone. This movement is projected from the icelandic south where two spreading axis can be observed, the Reykjanes-Langjökull Zone including the Katla ridge (Saemundsson, 1974) and the neovolcanic zone including the hotspot area around Grimsvötn volcano beneath Vatnajökull.

Finally the conclusion is reached, that the TFZ might be offset since its formation. To proof this thesis, a first investigation focusses on mapping the active volcanic vents. The island of Flatey is a direct result of volcanism in the area around it, since the interglacial lava is not tilted (Peturss, 1959). It seems to be active still, since it has risen by 1 m during the 20th century (Gunnarson et al., 1984); whether as an isostatic rebound from the Ice Age or as a response to geodynamic activity is not known. Fresh eruption products are found in the submarine area east of Grimsey at a bathymetric high called Nafir, which is connected to strong seismic activity. At the submarine Hóll (icel. "hill") postglacial basalts displaying near vent characteristics are dredged (McMaster et al., 1977), but no account of credibility towards the stability of the original position of the rocks can be given.

Fishermen report rising gas bubbles south of Kolbeinsey in 1974, but though some geothermal source is made out (Saemundsson, 1974), they cannot be attributed to an obvious volcanic edifice. Investigations by the submarine ALVIN at the East Pacific Rise in 1979 (Weiner, 1986) expands the knowledge of submarine fluid evolution towards the newly found hydrothermal vent-field. The first evaluation for an icelandic hydrothermal vent-field near Kolbeinsey appears by Olafsson et al. (1990).

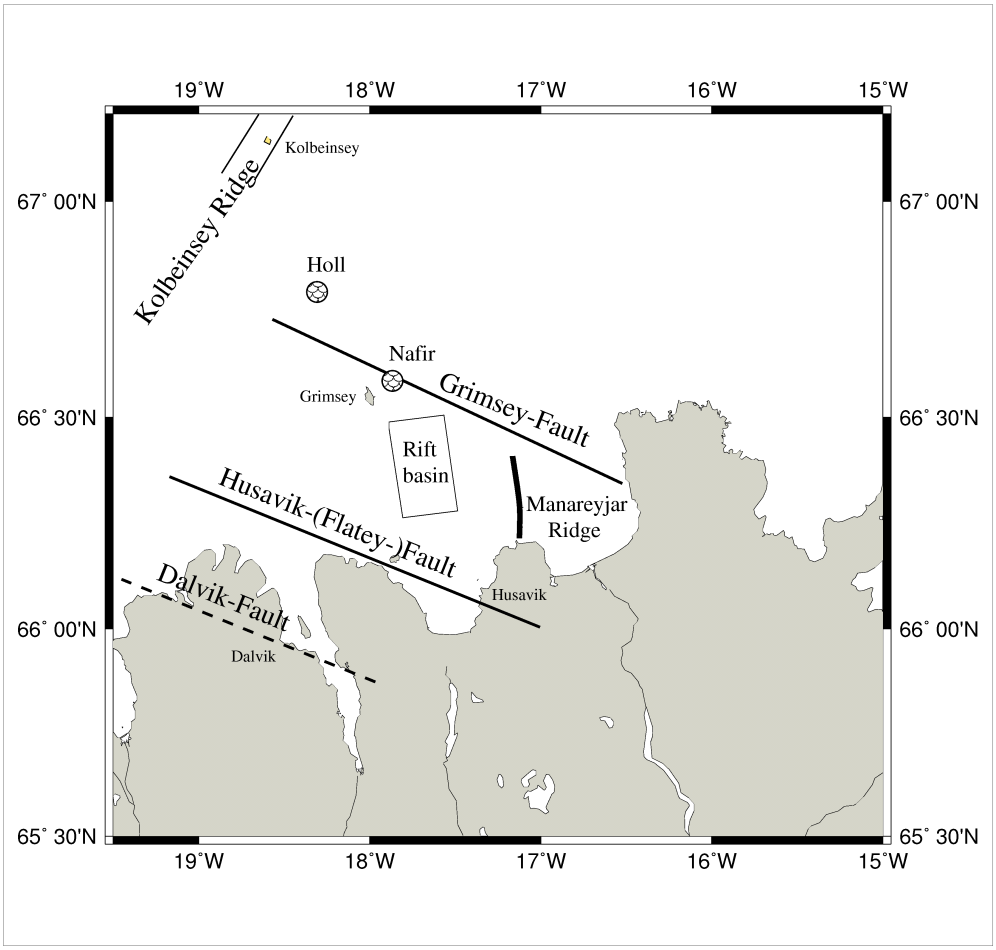

Figure 4: The tectonic system of the Tjörnes Fracture Zone as outlined by Einarson (1976) and some surfac expression as depicted by McMaster et al. (1977), i.e. the Mánareyjar ridge as a northern prolongation of the Theistareykir fissure swarm (fig. 2), the submarine volcanoes Hóll and Nafir and a rift basin. This picture does not explain seismotectonic events in Axarfjördur, nor can it show a compelling evidence for the connection of Husavik-Flatey-Fault and Kolbeinsey Ridge.

The modern picture of the TFZ is introduced by Einarsson (1976) derived from a differential locationing system for the northern epicenter region. He divides the belt into three major fracture zones, the already discussed apparent plate boundary, the Husavik(-Flatey)-Fault (HFF) plus the Grimsey Fault and the Dalvik fault (Fig.4). The activity of the Dalvik Fault, the only onshore structure, is lowest, but the zone is easily seen as a low in satellite topography. However, smaller scale surface expressions as foliations or crack are hard to find in the field. An offset along the Eyjarfjord south of the island of Hrísey is meant to be the continuation of this lineament, which is confirmed by the modern seismologic monitoring system Southern Icelandic Lowland Network (SIL) (Rögnvaldsson, 1998). The Grímsey-Lineament is a pure offshore structure and the first rough bathymetric surveys do not enable its detection on the surface. The passive rift system in Skjalfandi Trough and the active rift system in Axarfjördur of McMaster et al. (1977) are located above it and the submarine volcanoes Nafir, Hóll and the Mánareyjar Islands (Fig.4), as well.
Magnetic data of the area are as complex as the geological setting. Kolbeinsey Ridge is easily identified by a positive peak (McMaster et al., 1977, Vogt et al., 1980). A further substantial positive peak is measured north of the Tjörnes Peninsula and north of Melrakkaslétta Peninsula, whereas negative anomalies mark Grimseyjargrunn (Meyer et al., 1972). The negative anomaly is interpreted as a remnant of Matuyama volcanism in the area (Saemundsson, 1974). The decrease of magnetic amplitude from Kolbeinsey Ridge towards Iceland is explained by tidal and glacial erosion and

alteration (Vogt et al., 1980).

Seismic reflection surveys follow the magnetic surveys. Plans for an ODP drilling in the „volcano-structural discontinuity“ in Eyjarfördur to inspect the proposed connection between rift faulting in the discontinuity and Kolbeinsey Ridge (Flóvenz and Gunnarson, 1991) are declined. Confirming the en echelon model of McMaster et al. (1977), the TFZ fits quite well to clay models of strike slip zones. Typical formations of en echelon patterns which originated as Riedel shears provide a strong evidence. Seismic stratigraphy is examined to find constraints for the age and movement of the TFZ (Thors, 1982). Sediment thicknesses of up to 4 km in the dominant strike slip fault, the HFF, appear in a report of icelandic authorities on the gravity low (see above, Palmason, 1974). A drilling on the island of Flatey uncovers only volcaniclastic sediments up to a depth of 550 m beneath a thin layer of tilted lavas with a high sedimentation rate of 1km/Ma (Gunnarson et al., 1984).
Neben (1992) in his thesis highlights the southernmost part of Kolbeinsey Ridge and the transition to the TFZ. He shows the TFZ as a single fault crosscutting the actual Mid Atlantic Ridge which runs from Grimseyjargrunn to Kolbeinsey Ridge. Though this assumption follows the general mode at that time he observes some interesting structures. This is a hint on the location of the southernmost Kolbeinsey Ridge. In conjunction with modern topographic data this shows the end of Kolbeinsey Ridge south of the island of Kolbeinsey. Further north seismic amplitude polarity reversal hint on hydrothermal activity north of Kolbeinsey. Just southeast of Kolbeinsey very weak reflectors are interpreted as a magma chamber. The chamber, however, is not located directly under the prolongation of the ridge but offset to the east on the transition to Grimseyjargrunn. The hint from an inversion of seismic velocity is not unique. Typical velocities of the sediments in the TFZ are given as 1600 m/s to 1800 m/s and those of basalt as 3400 m/s to 3700 m/s.

In the 1990s computers introduce numerical models to the TFZ. Thus, there is a need to accumulate large sets of data to test them. Geologists in the field start off by counting dykes and fractures and determining their orientation. The direct result is the exact placing of those zones where the HFF meets the Theistareykir fissure zones (fig.2) and where the Grimsey Fault allegedly meets the Fremri-Namur and Krafla fissure swarms directly offshore the east of Melrakkasletta Peninsula (Gudmundsson et al., 1993). These structural indications are complemented by observations of curved fabric throughout Tröllaskagi (Långbacka and Gudmundsson, 1995) and Flatyeyjarskagi (Långbacka and Gudmundsson, 1995; Fjäder et al., 1994). Extension of the active rift zones on the icelandic mainland - the Northern Volcanic Zone (NVZ) and Kolbeinsey Ridge - is implied to be the driving force of the dynamics in the transform zone system. The structural finite element models predict the formation of the curved dikes due to this extension (structural geology calls these extensional features mode I cracks) at Kolbeinsey Ridge and the NVZ as they predict the formation of the HFF along the zone of maximum shear stress. The principal stress implied by the model is oriented parallel to the strike-slip lineaments observed. The future according to these models will see an increased overlap between HFF and the extensional features, thus resulting in a perpendicular rather than oblique transform fault. In their field measurements on land, Fjäder et al. (1994) find hints for extended alteration in veins along and crosscutting the dykes, the ramins of hydrothermalism. All models fail to predict the evolution of Dalvik and Grimsey Faults. There is, however, seismologic evidence - i.e. from evaluating focal mechanisms - that the Dalvik Fault is rather a north trending sinistral fault than a fault subparallel to HFF (Långbacka and Gudmundsson, 1995). So what happens in the ocean at the Grimsey Fault ?

1.3. The Grimsey Lineament

„Double, double toil and trouble;
Fire burn, and cauldron bubble.“
(Shakespeare, Macbeth)

The term Lineament expresses the lineation of epicenters and captures the impossibility to trace at in simple strike-slip fault structures near the surface. It is introduced to account for the complex surface expression of the structure. By including Nafir submarine volcano it incorporates the most seismically active part of the TFZ (McMaster et al., 1977), but hidden offshore the hazard probability is seemingly low. Earthquakes have occured along the lineament during the Krafla fires 1983/84 as a follow-up to the extensional rifting in the Krafla area (Gudmundsson, 1993), but no direct evidence of their counterplay has been found. The influence is obvious at least in the change of directions of minor faults at the eastern end of the Axarfjördur, where the strike continues from N2°W south of it to N20°W north of it (Gudmundsson, 1993). The graben structures have been described by McMaster et al. (1977). A first review of the area occurs in Rögnvaldsson et al. (1998), where faults and their activity are contrasted by evaluating the frequency and fault plane solutions for microearthquakes. The Icelandic Meteorological Office (Vedurstofa Islands) contributes an active Ocean-Bottom-Seimometer (OBS) survey in cooperation with japanese researchers (Mochizuki et al., 1995). The report issues p-wave velocities for basalts in shallow layers as 3.3 km/s to 4.5 km/s and in deeper regions (2-6 km) as 4.5 to 6 km/s. P-wave velocities of sediments are measured as 2 to 2.2 km/s. The active rift assumed by McMaster et al. (1977) is not supproted.

New undersea geothermal area discovered off north Iceland

A team of German, Canadian and Icelandic scientitsts have uncovered new undersea geothermal areas in the sea off north Iceland, near the island of Grímsey, and further north, to the south of the island Kolbeinsey.
Two areas were found off Grímsey at depths of 380-400m. One of those was quite large, 100m wide and 2-300m long, and very powerful. The expedition also found in Eyjafjördur fjord something no one had expected - an underwater geothermally formed stalagmite the height of a twelve-story building. The knife-sharp tower's base lies at a depth of 63m, from which it ascends to 34m below sea level. Nothing similar has ever been found in Iceland, or anywhere else in the world, to the best of anyone's knowledge.

(excerpt from Daily News from Iceland, 05/06/1997)

The region is finally in the spotlight, when a german-icelandic-canadian crew led by researchers from the University of Kiel discovers a hydrothermal vent-field east of Grimsey (Botz et al., 1999; Hannington et al., submitted), the first evidence for active geothermal activity. Interestingly enough a needle-like structure of hydrothermal precipitates is also prospected in the Eyjarfjord in the continuation of the apparent Dalvik Lineament.

1.4. Transform zones

As already indicated, the TFZ was originally described as a transform fault (Sykes, 1967) rather than a transform zone. In the North Atlantic, oceanic transform faults create zones of thin crust. Usually, these transform faults strike perpendicular to the ridge trend (Keary and Vine, 1996). In the case of the TFZ, the strike is oblique. Therefore, Saemundsson (1974) and McMaster et al. (1977) proposed a transform zone model for the TFZ. A transform zone is typical for continental landmasses rather than oceanic and is e.g. found in the San Andreas graben (Crowell, 1974). Transform zones consist of several strike-slip faults which move in conjunction with a principal rupture. The principal rupture

in the case of the TFZ is the HFF. The principal rupture of a transform zone is also known as a transform fault, so not the TFZ but the HFF is the transform fault. The dextral shear movement between HFF and Grimsey Lineament causes the formation of so-called extensional pull-apart basins and bifurcated faults which are commonly known as duplexes or Riedel shears. The extensional movement leads to a stretching and thinning of the crust.
In the case of oceanic transform faults, the thin crust typically consists of hydrothermally altered basalt and serpentinized mafic and ultramafic rocks (Detrick et al., 1993). Ultramafic or serpentinized rocks have not been drilled up to a depth of 2 km in the Flatey drilling in North Iceland (Gunnarsson et al., 1984). Hydrothermal alterations occur only locally. The serpentinization is explained as a consequence of peridotite production far from the few magmatic centers along slow-spreading ridges where magma rises to the surface and is altered by seawater to serpentinite (Cannat et al., 1995). The non-existence of serpentinite is thus a hint on recent magma production and thus on relative closeness to a magmatic center.
In the case of continental transform zones, magma rise to the surface or the presence of geothermal fields have been observed. The San Andreas graben system forms a pull-apart basin, which is termed Salton Trough where geothermal fields have been observed (Crowell, 1974). Such transform zones are called leaky (Thompson and Melson, 1972; Taylor et al., 1994).
The initial hypothesis for the TFZ proposed the formation of three major pull-apart basins, the Axarfjördur, Skjalfandi and Eyjarfjördur Troughs after shear between Grimsey Lineament and HFF (McMaster et al., 1977). The hydrothermal vent-field and volcanism would thus be expected in the center of these pull-apart basin, where the the crust is thinnest (Crowell, 1974). This hypothesis is challenged for the TFZ by geothermal fields along the Grimsey Lineament.
The alternative model is the icelandic model (Gudmundsson et al., 1993), which describes the TFZ as an oceanic transform fault. By rotation the obliqueness will eventually vanish and turn the transform zone into a typical transform fault. Whether this is the typical evolution of any continental transform fault cannot be implied by the present investigations. However, the alternative model suggests a singular bending of fractures at the end of the Grimsey Lineament, "where tension would be greatest". This bending is also an evidence for zones of high permeability (Barton et al., 1995), which is important for the formation of hydrothermal fields. Thus, the singularity of bending must be verified.

1.5. Database

A brief outline of the database already published shall follow. Bathymetric data (Fig. 5a) were compiled by Sandwell et al. (1997) from data of Meyer et al. (1972), the icelandic hydrographic survey and the satellites ETOPO5 and GEOSAT. Gravity surveys (Fig. 5c) (also compiled by Sandwell et al., 1997) were undertaken by Palmason (1974) and NOAA (1998). The magnetic reference dataset (Fig. 5b) was compiled from aeromagnetic surveys of Iceland (Johnsson, 1995) and Kolbeinsey Ridge (Vogt et al., 1980). The gravity field will be intepreted in relative terms, i.e. values of 30 mGal are interpreted as the local average (Fig. 5c), the magnetic field will only be used in terms of the Epoch they represent, i.e. Brunhes or Matuyama.
Published faults (Fig. 6a) (Neben, 1992; McMaster et al., 1977; Flovenz and Gunnarson, 1989; Långbacka and Gudmundsson, 1995) in the marine area were digitized once more to reduce the

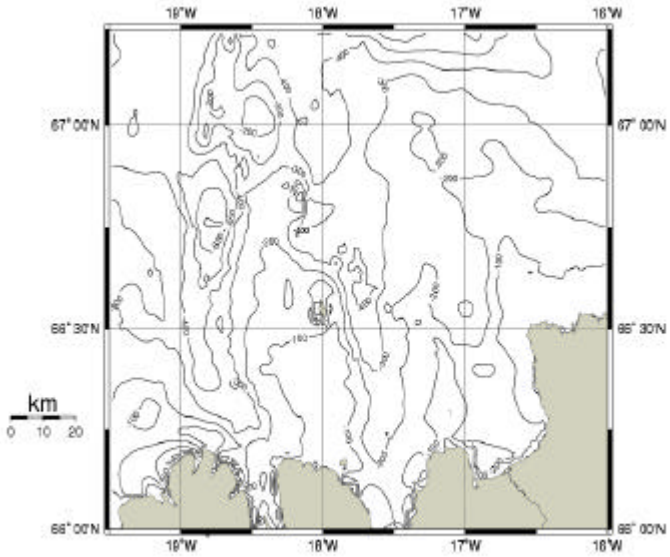

Figure 5: *a) The bathymetry contours in the TFZ show the dominating north-south trending fjord structures of Eyjafjördur and Skjalfandi Bay as well as Kolbeinsey Ridge in the north and the bathymetric high around Grimsey.*

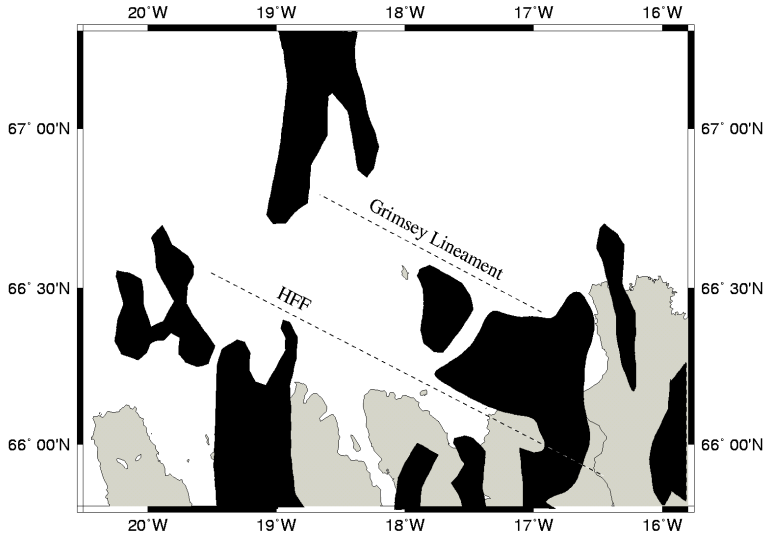

b) Magnetic lineations visualized by aeromagnetic surveys show broken structures. Kolbeinsey Ridge (positive anomalies are painted in black) is splitting in the south with one acis trending towards Tröllaskagi and another towards Tjörnes. Both peninsulas are showing positive anomalies. An interesting spot is the small positive anomaly southeast of Grimsey, which is located on the transition from Grimsey shoal to Skjalfandi Bay.

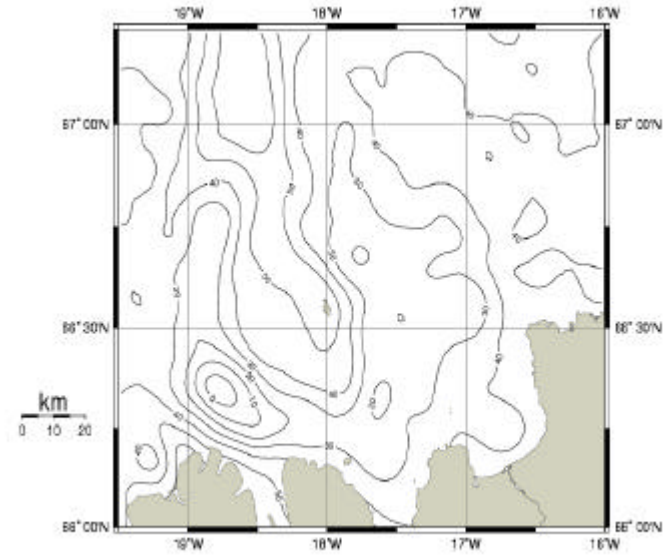

c) The free air gravity anomalies (annotation in mGal) show high values above the ridge and southeastward trending along the Grimsey Lineament towards Grimsey whereas the basins show the lowest values at 0 mGal, where HFF and the Eyjafjördur join. The Grimsey Lineament is evident by a gravity low, as well.

information to non-interpolated data. This allows a reinterpretation in the light of new data from a new survey. The land data adjacent to the TFZ were taken as published, because they are already known in a much higher resolution.
A preliminary earthquake catalogue of ~19000 quakes from 1994 to 2000 of magnitudes of 1.5 and higher (Fig. 6b) (Vedurstofa, 2000) was used as an interpretation tool for tectonic patterns and deeper layers. The application of the data for our purposes is reasoned in the Appendix.
All these data have been compiled to form a complete dataset to allow a detailed geological description and map of the TFZ. A new seismic survey in 1999 was complemented by bathymetric soundings, dredging, gravity coring, gasgeochemical sampling of the water column and diving by the submersible JAGO.

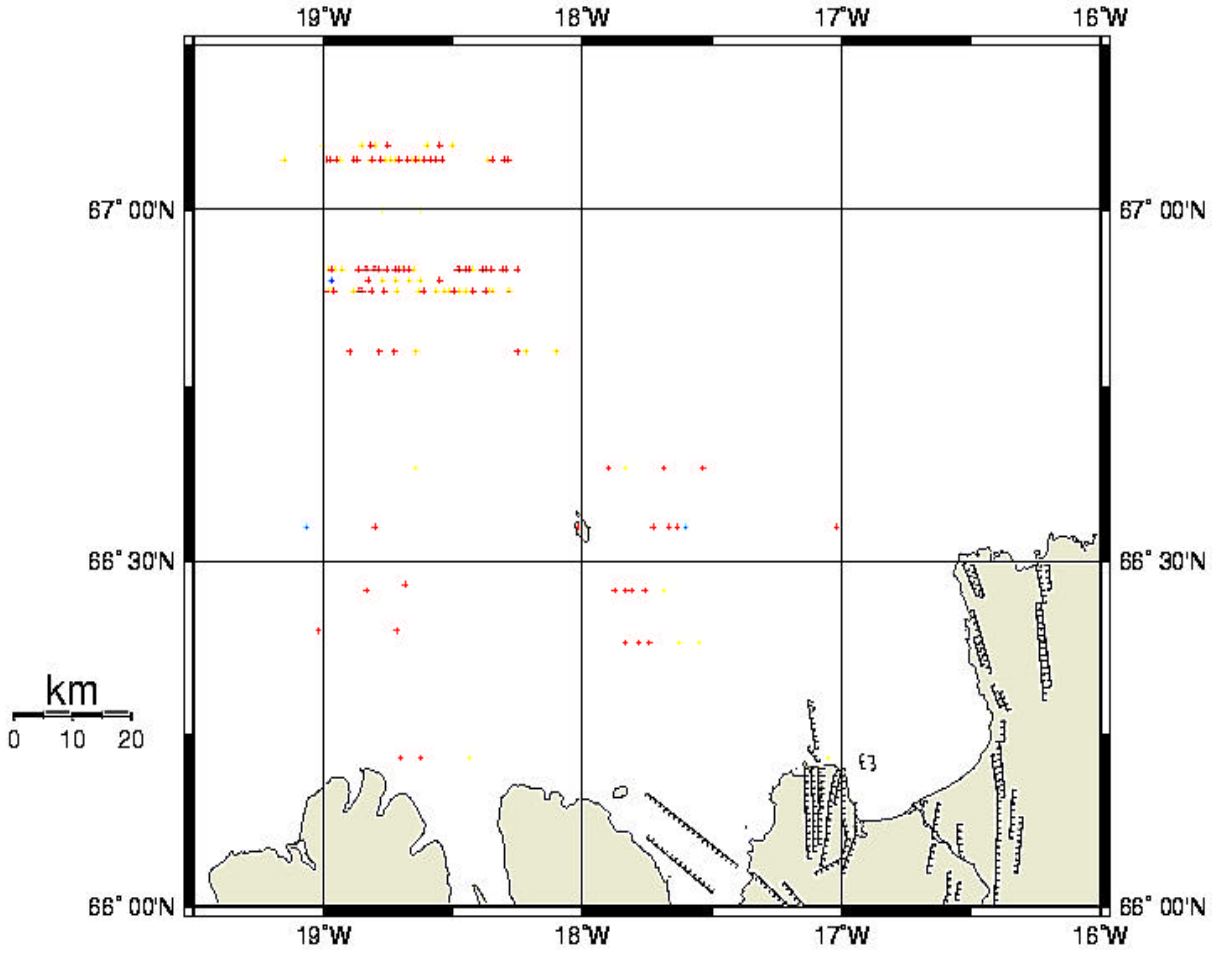

Figure 6: *a) The faults on land have been drawn as faults, whereas the marine faults have only been marked where they have been identified on reflection seismic profiles, where red marks east dipping faults and green west dipping faults. These fault outcrops have not been connected to leave space for further lines to enhance interpretation, which are provided by the new survey presented.*

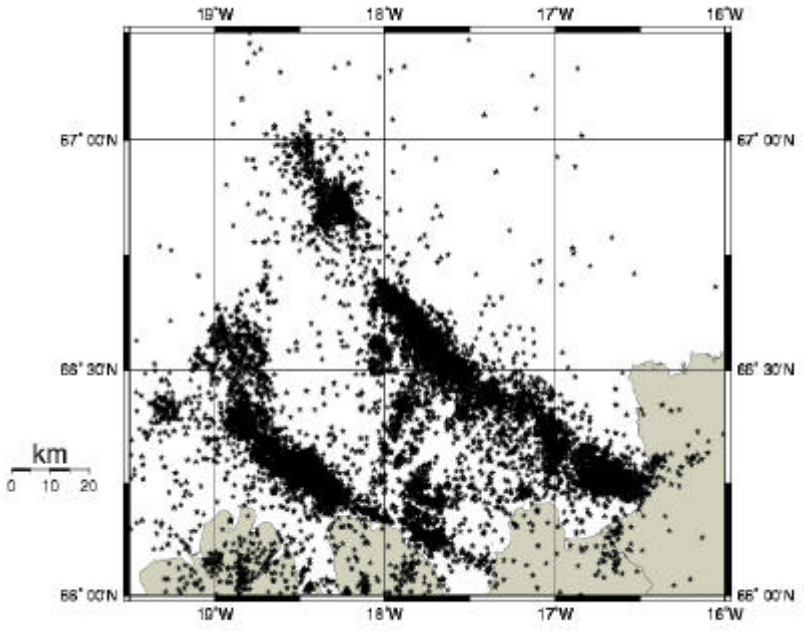

Figure 6: *b) The locations of hypocenters in the area mark clearly the major lineaments of the transform zone, the Grimsey Lineament slightly north of Grimsey up to Axarfjördur and further south, the HFF. In the north, joining Grimsey Lineament and Kolbeinsey Ridge a further clustering of hypocenters is observed as in the Eyjafördur, where it joins the HFF. Grimsey Lineament and HFF appear to be joined by a linear earth quakes pattern from Grimsey along Skjalfandi Bay. Most of the hypocenters seem to delineate deeper structures which are not reflected by published outcropping faults.*

To get a new bathymetric base, satellite data from GEOSAT, ETOPO5 and marine trackline data (NOAA, 1998) complemented the sounding campaign results (Fig. 7), because the Sandwell dataset is already gridded and does not provide original results. The described vent-field east of Grimsey was a main target of the campaign, thus the resolution was increased foremost in Skjalfandi Bay.
Dredging and coring in conjunction with older rock samples of the area (McMaster et al., 1977; Reimers et al., 1989, Devey, 1993; Oehmig and Wallrabe, 1993; Stoffers et al., 1997; Devey et al., 1997) finally supplied a list of locations for different lithologies in the area (Fig. 8).

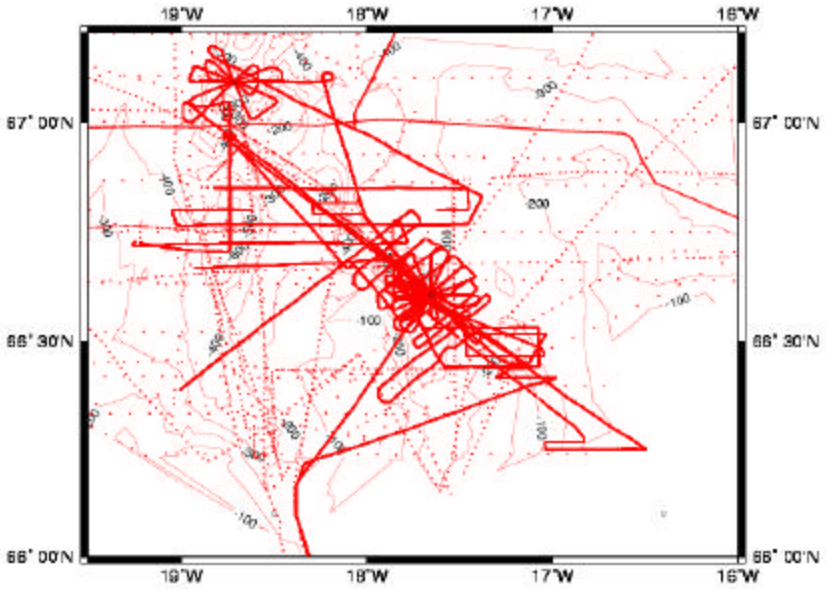

Figure 7: *The bathymetric soundings were complemented by satellite data (GEOSAT, ETOPO5) and marine trackline data (NOAA, 1998) to result in a new bathymetric grid for the survey area. The low resolution bathymetry is plotted in the background and will be used in all following depictions of bathymetry.*

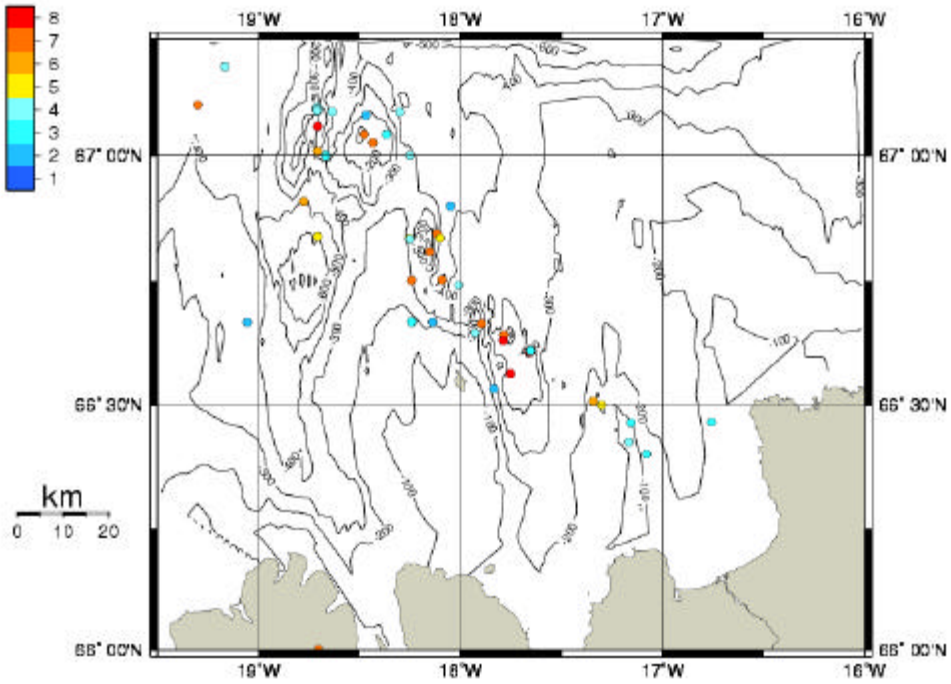

Figure 8: *The rocks sampled in the TFZ were compiled into 8 different classes: 1: Mud, 2: Ooze, 3: River gravel ,4: Conglomerates and sands , 5: Volcaniclastics, 6: Volcanic glass, 7: Basalts, 8: Precipitates (Anhydrites or Pyrites).*

1.6. A new survey

The seismic cruise as part of the combined geoscientific survey in 1999 is the focus of the present thesis. The reflection seismic survey was performed by single airguns (0.33l to 0.87l) and covered 36 profiles by a 600m streamer offset 230m from the source (Fig. 9). In a typical water depth of 400m in the area this covered reflection angles of up to 60° and allowed a detailed reflectivity analysis of the sea floor material. Shots were fired each 5 s or 10 s and the ship's velocity was kept constant at

~5 knots. The recorded shot gathers were sorted into Common Mid Points (CMPs). Although the Fresnel zone in 400 m depth is nearly 90 m for a a dominant frequency of 50 Hz, the CMPs are spaced 12.5 m apart from each other and reached 12-fold or 24-fold depending on the firing rate because of the constant offset of 25 m between the receiver arrays within the streamer. The data was processed to allow true-amplitude recovery from the seismic data for the sea floor.

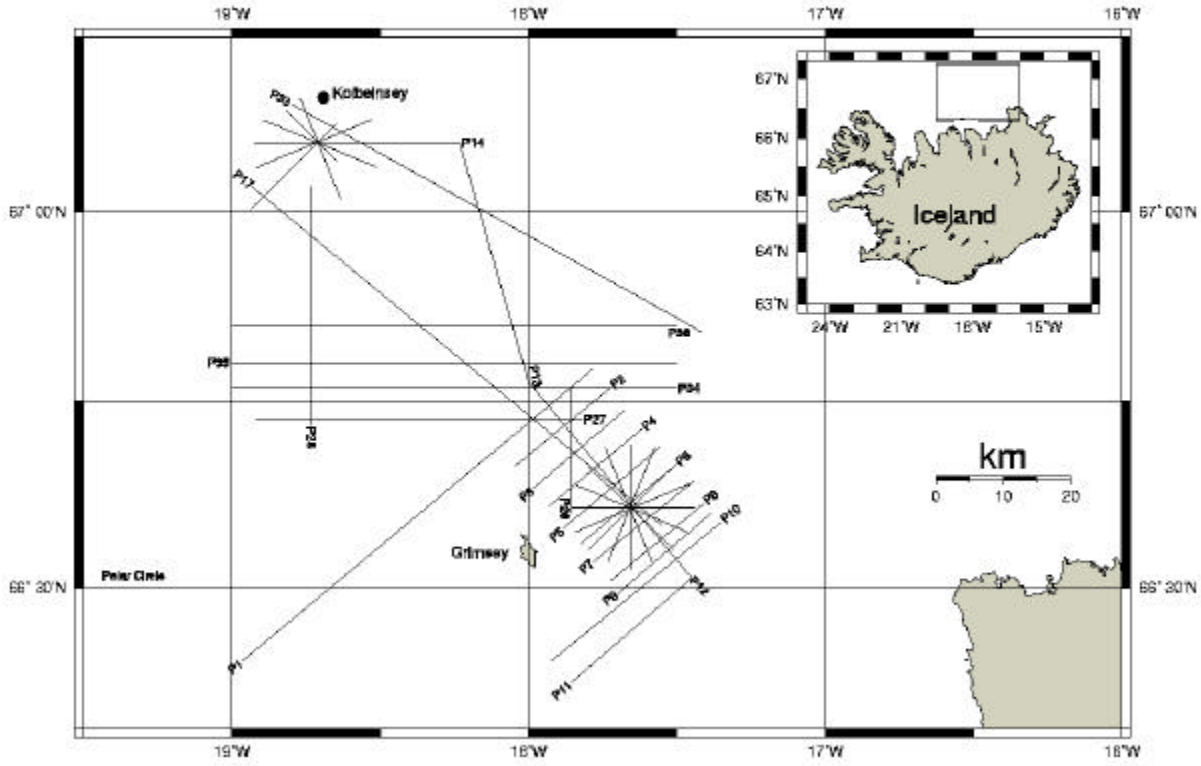

Figure 9: *The map shows all seismic reflections lines recorded during R/V Poseidon cruise 252. The numbers are printed at each beginning of a profile and will be used throughout this thesis with reference to this figure.*

1.7. Aim and scope of the thesis

The reflectivity analysis of the seafloor in conjunction with seismostratigraphic and structural interpretation was used to derive a geological map of the TFZ. This map is foremost representative for Skjalfandi Trough and the area around Grimsey Hydrothermal Field (GHF), whereas the coverage of the southern end of Kolbeinsey Ridge and Eyjarfjördur is more scarce. The transition from Kolbeinsey Ridge to Eyjarfördur is an interesting region, which is also presented in this thesis in brief.

First of all, the tools for deriving the geological map are presented in chapter 2. This is a technical chapter on seafloor mapping, describing the brief true-amplitude processing, the principal method of reflectivity mapping of the seafloor by aid of neural networks and the implications for lithology inferred from reflectivity and morphology of the seafloor.

Chapter 3 presents the results of chapter 2 along with the results of the presented database and new gasgeochemical data sampled in the area. That way, the expected pull-apart structures were mapped and their geodynamic roots uncovered, which explain the formation of the hydrothermal field, though the dynamics differ significantly from presented models.

The results and perspectives for the method and the area are presented in the conclusions chapter 4.

Self-Organizing
Seafloor
mapping

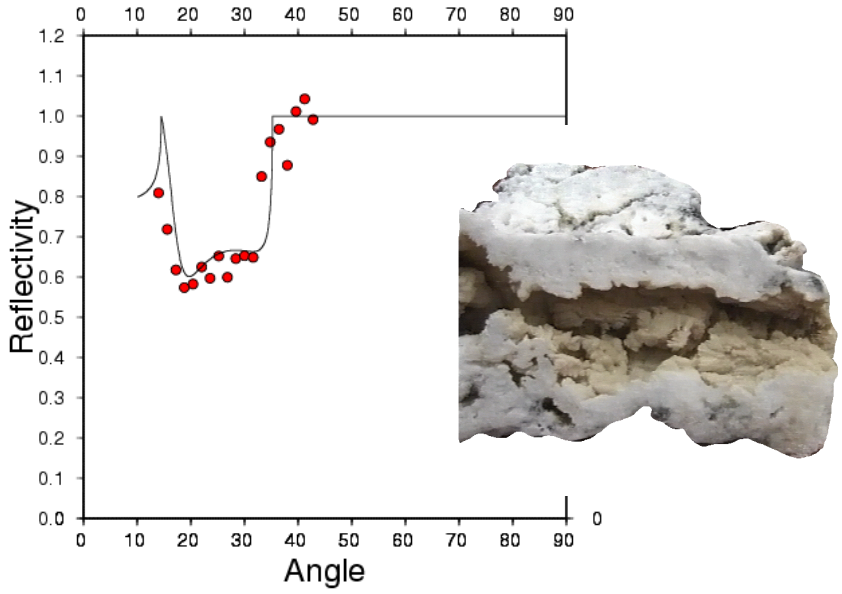

2. Self-organizing seafloor mapping

"Though this be madness,
yet there is method in''t"
(Shakespeare, Hamlet)

To unravel the lithology of the seafloor by seismic means is the key to develop a geological map of the Tjörnes Fracture Zone. In seismic surveys the seafloor is usually not the primary target. Projects that use the seafloor sound information are a common interest of oceanography (Stanton, 1995; Ross, 1922), geology (Jackson et al., 1986) and geophysics e.g. for military purposes (Lambert, 1988) in the detection of mines, platform locations or targets. The fundamental relation between physical and lithological rock properties is the quantity called reflectivity or reflection coefficient. Reflectivity is the amplitude ratio of a reflected ray to an incident ray. It can be derived for the elastic case (see Appendix) in terms of density ρ, compressional wave *(or p-wave)* velocity v_p and shear wave *(or s-wave)* velocity v_s for the layers next to a boundary (Fig. 10).

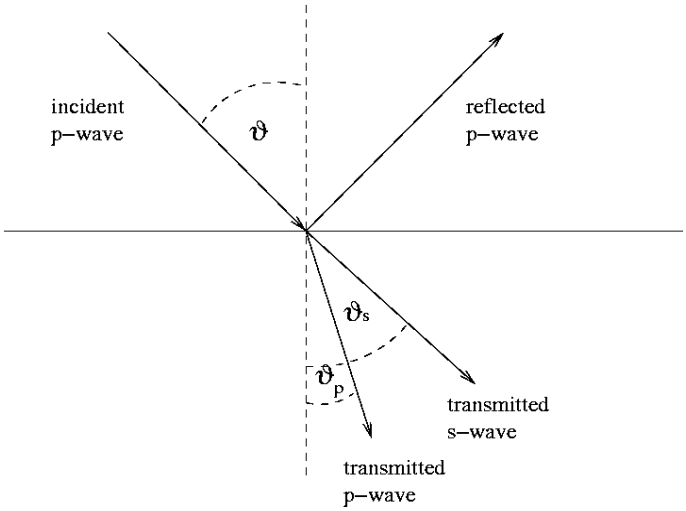

***Figure 10**: Fluid-solid boundary. The incident ray of a seismic wave is reflected into a p-wave and transmitted as p-wave and s-wave at the boundary, where reflectivity can be evaluated by the Rayleigh equation (0).*

The Zoeppritz equations link these physical rock parameters ρ, v_p and v_s and reflectivity R. Here they are presented for the seafloor case, i.e. for an elastic boundary between fluids and solids. One of the shortest expression to denote was published by Rayleigh (1886)[1]:

$$R(\vartheta) = \frac{z_p \cos^2 2\vartheta_s + z_s \sin^2 2\vartheta_s - z_{water}}{z_p \cos^2 2\vartheta_s + z_s \sin^2 2\vartheta_s + z_{water}} \quad , \qquad (0)$$

where ϑ_s is the angle of transmission for the s-wave and the z's are the impedances, i.e.

$$z_{water} = \frac{\rho_{water} v_{water}}{\sin\vartheta} \quad , \quad z_p = \frac{\rho_{floor} v_p}{\sin\vartheta_p} \quad \text{and} \quad z_s = \frac{\rho_{floor} v_s}{\sin\vartheta_s} \quad .$$

1***Important to note:***. *For angles of total reflection R(ϑ) is complex and for any case where $v_s > v_{water}$, the equation has to be calculated with complex numbers (see Appendix). That is particularly important when programming in C, which does not support complex numbers. Two critical angles will be present in this complex case, one where the p-wave is no longer transmitted into the floor and one where the s-wave is no longer transmitted into the floor. In the non-complex case, there will always be an s-wave transmitted into the seafloor after conversion of the acoustic wave at the fluid-solid boundary.*

ρ_{water} and ρ_{floor} are the densities of sea water and seafloor, v_p and v_s the compressional and shear wave velocity in the seafloor medium, v_{water} the acoustic velocity in water, ϑ is the angle of incidence and ϑ_p the angle of transmission for the compressional wave (Fig. 10). These symbols will be used througout this thesis (cf. list of symbols).

This is not the first attempt to map the physical and lithological properties of the seafloor. However, there is one distinct advantage of the present method. Whereas the petroleum industry (Brunson et al., 1985) or military methods (Lambert, 1988) want to resolve the seafloor properties for any individual spot on the sea bottom, the present method uses laterally averaged quantities and qualities that are deducted from a neural network approach. The aim is to uncover the dominant lithologies in a geologically complex area that is visible only spotwise by geological coring or submersible diving. Afterwards, this overall structure can be a key to unravel local structures of interest by evaluating deviations from the statistical mean. The interpretation of mean values will not diminish the influence of other physical properties of the seafloor which are associated with reflectivity, i.e. the small-scale structure of the seafloor represented foremost by roughness and thin layers. Both can be shown to be dependent on depth of the seafloor and the dominant frequency (i.e. wavelength) of the incident acoustic signal.
The Fresnel zone (*or correctly, first Fresnel zone*) which is related to depth and frequency constrains the lateral resolution. Anything smaller than the Fresnel zone and in a distance smaller than half the Fresnel zone inline or crossline to the common mid reflection point (CMP) will act as one reflector. Reflectivity input of smaller objects as boulders, dunes or small ridges will be termed *roughness effects* here. This is similar to the approach of Lerche and Hill (1985) or Stanton (1985). Some authors (Jackson et al., 1986) will also term effects of larger undulations roughness, however, in the present context these effects will rather be dealt with in terms of dipping strata (which is dealt with in the Appendix).
The length of the signal pulse which is related to frequency restrains the vertical resolution. The vertical resolution varies in 3 dimensions but can be approximated as a 2D effect, in which case anything smaller than a quarter wavelength is usually termed a *thin layer* (Widess, 1973).
The analysis of amplitudes in the way just described is commonly called amplitude variation with offset (AVO) (Castagna and Backus, 1993; Ursin and Ekren, 1995) or amplitude variation with angle (AVA) in reflection seismic vocabulary. AVO/AVA analysis can be performed by choosing the decisive reflector amplitudes, if the signal-to-noise ratio is high enough (Hampson and Russell, 1997). For calibration the reflection amplitudes are compared to seafloor multiple reflections (Castagna and Backus, 1993), because the ray can be traced easily to deduct the reflection angle. However, the amplitude recorded at the time of the multiple reflection is often a composite amplitude in an area where hard rock follows at relatively shallow depths and scattering may occur (Brink, 1980). The direct wave is often avoided, because the incidence of direct wave is nearly vertical to the incidence of the reflected wave and thus exhibits totally different effects at the receiver (Meißner and Stegena, 1977). In the present approach the direct wave will be used and its quality control will be outlined.

The first reflector in marine surveys is commonly the seafloor. In that case it is trivial to derive the reflectivity at various angles from AVA analysis, because for a homogenous sea water medium the traveltime of a wave and its incidence angle can be determined precisely (see Appendix). In the following chapters the term reflectivity curve or trend will be used to describe reflectivities at all recorded offsets, or respectively incidence angles to AVA.

2.1. Cluster analysis - a new strategy to map the seafloor

The principal problems and advantages of reflectivity analysis have been introduced. A new strategy will be developped to overcome old problems and arrive at the new goal of averaging seafloor

properties. The first step is classical. From the recorded traces two amplitudes are extracted, the direct wave amplitude and the first reflected arrival (FRA) amplitude, the direct wave amplitude is extracted for the nearest channel to the source, the FRA amplitude for every trace. The amplitude ratios are used to determine reflectivites. These are stored for each trace and the dataset is sorted into CMPs.

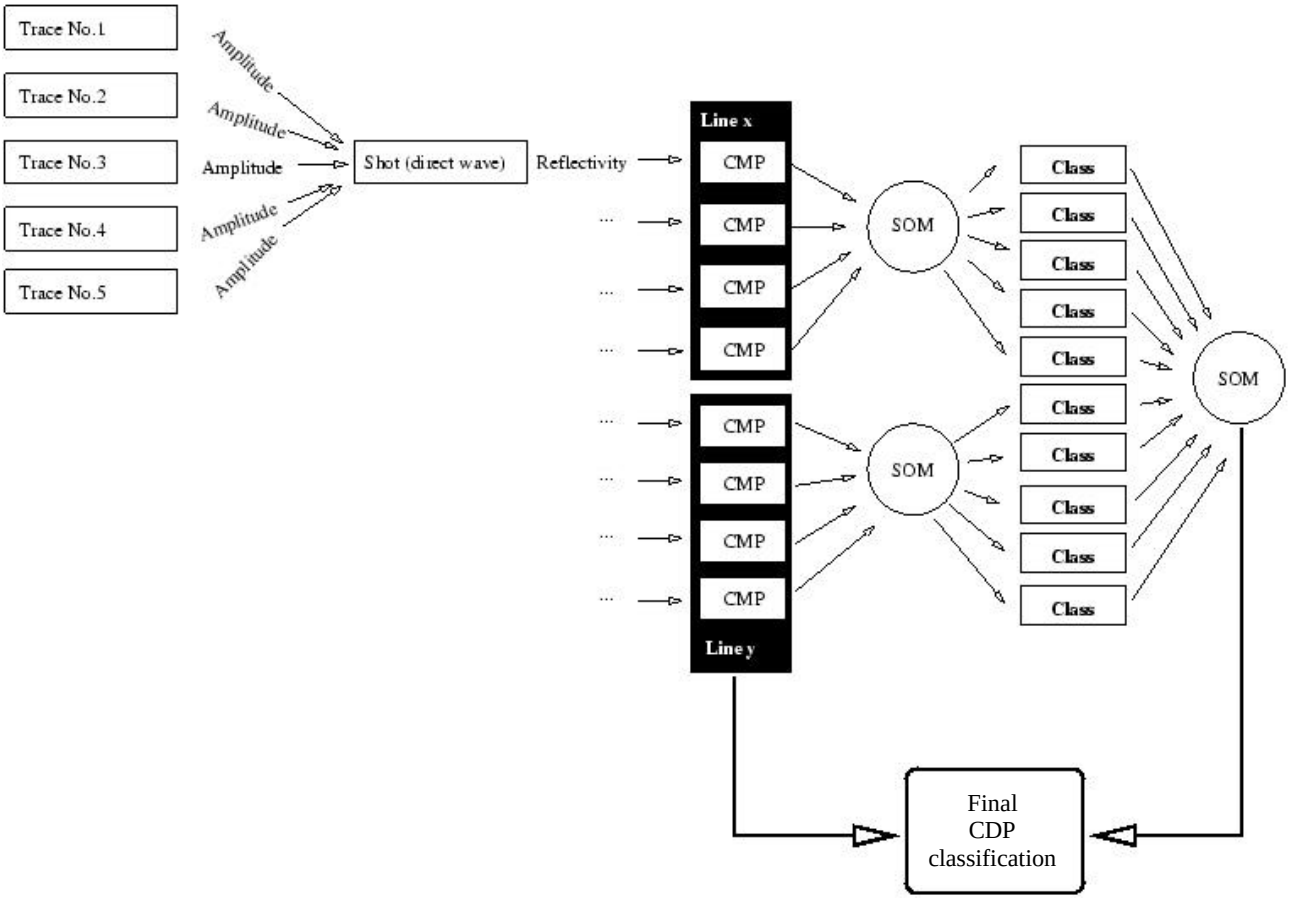

***Figure 11**: Amplitudes are extracted from the traces and they are compared to the direct wave of a shot, before the reflectivities are joined for CMPs and evaluated in 2 stages of cluster analysis which is performed by the Self-Organizing Map (SOM) algorithm (Kohonen, 1997).*

The reflectivities of all CMPs of a reflection line are evaluated in cluster analysis, i.e. a set of charateristic vectors is extracted from the set of reflectivities. The clusters are the characteristic vectors which form the center point of a st of input vectors, i.e. they are the multidimensional equivalent of mean values in the 1D-case. The input vectors in the present analysis will be sets of reflectivities at various angles. These clusters for each line are put into a second and final cluster analysis to get mean values for the whole dataset. One way of cluster analysis is the Self-Organizing Map (SOM), which will be applied during the course of this study. The final clusters are called classes, because SOM analysis is closely related to non-supervised neural networks and the neural network process is commonly called classification (Rojas, 1995).

The typical way of AVA analysis or sediment classification systems is to derive the physical rock properties from each reflectivity trend of a single CMPs (Ursin and Ekren, 1995) or by approximations (e.g. Shuey, 1995 or Aki and Richards, 1980). In the course of evaluation subtle differences in physical properties can be correlated to porosity (Trappe and Hellmich, 2000; Calderon-Macias et al., 2000) or pore pressure (Bruce, 1973). This is commonly established by a supervised neural network which takes into account well-logging (Trappe and Hellmich, 2000; Benaouda et al., 1999). In this case sonic logs of wells have not been published and cannot be referred to. To create a similar set of reliable information the reflectivity trends are statistically averaged by the cluster analysis. This allows us to find principal lithologies as they are commonly

depicted in geological maps, which can be compared to lithological samples in the area.
This series of processing is presented following the outline of the method before by using an example profile (P34 in Fig. 9) where approriate::

- the extraction of amplitudes (2.2.),
- the correction of amplitudes to minimize external effects and the evaluation of reflectivities (2.3., 2.4. and 2.5.)
- the neural network or SOM (2.6. and 2.7.) and
- the implications for principal lithologies (2.8.).

2.2.Automatic amplitude picking

The FRA amplitudes are extracted from the near-offset trace, which is used to derive the depth of the CMP and the end of the time window, from which the direct wave amplitude can be determined (Fig.12). This depth is used to predict an incidence angle for each offset and an expectation time for amplitudes on other offsets, which are picked accordingly. Adjacent CMPs within the Fresnel zone exhibit similar FRA times and these can thus be detected by finding the nearest maximum on a trace by trace base by a moving time-window (see Appendix). Where approriate, the picking algorithm is stabilized by manual picks, but in average not more than 2 picks per thousand CMPs were essential for a reliable result (Fig.13), which is probably an effect of the narrow spacing of ~4 CMPs within the Fresnel zone.

***Figure 12**: The direct arrival is picked as the maximum amplitude in the time window up to the first reflected arrival (FRA).*

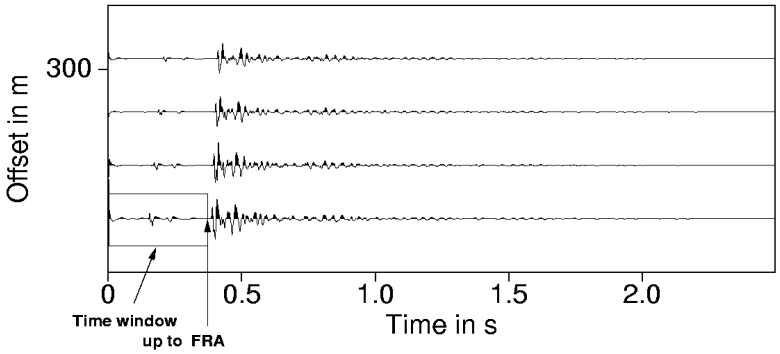

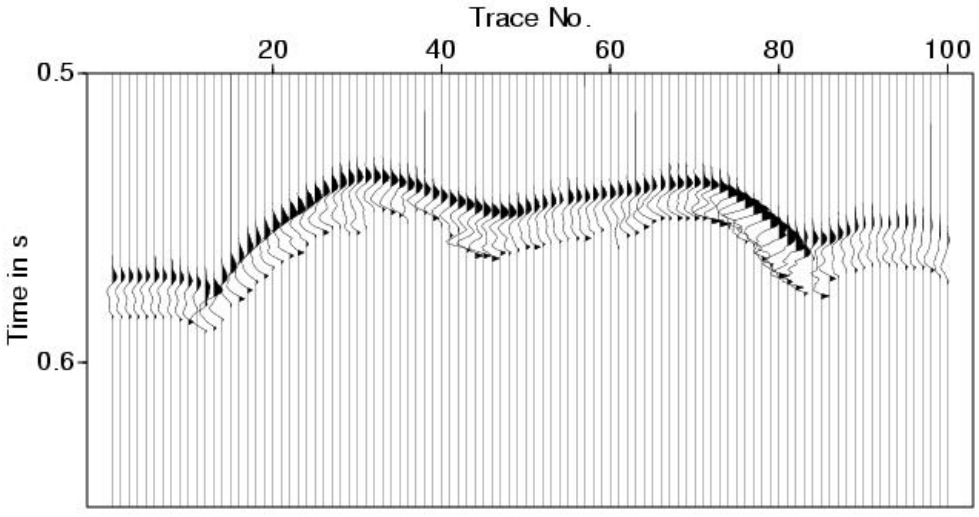

***Figure 13**: A typical automatic picking result (here a single channel line of P19 which shows more topographic undulation than the sample profile P34) and a surgical cut of the first positive and negative phase of the FRA after the automatic pick shows the stability of the algorithm (here without any extra manual pick other than trace 1) which was used to evaluate the relevant phases for reflectivity calculations.*

2.3.Extracting quality controlled reflectivity trends

A recorded seismic signal *s* is a convolution of an impulse function *i* with inputs from source, receiver and wave propagation (Sheriff, 1975). On top of this classical partitioning into output signal from the source *o*, the effect of source and receivers *eff* and propagation of the wave *p* in some medium, the ambient noise *n*, surface effects *sur* of the medium and the reflectivity of the earth's layers *r* have to be taken into account:

$$s=i*o*eff*p*sur*r+n\ . \qquad (1)$$

To directly relate signal amplitude and reflectivity, all other effects have to be deconvolved. To display the single effects a typical shot from the profile P34 picked in Fig. 12 has been selected.

*Original data from the source (**o**)*

Using amplitudes *I* instead of the output signal *s* is the first step in the deconvolution. This follows from approximating the source signal by a convolution of a delta function of amplitude *I* and a normalized stable source signal. The purpose of processing is to arrive at this delta function, which represents the reflectivity properties. The original signal is presented in Fig. 14.

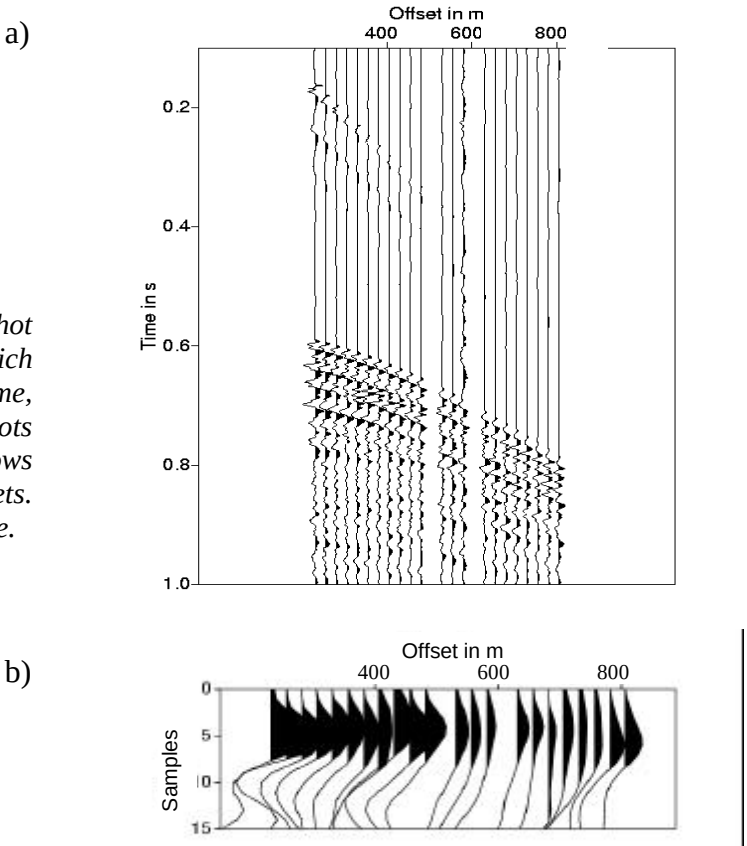

Figure 14: *a) The original shot record (shot 100 of P34) showing the direct wave which represents the source signal is linear with time, whereas the reflection hyperbola plots hyperbolical. b) The picked shot record shows decreasing amplitudes towards higher offsets. Two traces were deleted because of bird noise.*

The stability of a source signal is measured in stability of the peak-to-peak source amplitude -i.e. minimum to maximum interval - in different frequency bands (Dragoset, 1987). For the whole frequency band the relative standard deviation (deviation over average value) was computed as 10%. This reduces to 6.6 % percent for a frequency band of 20 Hz to 120 Hz and should be sufficient for the reflectivity evaluation of the FRA, although industrial standard promote 2% deviations (Dragoset, 1990), which can only be obtained by tuned airgun arrays.

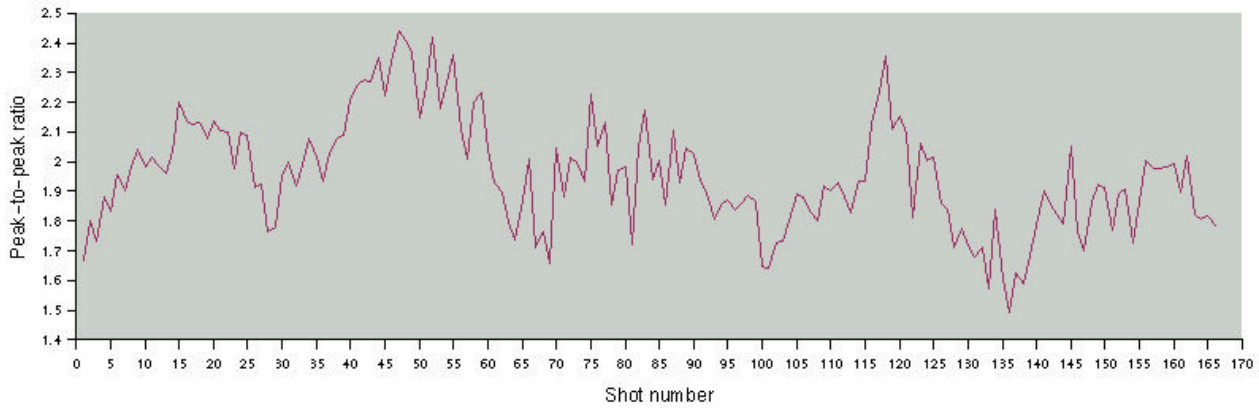

Figure 15*: The stability of direct wave amplitudes of the firts shots of sample profile 34 is shown. The values of peak-to-peak ratio (i.e. minimum to maximum) vary by ~0.2 at a level of 2, i.e. 10%.*

The survey was performed using small single airguns. Since single guns are subject to failure once a while, it is important to balance the energy and frequency content that has actually been transmitted to the ground before comparing the reflectivities from adjacent shot points. The frequency control is performed by a process called *thresholding* in the wavelet packet domain (see next chapter), amplitude control was established by normalizing the overall amplitude.
The wave that spreads from the airgun is homogenous in all directions, i.e. bowl-shaped, which is a valid assumption for the far wavefield (Parkes and Hatton, 1986). Thus, a directional source effect does not have to be taken into account, which is the base for the following discussion.

*Source and receiver effect (**eff**)*

The stability of the signal was shown to be stable from 20 to 120 Hz. The frequency-offset spectrum (Fig. 16) shows that the frequency spectrum delivered by the source is not equally strong throughout the frequency range. A strong amplitude decreade is observed between 70 and 90 Hz and more subtle decreases can be found at ~25 Hz, 40 Hz and 56 Hz. These smaller variations are caused by destructive interference of the direct wave and the ghost, i.e. the reflection from the air-water boundary. They are dependent on source depth, which was around 10 m in the present survey. With the exception of the band from 70-90 Hz, the energy up to 150 Hz still includes coherent data in small offsets. In conjunction with the 120 Hz limit found above, the significant information for reflectivity can be expected in a frequency band up to 70 Hz.

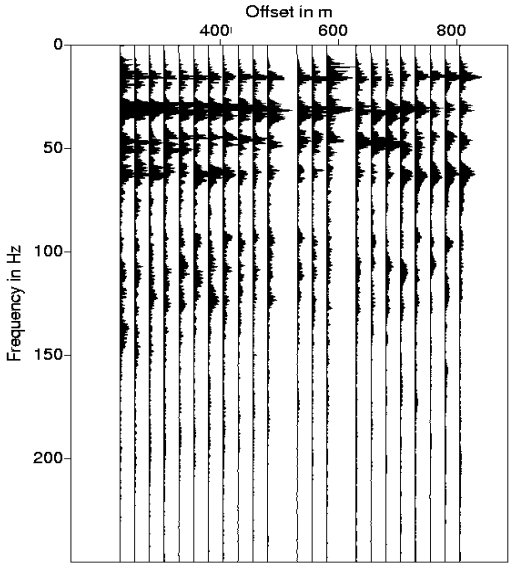

Figure 16: *The frequency spectrum of the single receivers (profile P34) are comparable and represent foremost the effect at the source (see text).*

The dominant receiver effect is the described ghost as well. Since streamer and source were located in the same depth, the same frequency distribution of signal interference can be assumed. Another effect follows from interference at adjacent receivers that are combined to provide a single signal (Meißner and Stegena, 1977). Once frequency bands of the signal can be processed individually, it is easy to get rid of. This can be dealt with in the wavelet packet domain in the next chapter. The effect *eff(f,J)* is dependent on incidence angle θ and frequency *f*. It is particularly strong in the high frequency range (Fig. 17):

$$eff\,(f,\vartheta) = \left| \frac{\sin\left(\frac{N\,\pi\,df}{v}\sin\vartheta\right)}{N\sin\left(\frac{\pi\,df}{v}\sin\vartheta\right)} \right| \quad . \tag{2}$$

N: number of hydrophone groups
d: internal spacing of hydrophones in group

It is easy to see that direct wave and FRA will exhibit different streamer effects. The streamer effect for the direct wave can not be calculated from the equation (3) if it is assumed that the ray forms an incidence angle ϑ of 90°. For any angle ζ close to 90° and small dominant frequencies, a simple approximation can be made, because the outer sine function is a sine function of small values and thus sin ζ≈ζ, i.e. the effect for the direct wave may be neglected, because:

$$eff(\mathrm{f},\zeta) \approx \frac{N\,\pi\,df\,\zeta\,v}{N\,\pi\,df\,\zeta\,v} = 1 \quad .$$

For smaller angles, the effect is shown in Fig. 17. Up to 50 Hz, no effect is observed at angles up to 60°, wheas up to 30° even 100 Hz can be imaged directly. The 120 Hz mark that was set before, includes one minimum of response, that needs to be corrected. All frequency dependent corrections will be performed in the wavelet packet domain (see chapter 2.5).

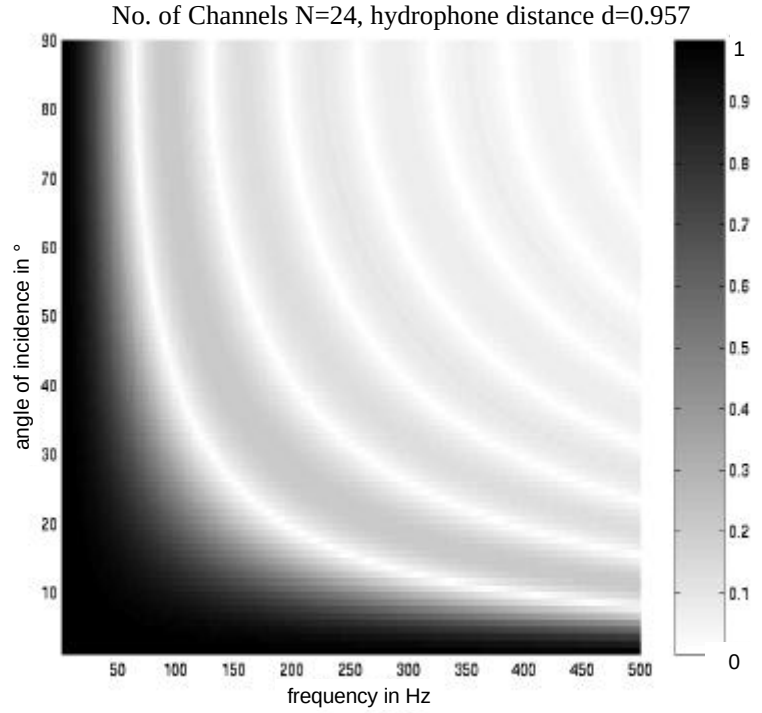

Figure 17: *The streamer effect of the employed streamer shows a strong interference, where the response of a hydrophone group drops to values of 0. This is only evident for high frequencies and angles.*

*Propagation of the wave (**p**)*

While the generated wave travels through a medium, it loses energy simply by propagating in three dimensions between two location at *x* and *x'*, typically known as spherical divergence or geometrical spreading effect. Sea water is assumed to be a homogenous medium, so the spreading effect follows from simple laws of optics (Halliday and Resnick, 1977) (Fig. 18):

$$\frac{I_x}{I_{DIR}} = \frac{x}{x'} \quad . \qquad (3)$$

I_x: amplitude of FRA at offset x
I_{DIR}: amplitude of direct wave at offset x
x': distance travelled by reflected wave, i.e. $x'=x \sin \vartheta$.

So, the spreading effect can be computed by evaluating the sine of the incidence angle. Another propagation effect is the absorption of energy in the propagation medium. The absorption in sediments for the covered incidence angles is small enough (Riedel, 1998) to be neglected here.

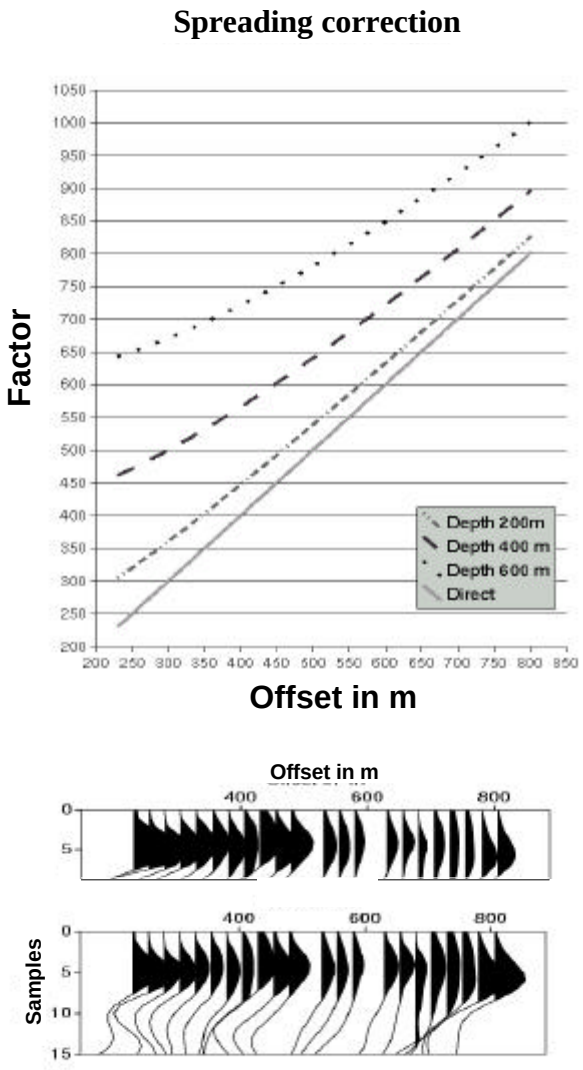

Figure 18: *a) The spreading correction for different offsets is shown for direct wave and different depth of the FRA, the corrected shot record of P34 is shown below. Whereas the amplitudes of the FRA are (b) visibly decreasing towards higher offsets the upper seismogram, they (c) do not display much variance after correction..*

*Ambient noise effects (**n**)*

Noise effects can be split into 2 groups, coherent noise and incoherent noise. Incoherent noise can be reduced by statistical averaging methods as e.g. stacking. During the course of finding principal clusters the same will happen. Coherent noise in marine environments (Larner et al., 1983) originates from the ship, the streamer birds, earthquakes in the area or ambient ocean noise. The ship's noise is at a constant level even when the airgun is not firing. A comparison to the amplitude is depicted in Fig.19. Bird noise influences the traces near to the bird in a strong but uncorrelated way. Thus, the traces near birds were removed (Fig. 14). The maximum earthquake registered during the time of acquisition occured on 30th of June 1999 and was a ~2.1 moment magnitude event at relatively shallow depth of 1.7 km, but could not be identified on the seismic record. So it was considered to be negelectable. Ambient ocean noise is a usually a small factor, but it can increase to a recordable size, when the weather gets rough (Fig. 19; Piggott, 1964; Burt, 1972; Hatton, 1986). It can be minimized in the wavelet domain (see next chapter).

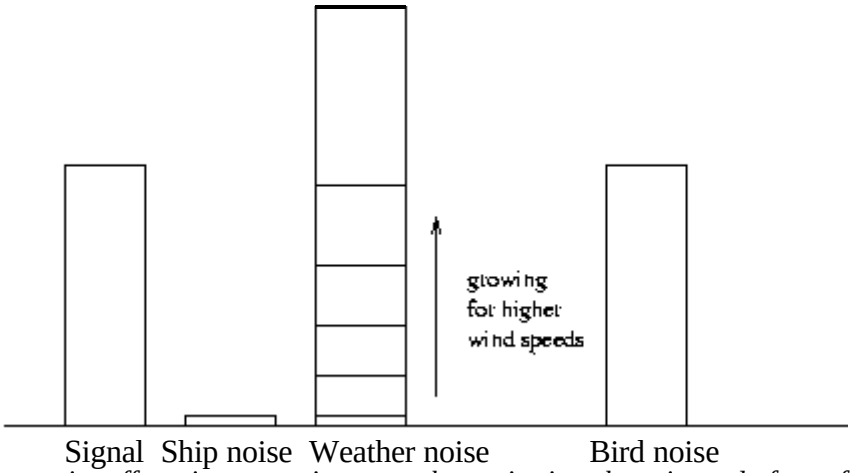

Figure 19: *Coherent noise effects in comparison, weather noise is only estimated after a formula of Piggott (1964) and Burt (1972): NL=B+20 n log(v), where NL is noise level, B and n geographical constants and v wind speed.*

*Surface effects (**sur**)*

Surface effects occur when the shape of the seafloor focusses or scatters the incident signal. This geometric filter cannot be deconvolved by a simple formula and needs to be modelled. Surface effects are part of the lithological descriptions of the reflecting material and will be covered later in the next chapter in terms of roughness and thin layers.

Reflectivity versus angle (RVA) gathers

A spreading correction C_{spread} for the reflected wave is computed for each single trace (Fig. 20), which is finally normalized by evaluating the ratio of its corrected first arrival amplitude I_{FRA} to the direct wave amplitude I_{DIR}. Thus we arrive at an absolute reflectivity value for various offsets:

$$R(\vartheta) = \frac{I_{FRA} C_{spread}}{I_{DIR} eff\,(f, \vartheta)} \quad . \qquad (4)$$

Each trace can be sorted into a CMP gather. After determining the depth of this CMP, offsets can be transformed into angles. The angle of incidence increases with offset and decreases with depth. Most of the survey area is at the depth of 400 m to 500 m and thus offsets from 230 m to 830 m plot in

angles of ~20° to ~60° (Fig. 20).

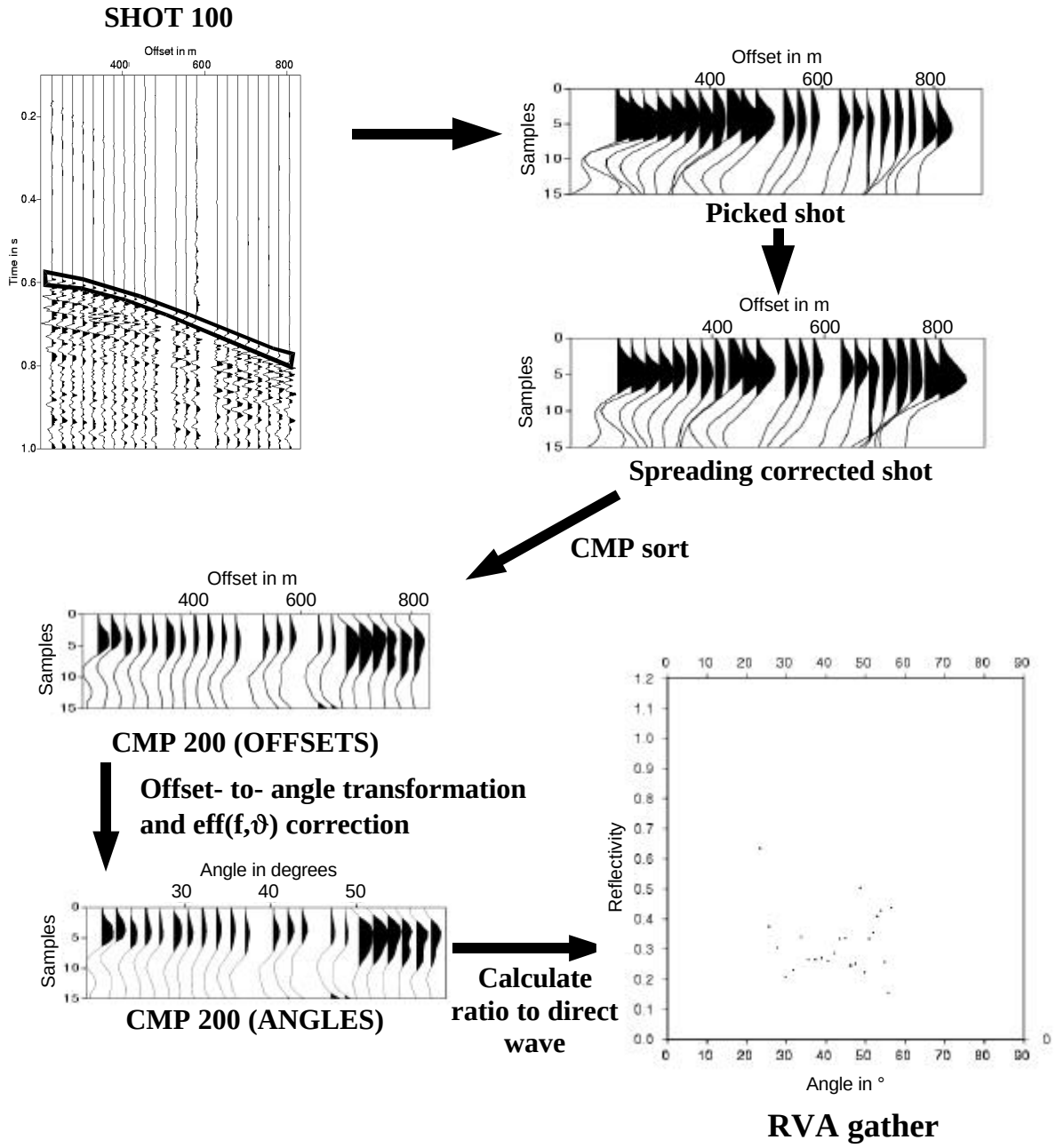

Figure 20: *The first arrival of the shots (here: shot 100 of line P34) are automatically picked, spreading corrected and sorted into CMPs. Since the CMP is a single point, the depth (here ~480 m) can be determined. This is used to calculate incidence angles at various offsets. By picking the first positive amplitude and calculating the ratio to the direct wave amplitude, a reflectivity versus angle (RVA) gather is achieved.*

The purely lithological dependent reflectivity trend $r=R(\vartheta)$ derived up to now is a physical measure for surface and volume properties and rather represents the function $r'=sur*r$ of equation *(1)*. This is especially important for the interpretation of the results presented later. These surface effects and the frequency effects discussed before will be covered in the following chapters, before evaluating the reflectivity versus angle gathers in a neural network approach.

2.4. Surface effects

It is a thin thread from reflectivity to lithology. Reflectivity at an elastic boundary is a measure of volume properties as well as a measure of near-surface geometry. The dependence of angle which is the key to the presented reflectivity analysis is also valid for microtopography, i.e. hills and valleys smaller than the Fresnel zone. They will produce a composite interference response of the seafloor boundary. This interference can account for reflectivities higher than 1 and a substantial decrease of energy with offset which is not possible in flat, uniform halfspaces.

2.4.1. Roughness and backscattering

Rough surfaces at fluid-solid boundaries have not been described analytically for elastic or even viscoelastic cases to my knowledge. The most reliable data are derived from physical models (Purnell et al., 1990) which showed that the effect of rough surfaces is biggest for 2-dimensional roughness, i.e. surfaces only undulating inline with the incident wave. The p-wave arrival stays unaffected, whereas the p-to-s converted wave displays smaller coherence and amplitudes. These surfaces are typical for basalt flows (Chapman and Scott, 1964). For 3-dimensional roughness, i.e. roughness inline and crossline, the amplitudes of the p-wave drop but the coherence of the signal is much higher. Coherence is not necessarily a measure of true amplitudes, so let us have a look at analytical solutions for the acoustic case.
It will be necessary to introduce the parameter of roughness h_{rms}. Roughness - in the terminology of Jackson et al. (1986) - is defined as the root-mean square depth deviation Δz from a flat surface, i.e.

$$h_{rms} = \sqrt{\sum (\Delta z(x,y))} \ . \qquad (5)$$

Roughness creates backscatter which is generally separated into two different regimes:

1. The *roughness regime* ($2\pi h_{rms} << \lambda$). If h_{rms} is far smaller than the wavelength, the Rayleigh-Rice approximation of the wavefield is valid. In that case h_{rms} is a good measure of the geometrical properties of the seafloor (Stanton, 1985).
2. The *diffraction regime* ($2\pi h_{rms} \approx \lambda$). If h_{rms} is in the range of the wavelength, strong interference occurs. The seafloor is comparable to a diffracting lattice in that case. h_{rms} cannot be used to approximate the wavefield, which is strongly influenced by interference particularly for normal incidence (Jackson et al., 1986) and the Bragg reflection angle is the best qualitative measure (see below).

Roughness regime

For the roughness regime, h_{rms} can be estimated from the ratio of power spectrum of a stacked single channel seismic time-series $P_{stacked}(f)$ to the average power spectrum of the non-stacked channels $P_{average}(f)$ from the relation from Dunsinger et al. (1981) and Stanton (1985):

$$CF(f) = \frac{P_{stacked}(f)}{P_{average}(f)} = \frac{1}{1+\gamma^{-1}}, where\ \gamma^{-1} = \frac{\pi}{3}\left(\frac{2\pi f}{v_{water}}\right)^4 h_{rms}^{\ 2} l_x l_y \qquad (6)$$

and l_x and l_y represent correlation lengths of the seafloor depth distribution in the two horizontal inline and crossline directions. Beamwidth was assumed to be π for the used airguns (see Appendix, Fig. 21). The ratio of power spectra represents the fraction of power which is coherent over a certain section of a profile and may thus be described as a coherence function.

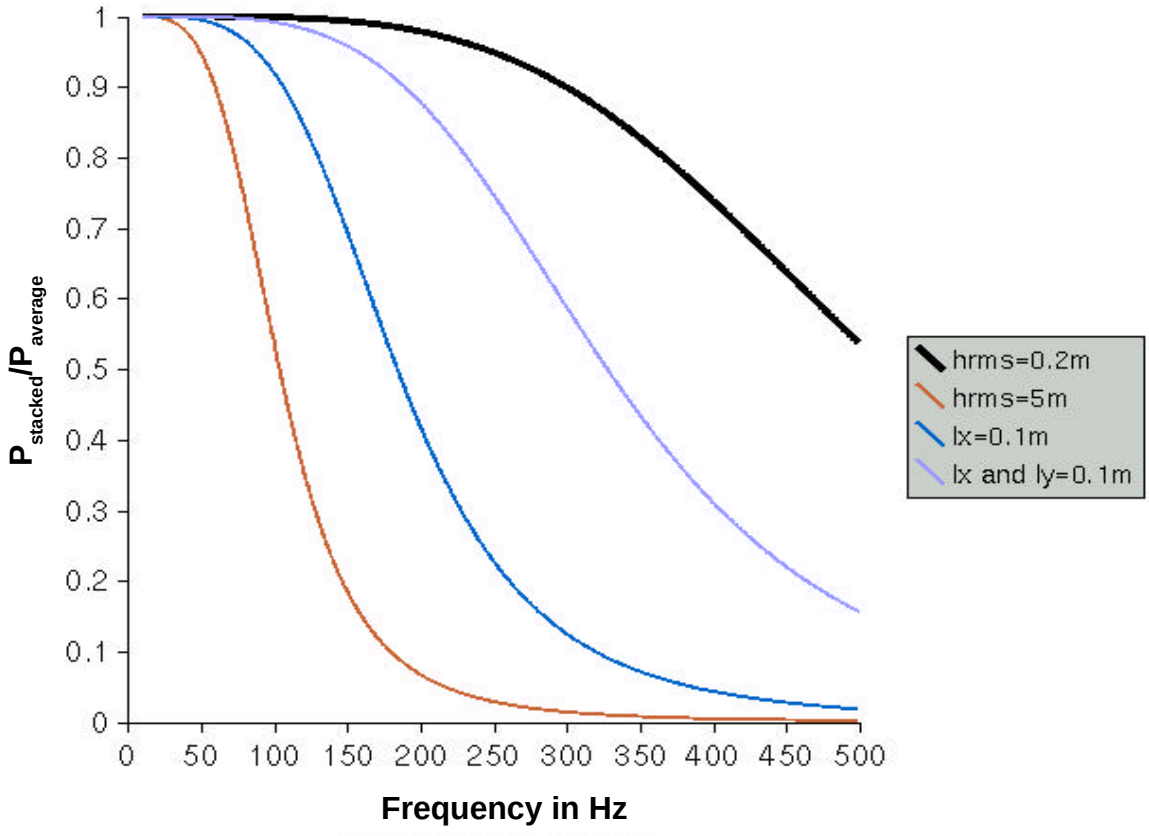

***Figure 21**: The coherence function drops significantly for roughnesses in the size of small mounds (h_{rms}=5m). For 2D roughness, i.e. only lx as a correlation length is small, the coherence is lower than for 3D-roughness. This was also shown in experiments by Purnell et al. (1990).*

h_{rms} is not the only unknown factor derived from lithology. The correlation lengths are unknown, as well, and equally typical features of the lithology of the seafloor. Small values of all these values are measures of relative smoothness. So the power spectra were calculated (Fig. 22 a) for the single channel line nearest to the source. Their ratio was evaluated where the coherence function is stable. Stability can be assumed between 60 Hz (maximum) and ~160 Hz (Fig. 22 b). This corresponds to results above, that the data in small offsets appeared to be coherent up to 150 Hz.

Because this function cannot be inverted to result in a single value, but are rather dependent on the product of h_{rms}, l_x and l_y, the roughness values were mapped in terms of the coherence function value. To find a typical value of the function *CF(f)*, the value inferred from the power spectra was evaluated for each 10 CMPs (which is roughly the size of the Fresnel zone) at the 160 Hz boundary where the biggest deviation occurs (Fig. 23). This is possible because the value at 0 Hz must be 1 and the reciprocal equation in (6) can be exactly represented by two defined values.

The strongly undulating function for each 10 CMPs was afterwards smoothed by a moving average, resulting in the same value for 100 CMPs in a row. Although only in this horizontal resolution of 100 CMPs, it is thus possible to map the coherence value, which is shown in Fig. 24.

a)

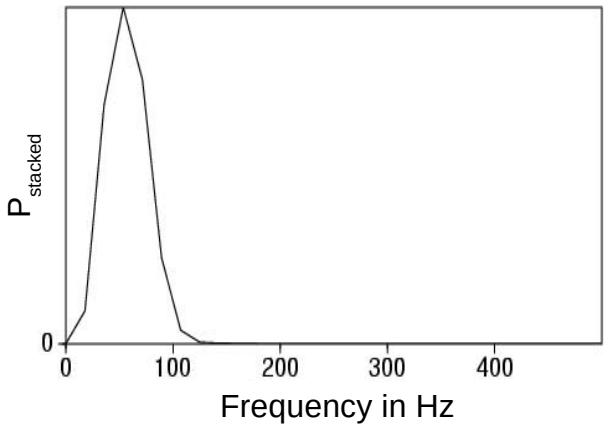

***Figure 22**: a) shows the power spectrum of the aligned and stacked first reflected arrival of line P34 from shot 1000 to shot 1010.*

b)

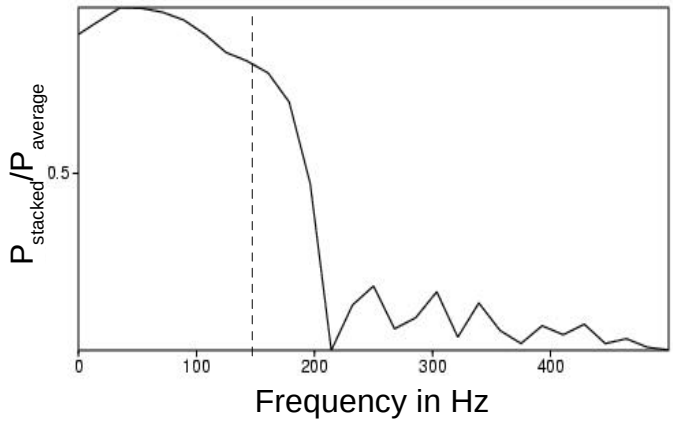

b) shows the ratio $P_{stacked}/P_{average}$ for these shots. The decreasing values compose a similar function as those in Fig. 21. The function is only stable to about 160-170Hz, which was taken as the maximum frequency to be evaluated.

c)

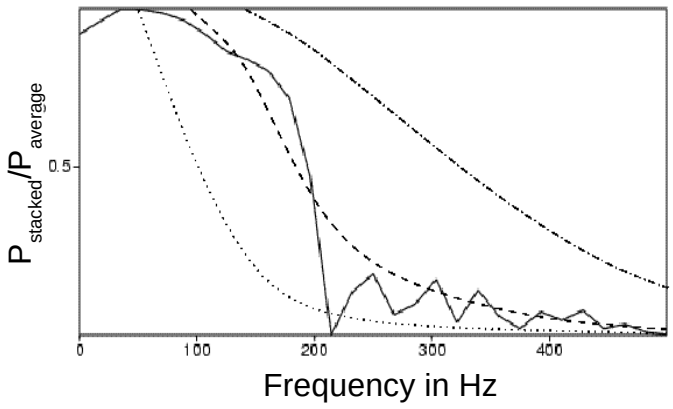

c) the curve taken from the example CMP gives a power spectrum ratio very similar to the function for 2D roughness, i.e. l_x=0.1 m. The functions of Fig.21 have been plotted in the background.

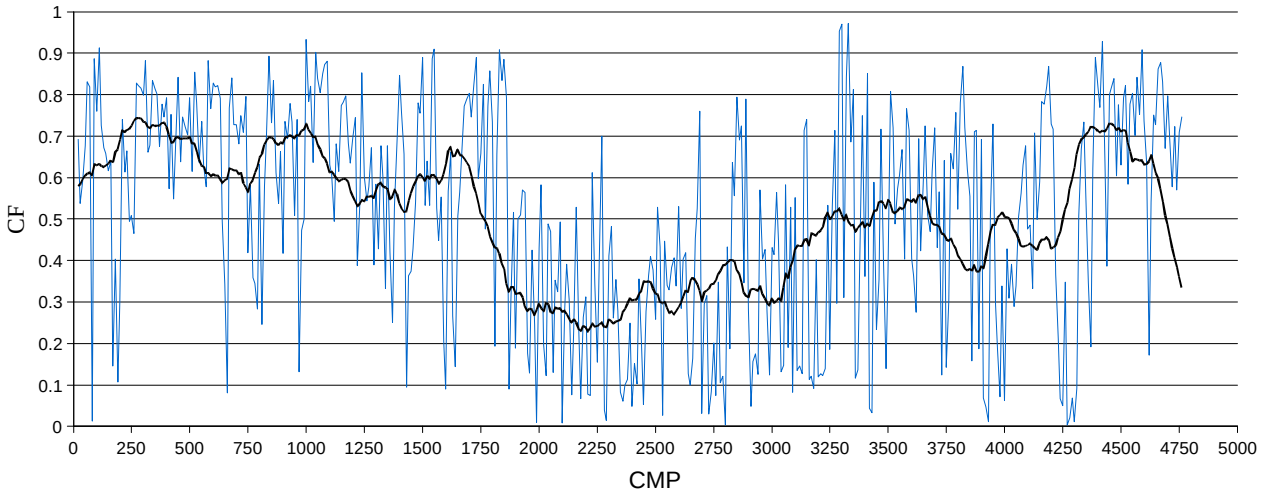

Figure 23: *The trend of the value of CF(f) is used a roughness measure for each CMP (here profile P34). The distribution of these values is shown in Fig. 24. Low values correspond to high roughness*

Distribution of roughness

The regional distribution of coherence function values is a first hint on lithology (Fig. 24). Basalt is expected to expose a rough surface (Purnell et al., 1990; Chapman and Scott, 1964), whereas sediments which posess low values of h_{rms}=0.1 and $l_x l_y \approx 3\text{-}30 \cdot 10^{-2} m^2$ (Stanton, 1985) are expected to be highly coherent layers.

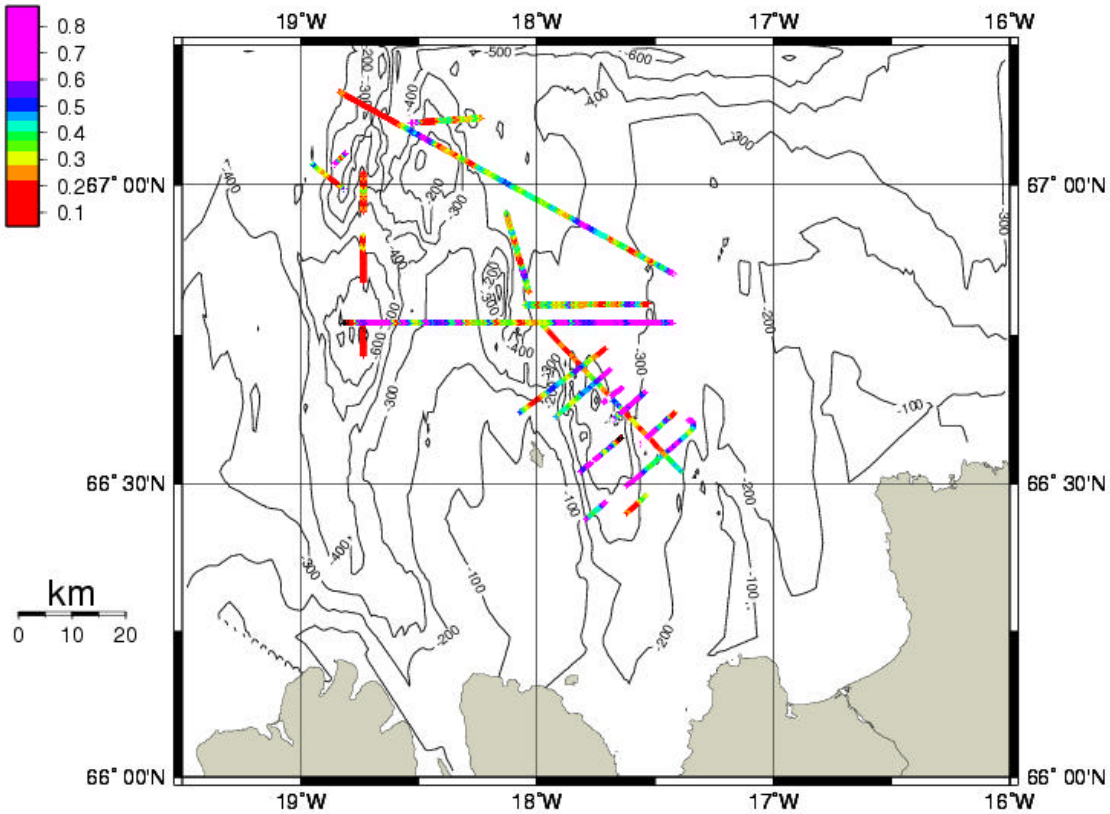

Figure 24: *The distribution of coherence function values at 160 Hz is depicted on the map. Smaller values occur in the northwest, high values in the topographic lows. These correspond to local geological features, i.e. the basaltic ridge in the northwest and probably flat-lying sediments in the topographic lows.*

Sediments accumulate in topographical lows, which should consequently show high coherence values. This is confirmed in Fig 24. Average coherence values are found in the northeast of the map, especially around 66°45' N and 18°W, where a volcanic edifice is expected. Directly adjacent in the southwest, very high values are exposed, maybe lava flows originating from this structure. These high values are mirrored in the expected ridge and rift structures in the northwest of the map.
Coherence as a measure of roughness is also a measure of reliability of the reflectivity data. It appears that exposed sediments are more easily investigated than igneous rocks, especially tectonically altered rocks and lava flows.
The roughness values will be discriminated into three classes. *Low roughness* (blue/violet) will be assumed for all seafloor sediments (i.e. $h_{rms}^2 l_x l_y$ <0.003 (Stanton et al., 1995)), which is equivalent to *CF(f)*>0.99 for up to 160 Hz. *Medium roughness* (yellow/green) will qualify a hummocky seafloor, represented by $h_{rms}^2 l_x l_y$ <1.7 and *CF(f)*>0.75 for up to 160 Hz. *Higher roughness* (red) is taken as an evidence for poor reliability and any interpretation of reflectivity values in such a scenario will be avoided.

Backscatter strength from rough surfaces

The amplitude effect of the roughness value h_{rms} is commonly computed by introducing the backscatter strength. Model descriptions for backscatter strength from roughness have been solved analytically for the acoustic case, i.e. the medium above and below the boundary are not resistant to shear and can be described by density and v_p alone (see Appendix). In the case of an incident acoustic wave of wavenumber *k* the following formula was derived by Eckart (1953):

$$<I> = I_0 \; e^{-2(k\,h_{rms})^2} \quad , \qquad (7)$$

where <I> is the average reflected amplitude of the rough surface and I_0 the amplitude of the flat surface.
A refined model for the backscatter of rough surfaces is the MacKenzie model, which is derived from Lambert's law in optics. In the case of seismic waves (acoustic model) it allows to calculate the backscatter response from an infinitesimal area dA (Hanrahan, 1980; Jackson et al., 1986) for incidence angles ϑ up to 60°:

$$dI = I_0 \frac{\mu}{y^2} \cos^2 \vartheta \, dA \quad , \qquad (8)$$

where μ represents the backscatter coefficient and *y* the length of the raypath after scattering. The law has been found to „hold for bottom backscattering in good many locations“ (Hanrahan, 1980). Integrating the law over the Fresnel zone results in

$$I = I_0 \mu \frac{\pi}{2y^2} d\,\lambda \cos^2 \vartheta \quad . \qquad (9)$$

The depth *d* which derived from the Fresnel zone formulation equals the geometrical spreading factor, but the term is still not indepedent of reflector depth, since y is also related to it.
Correlations between roughness and backscatter coefficient are empirical (Hanrahan, 1980). The backscatter coefficient lies in the range of 10^{-3} to 10^{-4} for typical sediments (Hanrahan, 1980) and $10^{-1.8}$ for basalts (Chapman and Scott, 1964). High backscatter coefficients can be correlated to high roughness (Stanton, 1985), but they are also a measure of high impedance contrasts (Hastrup, 1980) and this effect is generally stronger (Hanrahan, 1980). Thus, the roughness modulates the reflectivity

effect.
For near-vertical incidence ($y \approx d \wedge \cos^2\vartheta \approx 1$), the backscatter reflectivity is near to $0.5\pi\mu\lambda$, but not by far as high for higher angles. For λ=30 m (i.e. a dominant frequency of 50 Hz) $0.5\pi\mu\lambda$ can grow to the order of ~0.7. A result from FD modelling is shown in Fig. 25 and depicts a deviation from ~0.3 foremost near the first crititical angle. The coherence function (equation (6), Fig. 22) should be taken into account when determining lithology to estimate the order of the effect.

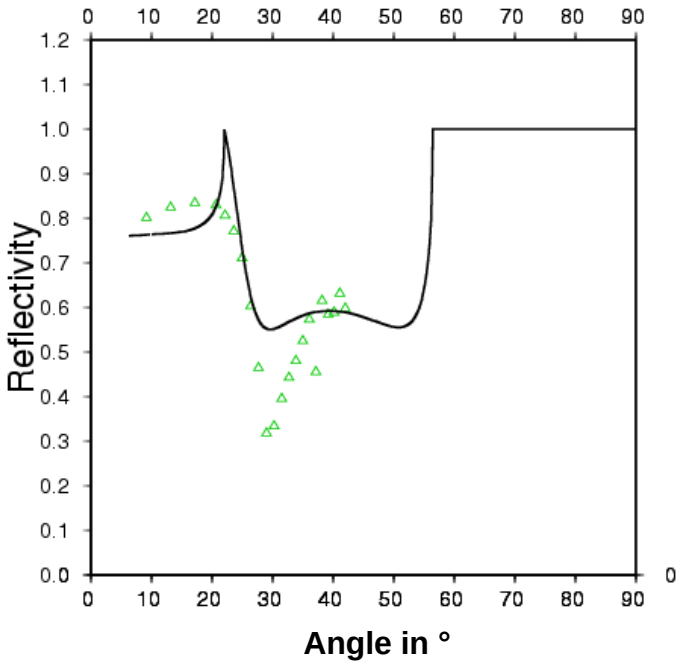

Figure 25: *Elastic 2D-FD modelled reflectivity trend for a rough anhydritic surface of h_{rms}»0.7m. The roughness was modelled as a sine function of 2 m wavelength and 1 m amplitude. The line represents the expected curve for a flat elastic surface and the green triangles the results from the rough surface.*

Diffraction regime

In the case of diffraction the reflection loss is generally bigger than in the case of roughness (Hanrahan, 1980). The determining relation is called Bragg's law (Halliday and Resnick, 1986) and is generally known for determining lattice distances in crystals:

$$2d \cos\vartheta = m\lambda \text{ , where } m \text{ is an arbitrary natural number.} \quad (10)$$

In case Bragg's law holds, there will be constructive interference and the amplitude will be at its maximum, which is twice the expected amplitude. In other cases, scattering angle and incidence angle determine the phase shift between rays, that arrive at the same receiver and the system gets complex.
Backscatter strength ($=10 \log_{10} \mu$) in high frequencies, i.e. the diffraction regime, can be used to determine sediment type by echo sounding (Stanton, 1985; Jackson et al., 1986), if typical roughnesses are known. For clay or silt h_{rms} lies in the range 10 cm, i.e. diffraction at the water bottom would occur at ~25 kHz, for a rough surface of basalt the roughness has not been determined yet, but for a frequency of 50 Hz, h_{rms} would have to be in the order of 50 m. A seafloor undulating 50 m in root mean square within the Fresnel zone is only likely if the Fresnel zone is more than 200 m, so that the slope would be less than 45°. In 400 m water of ~90 m Fresnel zone diameter this is unlikely. So the issue of diffraction can be neglected for the present case. It would be important for deep waters e.g. at the typical mid ocean ridge not on the elevated Iceland plateau.

2.4.2. Thin layers

Thin layers are another worst case scenario for seafloor reflections encountered thoughout the worlds's oceans. The classical texts of Widess (1973) introduced the quarter wavelength criterion, i.e. any layer thinner than a quarter of the dominating wavelength of the incident wavefield will not be resolvable in a seismic record. High frequency sources have been used in conjunction with airguns to resolve these thin sedimentary sequences on top of the subsurface. They were not available in the present case, but from coring in the TFZ, it is known that large parts of the offshore area are overlain by thin layers of hemipelagic mud or ooze (Scholten et al., 1999). In the strict sense the rule of Widess (1973) is only valid for normal incidence and cosine wavelets. Lin and Phair (1993) extended Widess' theory to all angles and derived the reflectivity of a thin layer in similar media above and below the thin layer as:

$$R'_t(\vartheta) = w_0 \Delta t_t(\vartheta)\, R'(\vartheta)\, cos\, \vartheta \quad , \qquad (11)$$

where $R'_t(\vartheta)$ is the reflectivity of the thin layer case, $R'(\vartheta)$ the reflectivity of the uniform halfspace, ω_0 the dominant frequency and Δt_t the two way travel-time through the thin layer of thickness h. Again, this strictly holds only for cosine wavelets and was extended by Bakke and Ursin (1998) by substituting the cosine term by a traveltime expression. However, for the seafloor the cosine is precisely known and $\Delta t_t(\vartheta)$ for a layer of thickness h may be calculated as:

$$\Delta t_t(\vartheta) = \frac{2h}{v_{thin} \cos\left(\arcsin\left(\frac{v_{thin}}{v_{water}} \sin\vartheta\right)\right)} \quad . \qquad (12)$$

If the thin layer consists of a material with a velocity v_{thin} which approximately equals that of water ($v_{water} \simeq v_{thin}$), e.g. ooze, equation (12) reduces to:

$$\Delta t_t(\vartheta) = \frac{2h}{v_{thin} \cos\vartheta} \quad . \qquad (13)$$

So we end up with:

$$R'_t(\vartheta) = 2\omega_0 \frac{h}{v_{thin}} R'(\vartheta) \quad . \qquad (14)$$

The effect of the thin layer in similar media at the seafloor is thus independent of the angle of incidence. For a frequency of about 50 Hz (i.e. ω_0=314 Hz) and a layer thickness of 2 m the factor is practically 1. This effect is similar to roughness backscattering in its dependency on wavelength or frequency. Herman and Blonk (1990) approximated analytically that roughness on a small contrast layer can be modelled by a thin flat transition layer with transitional physical properties of a thickness which was twice the roughness h_{rms}.

The strongest reflection loss by a thin layer of density ρ_{thin} and compressional wave velocity v_{thin} over a hard boundary of respectively ρ_{hard} and v_{hard} occurs in singularities of the reflectivity function. $\Delta R'$ can be approximated for the acoustic case by a complex formula (Hastrup, 1980), but the approximation by a cosine wavelet, i.e. the way of Lin and Phair (1993) or Widess (1973), supplies an approximation to the expected FRA amplitude. It is just necessary to determine the phase ϕ of the

second arrival and the composite reflectivity R' can be calculated from the reflectivities of the single boundaries from water to the thin layer R'_{thin} and from the thin layer to the hard layer R'_{hard}.

$$R' = R'_{thin} + R'_{hard} \cos \omega_0 \phi \quad . \qquad (15)$$

The phase of the second arrival can be determined by the travel time through the thin layer :

$$\phi = \frac{2hv_{water}}{v_{thin}^2 \sin \vartheta} \quad . \qquad (16)$$

R' for a thin transition layer above hard rock - in this case a typical anhydrite (fig.26) which will be used throughout the methodological part of this thesis - as a function of angle is shown in Fig. 26. The approximation of equation (16) is only valid in small angles, which was expected by the travel time approximation made in equation (13). As roughness the thin layer case modulates the reflectivity curves, imprinting further typical characteristics which are not connected to the physical properties of the material, but the geometry alone. This overprinted cosine function cannot be inverted without additional information. Roughness and thin layers may amplify the signal to apparent reflectivities above 1. Both scenarios may cause a significant drop of the signal in relatively high angles of 20° to 40°, which cannot be modelled by the Zoeppritz equations (Figs 25 and 26). This may help in the classification of the seafloor material.

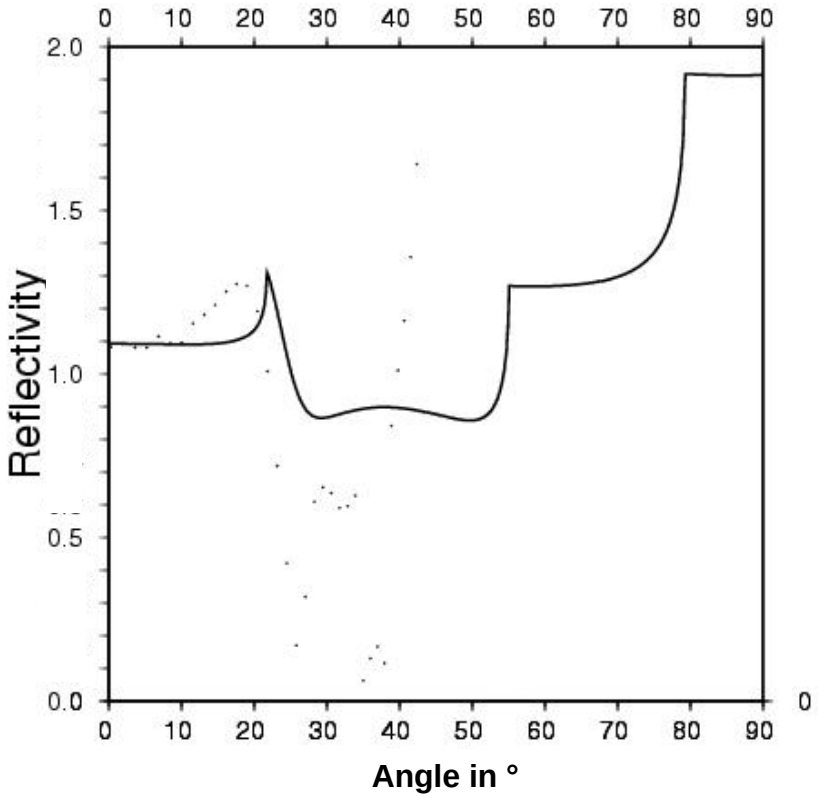

Figure 26: *Elastic FD modelling for a thin layer of the typical example of sediments (r=2 kg/m^3, vp=1500 m/s, vs=200 m/s) overlying anhydritic rock (r=2.8 kg/m^3, v_p=4000 m/s v_s=2800 m/s) is shown in dots, whereas equation (15) for the case is plotted as a line. It fits well in the small angles as expected, but in large angles (i.e. offsets) it is a bad approximation. Thin layers do often account for high reflectivities in small angles (Lin and Phair, 1993).*

2.5. True amplitude processing in the wavelet packet domain

It will be shown in this chapter that wavelet transform filters as Fourier transfom filters provide complete and non-redundant representations of the time-frequency plain and can be used for true-amplitude processing and consequently provide an improvement for reflectivity evaluation. This improvement does only effect the frequency effect function *eff* discussed before. A reader foremost interested in the results of the reflectivity evaluation can skip to the next chapter.

2.5.1.The Discrete Wavelet packet transform (DWPT)

The discrete wavelet packet transform (DWPT) of $n(=2^j, j\in\mathbb{N})$ samples is very similar to the Fast Fourier transform (FFT), but it is faster in performing synchronous frequency band (*Df*) filtering (scale) and time-band (*Dt*) filtering (shift) by splitting up the time-frequency plain into Heisenberg boxes (see Appendix): $\Delta t \Delta f = 1$.

In contrast to the Discrete Wavelet transform (DWT, see Appendix), the DWPT will split the time-frequency domain uniformly in frequency, whereas the DWT will split a time series into octave bands. Consequently, the DWPT allows a better separation in the high frequency range where the receiver effect varies the most, compared to the DWT (Fig. 27)

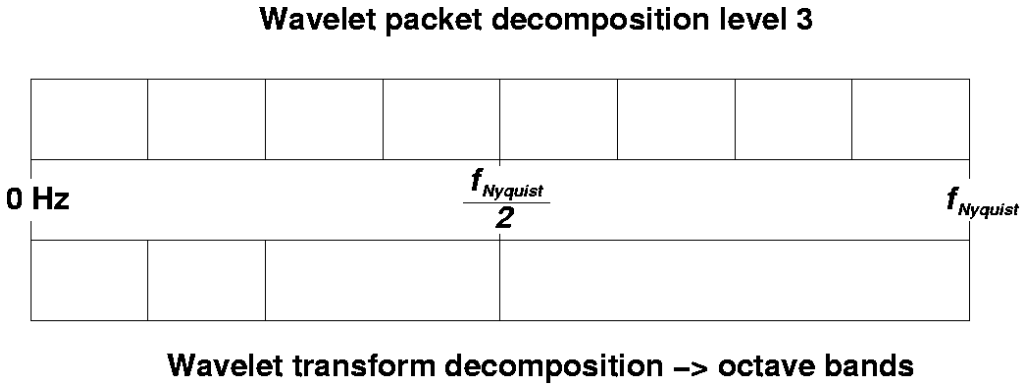

***Figure 27**: The discrete wavelet transform cannot provide a good frequency resolution in high frequencies because of its inherent quality of separating the data into octave bands from Nyquist frequency $f_{Nyquist}$ on, but using the Wavelet packet transform allows for equal bandwidths.*

The DWPT of a time series $s = \{s_k\}$, defined in a recursive way (Wickerhauser, 1993), can be presented as

$$DWPT(k,1) = \begin{cases} \sum_{i=0}^{n-1} g_i s_{i+2k-1}, if & 0 \le k < \frac{n}{2} \\ \sum_{i=0}^{n-1} h_i s_{i+2k-1}, if & \frac{n}{2} \le k < n \end{cases} , \qquad (17a)$$

and

$$DWPT(k,l) = \begin{cases} \sum_{i=0}^{n-1} g_i DWPT(i+2k-1, l-1), if & c\frac{n}{2^{l-1}} \le k < c\frac{n}{2^{l-1}} + \frac{n}{2^l} \\ \sum_{i=0}^{n-1} h_i DWPT(i+2k-1, l-1), if & c\frac{n}{2^{l-1}} + \frac{n}{2^l} \le k < (c+1)\frac{n}{2^{l-1}} \end{cases} \qquad (17b)$$

$$with \ (c \in N \wedge 0 \le l < 2^l)$$
$$and \ (l \in N \wedge 1 < l \le \log_2(n)).$$

$h=\{h_k\}$ and $g_k=(-1)^k h_{1-k}$ represent the high and low pass component of the exact quadrature mirror filters of the DWT (Daubechies, 1992; see Appendix), which are defined by j and y , i.e. the scaling function and the mother wavelet (Mallat, 1989). The DWPT algorithm recursively applies high and low frequency partitioning of high and low frequency bands from Nyquist frequency down to some frequency resolution (Fig. 28). Each application creates another set of redundant information at a certain level l. The higher the level l the finer the partitioning into frequencies at the cost of lower resolution in time. The highest level is obtained by taking $l=\log_2(n)-1$, and thus a result follows similar to an FFT, i.e. with no resolution in time.
A modification of the DWT algorithm of Press et al. (1992) was used as the DWPT here (see Appendix).

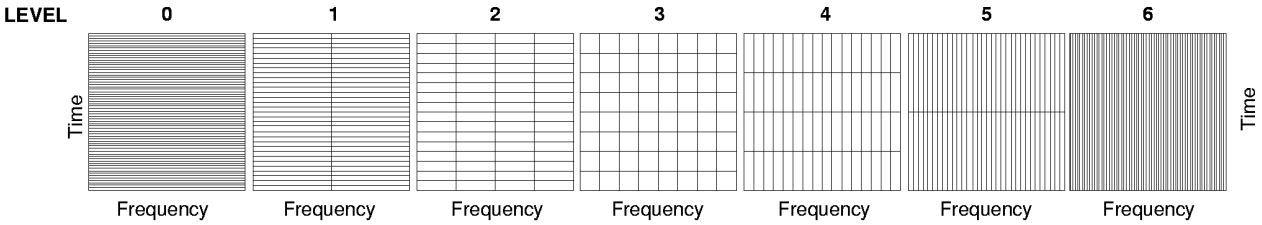

***Figure 28**: The Discrete Wavelet Packet Transform (DWPT) decomposes a time series (here 64 samples) into time-frequency cells or Heisenberg boxes. Each cells represents a sample. The higher the resolution in frequency, the lower is the resolution in time, a consequence of the Heisenberg Uncertainty principle. The highest level (here: $6=\log_2(64)$) is similar to the FFT, the lowest level 0 is the time-series itself.*

2.5.2.Application of the DWPT to seismic waveforms

The distinct advantage of the DWPT shows when applying it to a short time window. Whereas the Gibbs phenomenon restricts the FFT to relative wide time bands, the DWPT does perform equally well for small and wide time bands resulting from the time-frequency partitioning explained above. However, the application does not give equally well results for any wavelet or bandwidth. The better a wavelet (or rather wavelet family in the case of the DWPT) is adjusted to the waveform, the better the performance will be. Deighan (1997) showed that seismic signals show a good transform result for Battle-LeMarié-wavelets (Mallat, 1989), whereas Grubb and Walden (1997) investigated the performance of compact Daubechies wavelets (Daubechies, 1988) in the reconstruction of a time series by wavelet transforms and found the best results for long minimum-phase wavelets. Using the wavelets for computing reflectivity should be a similar task. Interestingly the wavelet packets provide the best results for the used wavelets (Battle-LeMarie and Daubechies), if the highest possible level decomposition was selected. In that case they provide very similar results (Fig. 29). In lower levels the deviation is much lower for Daubechies wavelets (compare Fig. 29a and c)
The major problem of DWPT and DWT is the shift variance problem. The shifting of the time series by one sample results in a non-linear change of the DWPT coefficients, which makes true amplitude analysis difficult. However, shifting the time-series did not result in a change of the perfect reconstruction in the maximum decomposition level, which makes the modified algorithm of Press et al. (1992) a valuable tool.
In the presented case the DWPT is applied for the preparation of reflectivity trend analysis, i.e. for the amplitude quality control of the FRA. This reflection occurs at different times from different locations and thus the shift variance problem will occur, when applying it to a full trace. By the automatical picking algorithm presented and levelling all maxima before transforming them to the wavelet packet domain, shift variance can be minimized. The method of applying time corrections before the transform was already performed successfully for a new developped stacking procedure for seismic data in the wavelet packet domain (Watts et al., 1999).

a)

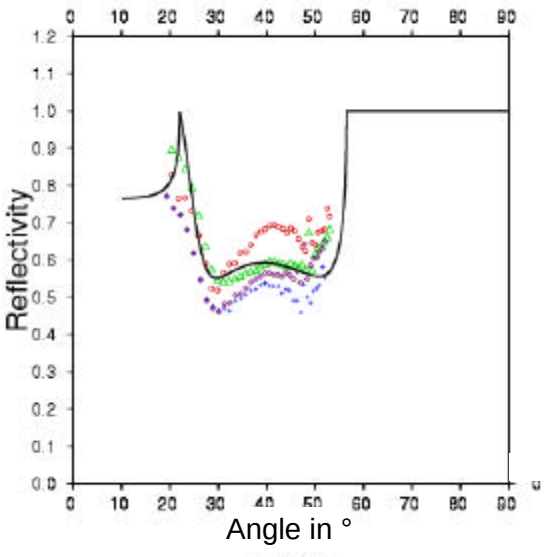

***Figure 29**: a) The green triangles show the best adaptation to the expected Zoeppritz curve and corresponds to a wavelet packet transform by a Daubechies-8-wavelet (minimum phase) at the highest possible level decomposition for a seismic time series of 64 samples. Higher values are found for a decomposition of level 3 (red circles), lower values for level 4 (blue crosses) and level 5 (violet diamonds) decompositions.*

b)

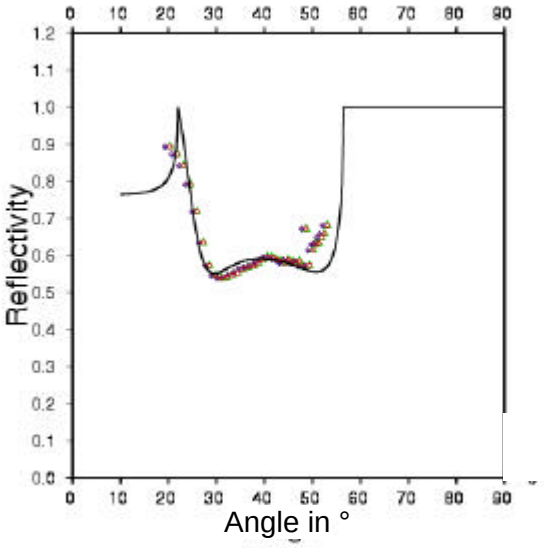

b) For the highest possible level decomposition the result of all wavelets is very similar, whether they may be Haar wavelets (blue crosses), Daubechies-8 (minimum phase / green triangles), Daubechies-20 (least asymmetric / violet diamonds) or Battle-LeMarié cubic spline-64 (red circles).

c)

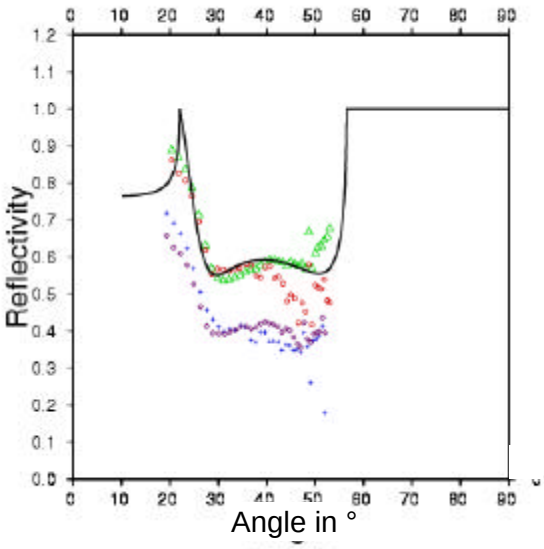

c) The adaptation of Battle-LeMarié wavelets (here the best adaptation overall, i.e. 24 cubic spline) is quite low compared to the Daubechies wavelets for medium-level decompositions (level 4 blue crosses and level 5 violet diamonds), whereas for low level (level 3 as red circles) and particularly at maximum level (level 6 as green traingles) they work very well.

2.5.3.Data correction by use of the DWPT

Thresholding the source

Having explored the use of wavelet packets, it is now time to apply the DWPT to the quality control issues. The first task to perform will be to provide a good signal-to-noise ratio. A typical way in using wavelet transforms for this task is the so-called thresholding (Donoho et al., 1993). Thresholding is applied after the transformation to the wavelet (packet) domain. All values smaller than a certain percentage of the highest coefficient are zeroed.

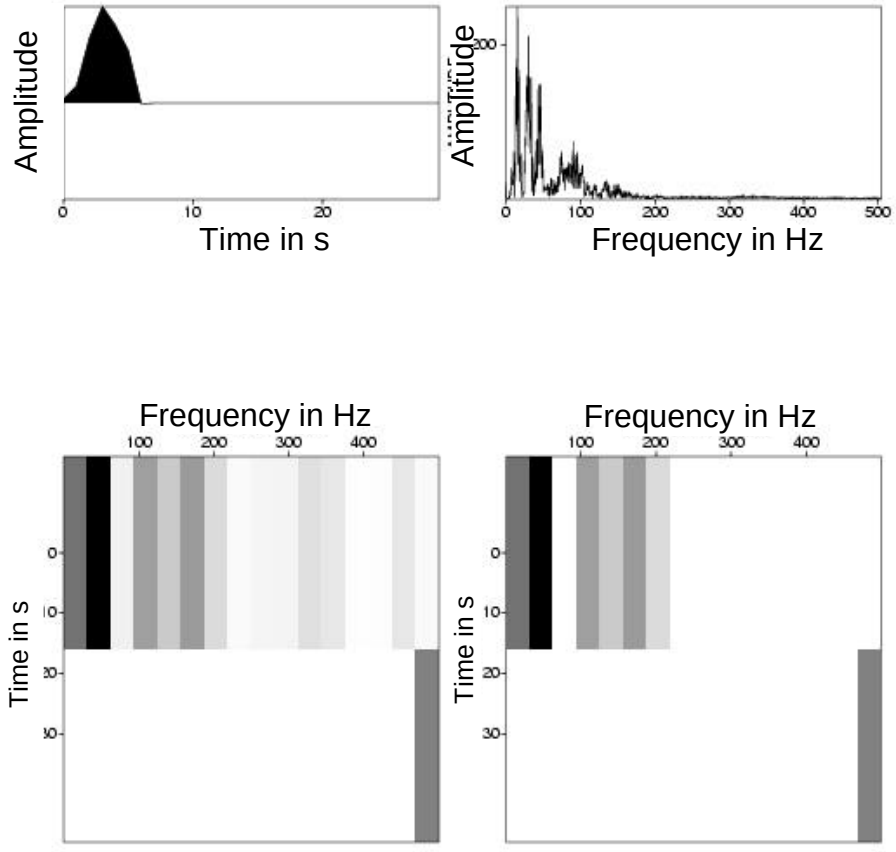

Figure 30: *Packograms, i.e. plots of the time-frequency plain where Heisenberg boxes represent the DWPT coefficients (in grayscale). The coefficients are dark, where data values are high, i.e. in the beginning of the time window (see upper left) and in frequencies up to about 250 Hz (see upper right). The right image show the packograms after thresholding of 20%, respectively. At 20% all noise information higher than ~220 Hz and at 70-90 Hz (water reverberation) have been deleted. The grey box at the right lower edge depicts a relatively high amplitude, which is derived from the wrap-around effect of the algorithm from Press et al. (1992).*

The thresholding process destroys information on Heisenberg boxes represented by small amplitudes, thus eliminating noise and improving the signal-to-noise ratio. The results of thresholding are presented in comparison to the original amplitude spectrum of the time-series in Fig. 30. Thresholding is essential to erase noise in high frequencies, foremost where ghosts and water reverberation diminish the signal energy, i.e. in the range from 70-90 Hz. The data which that were recorded in these minima of the source do only contain noise which would be amplified by inverting the streamer effect in the next step. The packograms (Fig. 30) before and after thresholding show the wrap-around effect of the used algorithm, which is not a problem for the present application, because at each step only the first coefficients are evaluated.

Correcting the individual Heisenberg boxes for the streamer effect and attenuation

After getting rid of the noise the streamer effect is inverted. The average of *eff(f,ϑ)* is approximated as a constant factor for a frequency interval Δf in the sum of equation (3). Because of the representation of a frequency interval by one distinct scale of a wavelet packet transform (see above), the transformed coefficients can be multiplied with the average effect after the angle ϑ has been computed from offset and depth. The average of the effect in a frequency band follows from integrating equation (3) and dividing by the bandwidth. The explicit integral is complex and beyond the scope of this project, so I used numerical integration, i.e. Δf was divided into subbands and the effect calculated at their center frequencies before averaging over the subbands. The same can be

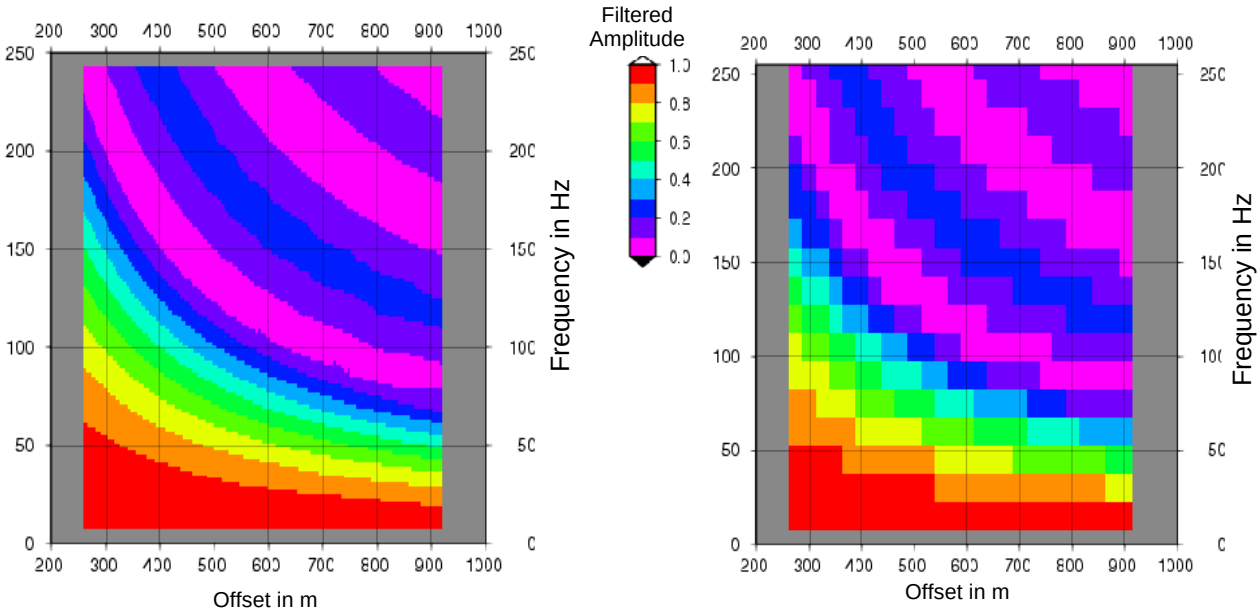

***Figure 31**: The streamer effect (left image) calculated from equation (3) is averaged for each channel and frequency band (right image) before its reciprocal is multiplied with the DWPT coefficients.*

Blame it on the weather noise...

Where weather noise (see above) infiltrates the record because of high wind velocities, a surgical muting of DWPT coefficients can visibly improve the record (Deighan et al., 1998; Fig. 32). This process, however, does not restore the actual amplitude and cannot be used in true amplitude processing. Weather noise did not occur during the recording of the TFZ data, but the area is generally known for strong winds and for further registrations an improved true amplitude processing tool based on the method could proove to be useful. [2]

Weather noise appears like a linear low frequency phase in a seismic shot gather (Fig. 32a), but a trivial high pass filter by Fourier transform still leaves phase shifts in the disturbed seismic time series (Fig. 34a). If a similar task is performed in the wavelet packet domain, i.e. all coefficients that represent low frequencies are zeroed at times where they turn up (Fig. 34c/d), the phase problem disappears (Fig. 34b).

The phase length in samples is higher for weather noise records, which can be inferred from the number of local minima or maxima counted per trace (Fig. 32b). So this is a measure to automatically localize weather noise infected traces in a gather.

2**Note:** All presented data in this chapter are an excerpt from industrial data of the Porcupine basin, because no suitable example could be found in the TFZ recordings.

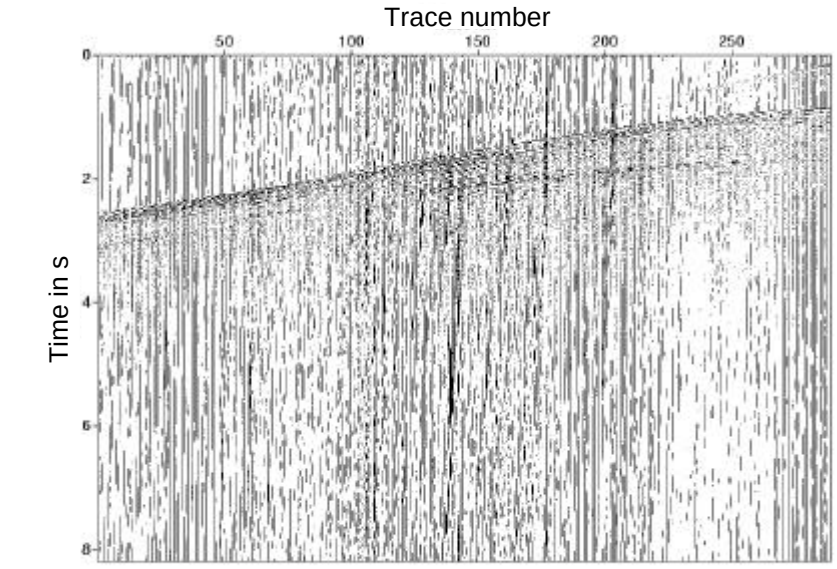

a)

Figure 32: a) *Weather noise appears as low velocity-low frequency noise on shot gathers (here an example of indutrial data from the Porcupine data), but high-pass filtering is often not enough to get rid of the effect (Hatton, 1986; see Fig. 28).*

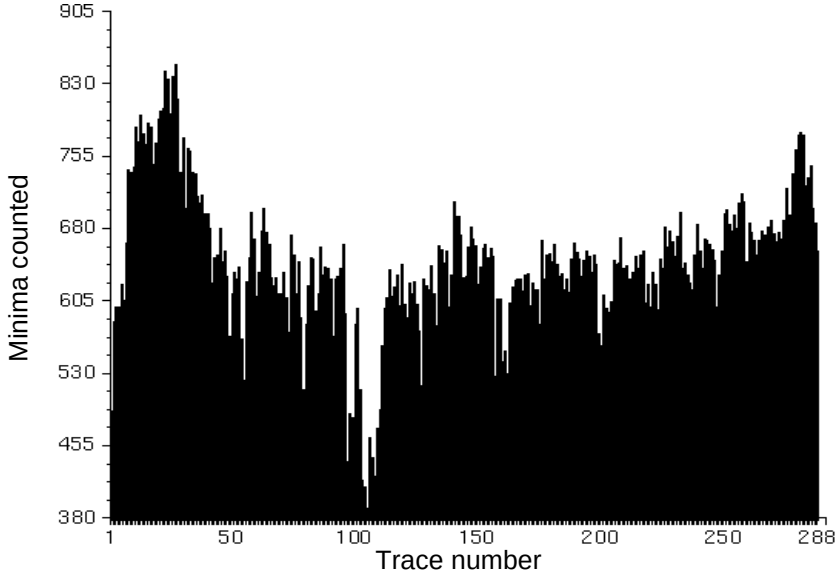

b)

b) *Numbers of minima counted per trace. Where weather noise blurs the information, the number decreases, which can be used for identifying infected traces.*

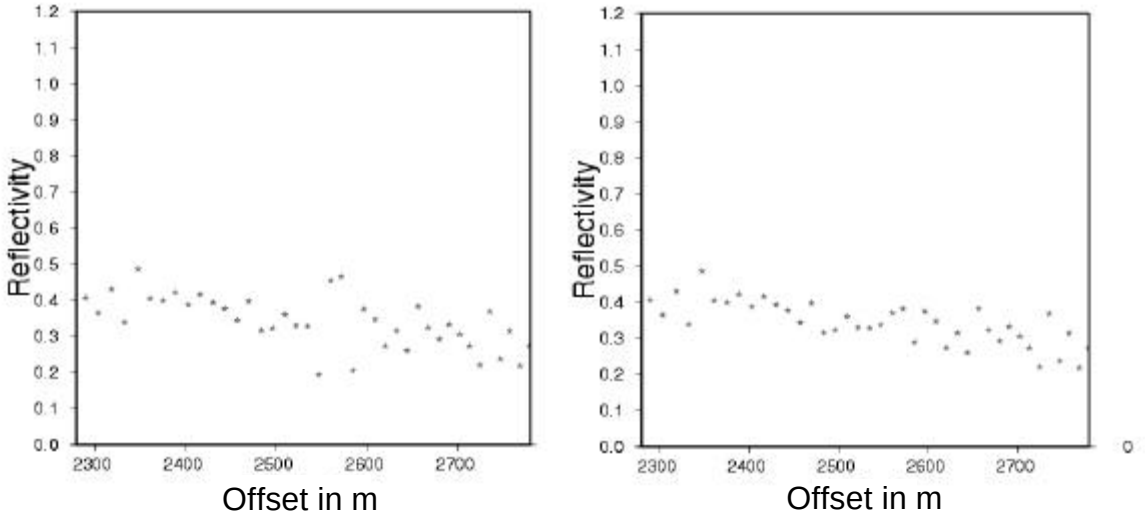

Figure 33: *Between an offset of 2500 m and 2600 m the AVO curve is smoothed by a wavelet packet background noise filter (right image) compared to surgical muting (left image). Deviations not originating from weather noise (between 2300m and 2400m) are not smoothed by the method.*

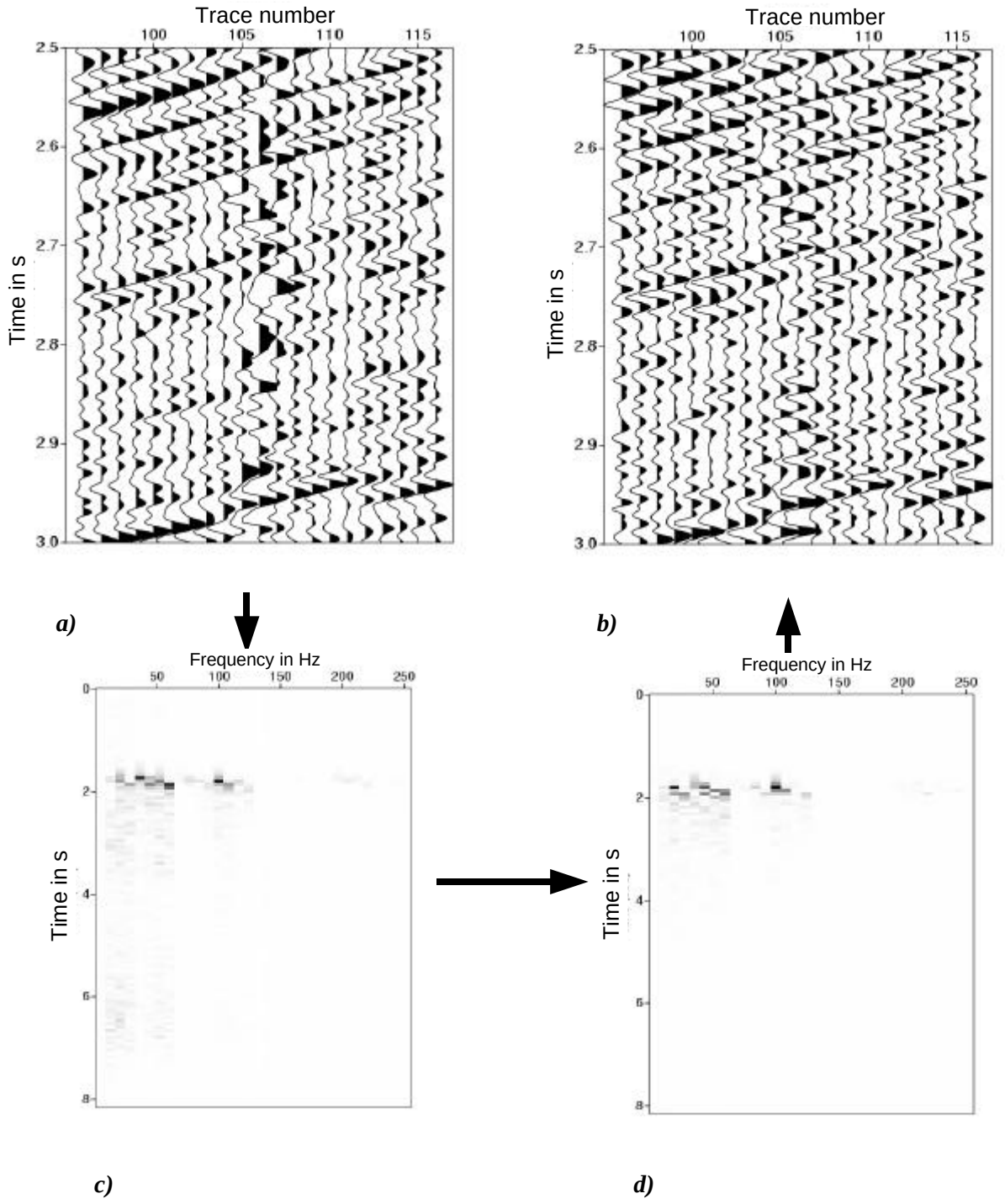

Figure 34: *After bandpass-filtering (a) the data are still infected with weather noise. Thus they are transformed to the wavelet packet domain (b) (here: trace 106 of the Porcupine record). A light grey shadow throughout low frequencies and the whole time-series following the first arrival is identified as the source of weather noise. This is cut out in (c), before transforming it back and the weather noise diminishes (d) (Upper pictures modified after Deighan et al., 1998).*

The amplitudes at the seafloor were not restored by the application (Fig. 33), but this classical surgical muting can be adapted for AVO investigations by applying a wavelet packet background noise filter, which deletes any coefficient below a certain level (typical thresholding - see above) and subtracts the mean value of all coefficients below the threshold from the coefficients above the threshold. The result is a smoothing of reflectivity curve for the noisy traces (Fig. 33).

2.6.A neural network approach

2.6.1. Neural networks

Artificial Neural Networks (ANN) are statistical algorithms that were originally designed to model the human brain and neural system. The original idea stems from the structure of the so-called McCulloch-Pitts cells, where several input signal x_i are added up to result in a „firing“ cell (Fig. 35) - i.e. an output $O(x_1,x_2,...)=O(\boldsymbol{x})=1$ occurs, if sum of the input signals is bigger than a threshold value T.

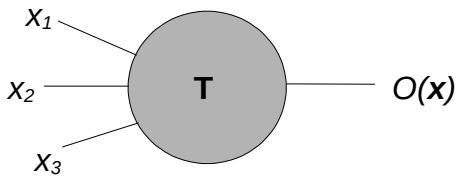

Figure 35: *The model of a McCulloch-Pitts cell with three input signal channels is the easiest model for a neuron in the brain where the input cells are the model of synapses and the cell is the model of the neuron (McCulloch and Pitts, 1943).*

The Minsky-Papert-perceptron generalizes the idea by factorizing the input signals (Rojas, 1995). The factors are called the weight coefficients w_i and „firing“ is conditioned by:

$$\sum_i w_i x_i \geq T \quad . \qquad (18)$$

By combining many perceptrons via signal output and/or input connections a neural network is established. The key to train this ANN is to shift the weight coefficients towards a function that will generate a stable output function from arbitrary input values, a process also known as *mapping.* It can be performed in two ways:
a) by supervising the learning process - i.e. comparing output and input, and establish empirical weight coefficients. *Example:* If physical rock properties are available from some samples from the seafloor and reflectivity information are available from seismic data at the same spot, it is possible to crosscheck their output and map them onto each other.
b) by a non-supervised learning process, i.e. partitioning the records into natural principal components by finding centers of attraction around which the scattered values of the input signals cluster. This is closely related to the so-called *cluster analysis* (Kohonen, 1982; Rojas, 1995; Benaouda et al., 1999), which requires that these principal components are an inherent quality of the dataset. *Example:* Reflectivity data of reflections from an infinite half-space are well ordered, i.e. reflectivity values lie in a defined range (from 0 to 1) and any value occurs nearly as frequently as any other. If distinct lithologies are dominant, they will plot on the same line or scatter around it, i.e. they form clusters and their centers can be found by cluster analysis algorithms.
In the geosciences neural networks have been widely applied for picking seismic data curves (e.g. in PROMAX), for storing databases into function for e.g. standard resisivity curves in geoelectrics or 1D velocity models of seismic refraction data (both by Calderón-Macias et al., 2000). Reflectivity has been adressed for mapping reflectivity deviations onto lithological parameters in 3D seismics (Trappe and

Hellmich, 2000) and comparing them to lithology and sonic logs in wells (Benaouda et al., 1999). Whereas the authors tried to highlight singularities of the seismic dataset, i.e. lithological parameters for any registrated trace, this study focusses on the recognition of the average medium penetrated by the seismic wavefield to deduct a lithological map characterized by the principal components of the dataset. A non-supervised algorithm specialized on such a task is the self-organizing map (SOM) or Kohonen network (Kohonen, 1982; Kohonen, 1997).

2.6.2.The Kohonen SOM

The background of the SOM algorithm is self organization. Self organization is mathematically described by two phenomena. The method must order the signals, in this case the weight vectors, without explicite desciptions in descending or ascending order and they must remain ordered after an arbitrary number of loops. The ordering method of a SOM can be regarded as a Markov process that will reach an ordered status with a probability of one after an infinite amount of steps (Kohonen, 1997) and shall not be discussed in this study. Remaining order is derived from the convergence of the learning rate factor (see below). What is trivially observed is that the number of steps that is needed for an ordered condition might be infinite, but once obtained it will be a stable condition because of the convergence condition.
The Self-Organizing Map uses a one-layer neural network with a number of *m* cells, where all inputs p_i are directly connected to all of the perceptrons C_k of the layer, but the perceptrons are interconnected only with their direct neighbour (Fig. 36) or their neighbours in a certain environment called neighbourhood. Distance in the neighbourhood is defined either by the values of the weight vectors of the cells or the position of the cells in the net.

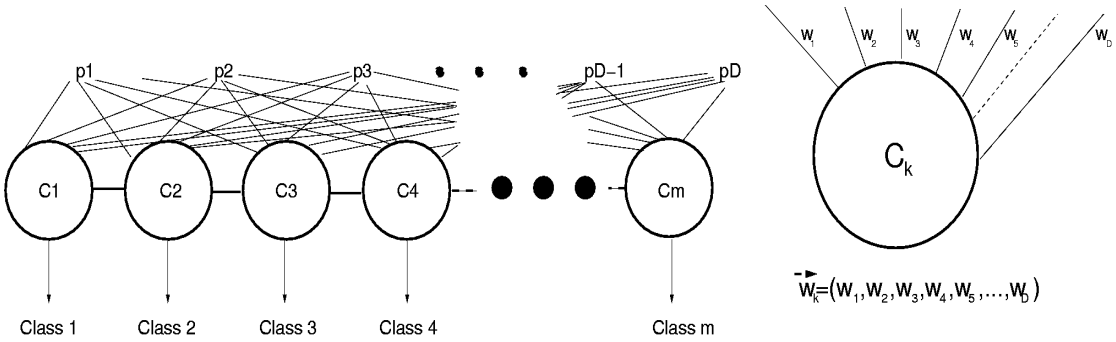

Figure 36: *A self organizing map uses a 1 layer neural network, where each cell C_k uses a weight vector* ***w*** *of the dimension D of input vectors* ***p****. The output is one class, i.e. in our case a reflectivity function per cell.*

General

The *D*-dimensional weight vectors of the connections to the perceptrons are initially determined per random, an initial maximum neighborhood radius r_i and and a learning rate factor *n(i)* are defined. Both will be dependent on the steps *i* already performed during the course of computations. For a certain number of steps *s(=max{i})*, a random vector $\boldsymbol{p}=(p_1,p_2,...,p_D)$ is taken from the set of input vectors. The perceptron, whose weight vector ***w*** is nearest to this vector, is firing. This principle is known as *best match*. All vectors in the defined neighbourhood up to a maximum radius of r_{max} are changed according to a learning rule.

The standard algorithm (Rojas, 1995) uses a neighbourhood φ*(s,r)* defined by the locality of the cell in the net and changes the radius according to:

$$r_{max} = r_i - \frac{1}{1 - \frac{i}{s}} \qquad (19)$$

The weight vectors of all cells within this radius are changed by ***Dw*** according to a Hebb-type learning rule:

$$\Delta w = n(s)\varphi(s,r)(\boldsymbol{p} - \boldsymbol{w}) \qquad (20)$$

The learning rate factor *n(s)* should be a function of the number of steps *s* and the distance from the activated cell *Dr* and must converge towards a greater number of steps to guarantee convergence of the SOM algorithm (see above; Kohonen, 1997). The following function is an example that fulfills the criterion and provides good results in the case of reflectivity data:

$$n(s) = \frac{1}{m(\Delta r - 1)D} \sum_r \sum_{i=s-100}^{s-1} \Delta \boldsymbol{w}(s-i) \quad . \qquad (21)$$

The results for the selected line 34 (~5700 CMPs) after 200000 steps is shown in Figure 38. Fewer number of steps *s* in conjunction with faster processing can be arranged with the commonly used "Batch Map".

Batch Map

In case of a small number of cells, the algorithm above can become unstable, because the net does not necessarily converge at the speed of the learning rate factor and has to be adapted to each specific case (Kohonen, 1997). There is a more stable version which is known as the "Batch Map " or Linde-Buzo-Gray (LBG) algorithm (Linde et al., 1980). All vectors which find their best match in a certain cell are hold in memory and at each step, ***w*** is defined as the mean over all vectors that were classified before and the new vector. This algorithm does not include the learning rate factor and neighbourhood. It is slow for small numbers of vectors and a large number of cells (Kohonen, 1997). In the present case the aim is to reduce up to about 5000 reflectivity trends of CMPs to less than 10 classes, which is the opposite case. In the SOM context, Kohonen (1997) has never encountered a convergence problem for this algorithm and no case was described for which more than 1000 times the number of input vectors had to be used (Rojas, 1995). The batch map has been applied successfully to the mapping of rain cloud albedos (Kohonen, 1997), which is a similar task as the mapping of seismic reflectivities.

2.4.3. Application of the SOM to reflectivity mapping

After quality control and true amplitude processing the reflectivity vs. angle gathers were computed. For our sample line P34 the full set of RVA gathers is shown in Fig. 38a. All reflectivity curves of one profile have to be input into the first SOM cycle. In

the case of a uniform half space below the seafloor, the value of reflectivity at different incidence angles will always lie between 0 and 1 and so the data are normalized from the beginning which accelerates any SOM algorithm (Kohonen, 1997).

How will the input vectors evolve from the reflectivity trend ?

The RVA gathers of all CMPs are interpolated linearly between the actually sampled incidence angles. Because they are dependent on depth and dip of the CMP, they cannot be selected arbitrarily. But the linear interpolation allow gridding in a constant angular sampling interval $\Delta\vartheta$, so that each reflectivity function $R'(\vartheta)$ can be converted into a vector $\boldsymbol{p}(x)=[R'(\vartheta_0),R'(\vartheta_0+\Delta\vartheta),...,R'(\vartheta_0+(D-1)\Delta\vartheta)]$.
Similar vectors are also derived for the initial weight vectors: these are either random values or the expected Zoeppritz reflectivity curves (see 2.5). The result of the Self-Organizing Map for both kinds of initial vectors is the same and interestingly, the number of steps for convergence are approximately equal. The number of steps is only dependent on the order of input of the vectors, which is random and unpredictable. Kohonen (1997) describes the same phenomenon of independence on the initial vectors, as long as the input dataset is poorly sorted. For 5 cells in 20-dimensional space which was the setup used this can generally be assumed to be true.
The process results are shown for the sample profile P34 (fig. 38). After the initial neural network, the weight vector present the best match of weight vectors for the input (Fig. 38b and c). Whereas in the case of the classical 1-dimensional SOM, convergence can be described in terms of distance - i.e. a scalar value -, a multi-dimensional SOM stays dynamical up to the end and each neuron approaches one of the classes in a circular manner because all offer a similar convergence trend. The ability of classification must be an inherent quality of the dataset and the classes are points of attraction for the SOM algorithm. The classical SOM algorithm can be used to find out how many classes exist. Cells that do not represent an inherent point of attraction will be representative of a very limited or even single input values (black spots in Fig. 37) only.

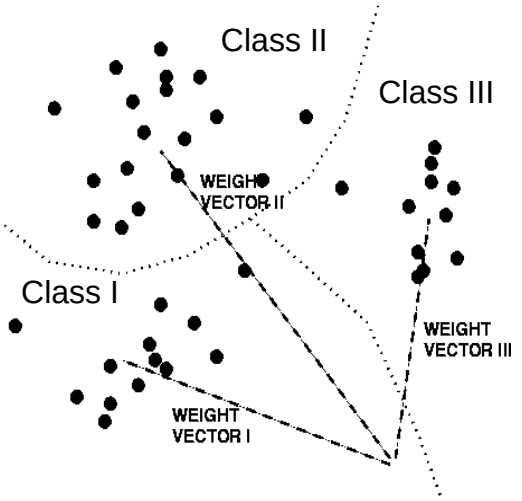

***Figure 37**: Clustering is the fundament of classification. This is only possible if the input values are not randomly distributed.*

Once a maximum number of classes, i.e. a series of weight vectors representative of the input vectors (black spots in Fig. 37) has been found by the classical algorithm, the batchmap algorithm should be used. The velocity of coherence is much faster, but the

batchmap will find as many classes as cells are defined (Kohonen, 1997). Another algorithm can be derived by modifying the SOM algorithm, so that intercell distance is represented by cell values, which is a problem for multi-dimensional vectors that cannot be represented by one scalar value.

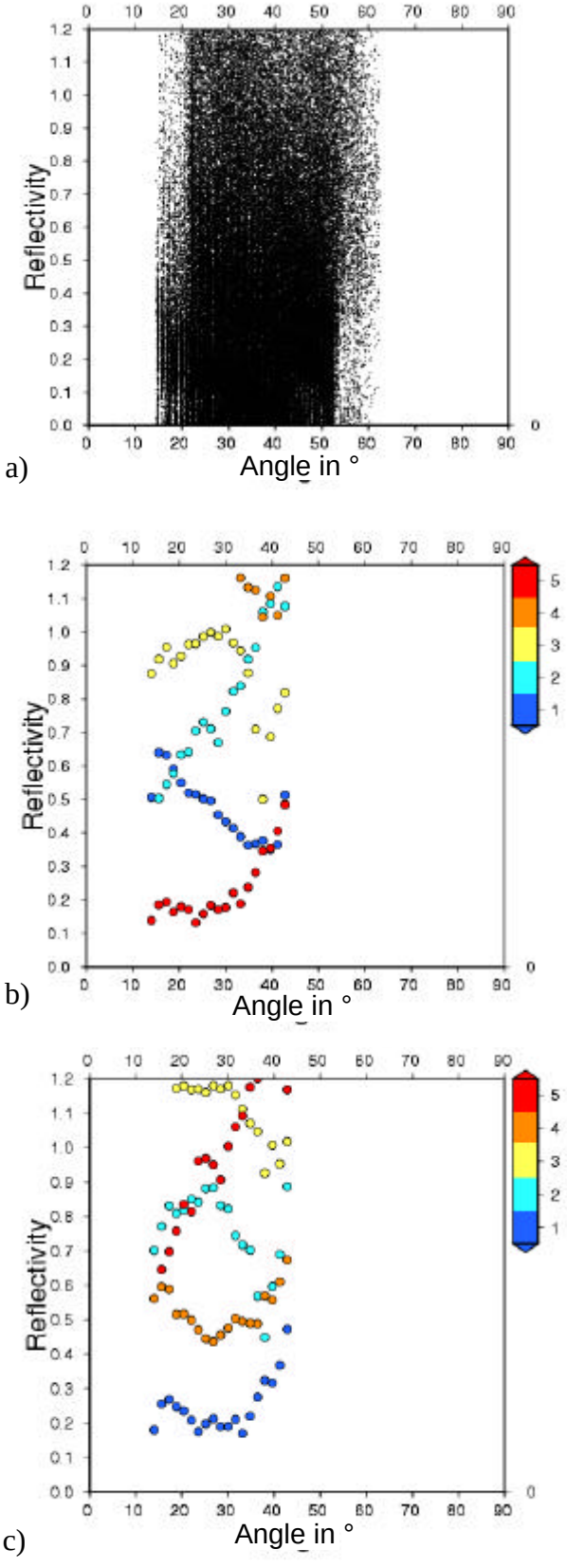

***Figure 38**: a) The assembled original reflectivity gathers and the comparison to a) the standard SOM and the b) batch map results for seismic line P34 reveals similar results for the 5 classes presented in the color scale in upper right corners, that cannot be trivially interpreted from (a). However, the standard SOM needed 200000 steps to end up with the presented values and the Batch Map needed only 80000 steps. Whereas the values are similar, the classes organize themselves in a different way (see text).*

2.7. Classes

After all the described amplitude corrections have been performed the profiles have been separated into a cluster of CMPs which are represented by a single property, the reflectivity class derived from the first SOM cycle. Each profile was evaluated by a 5 cell SOM. An angular spacing of 2° was used to resample the reflectvity data for the range of 20° to 60°, in which most recorded data plot. The gridded reflectivity curves of the 5 classes of each profile (Fig. 39a) serve as the input to the final SOM. Where the weight vectors of different classes in the same profile are similar, some of the profiles can be represented by less than 5 classes. Because the final weight vectors of adjacent profiles are also similar, the classes will reduce once more in the final SOM. The best result was obtained by 5 different classes which are presented in this chapter. To expand the final SOM to more than 5 classes leads to no further results, because there seems to be inherent ordering of the dataset into these 5 classes (Fig. 39b).

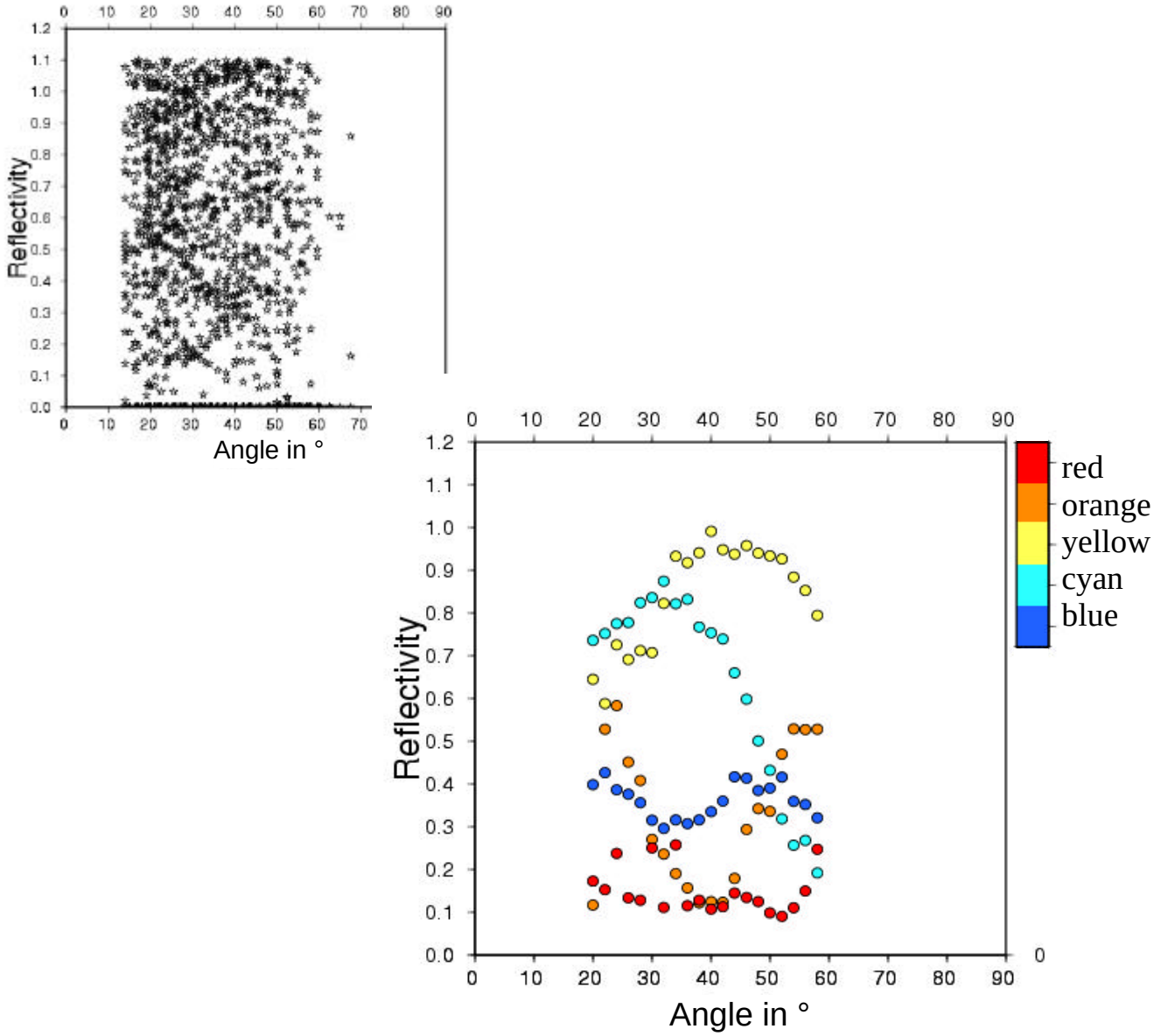

Figure 39: *a) On the upper left side, the original results of the single profiles are depicted, b) on the lower right side, the reflectivity trends of the final SOM incldluing all profiles are shown. The red class and the blue class show smooth curves of small amplitudes. The orange class shows a minimum at 40°, whereas the cyan class depicts a maximum at 30°. The yellow class shows strong reflectivities throughout. Therefore cyan and yellow were interpreted as hard rock and the others as weak in a first classification. The blue and yellow class can already be detected in a) as "centers of attraction".*

The root mean square error made by approximating the measured reflectivities by the SOM classes is denoted in Table 1. The errors scatter from 0.05 to 1.9, because single values show higher values than 1 which is typical for thin or rough layers (see above). Small values occur at smaller values and where classes represent a large part of the input vectors.
The final CMP classification was performed by evaluating the best match between the final SOM classes and the CMP reflectivities of the single profiles. The process is displayed for the CMP of the sample line P34 (Fig. 40) that was used earlier on (fig. 20).

Line No.	***Class 1***	***Class 2***	***Class 3***	***Class 4***	***Class 5***
	RMS-Deviation	RMS-Deviation	RMS-Deviation	RMS-Deviation	RMS-Deviation
P1	0,16	0,21	0,44	0,91	0,43
P3	0,05	0,1	0,03		0,29
P4	0,07	0,21	0,09		
P5	0,11			0,41	0,41
P6			0,3		
P7	0,24		0,61		0,7
P8	0,24	0,27	0,29		0,05
P10	0,17		0,53		0,37
P11	0,1			0,22	
P12			0,61		
P13	0,07	0,06	0,11		0,09
P14	0,05	0,11	0,03	0,03	0,02
P16	0,05	0,15		0,03	
P17	0,11			0,02	
P28	0,03	0,05	0,08	0,11	0,75
P33	0,14			0,8	
P34	0,34	0,41	0,46	0,8	~~**1,9**~~
P35	0,28	0,3			0,34
Average	**0,12**	**0,19**	**0,3**	**0,37**	**0,35**

Table 1: *The root-mean square deviations from the mean curve derived from the SOM are smaller for smaller reflectivities. For class 5 the results for some profiles reach very high values, the highest was eliminated for the investigations. The highest trend is the attractor for high breakaway values, which are frequent on line 34. Where no value is printed, the class is representative of a single value.*

In the further work of this thesis, the classes will be expressed by representative colors: red, orange, blue, yellow and cyan. A first glimpse shows that some classes dominate in certain areas, e.g. the red class in the topographic lows of the survey area, the yellow class in the southeastern part close to a ridge and cyan near Grimseyjargrunn and on Southern Kolbeinsey Ridge. To connect these representative colors to lithological classes, the physical properties related to the reflectivity trends of each of the colored classes have to be evaluated, after the numerical SOM reflectivity classes have been obtained by the presented new method.

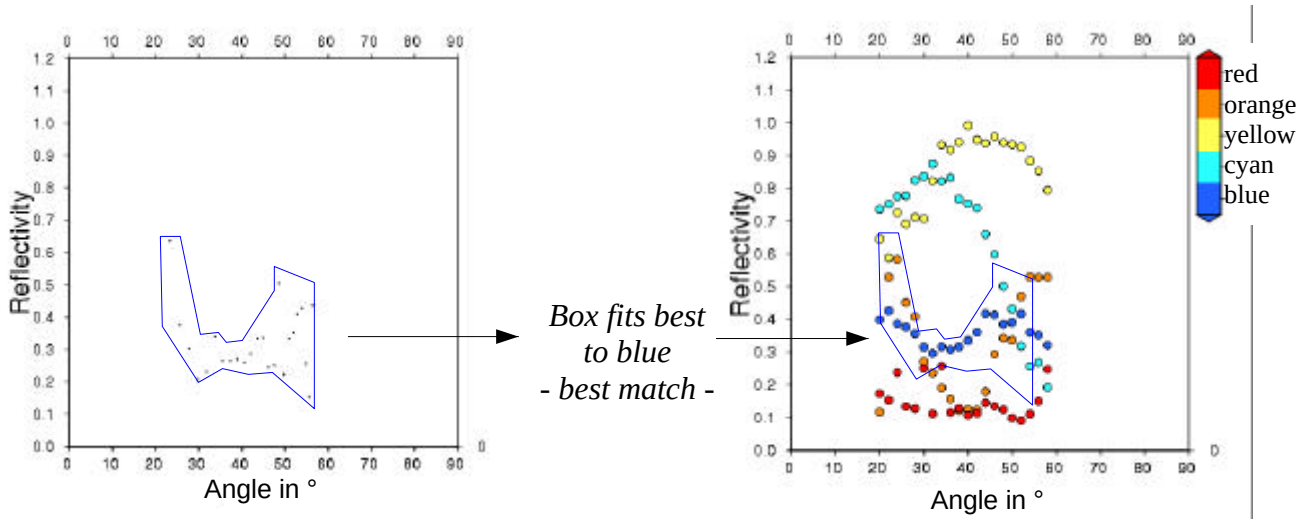

Figure 40: *The sample RVA gather of Fig. 20 is compared to the classes of the final SOM from Fig. 39b. Close inspection reveals a similarity of the gather (windows of extreme values shown as a box in both graphs abovw) with the blue class, i.e. the square sum of the error made by expressing the reflectivity gather by one of the classes is smallest for the blue one. So „blue“ the "best match" for the sample CMP.*

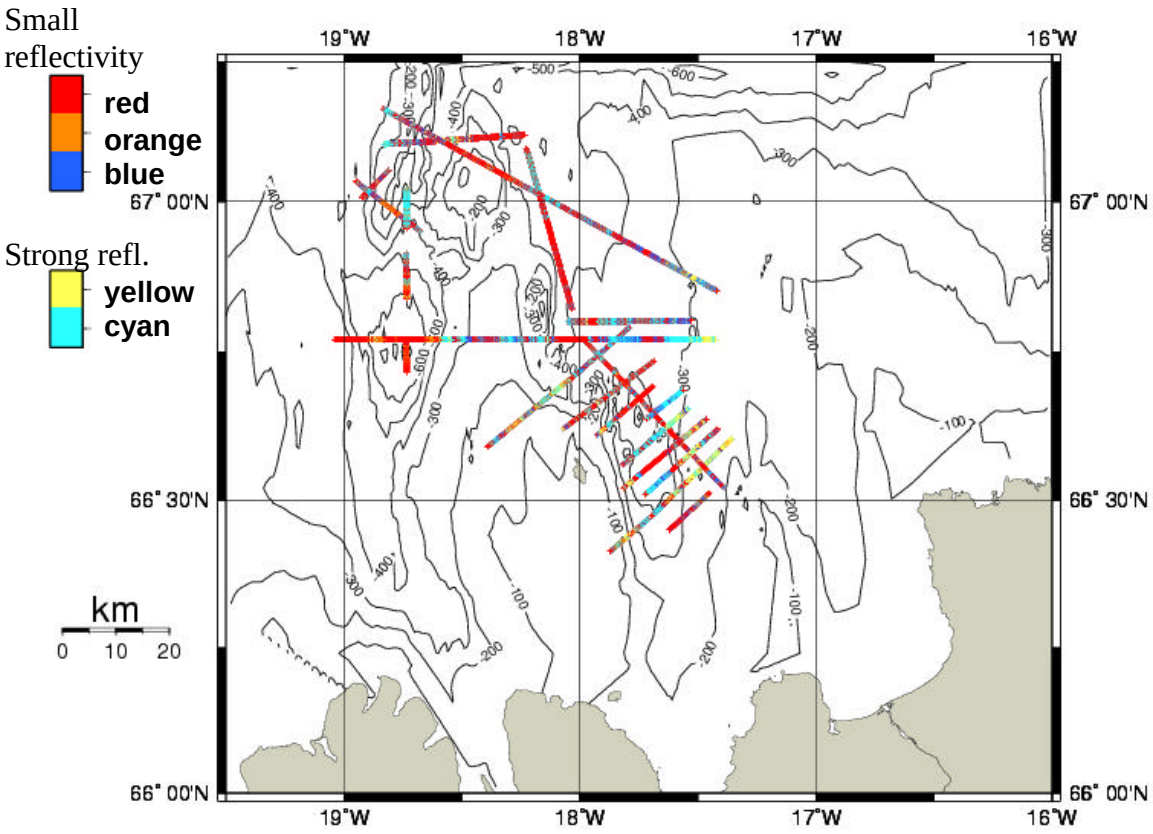

Figure 41*: The map of classified CMPs from the survey shows regions, where the classes denoted at the left upper edge are distinctly representative. For example, the red class is definitely found in the bathymetrically lower regions of the survey area, whereas the yellow class is foremost depicted at the eastern edge of the map, where a smoothly rising ridge is visible.*

Reflectivity and roughness - a comparison

Comparing the reflectivities to the coherence function values of Fig. 24 allows a qualitative estimation of the reflectivities, since the coherence and consequently roughness of the amplitude is a

measure of reliability of the data. The low coherence (*CF(*160 *Hz)* <0.2, i.e. high roughness) values in the northwestern part of the survey area are mirrored in chaotic series of reflectivities. From former surveys (McMaster et al., 1977; Saemundsson and Hjartarsson, 1994) it is known that the area is dominated by basalts and the topography is ragged. The ridge area can apparently not be imaged by the seafloor reflectivity mapping method and the same might apply to all areas where low coherence was found. Major coherence shifts occur where reflectivities change from one class to another, which shows that roughness and reflectivity are influencing each other. However, reflectivity shows variation where roughness cannot be used to distinguish within the classes, e.g. medium roughness (*CF(*160 *Hz)*<0.6) can occur for any reflectivity class. Counting the occurrence of coherence function values for each of the classes reveals a maximum in the range from 0.2 to 0.4 for all the classes (Fig. 42). Insterestingly, only in the case of the yellow - hard rock - class the

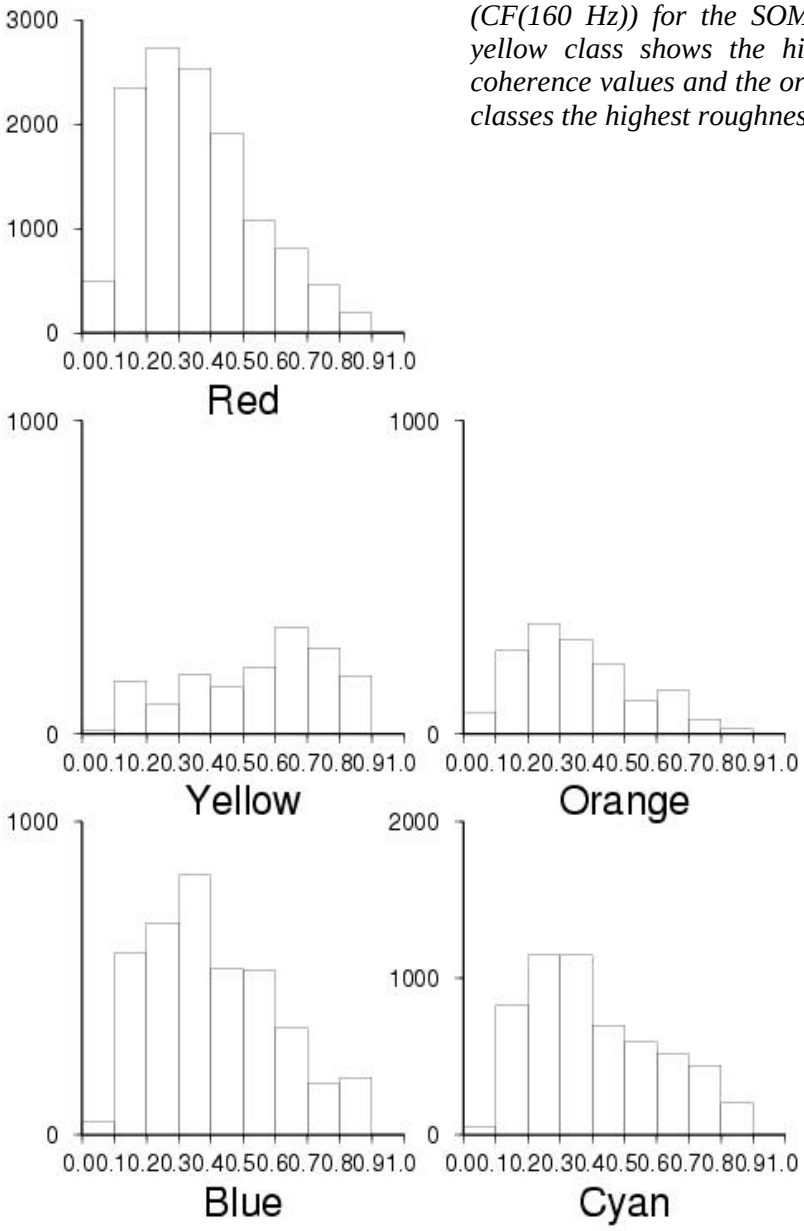

Figure 42: *Frequency of occurence plotted against the coherence values (CF(160 Hz)) for the SOM classes. The yellow class shows the highest relative coherence values and the orange and blue classes the highest roughness.*

most frequent coherence value is higher. The most high coherence values in absolute numbers occur for the cyan, yellow and red class rather than yellow. The likeliness of the distributions implies that the roughness seems to be foremost typical for the morphology of the area (here: the TFZ) rather than the lithologies.It is impossible to imply the reflectivity from roughness, and it is likewise a complex task to deduct roughness from reflectivity. Roughness is thus a measure of the morphology of the seafloor rather than lithology. It is impossible to deduct the variation of amplitude with increasing roughness from real data, because more than 90% coherence is rare. The geological context is necessary to explain the variations of both parameters and therefore a detail analysis will be essential.

2.8. Interpretation - The link to geology

The connection between lithology and physical parameters is more complex. Though physical properties will be discussed, it will turn out that no unique interpretation of the geological boundary conditions is implied by these models. There are all sorts of model and approximations especially for sedimentary units, but it is easier to review the regionally expected rock types first to provide expectation values for limit the interpretation possibilities. The same experience was obtained by former reflectivity mapping methods (Lambert, 1988). By the use of the neural network this least unique part has been shifted to the end of the method to minimize the follow-up error. This has never been reported before. It splits the physical and geological part of the method. The reflectivity trends and classes will hold, even if the link to geology cannot be established.
In the TFZ seismic reflection investigations have been performed before and geological samples have been taken (see Chapter 1). Table 2 presents the expected rocks and the parameters which are important for a discussion of the physical properties. Porosity, permeability or grain-size are partially known but are of secondary importance for the discussion of lithology.
These sampled rocks are not actually the pure rocks for which physical properties are known, but represent mixtures, e.g. of basalt with glass crusts (Devey, 1997) or anhydritic ooze with traces of pyrite (Scholten, 1999). Salisbury et al. (1996) showed that mixing between sulphides and host rock will also cause physical properties of average values between the pure species. Velocities and densities can be interpolated from the end members of the mixing process. Applying this principle to the present situation of the TFZ, the range of p-wave velocities alone is very coarse measure of the rock type (Fig. 43a). Most of the typical rocks in the TFZ - with the exception of rare bits of heavy precipitates as talc or massive sulphides - plots along the worldwide expected Gardner's rule (Gardner et al., 1974) or the Nafe-Drake-curve (Ludwig et al., 1971) which is a distribution of thousands of measurements that scatter around the values calculated by this rule (Fig. 43b):

$$\rho = a \sqrt[4]{v_p} \quad \text{, where } a\text{=0.31 and v is in m/s. (22)}$$

Compressional wave velocity and density are not independent parameters for the main part of the sampled rocks and thus a third parameters needs to be taken into account, the s-wave velocity. For most rocks there is again a typical value which is determined by a rule of thumb. v_p and v_s expose a typical ratio (Telford et al., 1990) of:

$$\frac{v_p}{v_s} = \sqrt{3} \approx 1.7 \qquad (23)$$

The v_p/v_s ratio is particularly a measure of lithology where it rises anomalously to values of ~100, which occurs in soft marine sediments (Ayres and Theilen, 1999) or 2.2 in igenous rocks as Andesite (Maercklin, 1999) or Basalt. Hydrothermal precipitates like Anhydrite also show unusually low v_s-values (Ludwig et al., 1998) and v_p/v_s ratios can reach values of 2.5 and more.

type	***published in***	***parameters measured***	***v_p in km/s***	***v_s in km/s***	**ρ in g/cm^3**
Basalt	N	v_p	**3.5 - 4.8**		*(T 2.7-3.3)*
	LW	*type*			
	M	*type*			
	S	*type*			
	McM	*type*			
	SM	v_p, v_s	**3.7 - 4.5**	**2.1 - 2.6**	
	St	v_p, v_s	**5.5**	**3**	
	F	v_p	**3.0 - 5.0**		
	D	v_p	**4.1**		
	Min	v_p, v_s, ρ	**4.7 - 5.8**	**2.8 - 3.4**	**2.79**
Anhydrite	TS	*type*	*(L,T 3.8-6.2)*	*(L 1.8-2.2)*	*(L,T 2.1-3.0)*
		v_p, v_s, ρ			
Pyrite,	H	*type*	*(Sa 7.9-8.0)*		*(T 4.7-5.2)*
Marcasite	TA	*type*			
Talc	TS	*type*	*(C 6.3)*		*(C 2.8)*
Barite	H	*type*	(Be 4.5)	(Be 2.5)	*(T 4.3-4.7)*
Conglomerate	S	*type*			
	TS	*type*			
	D	v_p	**3.3**		
Silty clay,	LW	*type*		*(A 0.04-0.8)*	*(T 1.6-2.6)*
ooze, mud	TS	*type*			
	N	v_p	**1.6 - 1.9**		
	B	v_p, *type*	**1.6**		
Sand	LW	*type*		*(A 0.04-0.8)*	*(T 1.5-2.7)*
	JS	*type*			
	M	v_p	**2.1**		
	SM	v_p	**2.4**		
Volcaniclastics	LW	*type*	*(C 2.5-4.0)*	*(C 1.0-2.0)*	
Volcanic glass	LW	*type*	*(C 5.4-5.8)*	*(C 3-3.2)*	*(C 2.7-2.85)*

Table 2: *shows the physical properties of the expected rock types at the sea floor in the TFZ. Physical properties which are only known in general, but not for the particular region are written in brackets. The abbreviations depict the source for the values : A: Ayres and Theilen (1999), B: Broser (2000), C: Carmichael (1982), D: Darbyshire et al. (2000), H: Hannington et al. (submitted), JS: Johannesson and Saemundsson (1998), L: Ludwig et al. (1998), LW: Lakschewitz and Wallrabe-Adams (1991), M; Mochizuki et al. (1995), McM: McMaster et al. (1977), Min: see Appendix, N: Neben (1992), S: Saemundsson (1974), Sa: Salisbury et al. (1996), St: Stefansson (1999), SM: Staples et al. (1997), T: Telford et al. (1990), TS: Theilen and Scholten (2000).*

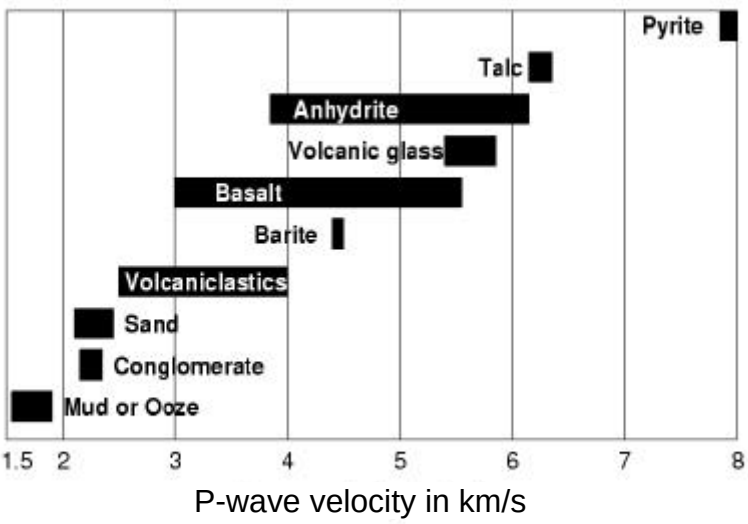

Figure 43: *a) The range of p-wave velocities from 1.5 km/s to 8 km/s is spanned by the rocks found at the seafloor in the TFZ. Basalt and Anhydrite span a similar range and both are equally frequent near the hydrothermal centers (Scholten et al., 2000) in the area.*

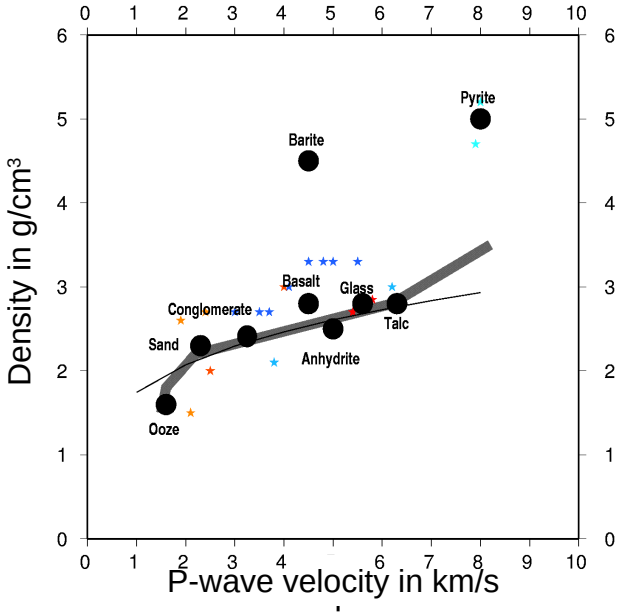

b) The density-compressional wave velocity distribution is still not the suitable tool to determine rock lithologies because the most frequent rocks (Basalt, Glass) are too similar to the most frequent precipitates (Anhydrite, Talc) in the TFZ. The stars represent the boundary values printed in Table 1, whereas the black spots show the typically expected value interpreted by averaging over the sampled rocks and the expected grey Nafe-Drake curve (or Gardner's rule (black line)).

Average rocks, that can account for the seismic velocities already measured in previous surveys (Neben, 1992; Staples et al., 1997; Stefansson, 1999 etc.) and have been sampled in the TFZ are represented by black spots in Fig. 42. The reflectivity response of these rock compositions was modelled by the elastic Zoeppritz equations (Fig. 44).

The resulting reflectivity trends were compared to the curves of the final SOM. The five SOM classes can be described in terms of reflectivity, which can here be connected to physical properties and thus lithology. To test the thesis, that the numerical SOM classes are equivalent to these presented lithological classes, a detailed investigation of geochemical, geophysical and geodynamical features of the survey area was performed which is subject of chapter 3.

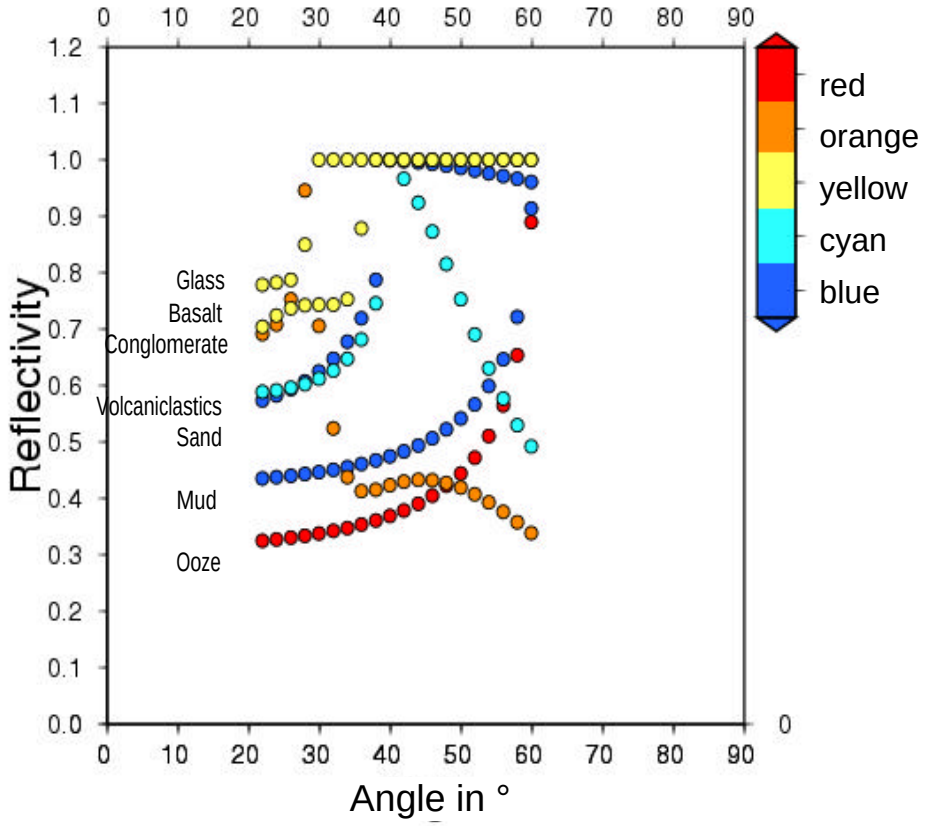

Figure 44: The Zöppritz curves for the expected rock samples (without precipitates) are shown in the colors of classes, they might represent. The sand class is probably not resolvable between the others and glass and basalt are also too similar to differentiate. Volcaniclastics are not depicted in Fig. 43, they are assumed to plot somewhere between sand and conglomerate here.

1) The ***Yellow*** class: In angles higher than ~30° the value of reflectivity is 1, which corresponds to the modelled results for basalt and volcanic glass. Further more, the values of the SOM reflectivity in small angles are scattered between the curve of basalt and glass, so the yellow class is best explained by igenous, basaltic rocks. The low roughness of the yellow class can only be explained by the fact that very rough basalts blur the signal in such a way that the real reflectivity cannot be calculated by the presented method.
2) The ***Cyan*** class: The cyan class of the final SOM is characterized by a maximum at ~30° and very steep decrease afterwards. This resembles the curve of volcaniclastics, but is also very similar to the thin or o rough layer case discussed in 2.4.2. So, this class is ambiguous and has to be investigated in detail. The distribution of roughness is similar to most of the other classes, but high coherence is relatively frequent. So, a first clarification can be the coherence value. Where coherence is high, it will represent a soft sedimentary class, i.e. probably a thin layer of sediments above hard rock (see e.g. Fig. 26).
3) The ***Orange*** class: Orange is distinctly different from the other classes, because it represents a curve that is dropping steeply before rising as steep towards higher angles. This feature cannot be modelled by any Zöppritz curve in the decisive range. However, it is found relatively often in coherence values around ~0.2 and thus could be explained by a conglomeratic material, because ist high roughness can imprint a steep increase of amplitude in relatively small angles. In conjunction with the conglomerate trend depicted in Fig. 44, this is the most likely solution.
4) The ***Blue*** class: It is difficult to relate a Zöppritz model to it. Mud or soft sands can best explain the curve, but since sediments are very often deposited in thin layers, it might as well represent thin sandy layers beneath mud, so the crude thesis is: blue is a class for compacted sediments.
5) The ***Red*** class: No values as low as those found for the red class can be found for the rocks

modelled by the Zöppritz equations. This is probably due to the fact, that most of the rocks represented by the red class have only been deposited very freshly and are not compacted yet. The gradual compaction does not create another decisive reflection and thus the signal response arrives from the loose material. Most loose material that was sampled in the TFZ was silicic and thus red is probably indicating ooze. Any loose material whether muddy or of volcanic origin will be similarly represented by red. Red is the class for soft, loose sediments. The frequent occurrence of high roughness in the red class (Fig. 42) can have many causes. One of them may be the strong amplitudes decrease where diffraction occurs, but mainly high roughness will occur in weak layers where scattered boulders and terrigenous material are scattered on the seafloor, which is the case in Northern Iceland (Eiriksson et al., 1990).

„The night has been unruly: where we lay,
Our chimneys were blown down; and, as they say,
Lamentings heard i' the air; strange screams of death,
And prophesying with accents terrible
Of dire combustion and confused events
New hatch'd to the woeful time: the obscure bird
Clamour'd the livelong night: some say, the earth
Was feverous and did shake.“
(Shakespeare, Macbeth)

Detail analysis
of geodynamical features

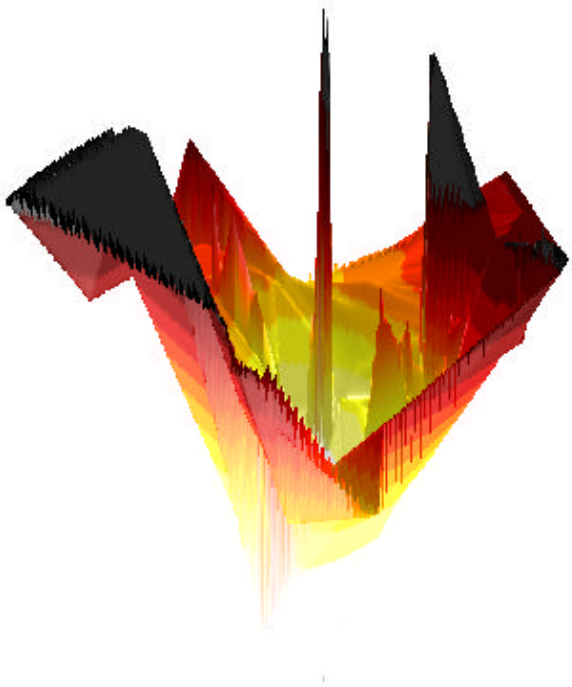

3. Detail analysis of geodynamic features

The seafloor mapping showed that a reasonable model of the subsurface cannot be produced by the method without previous knowledge about the area. In this chapter this will be tested on certain subdivisions of the Tjörnes Fracture Zone. Not the whole of the transform zone was investigated in the seismic survey and so, as a guideline for the reader the single areas will be presented in a short overview before discussing their details.

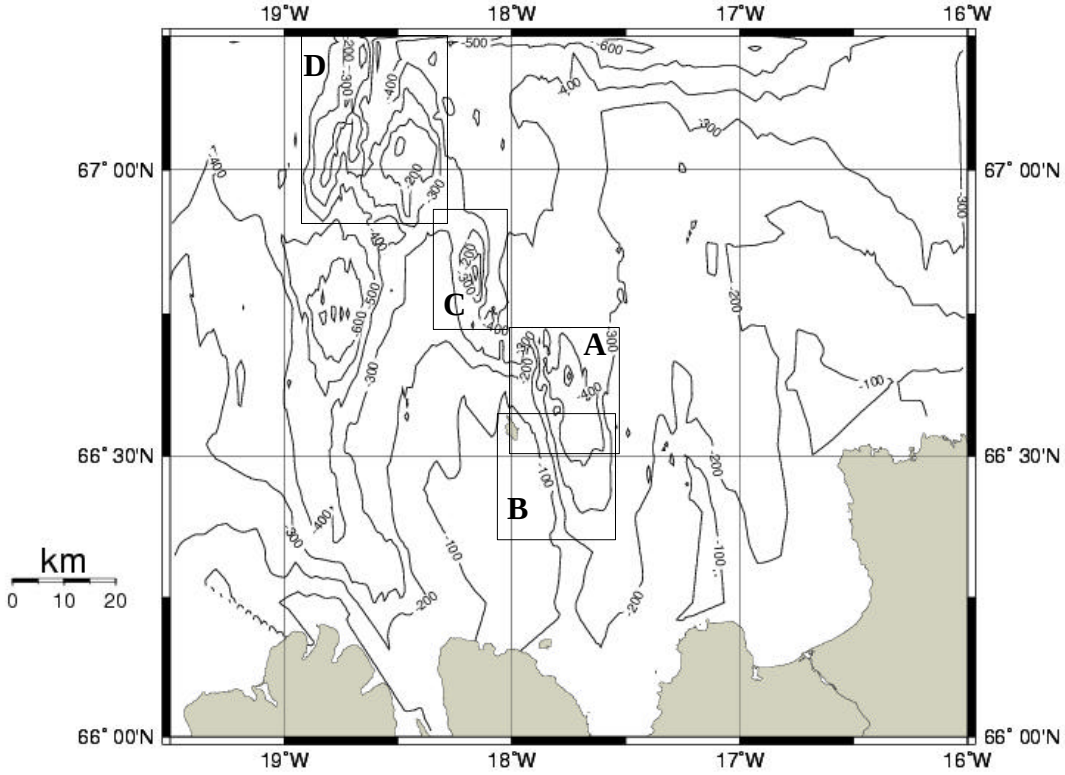

Figure 45: *The areas in the boxes will be presented in this chapter: A: Northern Skjalfandi Bay, B: Southern Skjalfandi Bay, C: Hóll complex, D: Kolbeinsey Ridge.*

The areas are displayed in Fig. 45 and cover two troughs (Skjalfandi Trough and Eyjarfördur Trough), Kolbeinsey Ridge and a volcanic complex (Holl). The areas A and D were the main focus of the survey because they include hydrothermal fields. For hydrothermal fields some properties of the seafloor mapping method had to be tested in 3.4. while presenting Northern Skjalfandi Bay. Eyjarfjördur Trough was only covered by profiles in the north, but a new fault pattern was derived by integrating other publications. The Holl complex is the highest submarine volcano (McMaster et al., 1977) which is not part of Kolbeinsey Ridge, thus the highest volcano of the offshore part of the TFZ and was a further focus of interest. Skalfandi Bay, though close to the northern icelandic coast, has never been described in detail, but the information from various geoscientific surveys will show its importance in the TFZ system.

3.1. Skjalfandi Bay - a fault-wedge basin

Northern Skjalfandi Bay is dominated by tectonic and depositional structures from the so-called Skjalfandi Trough (Fig. 46, Hannington et al., submitted). The northeastern corner of Skjalfandi Trough was a focus of the investigations during the presented survey, because hydrothermal venting has been discovered in the area, which is is marked as Grimsey Hydrothermal Field (GHF) in Fig. 46. The west of the trough is bordered by Grimseyjargrunn to the south and the submarine volcanic edifice of Nafir to the north (Fig. 46, McMaster et al., 1977).
Reflectivity can supply important information about the surface of the trough and the extents of sedimentation within, which is correlated to the geological history. Structural and stratigraphic examinations can be used to test the reflectivity investigations in the basin. Decisive deep lying structures cannot be revealed by the presented reflection seismic data, so hypocenter distributions will be used instead.
To unravel the basin dynamics, it will be rewarding to have a look at the GHF venting area, where fluids are rising to the surface. These fluids reveal gasgeochemical properties, which deliver additional constraints on sediment cover and deep migration paths. These points will be stretched out in the following chapters.

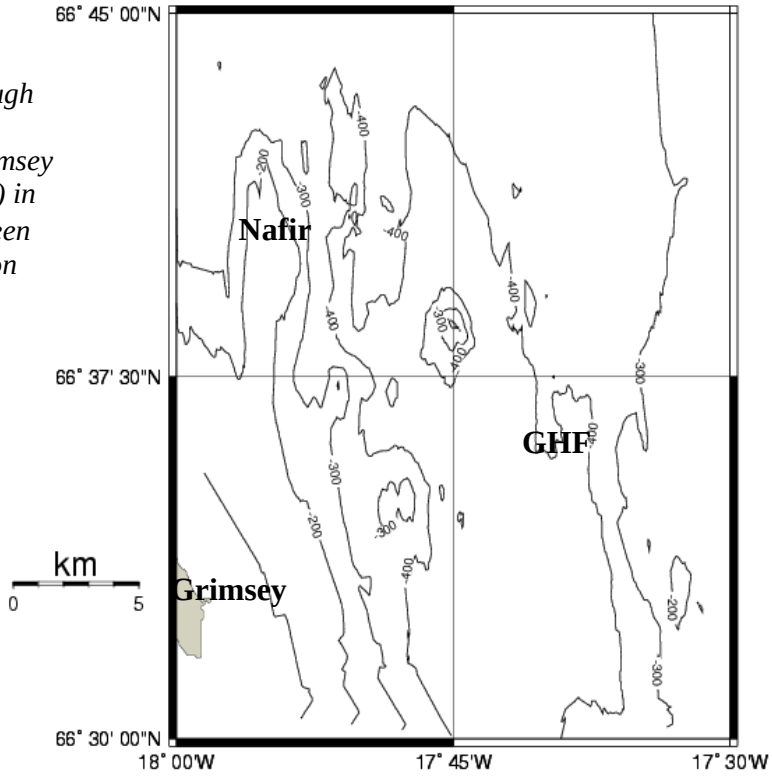

Figure 46: *Skjalfandi Trough ranges from a line Nafir-Grimsey in the west to Grimsey Hydrothermal Field (GHF) in the east. The basin inbetween is a result of ice age erosion and modern day tectonics.*

3.1.1. Structural analysis of the seismic data and the seafloor

Structural information of Skjalfandi Trough, i.e. the extents of faulting and dominating strike and dip can be extracted from reflection seismic profiles by isolating reflector discontinuities. The style of faulting in the area is known from fault plane investigations of the earthquake catalogue (Rögnvaldsson et al., 1998). Where seismic profiles cover the subsurface in a narrow grid, it is possible to relate seismic and seismologic data and thus to detect the outcrops of shallow active faults. In addition to the processing steps already described, it was important to migrate the

reflection seismic profiles from offset-time to offset-depth dimensions:

- to regain the actual dips of faults and
- to make earthquake catalogue and reflection seismic dimensions comparable.

A pre-stack Kirchhoff depth migration of the Seismic Unix package (Cohen and Stockwell, 1998) was used for this task. Laterally constant seismic velocities in layers of varying thickness were assumed.

The layers were foremost separated by their internal reflection characteristics, i.e. seismic facies (Fig. 50):

- a top layer of unambiguous fine subparallel layering, the sediments (1600 m/s),
- an ambiguous layer, partially made of deep sediments and outcropping altered basement (2300 m/s) and
- the basement of "apparent" hummocky internal reflections dipping east (3000 m/s) which are visualized on automatic gain controlled records.

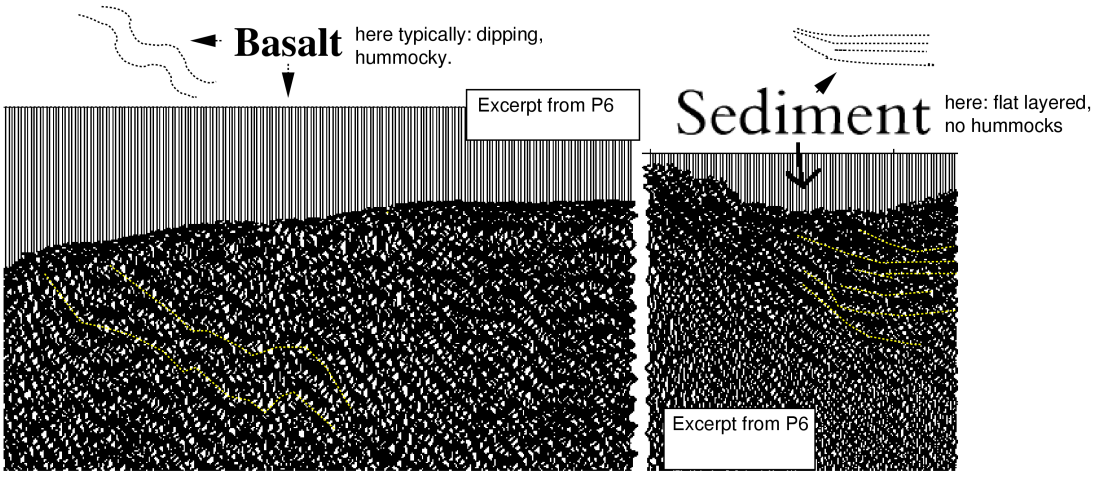

Figure 47: *After Automatic Gain control, the basalt layers reveal a dipping and hummocky internal structure, whereas the sediments are finely layered horizontal reflectors.*

For basalt structures, a frequent observation is the formation of diffraction hyperbolae originating from the seafloor (Fig. 48) which corresponds to low values of coherence. Thus basalt exhibits rough behaviour both in the diffraction and in the roughness regime. Deeper reflections than 1.2 km cannot be resolved in the dataset, because the recording time of 1.5 s and the energy of the airguns limit the resolution.
Where the hummocky, diffracting basalt was suspected, the yellow reflectivity class was observed (Fig. 49)
Line P6 is one of the best reflection lines. Clearly fine ine layering can be observed in the near-surface structures of its southwestern part (Fig. 50a), whereas hummocky units make up the deep structure (Figs 47 and 50 a). These approach the surface at two *topographic highs* to the *west* (THW) and *east* (THE) of the main fine layer unit.

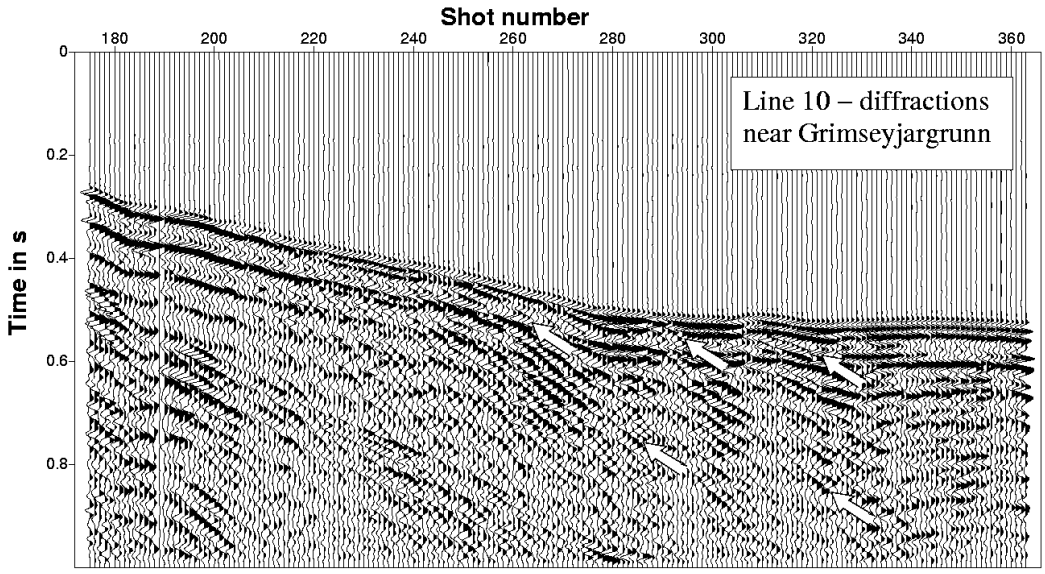

Figure 48: *Where the roughness is high, diffractions originate from near the seafloor on Line P10, which are highlighted by white arrows, thus hinting on roughness in various scales.*

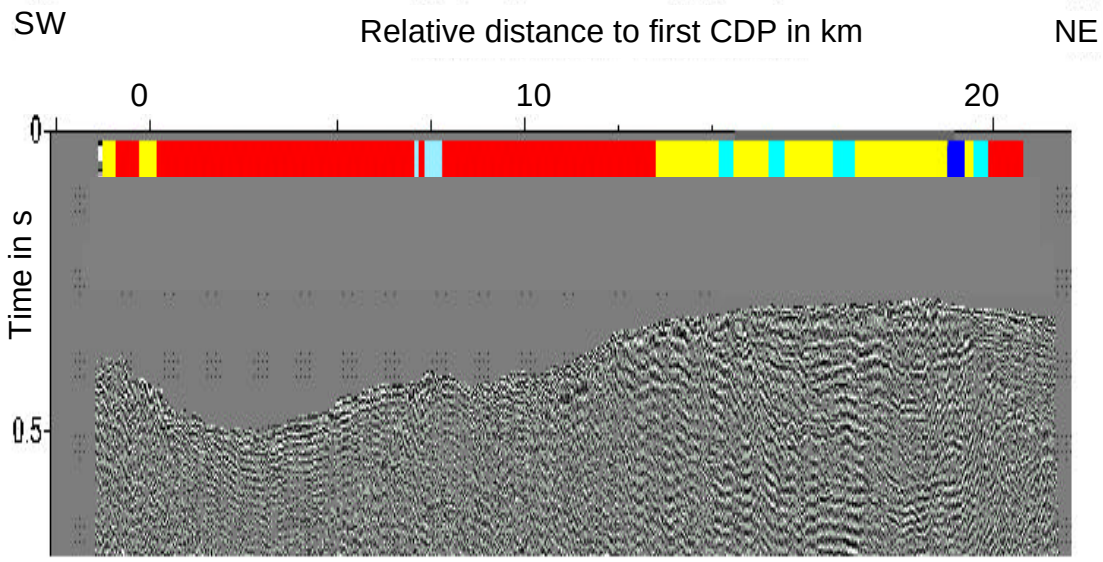

Figure 49: *The reflection line P6 is displayed with the colors representing the classes from seafloor mapping. Where the hummocky layers crop out, yellow prevails, another evidence for basaltic origin.*

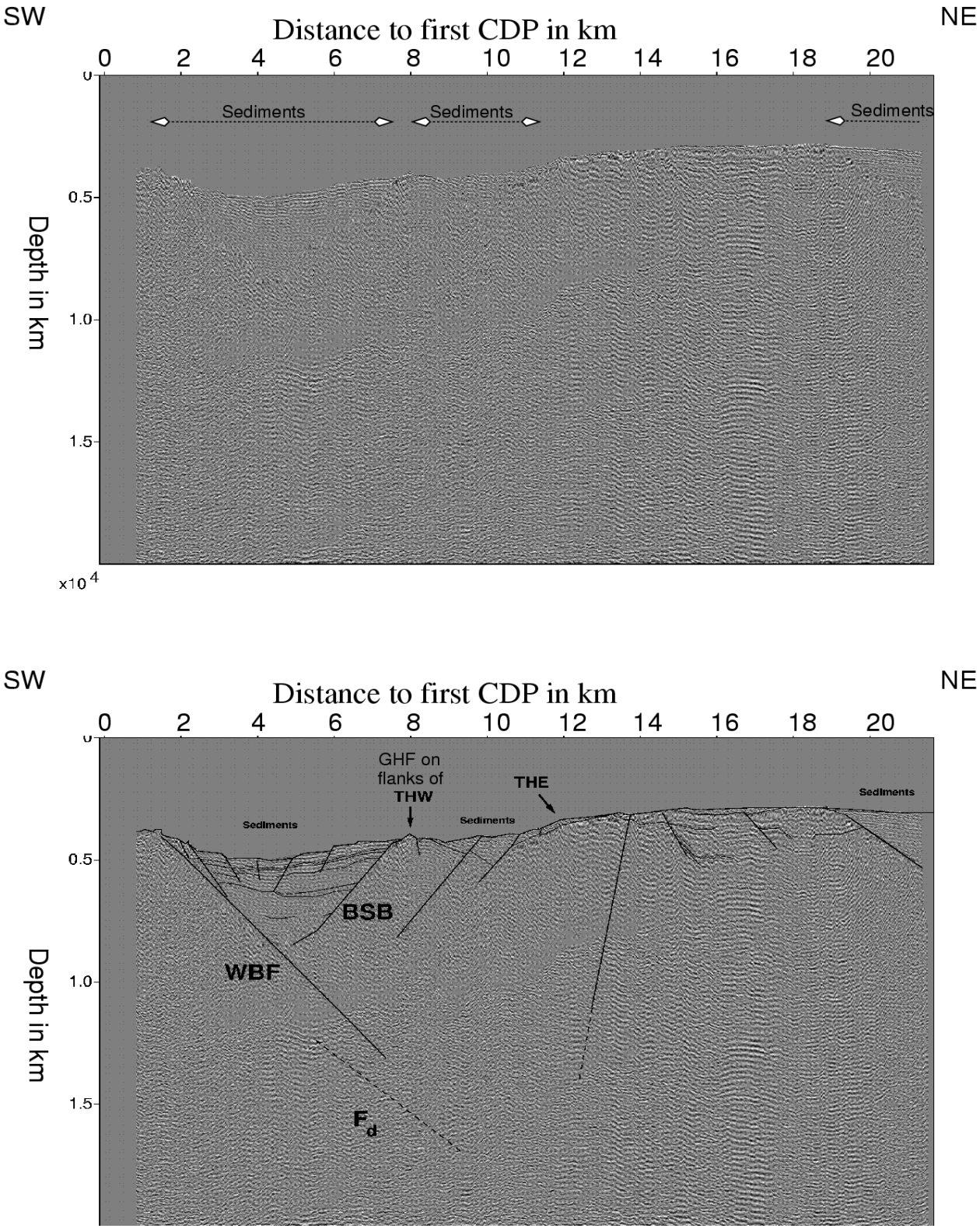

Figure 50: *Reflection line P6 is a cross section through the sedimentary basin of Skjalfandi Trough and Grimsey hydrothermal field (GHF), which is located on the flanks of the topographic high (THW) to the west of the trough. The thopographic high to the east (THE) is probably part of the Manareyjar Ridge lava flowfield and is composed of igneous rocks. In the upper section the sediment as implied by the reflectivity study (Fig. 49) is depicted, whereas in the bottom section a structural interpretation was performed. The lines show projections of fault planes which are implied by the truncations or diverting of reflections.*

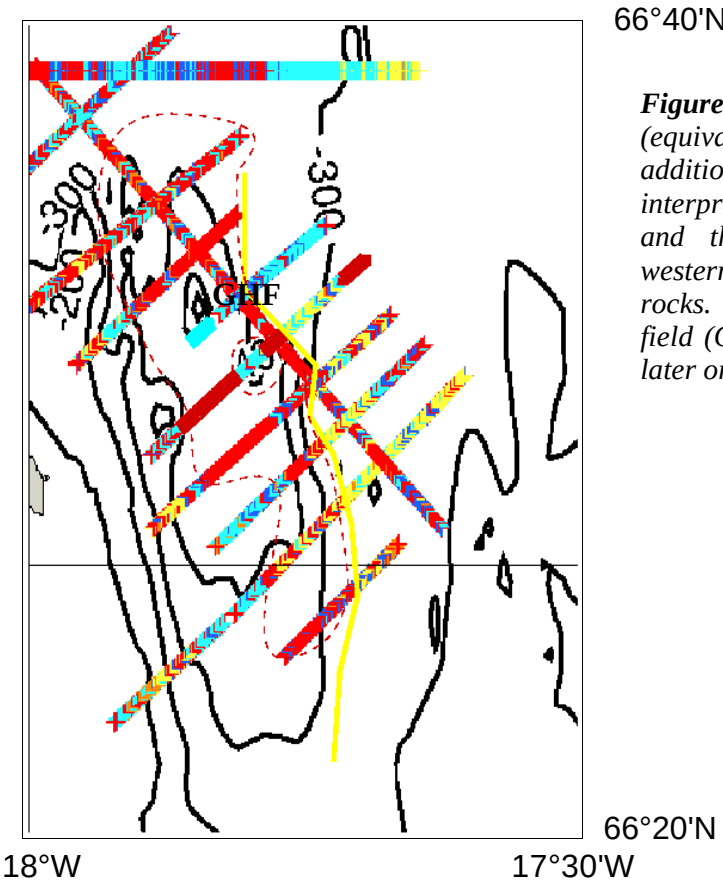

Figure 51: *This is an excerpt of Fig. 41 (equivalent to area A of Fig.45) with two additional lines, a dashed red line interpreted as the extents of sediments and thick yellow line marking the western end of outcropping igneous rocks. The rocks of the hydrothermal field (GHF) are not classified here, but later on in the chapter.*

Throughout the trough, the red reflectivity class dominates, whereas the eastern and western border are clearly marked by the yellow class (Fig. 51). In the central northern trough northwest of the GHF, the cyan class is shown. Roughness is generally low in the deep parts of the trough (Fig. 24). These observations lead to the conclusion that loose sediments prevail, which correlates well to the fact, that hemipelagic mud and silicic ooze were cored in the area of GHF (Theilen and Scholten, 2000). They will make up the major part of the lithological classes colored in red. The trough is probably the bathymetric expression of a sedimentary basin.

In the yellow dominated region, basalts and basaltic glasses have been dredged, which confirms the idea of a basaltic ridge in the east of the basin. The igneous rocks cropping out in the western and eastern topographic highs are confirmed by the high roughness values.

The cyan class in the central basin may be evidence for a thin layer or volcaniclastic deposition. The thin layer would consist of hard rock beneath a loose sedimentary cover. In a sediment dominated area this might hint on shallow igneous intrusions, intense compaction or cementation by mineral-rich fluids. Processes associated with the formation of any of these layers require a heat source, i.e. a magmatic or volcanic enter in the area. But there is no hint on a magma chamber cannot in the reflection data. A small volcanic edifice, however, is supported by bathymetry.

Grimsey Hydrothermal Field is not adequately represented by these reflectivity investigations. It is the focus of another self-organizing map of higher lateral resolution, which is presented later on.

The southwest of the basin is shown enlarged in Fig.52. It is dominated by a magnetic positive Brunhes anomaly, which hints on magmatic movement in the shallow subsurface. The seafloor consists of patterns following the borders of the anomaly, yellow directly at the border, cyan inside and red outside. The yellow outcrops could

be remnants of lavas of the Brunhes epoch. In this interpretation cyan would most likely be a thin layer of sediment above this basalt layer. The occurrence of the yellow and thus basalts is supported by relative high coherence values (Fig. 52 b). So the sedimentary basin is limited to the south by igneous rocks of young age.

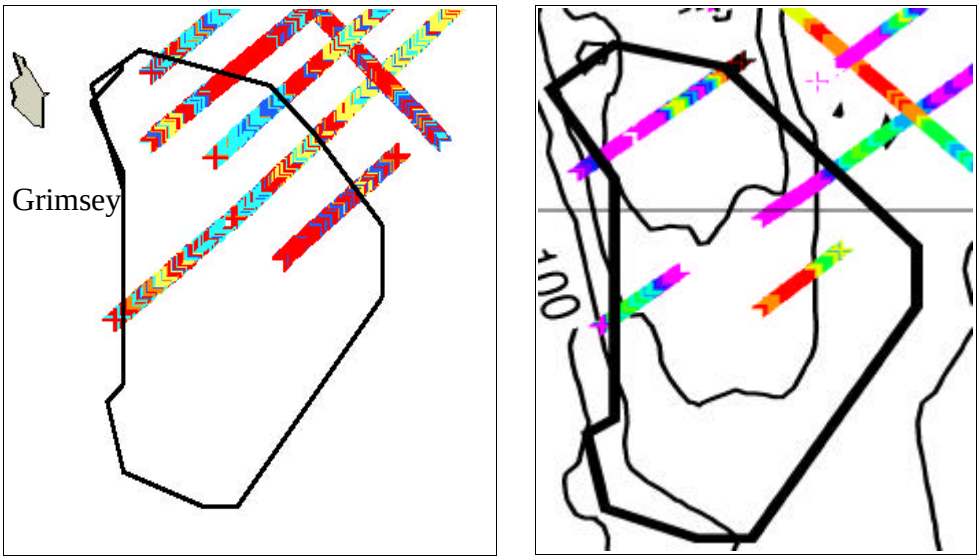

a b

Figure 52: *In southern Skjalfandi Bay (area B on Fig. 45) an isolated magnetic anomaly can be found (black polygon), which coincides clearly at its boundaries a) with the yellow reflectivity class, b) a medium to high roughness and the bathymetric contours (annotated in meters). The dashed black box in a) marks the part of Line P10 visualized in Fig. 48.*

Seismic facies and sampled rocks confirm the results of self-organizing seafloor mapping. The automatic recognition by self-organizing seafloor mapping eased the stratigraphic interpretation of the seismic record which was used to determine the extents of sedimentation in conjunction with structural and stratigraphic interpretations.

The strata have to be separated by discontinuities to detect them in the subsurface. These discontinuities are formed by faults or subhorizontal reflectors. Reflectors are foremost found beneath the sedimentary surfaces, but one such boundary can also be found in the northeastern basalts (Fig. 50b). Structural patterns are trivially derived from prestack-migrated sections because depth migration destroys the balance of frequency throughout the records. Faults were drawn where reflectors strongly undulate or appear discontinuous, so that finally a picture like Fig. 50b was obtained.

The Western Boundary Fault (WBF) of the basin and the Basalt-Sediment Boundary (BSB) are located between sedimentary and basement layers. The BSB marks the continuation of the bathymetric ridge spreading out north from Grimsey Hydrothermal field. Both faults expose dips of ~30°, when the displayed slope gradients (Fig. 50 b) are rotated towards their maximum. This is a typical thrust fault dip. The small faults within the basin exhibit dips of 60 to 70°, which is a typical normal fault dip. Normal faults hint on extensional structures. The same observations were derived from all profiles in the Skjalfandi Trough area, i.e. P3, P4, P5, P6, P7, P8 and P12 (Fig. 9). P6 was chosen because the sedimentary basin reaches the maximum recorded depth there. The fault marked F_d on Fig. 50b is probably an artifact or a multiple, thus it is only marked as a dashed line.

The WBF acts as a gently dipping footwall to the extension movement. The BSB

seems to be based on the WBF, thus both blocks are connected and move in accordance. The western part of basin must have opened up between them. The hummocky dipping layers of basalt are perpendicular to the BSB. Assuming horizontal deposition (e.g. lava flows), this is a sign that the BSB tilted during the ages.
The bathymetric surface of Skjalfandi Trough is plotted above the boundary from the sedimentary infill of the basin to the igneous basement (Fig.53). The deepest parts of the basin are identical with the deepest parts of the trough.

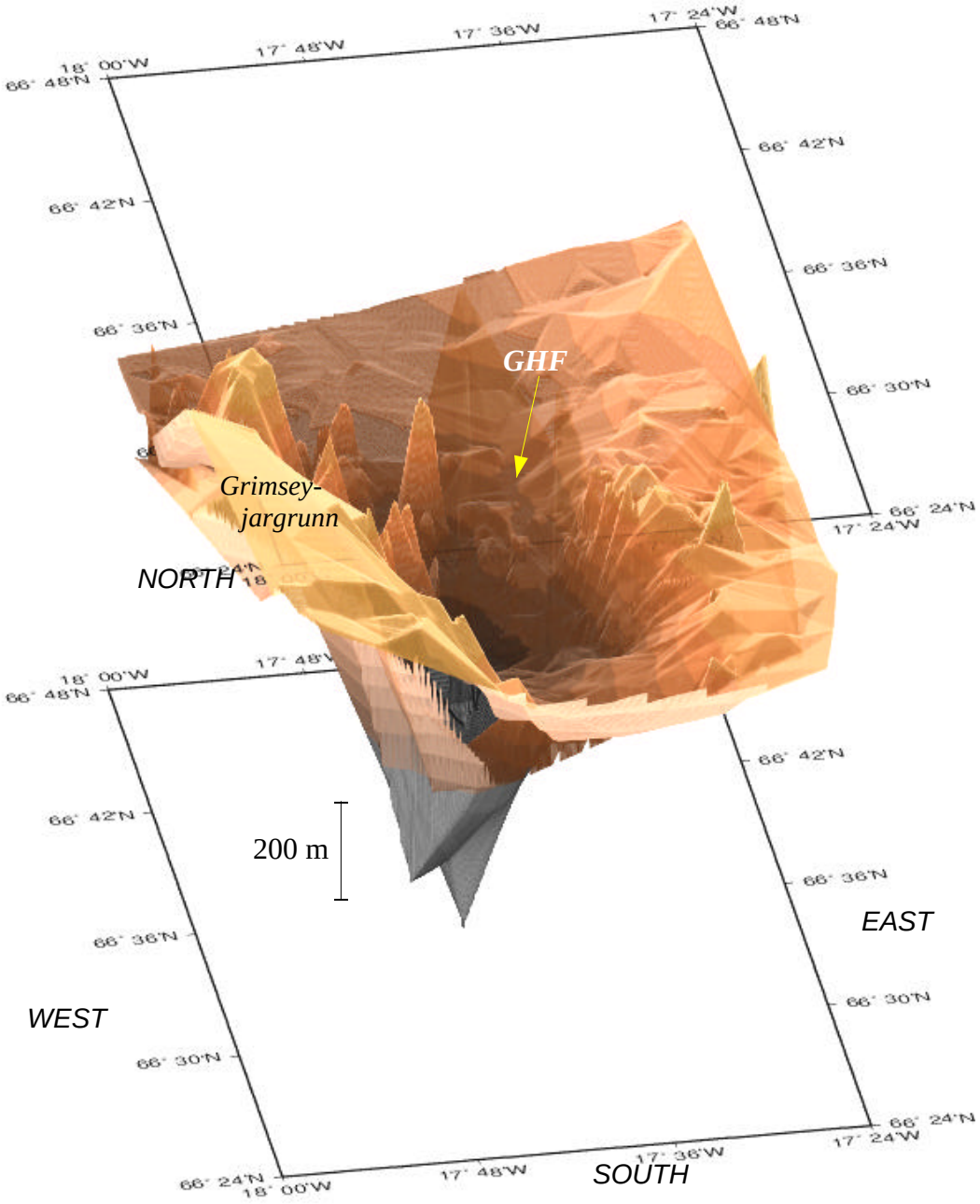

Figure 53: *Skjalfandi Trough is depicted in a 3D-plot of bathymetry as seen from Tjörnes Peninsula. The underlying basin may be recognized shimmering through the surface. It is about twice as deep as the trough and is filled with sediments, which can be clearly inferred from the reflectivity trends (Fig. 51) and seismograms.*

Basement

Stripping away the sediments reveals a goblet-shaped basin with its tip near the deep central part of P6 (Fig. 54). The western part of the basin exhibits small basement structures rising to points near the surface, whereas the eastern part is relatively undisturbed with the exception of a small ridge linked to GHF. In the northern part of the basin - on line P5 - , a basement structure rises steeply to the surface, which imprints a look onto the basin like a flower in bloom (see front page of chapter 3). This basement structure looks like a pipe from the base of the basin towards the surface. Unfortunately, it is located at the end of line P5 and cannot be imaged entirely, so its thinness must be considered an artifact. However, being situated beneath a local bathymetric high, it could mirror in situ properties and would explain the occurrence of the cyan reflectivity class as a thin sediment cover above igneous rock. The Grimsey Hydrothermal Field is marked as a basement high which is connected to the structures in the southwest. Thus the bathymetric hogh associated with the GHF, whichs spreads out to the north cannot trivially be interpreted by the same geodynamic movement.

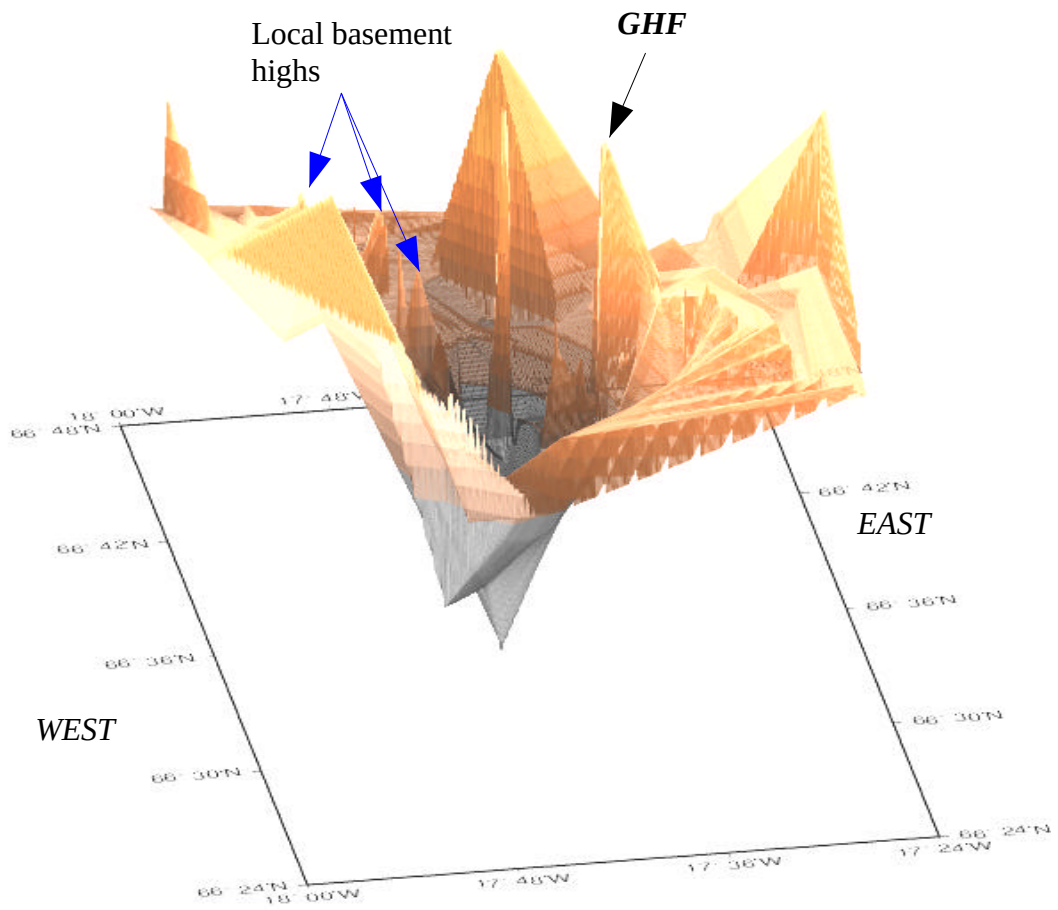

Figure 54: *Stripping away the sedimentary input reveals a goblet-shaped basin, which is typical for pull-apart basins and is often called "flower structure" (see also front page of chapter 3). From somewhere near the deepest part of the basin, a steep structure rises to the surface, which is probably a volcanic edifice*

Sedimentary basin

Additional information can be derived from the sedimentary deposition processes that took part in Skjalfandi Basin (Fig.55). The maximum thickness measured is 400 m. Eirikson et al. (1990) calculated a deposition of 0.2 to 1.5 m/ka sediments in the Tjörnes Fracture Zone from measurements on Flatey and Tjörnes Peninsula. So it would follow that the formation of the basin took place 266 ka to 2 Ma ago. This corresponds well with a shift of the volcanic axis from Skagi Volcanic Zone on Skagi Peninsula to the Northern Volcanic Zone in Iceland now, which took place 1 Ma ago (Saemundsson, 1974).
The layering of basalts suggested a tilting of the Basalt-Sediment boundary (BSB) during the ages. This is confirmed by a chronogram where the amount of sediments deposited between marked unconformities is displayed depending on relative time of deposition in Fig. 55. Of special interest are the depositional sequences that developped when the basic fault was tilting. These deposits are described as *syntilt* whereas later, shallower movements of the normal faults within the basin are marked as *synrift* sequence.

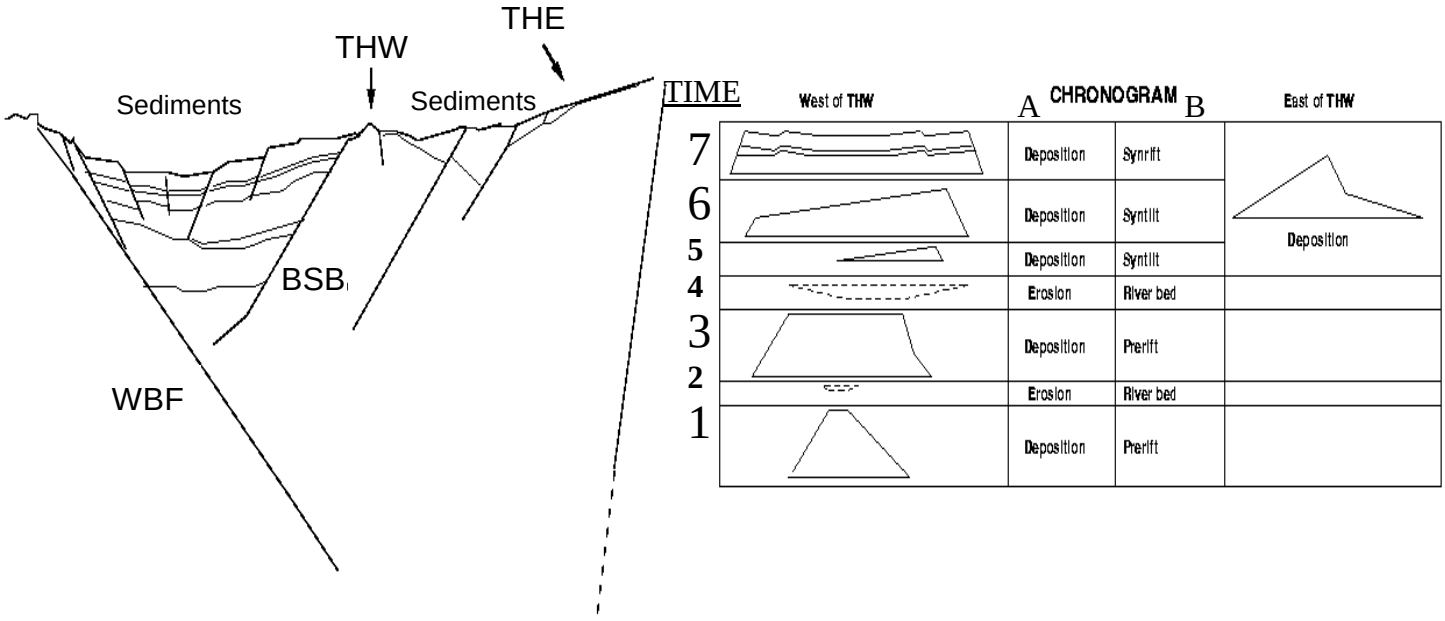

Figure 55: *Line drawing of cross section through basin (line P6) and the adjacent chronogram, which shows a the amount of sediment deposition, where each prominent reflector in the sediment is interpreted as isochronous. Time is displayed in numbers from 1 (earliest) to 7 (youngest). Column A shows the dominating process during the single ages and column B the subsequent environmental situation.*

The earlier stages in basin dynamics (1-4 in Fig. 55) are dominated by erosional unconformities. These can be interpreted as alternating fluvial deposition and erosion processes, probably related to regression and transgression events defined by the velocity of the moving waters from Iceland. Regression is related to ice ages and is the last stage imaged before initial tilting, so tilting and the formation of the basin could have taken part in one of the last ice ages, an age which is also connected to volcanic activity of Kolbeinsey (Saemundsson and Hjartarsson, 1994) and Grimsey (Saemundsson, 1974).
Deposition and erosion in the vicinity of the BSB in ages 5 and 6 is faster than along

the WBF (Fig. 55). This fan-shaped deposition is a clear sign of tilting towards the east.
A second basin was formed further east probably in response to tilting of the Block east of the THW. South of Grimsey Hydrothermal field, both basins join into a common basin. North of GHF, a bathymetric ridge is spreading out. The reflectivity imaged cyan and red values and the prestack migrated records show fine horizontal layering which both hint on sedimentary deposition. Since the ridge has not been levelled yet by erosion or deposition, the sediments must cover a region of recent geodynamic activity. With the GHF along the southern tip of this ridge, it is trivial to assume a common source for the formation of ridge and basin.

3.2. The distribution of faults

A new fault pattern of the TFZ was deducted from the integration of the new reflection seismic results and results from former surveys presented in Chapter 1. Identical fault dip directions on adjacent seismic records were picked in the dataset and marked on the map. Only faults, which are at least present on two lines were used for interpretation.

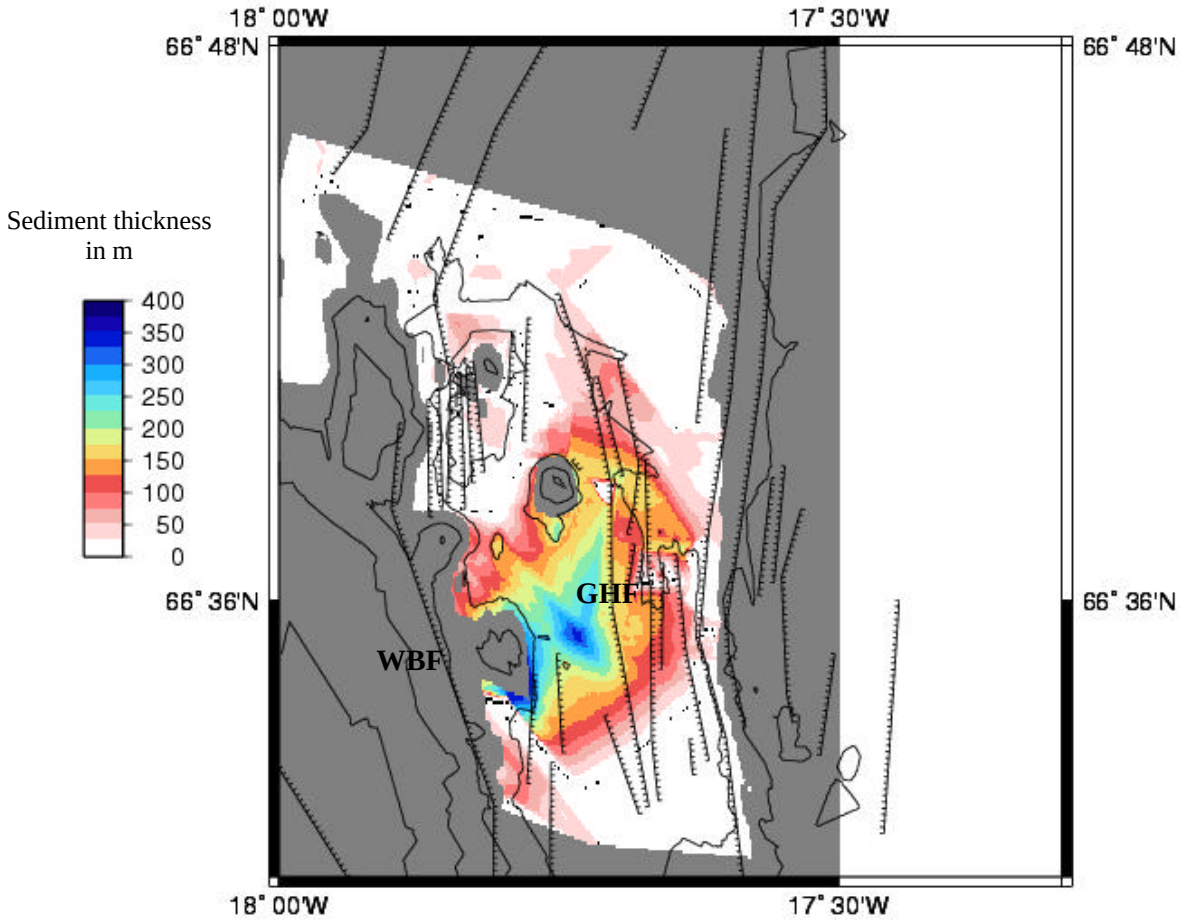

Figure 56: *The thickness of sedimentary layers is depicted in colors above. The deepest part of the sediments are found in the central part of the basin. The northern part is not filled with sediments thick enough to resolve. Some of the fault structures above this deep part of the basin are very short and cannot be traced over many profiles (see Fig. 51). Grimsey Hydrothermal Field (GHF) and one of the deep reaching faults of P6, the Western Boundary Fault (WBF), are marked.*

The resulting fault pattern for Skjalfandi Trough along with the thickness of sediments (in colorscale) and the bathymetric contours is presented in Fig. 57. The west of the basin is dominated by east dipping normal faults and vice versa, which is a typical extensional pattern of converging normal faults. The westernmost fault, the WBF, however, is a thrust fault. Whereas most of the normal faults strike roughly 0°, i.e. in north-south direction, the WBF bends as does the BSB just west of GHF towards a strike of ~20° W. The direction of main stress is the direction of the Grimsey Lineament or the Husavik Flatey Fault, i.e. ~55°W (Gudmundsson et al., 1993). Thus, there appear no GL strike-slip faults on the surface. Activity of the faults is closely associated with bending towards the direction of main stress (Ingebritsen and Sanford, 1998), which confirms that tectonic and geodynamic movement in the basin is connected to initial movements of the WBF. Bending is a barrier to the detection of interfault connections which might turn to be inline to the 2D seismic lines, but many of the single faults probably have to be interpreted as extensional duplexes, i.e. they diverge from the WBF and, perhaps, some subparallel ruptures which cannot be identified by the resolution of the seismic survey. The formation of duplexes is related to strike-slip movement, which imprints a typical stress field of so-called Riedel shears. They develop in areas where active faulting is oriented oblique to the line of main stress.
The faulting pattern is very similar to the one expected for a pull-apart basin (Woodcock and Fisher, 1986; Harding, 1985). Bending and duplexes have also been found farther south onshore, where the GL joins Iceland's mainland (Gundmundsson et al., 1993). So, not only does the faulting pattern reveal a pull-apart basin structure beneath Skjalfandi Trough, but the similarity to structures adjacent to Axarfjördur suggests the same formation for that basin. Pull-apart basins are usually formed between two major lineaments of a strike-slip fault. However, north of Grimsey Lineament no other lineament is found, so the formation of Skjalfandi Basin, which is located north of the GL cannot be explained that way, whereas the Axarfjördur basin might well be formed by the interplay of HFF and GL.

3.3.The distribution of earthquakes and the activity of faults

The WBF is the most active shallow fault as can be shown by the distribution of quakes shallower than 4.5 km (Fig. 57). The depth of hypocenters increases from the surface at 300 m water depth to a depth of 3-4 km towards the northeast. This corresponds to a dip of 34° to 37°, which is similar enough to the ~30° derived from reflection seismic survey to imply that the hypocenters form the WBF fault plane. Another center of shallow quakes is Grimsey Hydrothermal Field and a lineation of quakes, that may define the connection between BSB and WBF. The style of shallow faults imply a convergence of faults towards greater depths.
Basins that exhibit lots of duplexes as Skjalfandi Trough characteristically show this convergence of faults in depth (Harding, 1985; Woodcock and Fisher, 1986) which is called "flower structure". The first observation that the basement looked like a flower in bloom was not as far off as thought. The convergence of faults can already be inferred in a depth of 1-2 km on seismic line P6 (Fig. 50b) corresponding to the ~2km as inferred from seismology (Fig. 57). The resolution of the reflection seismic survey should be higher in these depths. So the dip of the active centers along hypocenters will also decrease to values of ~30° rather than 35° in situ. But both surveys show a surprisingly good agreement.

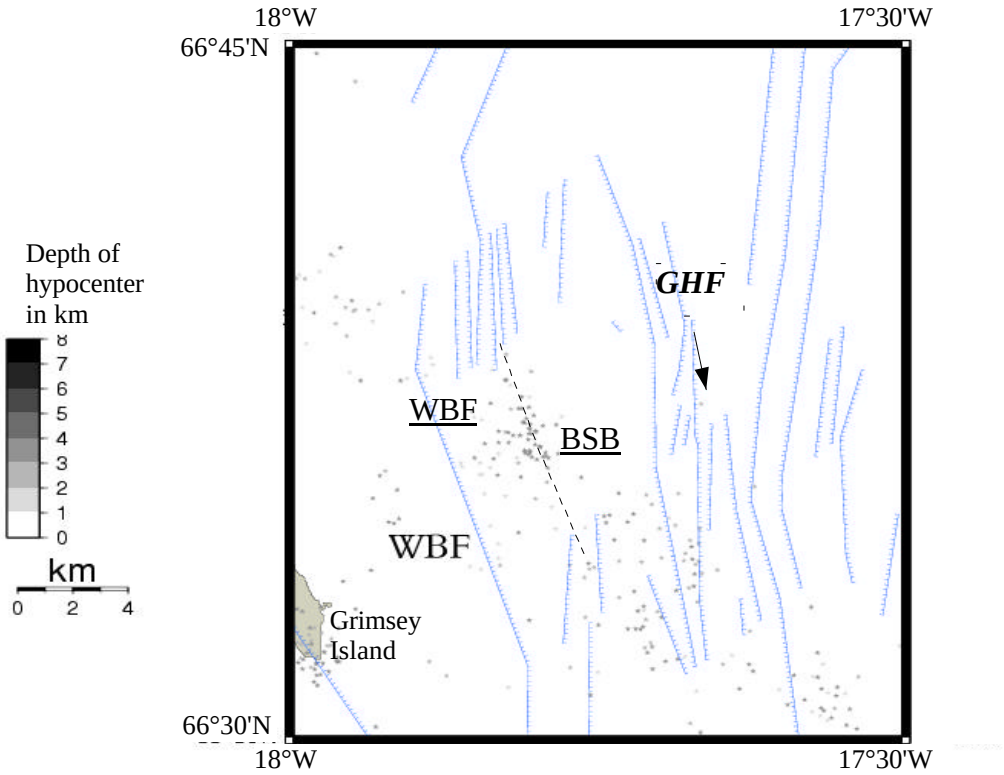

Figure 57: *The depth of hypocenters (gray stars) is increasing from the WBF towards the northeast and reaches values of 3 to 4 km in a distance ~4 km from the WBF outcrop (marked* **WBF***), this corresponds to a dip of ~35°. The underlined abbreviations* WBF *and* BSB *mark the surface area underlain by the fault planes. The dashed line show where these planes meet according to the reflection seismic profiles. From this line further to the northeast the hypocenter depth clearly decreases.*

The dips increase to 70-90° in even greater depths (Rögnvaldsson et al., 1998), i.e. near vertical. Most of these deep faults, that comprise the actual Grimsey Lineament, are located beneath the sedimentary basin and are called "*Grimsey Faults*" here (Fig. 58). The earthquake catalogue can be used to highlight some of the active structures. Hypocenters in a narrow band of 0.2° around line P6 are plotted in Fig. 59, where dashed lines represent possible fractures of ~70° dip. Up to a depth of ~10 km the hypocenters clearly converge, in deeper regions the hypocenters are distributed more diffuse. Seismic activity and thus the dynamics to the west of the basin is higher than in the eastern part. So one of the major faults along the western part of Skjalfandi Basin, i.e. probably the WBF, will also define the basic fault which dictates the extensional movements.

The Western Boundary Fault may represent a basal detachment zone with ist dip of ~30°. In that regard structures in Skjalfandi Trough are similar to continental transform zones as in the vininity of the San Andreas Fault. Earthquake data in the San Andreas area showed that the plate boundary at depths is situated horizontally displaced from the shallow faults (Nicholson et al., 1986), which was interpreted as a sign of detachment between shallow and deep structure. The distribution of epicenters in the TFZ confines a similar detachment situation. The strike of the deep seismic lineament defined by the accumulation of epicenters (~55°) is oblique to the strike of shallow faults (~20°) (Fig. 60). Most of the epicenters are found in the southwest of the basin. They clearly define a zone where the shallow faults bend thoughout the entire basin, probably due to the stress beneath. The bended parts of these faults are also those most likely critically stressed for

failure (Rubey and Hubbert, 1959; Zoback and Healy, 1984).

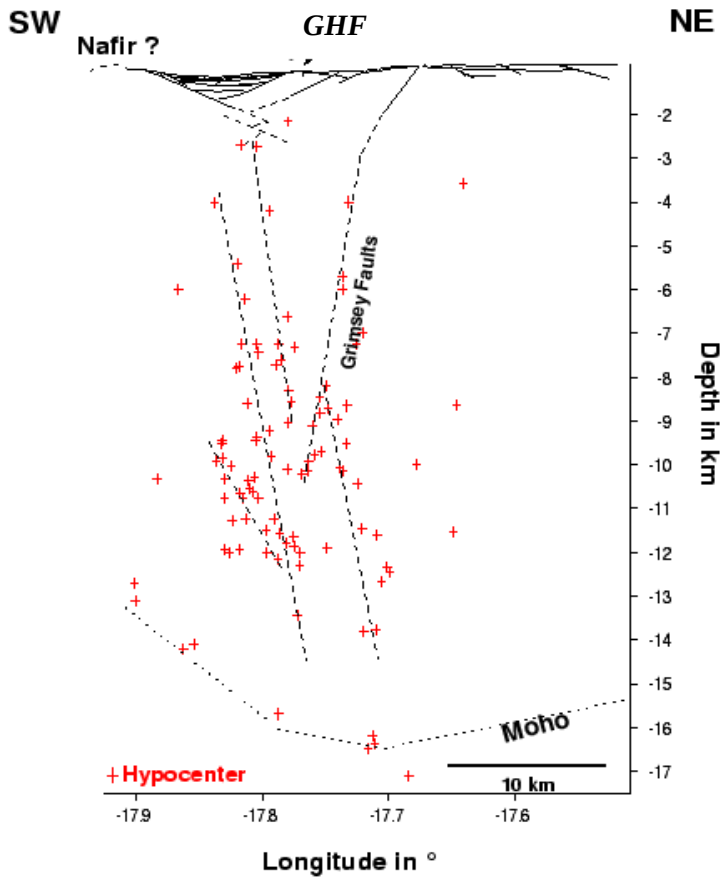

Figure 58: *The hypocenters which define the Grimsey Lineament cluster along a narrow area below the basin. Shallow quakes are only present near the convergence of WBF and BSB.*

At the depth of ~16 km, hypocenters vanish (Fig. 58). In Iceland, this is commonly associated with the 1200°C isotherm (Flovenz and Saemundsson, 1993) which is the temperature of molten magma and is thus expected at the crust mantle-boundary. In typical oceanic ridge systems, earthquakes are expected to cease below the 800°C isotherm (Bergman and Solomon, 1984). Since the Moho is expected in depth of ~16 km (Darbyshire et al., 2000) near Grimsey, this disqualifies the area as typically oceanic.
The presence of fluid accumulations appears to lower the number of earthquakes. The spatial occurrence of earthquake has already been shown in a 2D projection of hypocenters (Fig. 6b). The regional b-value of earthquakes is a measure of their frequency-magnitude distribution and thus of spatial recurrence of quakes of various sizes. The b-value - thus the ratio of large quakes to small earthquakes - increases where effective stress decreases. Because fluids in magma chambers pose as buffers for effective stress (Daines, 2000), this may be a sign for accumulation of magma. Thus Wiemer and McNutt (1997) found high b-values at Mt St Helens and Crater Peak (Alaska). Results of Wyss et al. (1997) for volcanoes in Japan support these findings. Müller and Jokat (2000) showed that high b-values in the Arctic Ocean are mirrored in an increased number of non-double-couple events, which are typical for volcanic and magmatic events (Nettles and Ekström, 1998). The 2D projection of the b-value of all earthquakes (see Appendix) in the TFZ deeper than 2.5 km and picked by Vedurstofa

(2000) is shown in Fig. 59a. Less small earthquakes occur in the southwestern edge of Skjalfandi Basin. A depth cross section through this area confirm the higher b-values between surface and a depth of ~16 km. Interestingly, this is the area marked by the magnetic anomaly and the yellow (igneous) reflectivity class described in Fig.52.

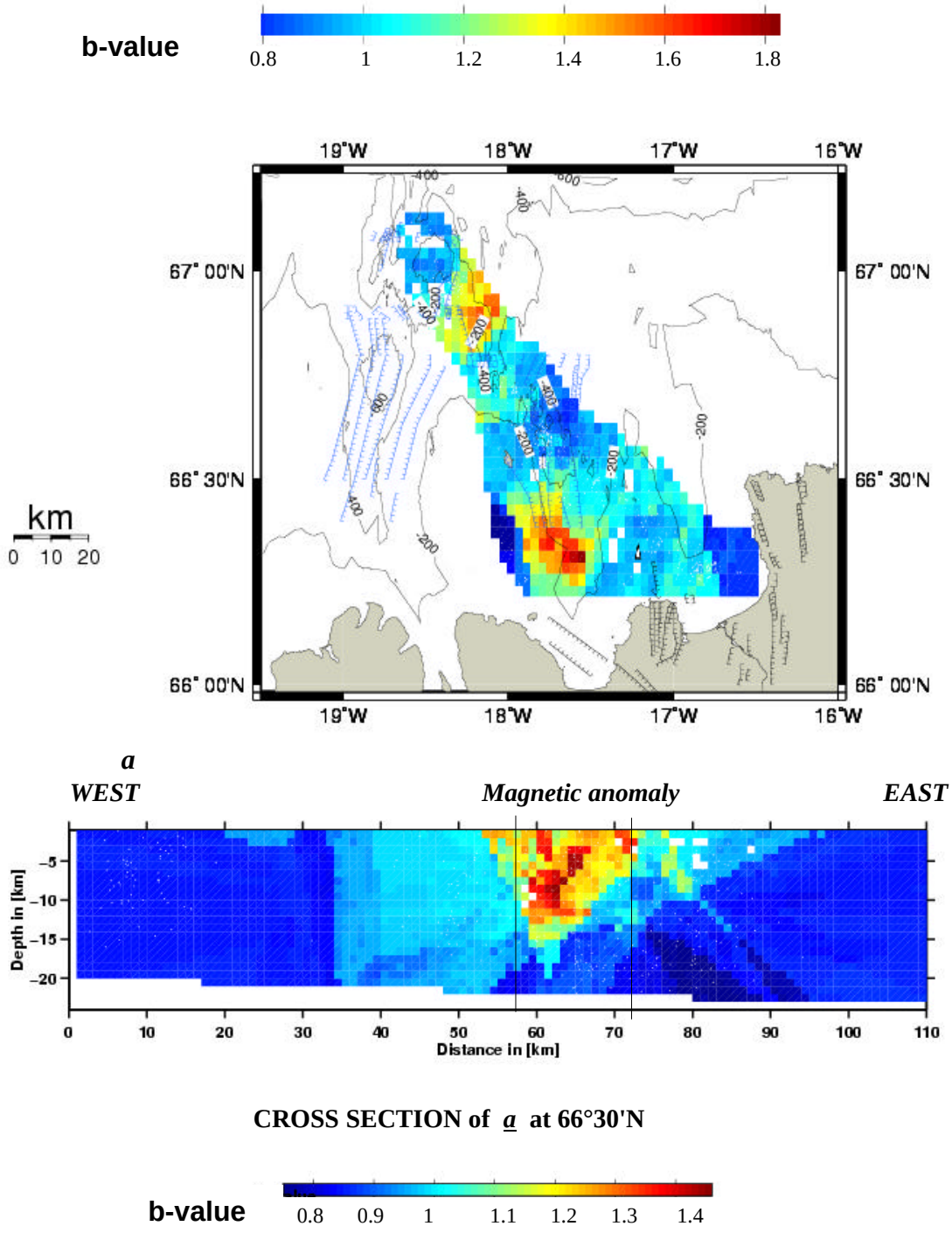

Figure 59: *a) A 2D-projection of b-values in the TFZ of all confirmed earthquakes deeper tahn 5 km. b) The b-value cross section below the magnetic anomaly (marked by two lines) may reveal a shallow magma chamber underneath south western Skjalfandi Bay (Graphics by ZMAP, Wiemer and Zuniga, 1994).*

There seems to be magmatic activity in the southwestern part of the trough which may be the geodynamical force driving the whole tectonic system. The hydrothermal field (GHF) up to a depth of ~1km, however, is not only an area of less small earthquakes but rather a quiescent zone like the area in the center of the apparent magma chamber system (Fig. 61). This is consistent with experiments of induced seismicity (Raleigh et al., 1976; Zhao et al., 1995). Earthquakes occur along the most permeable faults and not in the direct environment of fluid injection - after an initial hydraulic fracturing process during the first injection through a well. The most permeable faults are those which are most active (Barton et al., 1995). In shallow levels, the highest activity is bound to the WBF and its connection to faults of GHF and its water reservoir. The presence of large amounts of water as magma seems to buffer the quakes, a common quality derived from their fluid nature.

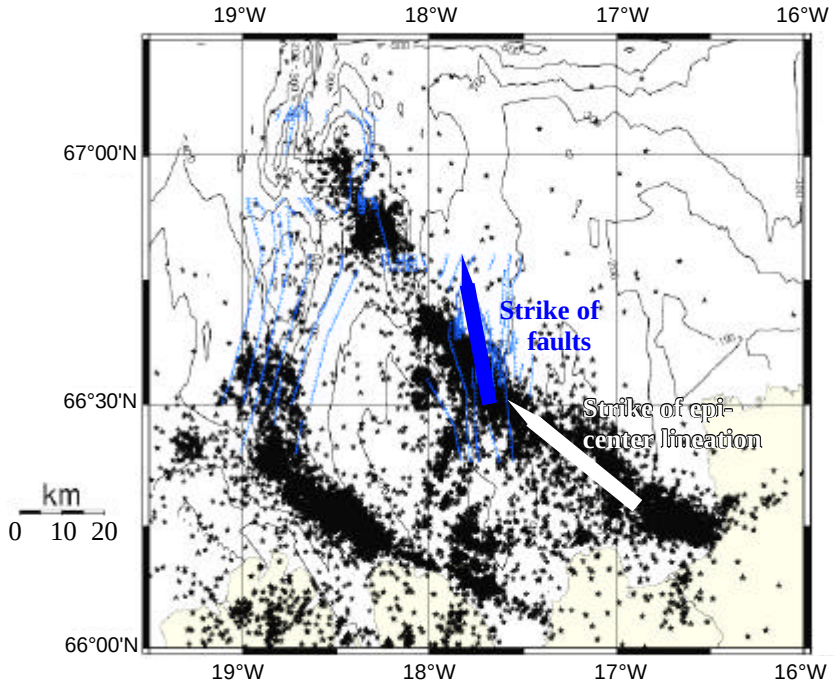

Figure 60: *The epicenter lineation of the Grimsey Lineament (black dots) strikes at an oblique angle to most of the shallow faults (in blue). Average strikes are highlightes by arrows.*

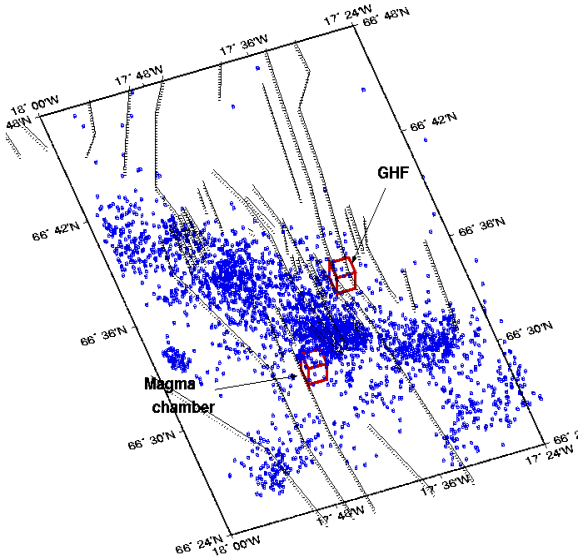

Figure 61: *A flat 3D view of hypocenters shows the relative quiescent regions of Grimsey hydrothermal field (GHF) and of the apparent magma chamber in southern Skjalfandi Trough along the borders of the most active part of Grimsey Lineament, Skjalfandi Trough.*

3.3.1 On magma chambers in the TFZ

Just north of the Holl complex, the b-values are higher than ~1.6 for earthquakes deeper than 5 km (Fig. 59a). As for the area southeast of Grimsey it indicates a magma chamber in the area. A sill related to this chamber was imaged in a previous reflection seismic survey (Neben, 1992) in the western outskirts of the b-value anomaly. The distribution of quakes of the major anomaly plots along the depth axis and thus resembles a dike rather than a sill. This dike-sill system may feed active volcanism at the Holl and Kolbeinsey complexes. Dike intrusions are typical for the Kolbeinsey Ridge system. This has been shown by earthquakes further north (Riedel et al., 1999). The magma chamber is also confirmed by a gravity high and its northern part exhibits a Brunhes epoch magnetization (Fig. 6). The crystallization depth of the basalts from Kolbeinsey Ridge was inferred to lie at a pressure of at least 1.5 kbar by its chemical composition (Michael and Cornell, 1998). This corresponds to ~5 km thickness of crystallized basalt above the magma chamber, which fits well to the dike structure.
An apparent magma chamber reflection (AMCR) that was found to the west on reflection line P28 during the survey in the transition from Kolbeinsey Ridge to Eyjarfördur (Riedel et al., 2000; Petersen, 2000) cannot be confirmed by the b-values, gravity or magnetic survey. It would lie at a maximum depth of 3 km. A similar difference was reported for magma chambers along Reykjanes Ridge and the East Pacific Rise. If the scattering of seismic waves at ridge crests is taken into account, models predict the emergence of diffractions which line up to apparent seismic reflections (Calvert, 1997). The quality is often improved by migrating the record at water sound speed (~1500 m/s) in 2D, thereby enhancing diffractions from the seafloor, as well. For the AMCR this was confirmed by modelling single scattering from the bathymetric seafloor gridpoints (Petersen, 2000).

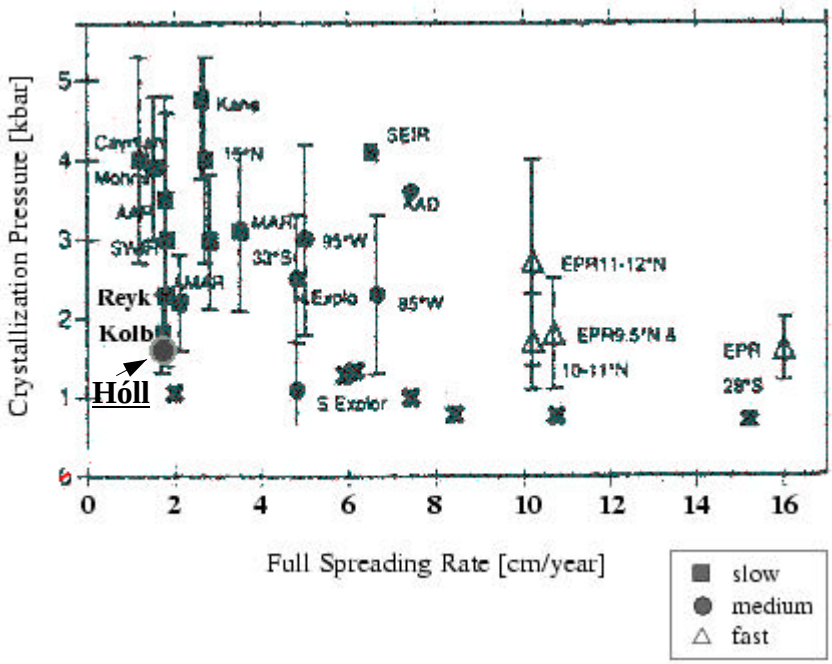

Figure 62: *The dike north of Hóll imaged by reflection seismics (Neben, 1992) and b-values (this work) fits well to the chemical composition of rocks dredged in the Kolbeinsey Ridge system represented by crystallization pressure here (Michael and Cornell, 1998).*

3.4. Grimsey Hydrothermal Field (GHF)

Grimsey Hydrothermal Field is known from the mapping of gas venting (Riedel et al., 2000; Scholten et al., 1999). It is located in the submarine valley along the flanks of the THW (Fig. 50, Fig. 63). The THW is strongly faulted and made of several submarine hills some hundred meters in diameter. To classify the hydrothermal system, the geoscientific data registered at GHF are presented along with general information on hydrothermal areas. The hydrothermal field exhibits a higher variety of expected lithologies than its environments and moreover, propagating waves will be influenced by the hot vented hydrothermal solutions.

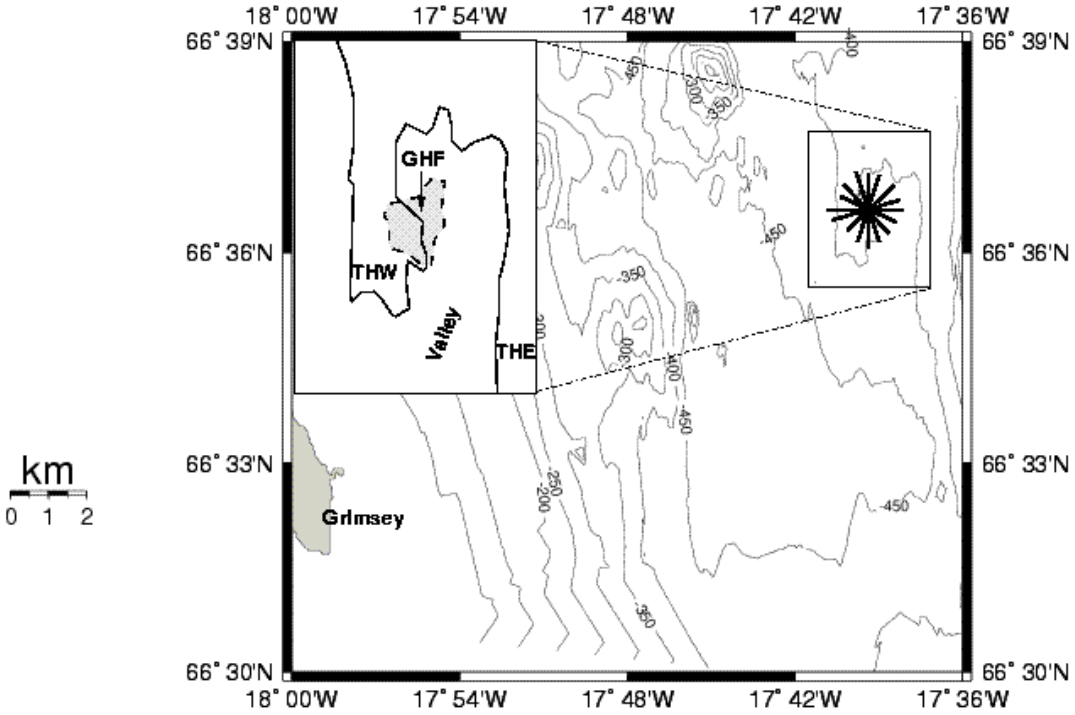

Figure 63: *Bathymetry (in m) of the environment of Grimsey Hydrothermal Field (GHF). The most important features, i.e. the extents of the plume of the hydrothermal field (shaded in grey), the valley in which most of the vents are found, the topographic highs to the west (THW) and east (THE) of GHF, are marked in a zoomed excerpt. Those parts of the seismic lines which will be presented are marked as black lines in the basemap.*

3.4.1. Hydrothermalism at GHF

Hydrothermal areas are subdivided into two main groups, geothermal areas, where hot water or vapour is boiling subaerial and venting areas where the same occurs in a submarine environments. These submarine features have only been recognized in plate boundary settings, i.e. mid-ocean ridges, subduction zones and, in the case of the TFZ, leaky transform zones.

The hot spot beneath Iceland is a source of pressure, temperature and geochemical anomalies within the Mid-Atlantic Ridge system. It built a plateau of shallow water depth and drives hydrothermal systems that even produce gold reserves (Malmis, 1990). The coastal and oceanic hydrothermal systems produce metal reserves, because the circulating seawater provides a valuable source of metallic ions from depth. These ions are bound into valuable metal ores, mostly sulphides. After being exposed on

subaerial surface, these type of deposits are known as volcanic-hosted massive sulphide deposits (VMS), which host the mines of highest metal recovery rates in the world (White and Herrington, 2000). They are commonly found in ancient oceanic settings as ophiolite complexes (Varga et al., 1999).

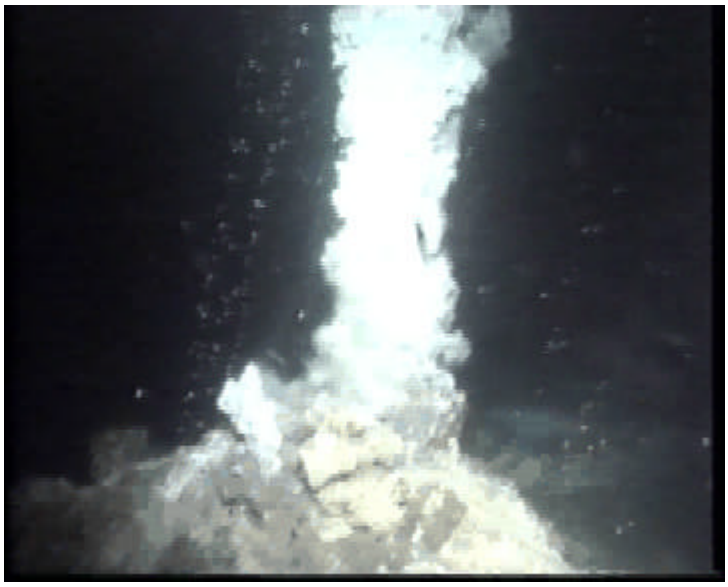

Figure 64*: Bubbles are rising from the single mounds of Grimsey vent field. These bubbles unite into a bubble plume. This picture was taken in the JAGO submersible in 1999.*

Around Iceland hydrothermal venting was found in various environments from shore waters (Reykjanes system near Reykjavík in southwestern Iceland; Stefansson, 1983) down to the rift valley of Reykjanes and Kolbeinsey Ridge. In a water depth up to about 400 m the Tjörnes Fracture Zone hosts Grimsey Hydrothermal Field (GHF) at 66°36,5'N, 17°39,5'W, Kolbeinsey Hydrothermal Field (KHF) at 67°05,5'N, 18°43'W and the Eyjarfördur Hydrothermal Dome (EHD) at 65°49.73'N, 18°06.69'W. In the introduction it was mentioned that they were detected after the discovery of rising gas bubbles at the sea surface near Kolbeinsey (Olafsson et al., 1990) and following the discovery of hydrothermal mineralization products near Grimsey (Hannington et al., submitted). In both explorations local fishermen gave the decisive hints.
Diving campaigns revealed *white smokers* (Fig. 64) and *diffuse vents* in these areas. White smokers are spires made of anhydrite and talc, from which hot fluids are rising. These hot fluids are visible as shimmering water. Shimmering water can be the only hint on venting where the seafloor is relatively unaltered. This is called diffuse venting.

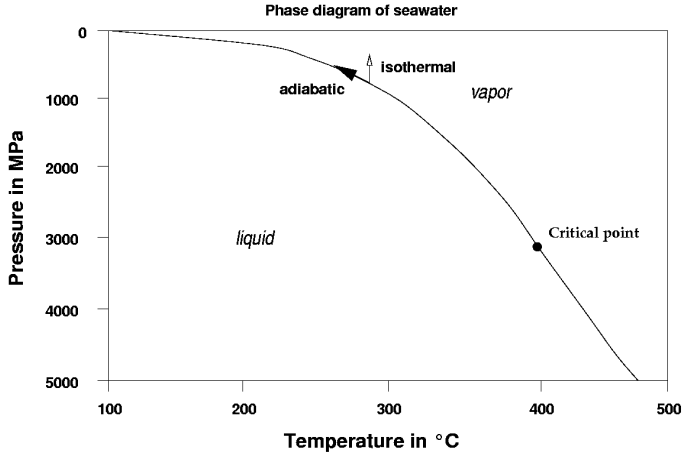

Figure 65: *The phase diagram of seawater depicts where liquid salted water is turned to vapor. For shallow waters (i.e. low pressure) the boiling temperature rises quickly with pressure.*

The temperature of the vent fluid is restricted by the boiling temperature of the surrounding seawater (Fig. 65). Where the vents are deep enough to allow sulphide precipitation, the presence of metallic ores can stain the white patches of sulfates and dark chimneys dyed by those sulphides would be known as *black smokers.* These were not found in the TFZ.
The seafloor in the northern icelandic GHF can be approximated as a series of mounds of anhydrite ($CaSO_4$) and talc ($Mg_3Si_4O_{10}(OH)_2$) of ~10 m thickness (Hannington, submitted). Sulfate (SO_4) is the second most abundant anion in seawater and with the fluid temperature rising, seawater becomes saturated with $CaSO_4$ before precipitation takes place in the form of anhydrite at ~150°C (Fig. 66).

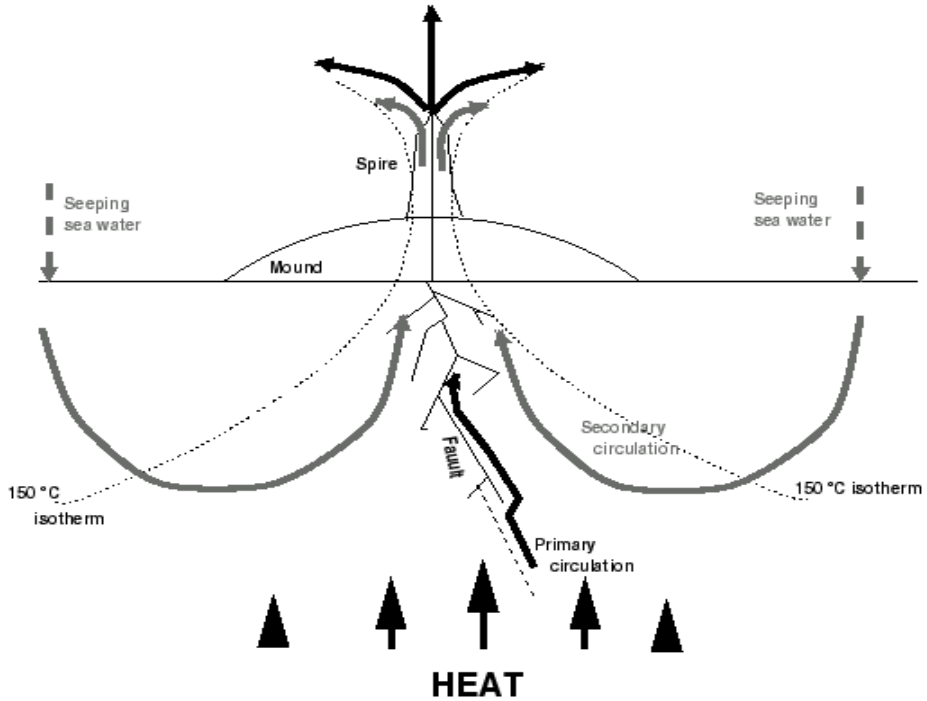

Figure 66: *Primary and secondary circulation at the hydrothermal fields north of Iceland. The primary circulation carries the heat from deeper layers to near-surface areas, where seeping water is heated up and a secondary circulation is established similar to a cooling loop in a power plant. Both waters will come out along the mounds or spires.*

At shallow water depth seawater will seep into the active hydrothermal area and will heat up along the rising hot water from the deeper subsurface (Fig. 66). This secondary circulation depends on highly permeable crust. It supplies anions (e.g. SO_4^{2-}) for the precipitation which forms about 1 km long Anhydrite layers (Stoffers et al., 1997; Hannington, submitted) along the permeable zones. High permeability is either provided by high porosity or crack linkage, so typical hostrocks could be loose and not-well cemented sedimentary rocks or lavas from volatile-rich sources. The percentage of exsolved volatiles in magma increases with decreasing pressure implying higher porosity in shallower subsurface regions (roughly 1% more exsolved gases per 1 MPa reduced pressure (Wallace et al., 1995)). On top, the tectonic stress present in the TFZ enforces a high degree of crack linkage (Stéfansson, 1999). Deeper migration of the water will take place along major, active fractures that are critically stressed for failure (Barton et al., 1995).
Along with Anhydrite, talc is commonly found north of Iceland. Talc (Magnesium Silicate Hydroxide) is a clay mineral and is produced by the alteration of silicate rich minerals as olivine or amphibolite. Olivine is primarily delivered from the icelandic

basalt bedrock in the present case. Some geothermal reservoirs on land in northern Iceland, e.g. Krafla, are made of highly porous rhyolith in the subsurface (Orkostofnun, personal communication). This would also explain the high silica content in the fluids expelled in the neighbouring submarine GHF. But talc can also be derived from sediments. The presence of massive sulphides can alterate the sediments to talc. (Zierenberg et al., 1994).
Near GHF, singular veins of pyrite were found surrounded by baked mud (Theilen and Scholten, 2000). The formation of pyrite veins in baked mud may occur where fluid flow raises the environmental pressure by dynamic fluid flow forces, i.e. along the fluid migration pathways, and allows sulphide formation where H_2S content in the hydrothermal fluids is high and metallic anions are present. Pyrite will also form where iron anions are present and sulphate is reduced by bacterial activity (Fossing et al., 2000; Aharon and Fu, 2000), but this is unlikely in temperatures higher than 115°C. In GHF, H_2S was found in chimneys that were hieved up to the surface (Hannington, submitted). Fishermen found rare bits of sulphide rock samples in their nets at scattered places in Skjalfandi Trough. Their origin is unknown, but they may be attributed to the GHF. Local accumulations of sulphides if large enough can be explored by seismic methods (Salisbury, 1996; Adam et al., 1997) because of the outstanding physical properties of the material (see chapter 2.8). Talc posseses similar physical properties as sulphides. Anhydrite is similar to Basalt in its physical properties and will be to distinguish (Broser, 2000). The thin layering of Anhydrite (10 m in contrast to a quarter wavelength of ~8 m for 50 Hz) will limit the method further which could modify the reflection signal especially where it overlies soft sediments.

3.4.2. Hydrothermal gas and bubbles

Gas indicators in the water column

Hydrothermal circulations in the icelandic hot spot environment create too much gas in the subsurface to guarantee full solubility of the rising gases and thus gas bubbles develop in the water column (Fig. 63). The gas captured in the bubbles mainly consists of methane (CH_4) and carbon dioxide (CO_2) (Botz et al., 1999).
Because they are barriers to wave propagation (Fig. 67), these rising gas bubbles can be imaged by acoustic investigations. The sound that the hydrophone registers may be caused by the cavitation of bubbles (Ross, 1922), but most signals are created by scattering of the incident pulse in the water column (German et al., 1994).
The signals are recognizable beneath a water depth of 200 m near the GHF (Fig. 67). Above this depth almost no bubbles were registered, which is probably due to the collapse of the bubbles which expand while rising and thus lower their surface tension and the dissolution of CO_2 in the water column. Due to the lack of further information, the water depth of 200 m is here defined as the average collapse depth of the bubbles.

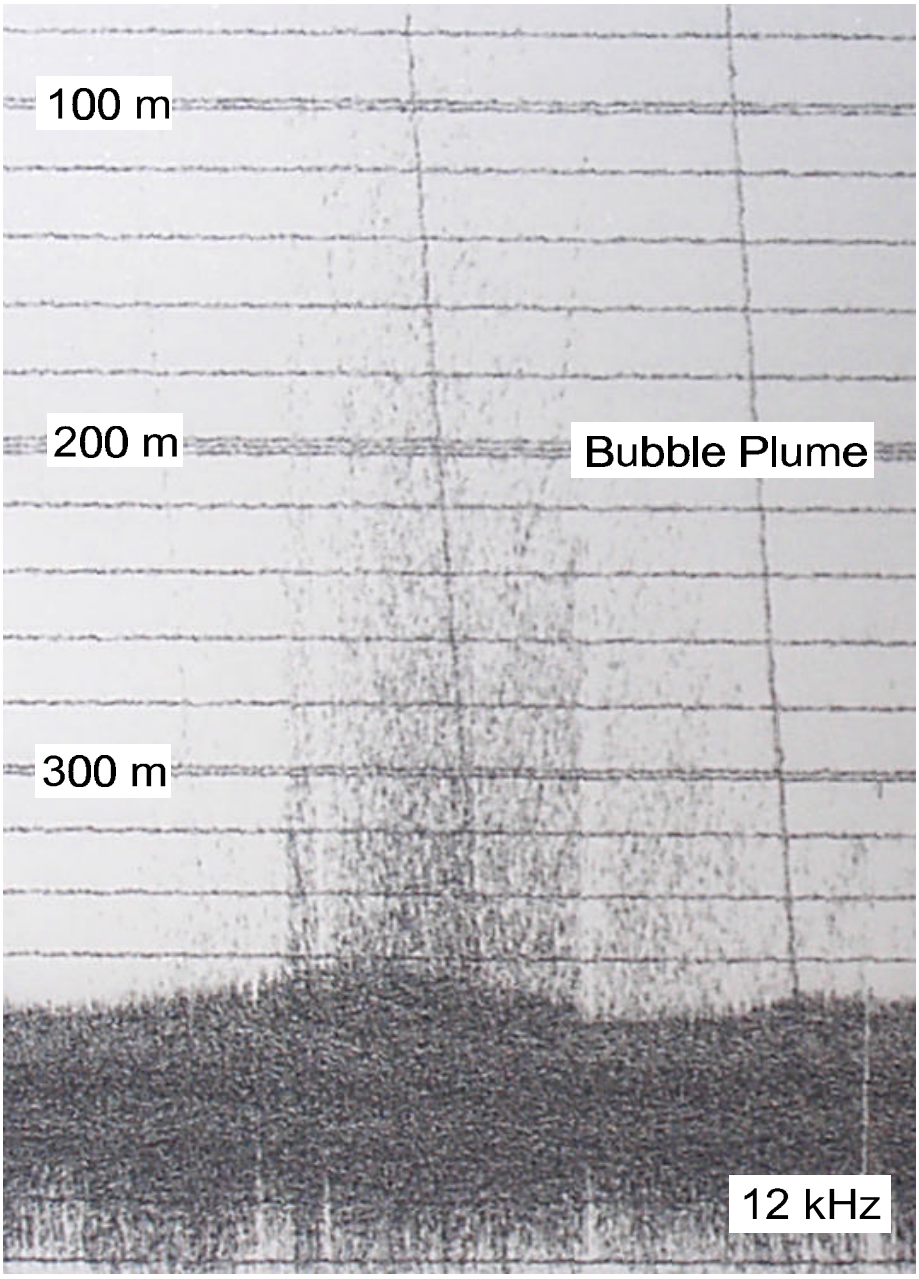

Figure 67: *The bubble plume at Grimsey Hydrothermal field imaged by a 12 kHz echo-sounder (Scholten, 1999). The dark streaks indicating the bubbles are foremost visible beneath 200 m water depth.*

Free vented gas or fluid of high gas content will show up at the sea bottom because of low impedance and thus a negative impedance contrast to water, which will display as a polarity reversal in the first reflected arrival (Telford et al., 1990). These reversals have been noticed in the TFZ in a previous survey (Neben, 1992). During the presented survey they were mapped systematically. Gas-in-water measurements were registered in the same strike as reflection line P24 and a comparison between the amplitude trend of the single channel line and methane-in-water contents is presented in Fig. 68. Where the methane content is highest, the amplitudes at the seafloor change their polarity.

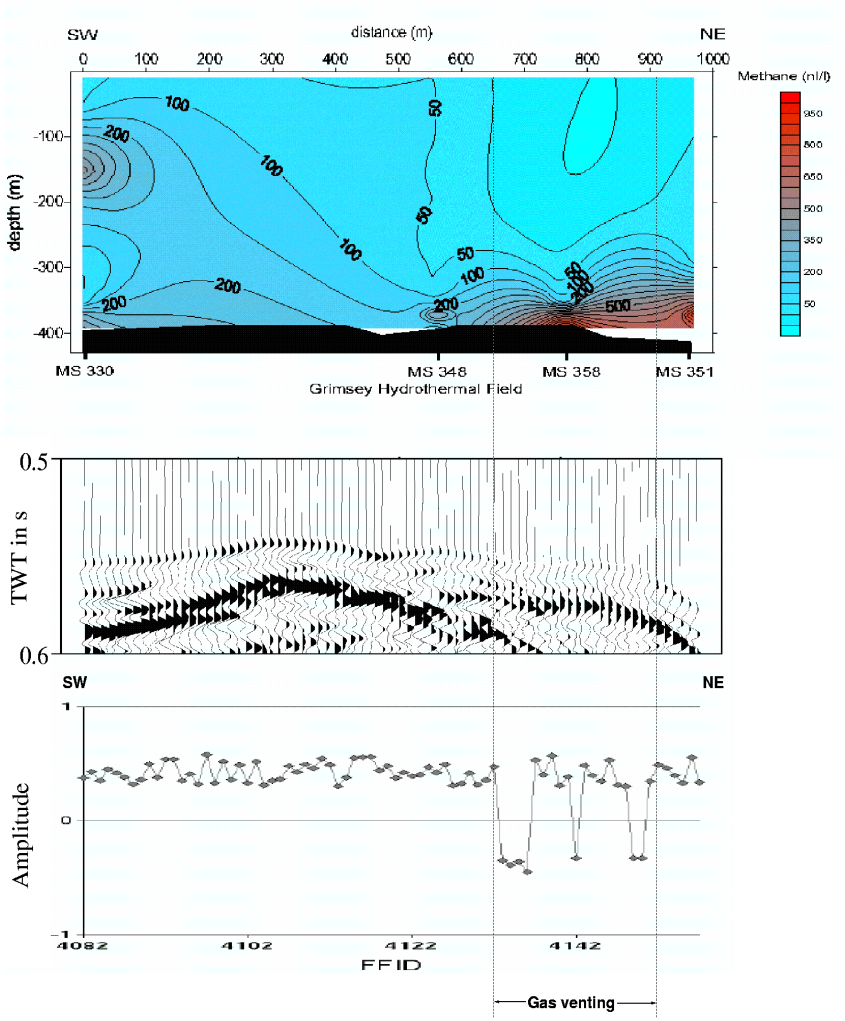

***Figure 68**: A polarity reversal is noticed when recording the amplitude of the first reflection at the eastern flank of the THW (here on line P24). This is due to large accumulations of gas in the area, which show up in high methane contents in the water column (Riedel et al., 1999).*

Influence on seismic wave propagation

The influence of the gas appears to alter the seismic registrations in travel time and amplitude substantially. It will be important to quantify these qualitative observations. Therefore some assumptions have to be made, which include:

- Gases are captured in the bubbles near the seafloor, where saturation should be highest and thus the bubbles capture the pressure p_0 of the near-

bottom region.

- The size of all bubbles in the same depth is equal, which enables us to define a characteristic radius of all bubbles averaged over all depths.
- Scattering in the water column will result in an apparent reduction of the sound speed in the bubble plume, because additional time is needed for the wave while travelling from bubble to bubble. The velocity and the absorption of energy in the bubble plume will vary with the compressibility of the mixture of water and bubbles, which depends on bubble radius *r* and volume fraction *n* of the bubbles in the water (Muckelmann, 1985).
- Bubbles rise without an initial acceleration phase i.e. they exhibit a constant velocity which is the terminal velocity, a common assumption in bubble physics (Fan, 1990).

Characteristic radius

The characteristic radius r_c is derived in a complex way in the Appendix, but it turns out that the sound velocity in the present case is nearly independent on this radius. The result of the calculus based on the previous assumptions is known from computing collapse radius at the depth where surface tension equals internal pressure. This is presented in the appendix, the result is:

$$r_c = 1.26\ mm.$$

The characteristic radius can be used to compute the resonance frequency of the bubbles. This is the frequency of acoustic waves, which would either develop when the bubbles cavitate and which are absorbed most (Ross, 1922; Domenico, 1982):

$$f_m = \frac{1}{2 r_c}\sqrt{\left(\frac{p}{\rho_{water}}\right)} \approx 17500\,Hz \quad . \quad (24)$$

The frequency is of the same order as the dominant frequency of the employed echo-sounder (12 kHz) for a water depth of around 200 m, which explains why the energy is scattered so drastically in contrast to the airgun pulse.

Volume fraction of exsolved gas in water

Bubbles of the hydrothermal vents were sampled for their gas composition during JAGO submerisble dives and at two distinct locations the time was measured that was used for sampling the gas. The volume fraction of gas was measured to be ~0.5*l* maximum (at room temperature and atmospheric pressure) after 10 minutes and ~0,2*l* after 5 minutes (Dive 386) (Theilen and Scholten, 2000), or respectively 300 seconds. Whereas CO_2 is dissolved easily in seawater at any temperature, CH_4 will not dissolve well in cold water (Wood and Hewett, 1984), so the molar gas fraction will assume the constant molar fraction of methane (~50 *ml/l* (Table 4)) during ascent. Given the terminal rise velocity of an ideal bubble in a liquid (Fan, 1990)

$$v_{terminal} = \sqrt{\left(\frac{1.4\sigma}{\rho r_c}\right)} = 8.8\,m/s \quad ,$$

it is now possible to estimate the volume fraction of exsolved gas in the water column, An ideal gas which fills 200 ml under atmospheric pressure, compresses to ~1/20 in 200 m water. The bubbles which carry this amount of exsolved gas need a time of 22.3 s to rise from 400 m to 200 m, i.e. they fill a volume fraction *n* of

$$n = \frac{22.3\,s}{300\,s}\frac{1}{20}50\,ml/l \approx 185\ ppm \quad .$$

If the collapse depth would be 100 m, this value would rise to ~ 500 ppm. Both values will be considered as limiting values.

Seismic velocity in bubble-rich seawater

Muckelmann (1985) describes how to calculate the attenuation and velocity of bubble rich fluid from a real and imaginary part of the Young modulus:

$$k_r = \frac{c_f k_g^2 (1-n)((w_0^2 - w^2)^2 + d^2 w_0^4) + n k_g^2 (w_0^2 - w^2) w_0^2}{c_f^2 k_g^2 (1-n)((w_0^2 - w^2)^2 + d^2 w_0^4) + 2 c_f k_g n (1-n)(w_0^2 - w^2) w_0^2 + n^2 w_0^4} \quad (25a)$$

and

$$k_i = \frac{n k_g d w_0^4}{c_f^2 k_g^2 (1-n)((w_0^2 - w^2)^2 + d^2 w_0^4) + 2 c_f k_g n (1-n)(w_0^2 - w^2) w_0^2 + n^2 w_0^4} \quad (25b)$$

Parameter	**Description**	**Value**
c_f	Compressibility of water	$0.45*10^{-9}$Pa^{-1}(Muckelmann, 1985)
k_g	Young modulus of gas bubble (methane) in equilibrium in 400 m deep water	5.2 MPa (Flexware, 1999)
d	Damping constant of gas (air)	~0.1 (Eller, 1970)
r_f	Density of seawater around Iceland	1025 kg/m^3
r_c	Charateristic radius of bubbles	1.26 mm (see above)
n	Volume fraction of gas	185-500 ppm (see above)
w_0	Resonance frequency x 2π	~110000 *Hz* (see above)

***Table 3**: Employed parameters in the calculation of the compressional wave velocity in a bubble rich fluid.*

Inserting the parameters in Table 3 results in:

$$v_p = \sqrt{\frac{2((k_r^2 + k_i^2) + k_r\sqrt{(k_r^2 + k_i^2)})^2}{r_f (k_r + \sqrt{k_r^2 + k_i^2})^3}} = 1337 - 1417 \text{ m/s}, \quad (26)$$

calculated for the two limiting values for the volume fraction (185 ppm, 500 ppm).

This corresponds to a value of Q≈137 following a formula from the same source (Muckelmann, 1985). A decrease of velocity from 1472 m/s to about 1440 m/s to 1450 m/s has been observed in the area (Broser, 2000). This indicates that some of the CH_4 will probably dissolve during bubble ascent. The value of 1440 m/s can be estimated under the assumption that 100 ppm (ideal gas) CH_4 remain in bubbles up to the collapse depth. The Q value would rise to 250. The seismic velocity is independent of frequency in the decisive range of 1-500 Hz and of bubble radius in a wide range from (0.2 mm -2 cm), since it is far from the resonance wavelength.

3.4.3.Modelling reflectivity for the seafloor of vent-fields

The typical physical properties of hydrothermal fields and the water column above have been laid out. The wave propagation through a vent-field will be modelled to investigate whether these influences prevents the use of the self-organizing mapping method. Gas bubble filled water is described by viscoacoustic properties (Q=250, v=1440 m/s). The propagation of a wave through this bubble plume will alter reflectivity of the bottom material. A typical anhydritic rock (ρ=2.8 kg/m^3, v_p=4 km/s, v_s=1.8 km/s) (Ludwig et al., 1998) is modelled as bottom material. The viscoelastic 2D-Finite-Difference modelling (Bohlen, 1998; see Apeendix) result is compared to the elastic Zoeppritz trend (Fig. 69).

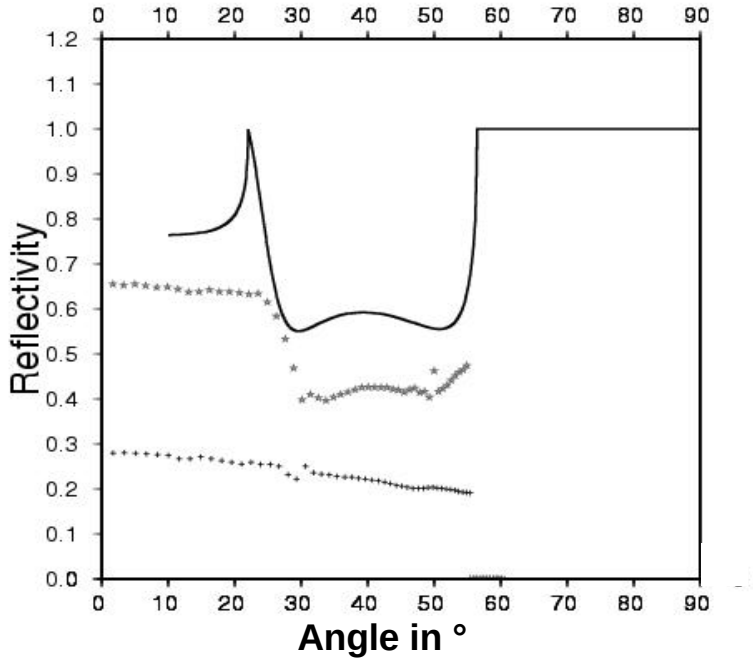

Figure 69: *The low q values associated with bubble plumes attenuates the amplitude, but does not disturb the trend of reflectivity (stars). The layer of Anhydrite discovered by submersible is not recognizable, if it its thickness is in the range of 10 m (crosses).*

The difference of the modelled values to the elastic Zoeppritz trend is easily observable (Fig. 69) as a change in reflection strength, but the trend of the reflectivity curve is confirmed. The first critical angle cannot be resolved (see Appendix). A further problem will arise if the Anhydrite layer is in the range of 10 m, which was suggested by Hannington et al. (submitted), and overlies muddy sediments (ρ=2 kg/m^3, v_p=1500

km/s, v_s=0.2 km/s). The combined effects of low Q, thin layer and low frequency (50 Hz in this case) make it impossible to detect Anhydrite at the seafloor.

3.4.4. Mapping the seafloor of Grimsey Hydrothermal Field

Despite the discouraging modelling results, the structure and surface of GHF was closely investigated by a star-shaped cluster of reflection lines (Fig. 70) and the interval between two shots was shortened to half to arrive at a bigger fold, i.e. a better lateral resolution concerning the reflection angles. To unravel the rare occurrence of precipitates, this cluster of 8 profiles was investigated in an additional neural network process independent of the rest of the recorded lines.

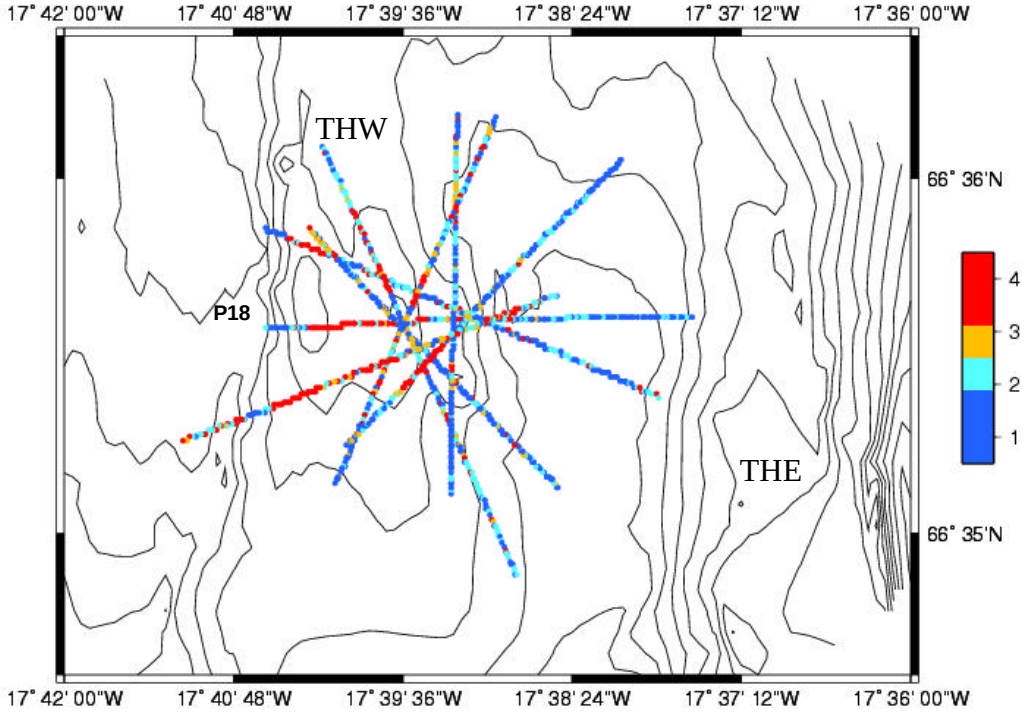

***Figure 70**: The regional distribution shows the dominance of class no.4 crosses on top of a bathymetric high and class no.1 dominance in the outer fringes of the hydrothermal field.*

The result of the final weight vectors of the classes obtained by the algorithm is shown in Fig. 71a. Only 4 characteristic classes were discovered in the hydrothermal field area. Two of them are very similar to each other. They are numbered to distinguish them from the classes presented before, which were denoted by colors. The rms-error of the class vectors increases with increasing reflectivity values (Fig. 71b), but class no.4 shows smaller deviations in higher angles than class no.2 and 3, because it is representative of more input values.

The regional distribution (Fig. 70) shows the prevailing low impedance rock influence from class no.1 (*here in blue*) and frequent occurrences of class no.4 (*here in red*). Class no.4 implies a hard rock best modelled by ρ=2.8 kg/m^3, v_p=5.5 km/s and v_s=2.7 km/s. Is foremost present on the submarine hill (THW) west of the vents and crossline to the trend of the hydrothermally active valley. The physical properties are intermediate between typical Basalts and Anhydrites (Broser, 2000). They are best modelled by an Anhydrite-Pyrite mixture (properties from the TAG Hydrothermal Field at 0.5 MPa from Ludwig et al., 1998). Anhydrites-pyrite mixtures were cored in

the hydrothermal valley (Theilen and Scholten, 2000). Anhydrites covers the hydrothermal valley in up 10 m thick layers (Hannington et al., submitted). The possibility that Basalt is the porous hostrock on top of the THW is implied by the structural records (Fig. 51) and was described in the submersible dives (Theilen and Scholten, 2000). These igneous rocks have been dredged east of the actual hydrothermal field.

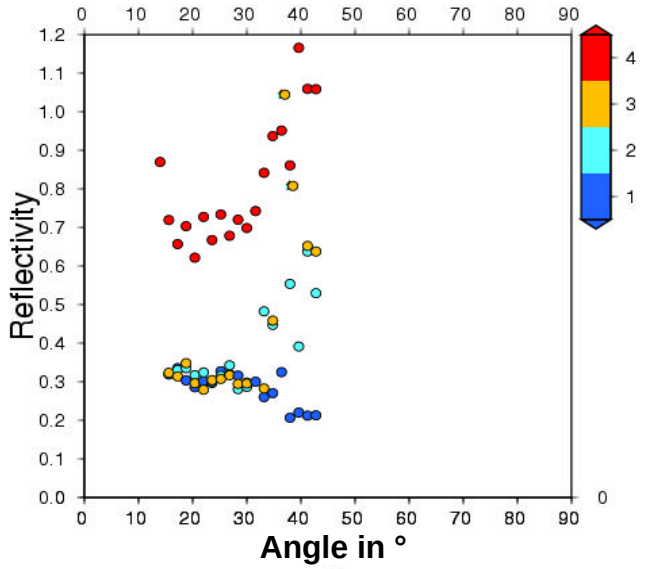

a)

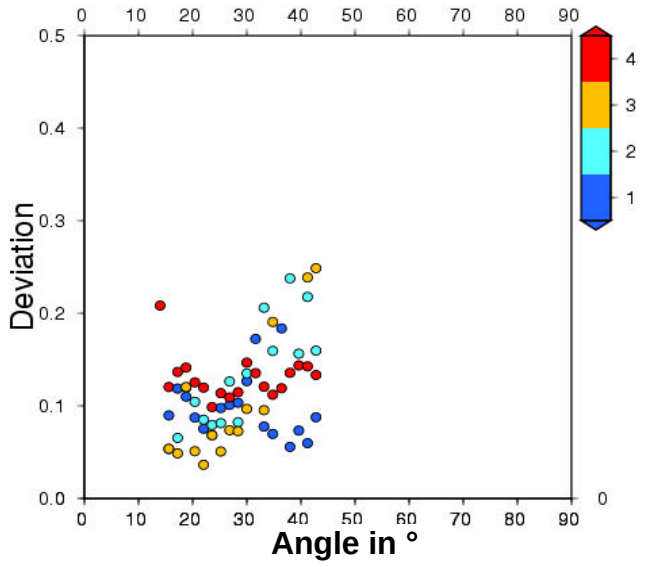

b

Figure 71: *a) shows the reflectivity trends for the classes at the hydrothermal field.*

b) depicts the standard deviation (rms-error) of the single CMP trends from the overall classified reflectivity trends.

Class no.3 (*here in orange*) is rarely imaged, but it is the most interesting since it occurs in the active venting area. The curve resembles clearly the curve of class no.2 but on a lower level (Fig. 71a). This may be caused by the bubble plume (see chapter 3.4.3). It exposes a distinct peak at ~38°, where the second critical angle of class no. 4 is discovered. This implies a thickness of more than 10 m made of the hard rock to account for the critical angle.
Class no. 2 (*here in cyan*) is alternating in high angles but the overall trend is the same as for class no. 3. Class no. 2 is always paired with class no.1 - the low impedance

sedimentary lithology - (Fig. 70), but occurs foremost in the western and northern part of the valley, i.e. directly east of the venting zone. It shows intermediate values between class no. 3 and class no.1. Applying the mixing rule it might represent gaseous hydrothermal precipitates in a sedimentary hostrock. Periodically rising gas would explain the alternating values. Since large angles occur at large offsets, an alternative explanation could be that the seismic waves progagate foremost through undisturbed water for large offsets. So large offsets could approximate the undisturbed trend, whereas signals recorded at small offsets and angles are substantially attenuated by bubbles. Class no.3 at values of 0.4 to 0.6 indicates compacted sediment, which again implies hydrothermal cementation processes.

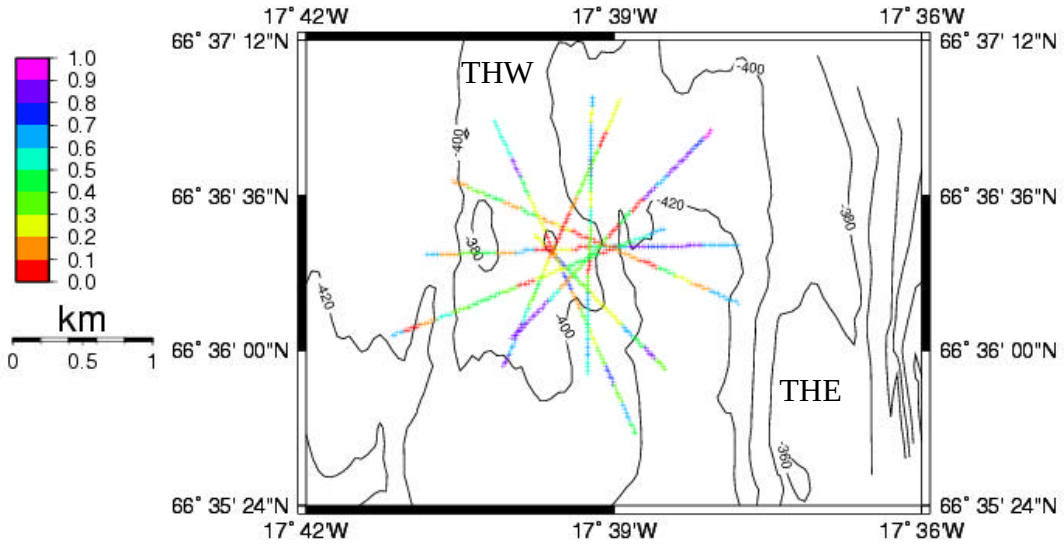

Figure 72: *The roughness in the area is intermediate, which is depicted in values (0.2 to 0.6) at 160 Hz (see scale). In the adjacent basins, the roughness is lower. The highest roughness is found at the vents of the hydrothermal field (see red values in the middle of the star).*

Roughness cannot supply additional constraints on lithology in this case. In the center of venting roughness is high, which is probably explained by complicated raypaths created by the presence of free gas, hummocky mounds and vertical spires. On top of the THW roughness is similarly high (Fig. 72). The valley is implied to be smoother by higher coherence levels which formerly indicated not yet compacted sediments of low impedance. So, in the topographic lows class no.1 will likely account for sediments. Alternatively it indicates a thin layer case, because the classified curve in Fig. 71a is nearly identical to the thin layer case in Fig. 69. In that case it would still indicate low impedance sediments below a thin hydrothermal sedimentary cover. Hemipelagic mud was cored (Scholten et al., 1999) and river gravel dredged (McMaster et al., 1977) here. So there is no evidence for a hydrothermal cover.

Since the bubble plume blurred reflectivities are probably least reliable, the bordering lithological units were investigated. The prevailence of hard rock (class 4) on the THW contrasts the sedimentary units (class 1) on the eastern side (Fig. 73) of the vents. Faulting is likely between such various units and prevents the recognition of lithological units by comparison with ther neighbours. The rough transition from one lithology to another is indicated in Fig. 74. It will play a significant role in the evolution

of vented gases.

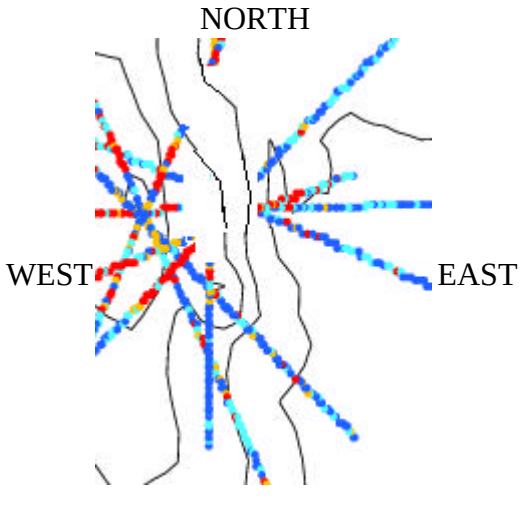

Figure 73: *At the center of the profiles, where the presence of free gas at the surface blurs the reflectivity values, the lithology has to be inferred from the surrounding lithologies. There, class no. 1 (in blue) and class no.4 (in red) dominate.*

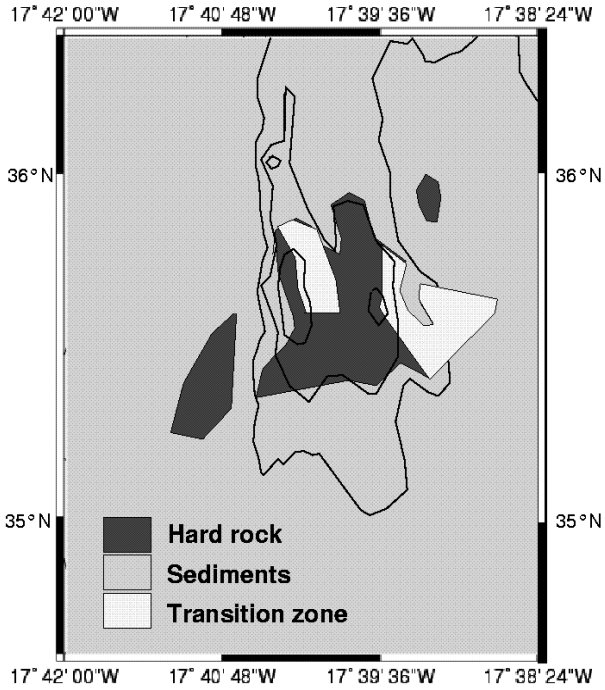

Figure 74: *The surface of the environment of the hydrothermal field can be subdivided into two major lithologies, the loose sediments, which have accumulated in Skjalfandi Trough and the hard rock which is built up of the hostrock and precipitates of the hydrothermal field. Transition zone represents an area where transition between the other zones was implied according to interpolation as indicated in Fig. 73.*

3.4.5. Structural information

Additional information on the seafloor comes from structural investigations. Particularly, reflection line P18 (see Fig. 70), which crosses the hydrothermal field on an east-west profile where the plume extents are smallest, can be used to constrain the composition of the transition zone.

The seafloor undulates and small normal faults dominate the near-surface structures.

One of these faults is directly found, where active venting was discovered by a local polarity reversal. In the surroundings class no.2 and class no.3 dominate the seafloor reflectivity trends (Fig. 75), which indicate the influence of the low Q values in the water column and/or hydrothermal cementation. This is clearly the transition zone. It will be shown that it is made of Anhydrite interspersed by gas supplied from the subsurface.
Pre-stack migration of the high frequency partition (>30 Hz) highlights the sediments as horizontal layers east of the vent-field in a distance of ~200 m from the vent. This area is imaged as SOM class no.1, which confirms the assumption deducted from roughness investigations. The reflections directly west or east of the vent are dominated by the class no.4, i.e strong reflections. It indicates the hydrothermal deposit of the active venting zone.

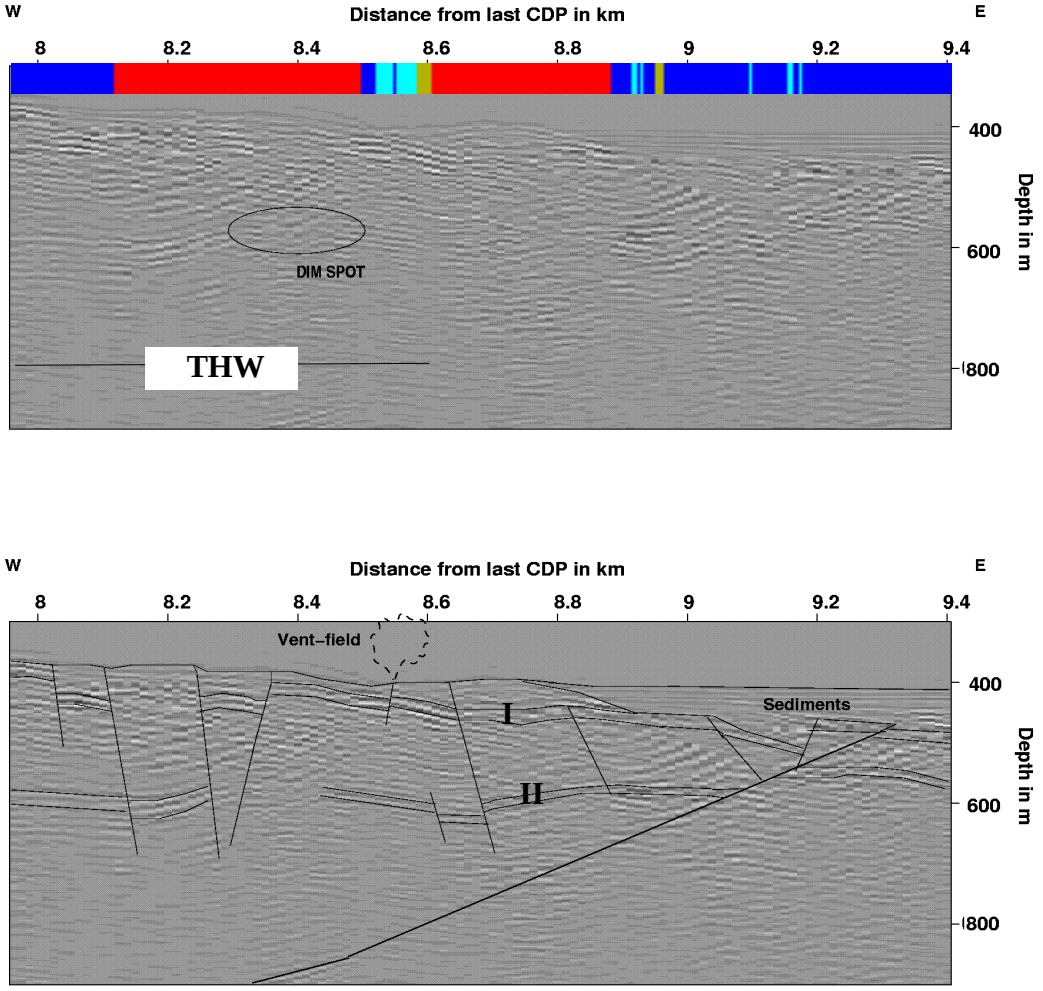

Figure 75: *Reflection line P18 is shown in a) a pre stack-migrated section across the hydrothermal field and the reflectivities are shown as colors of the classes in chapter 3.4.4. (Fig. 71) above the record, b) the small-scale structure of the field is made up of many normal faults in the transition from hard rock (red,class no.4) to sediments (blue,class no.1).*

In the subsurface a first large impedance contrast occurs at a depth of 20 m beneath the vent. This reflector (I in Fig. 75) is continuous, but disrupted along the profile, hinting on strong faulting. Its reflection amplitudes are high beneath the vent and beneath the sedimentary part.

Assuming the continuous reflector I represents the same material throughout, the similar amplitudes imply similar material above the reflector. Low amplitudes within the sedimentary sequence in the east and the similarly low amplitude at the top of the sequence, i.e. the seafloor, indicate low impedance sediments at the transition to reflector I. To account for the similar amplitudes of reflector I below the hard rock of the THW, the impedance should gradually decrease from the surface towards reflector I. From JAGO diving (Hannington et al., submitted; Theilen and Scholten, 2000; Stoffers et al., 1997) , it is known that the seafloor is covered with Anhydrite (Hannington et al., submitted) around the vents, which provides the observed strong reflections. No further reflector is imaged between the seafloor and the considered reflector, so the gradual decrease in impedance in the uppermost layer could originate e.g. from higher gas content.
A second reflector (II in Fig. 75) was recorded ~150 m below. Just west of the vent, its amplitude decreases. If both strong reflector are considered to be high impedance reflectors, this amplitude decrease can be considered a dim spot. It is a typical gas indicator in high impedance layers. High impedances of reflector I and II would indicate lava flows. In the vicinity of a volcanic ridge - as the sidearm of Manareyjar Ridge, which shows in topography as THE, this is probable.

3.4.6. Hydrothermal gasgeochemisty

"Who put the the bore in borosilicate ?" (I. Banks, The Crow Road)

The composition, particularly stable isotope compositions, of the vented gases can tell us about their origin. Typical vent gases have been described from various sources throughout the world's oceans (Butterfield, 2000). Main gaseous compunds in vent gases are carbon dioxide and methane, but the solutions are also enriched in metallic ions. Usually methane and total dissolved manganese are well known tracers of hydrothermal fluid input even in the vicinity of the Iceland plume (German et al., 1994). The hydrothermal activity along transform zones of the Mid Atlantic Ridge was investigated by Bougault et al. (1993), who found that the fluids are often less enriched in manganese than in ridge environments (Fig. 76).

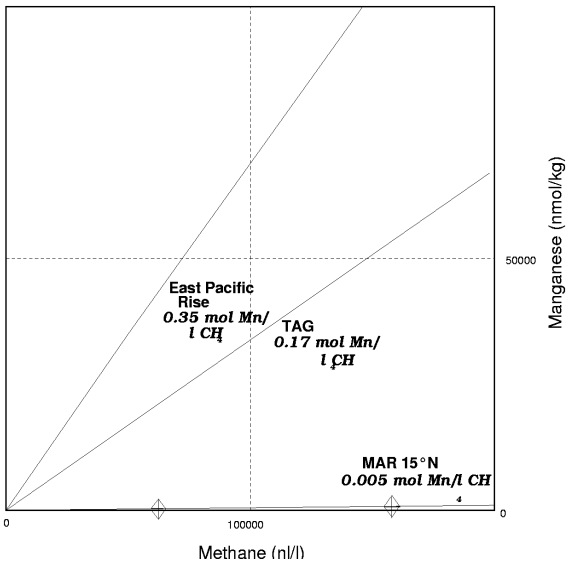

Figure 76: *The total dissolved manganese (Mn) is relatively less enriched in the hydrothermal fluids north of Iceland (diamonds) compared to the methane (CH_4) content, which is typical for Mid Atlantic Ridge fields near transform zones, although the Trans Atlantic Geotraverse (TAG) field is not far from a transform zone, as well.*

This relative depletion of manganese and/or iron is explained by ultramafic deposits,

which during the course of serpentinization of olivine catalyze a series of Fischer-Tropsch reactions (Berndt et al., 1996), so that methane and higher hydrocarbon homologues are formed by the following chain reaction which stops after chains of 36-40 carbon atoms in modern reactors (Shell, 2000):

$$CO+3H_2 \rightarrow H_2O+ CH_4 \qquad \text{(Methane)}$$

$$CH_4+CO+3H_2 \rightarrow H_2O+C_2H_6 \qquad \text{(Ethane) and so on...}$$

Free hydrogen (H) is generated during serpentinization. Carbon monoxide (CO) as carbon dioxide (CO_2) are in equilibrium with each other at higher temperatures and originate in magmatic fluids, probably during magma ascent when dolomite from the mantle is cracked up (Wallace and Anderson, 2000). But the Fischer-Tropsch reaction needs a catalyst, which is thought to be magnetite (Yoshida et al., 1993; Berndt et al., 1996), where forsterite (Mg_2SiO_4), carbon dioxide and water react to form serpentine ($Mg_3(OH)_4[Si_2O_5]$) and magnesite ($MgCO_3$).

$$2Mg_2SiO_4+CO_2+2H_2O \rightarrow Mg_3(OH)_4[Si_2O_5]+MgCO_3$$

Fayalite is released during the process from Olivine and through metastable phases tends to form magnetite and free hydrogen. The products of the Fischer-Tropsch chain reaction show a characteristic Schulz-Flory distribution, i.e. a logarithmic decrease of molar fractions - or in the case of ideal gases volume fractions -with carbon number (the number of carbon atoms in a molecule). In Grimsey Hydrothermal Field, hydrocarbons up to n-Butane have been sampled (Botz et al., 1999) in the gas-sampling stations (Fig. 77) described by Botz et al. (1999). The logarithmic distribution of hydrocarbons is shown in Fig. 78. The higher hydrocarbons (Ethane to Butane) follow the law, whereas methane concentration is higher than predicted, i.e. not all of the methane can be explained by the chain reaction.

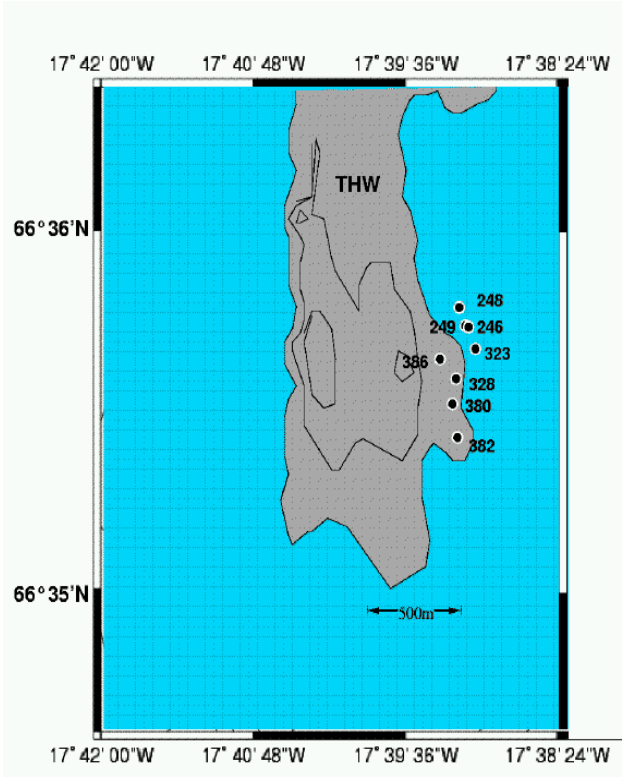

Figure 77: *The gas sampling stations of two surveys are presented, which were used in the discussion.*

Olivine for serpentinization is delivered by magma, particularly picrites (i.e. basalts of 90% olivine and pyroxene) which are commonly found in northern icelandic volcanoes of the Theistareykir fissure swarm (Mertz et al., 1991). These picrites frequently occur in transform fault volcanism (Perfit and Davidson, 2000; Perfit et al., 1996) and are typical for metal-rich hydrothermal deposits of the North Atlantic igneous province e.g. at Nussusuaq/Greenland (Graham et al., 1998, Saunders et al., 1998).

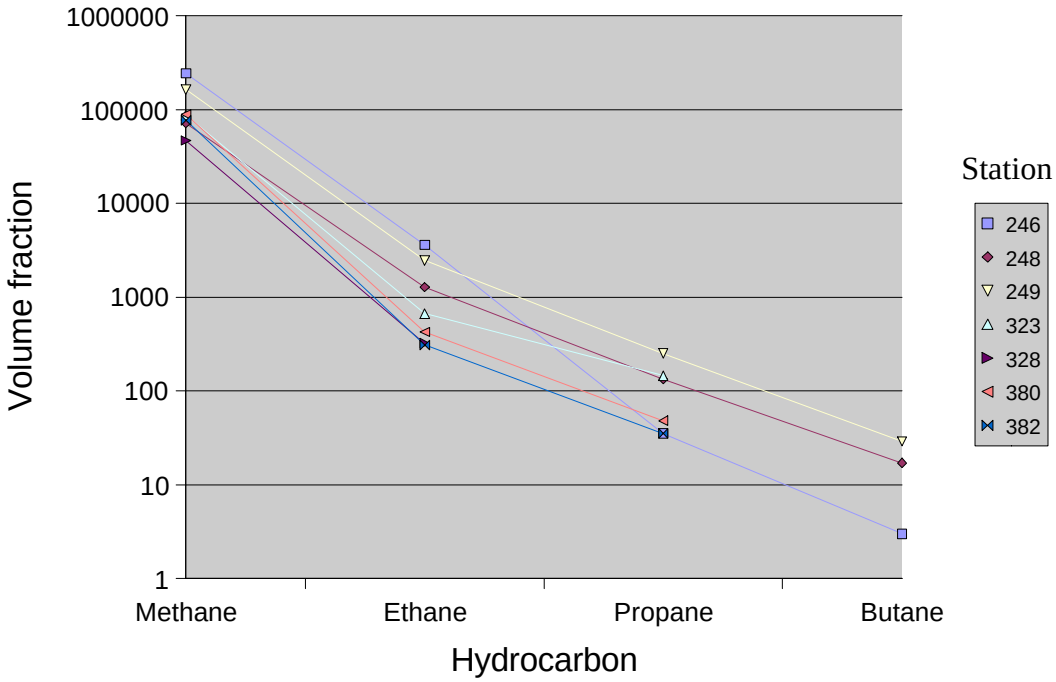

Figure 78: *On a logarithmic scale the distribution of hydrocarbons concerning volume fraction is nearly linear, which is called a Schulz-Flory distribution and is typical for a Fischer-Tropsch reaction.*

The produced magnesite can be the base material to produce talc in silica (SiO_2)-rich environments by:

$$MgCO_3+4SiO_2+H_2O->Mg_3(OH)_2[Si_4O_{10}].$$

Talc was observed in large amounts in the surfacial precipitates (Hannington et al., submitted) and silica compunds rise up to ~2 *g/l* (Stoffers et al., 1997) compared to a normal value of ~1.2 *g/l* in hydrothermal fields (Butterfield, 2000). So, the Fischer-Tropsch reaction is probably the main source for hydrothermal trace gases, however, no serpentinites have been reported in the TFZ.

Still there must be another way for creating methane. High methane (CH_4 or C1) concentrations in hydrothermal fluids is also thought to be derived from secondary circulation in sedimentary basins, which contain thermogenic components, i.e. components derived from thermal degradation of organic material. In anoxic conditions in the subsurface, where the temperature is high enough, kerogenes react to form methane and higher hydrocarbons, a process which is called catagenesis. Usually, this reaction takes place in an environment of 300-400°C and higher (Butterfield, 2000), whereas in the presence of methanogenic microbes (which are present in organic material) it can proceed faster and already take place in temperatures lower

than 110°C .

Lighter isotopes will more likely react than their heavier counterparts (Welhan, 1988), so Carbon-13 (^{13}C) will be depleted in this methane, because its stable counterpart is the lighter Carbons-12 (^{12}C) isotope. In Guaymas basin, hydrothermal fluids expose higher hydrocarbon homologues in addition to methane, which was again interpreted as the influence of organic matter from sedimentary basins (Welhan, 1988).
Thus, to differentiate between different processes of hydrocarbon development in hydrothermal environments, the isotopic ratio of $^{13}C/^{12}C$ was analyzed:

$$\delta^{13}C_{CH_4} = \left(\frac{\left(\frac{^{13}C}{^{12}C}\right)_{sample}}{\left(\frac{^{13}C}{^{12}C}\right)_{standard}} - 1\right) \cdot 1000$$

The standard is often the Peedee Belemnite (PDB) standard (i.e. 11237.2±2.9 ppm), denoted after composition of a carbonate rock in California. δ is the difference of the stable isotope ratio between sample and standard. The carbon 13 depletion is shown in Fig. 79 and 80 Table 3. The ratio of methane to ethane (C_2H_6 or C2) is also indicative of the source of fluids - higher homologues can be neglected (Fig. 78, 79 and 80, Table 3).
Where sediments influence the vented fluids, the $\delta^{13}C$ value shows value of -26.1 to -29.8. Closer to shallow igneous rocks, they are more positive and ethane production is higher in the sedimentary environment. This confirms the occurrence of sedimentary units indicated by seafloor reflectivity mapping and seismic stratigraphy (Fig. 76). However, the northern stations are also closer to the THE. The THE is connected to Manareyjar Ridge which again is associated with the Theistareykir fissures, i.e. picritic (olivine-rich) volcanism. Thus, the northern stations will more likely reveal serpentinization processes and triggered Fischer-Tropsch reactions.

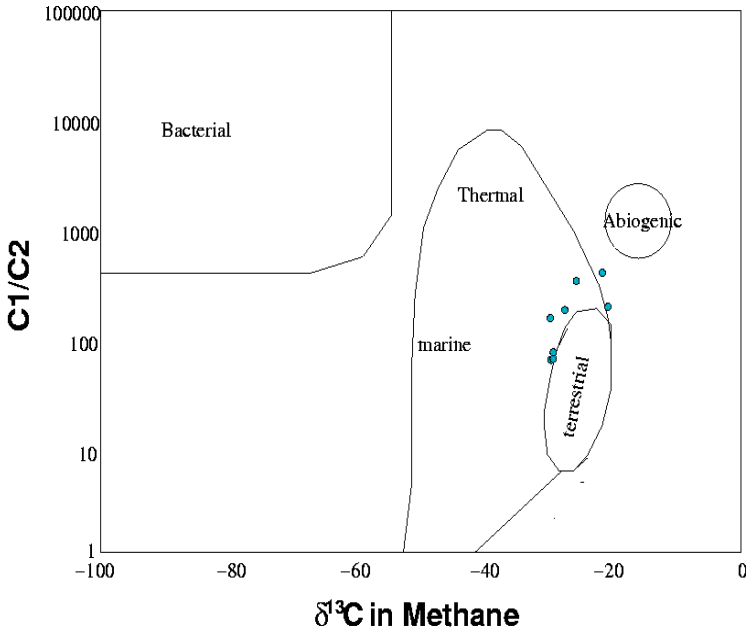

Figure 79: *The ratio of C1/C2 and d13C_{C1} value can be used to determine the origin of hydrocarbons. The circles represent the presented values of Table 3.*

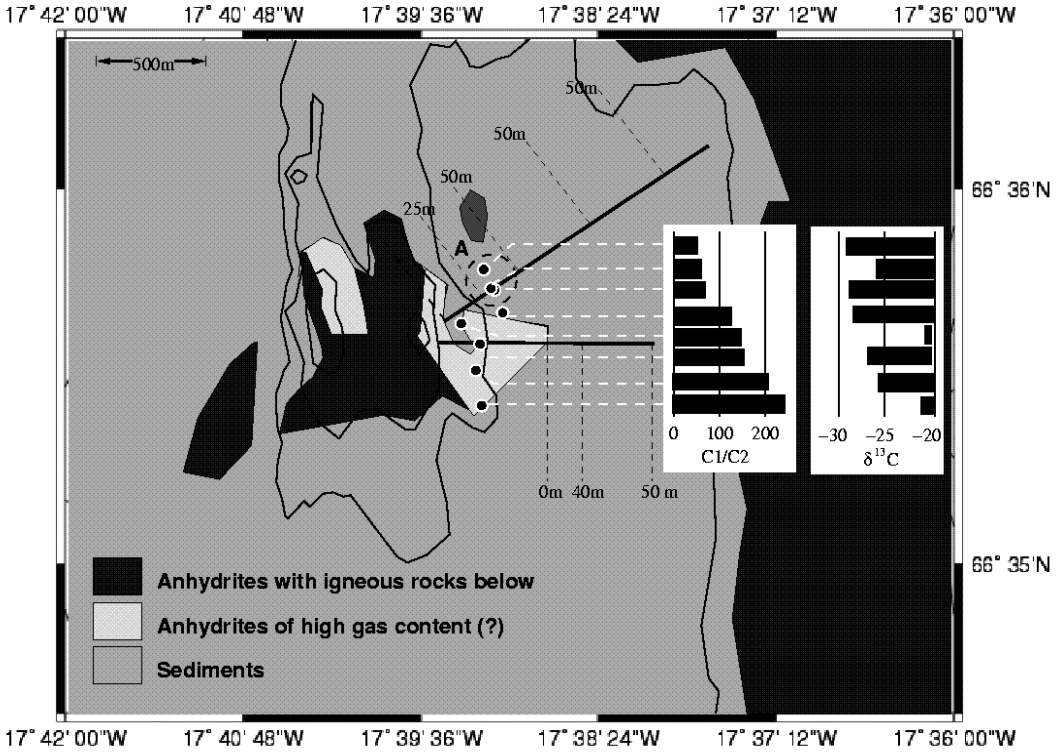

Figure 80: *The methane to ethane (C1/C2) and carbon-13 (^{13}C) partition in methane is displayed in conjunction with surface lithologies derived from seafloor mapping. The black lines are two of the seismic lines (P24 northeast and P18 east of the ridge) where sediment thickness has been displayed. The black spots represent gas stations sampled by JAGO (Botz et al., 1999; Scholten et al., 2000; Riedel et al., in prep.). The classification of rocks depicts the situation discussed in the stratigraphy chapter (3.4.5).*

The C1/C2 ratios and ^{13}C values indicate thermogenic hydrocarbons derived from terrestrial to marine organic matter, which is a good description of the sedimentary sequences discovered in the TFZ environment (Eirikson et al., 1990). At least, a part of the production of methane is influenced by abiogenic sources, e.g. the Fischer-Tropsch reaction chain shown before.

The influence of the primary circulation, i.e. magmatic components, can be revealed by the isotopic composition of vented Helium. The $^3He/^4He$ ratio in fluids or fluid inlcusions stores information about the influence of crust and mantle. Whereas ^4He is foremost produced by radioactive decay of Uranium and Thorium, ^3He consists of primordial helium from the mantle and small percentages derived from beta decay of tritium, which again develops by alpha decay from Lithium (Winckler, 1998). A normal atmospheric $^3He/^4He$ ratio of $R_{atm}=1.384\cdot10^{-6}$ serves as a base for comparison (Clarke et al., 1976).
Deep mantle sources are enriched in ^3He, because the deep part of terrestrial planets is similar in composition to chondritic meterorites (Strobach, 1991) which exhibit $^3He/^4He$ ratios of $2\text{-}4\cdot10^{-4}$. Hot spot areas as Hawaii or Tristan da Cunha, or respectively the mid-ocean ridges supply the upper crust with parts of these higher amounts of ^3He, giving ratios of up to $26\cdot R_{atm}$ in icelandic basalts and geothermal fields (Kurz et al., 1985; Poreda et al., 1992). In the basalts (picrites) of the Theistareykir area, they drop to values at 8-10 R_{atm} (Breddam et al., 1999) with rising distance from the plume centre. Along Kolbeinsey Ridge, basalts exhibit a constant ratio of 10.3 to

12 R_{atm} (Poreda et al., 1986; Schilling et al., 1999). This is very interesting for the TFZ, because values of 10.9 R_{atm} were discovered at Kolbeinsey Hydrothermal Field (KHF), whereas Grimsey Hydrothermal Field (GHF) exposes values of only 9.8 R_{atm} (Botz et al., 1999) (Table 4). These values are considerably higher than the average mid-ocean ridge and lower than the typical hot spot environment, i.e. they display values relating to hot spot-ridge interaction. From isotopic ratios of various materials, Mertz et al. (1991) concluded, that the TFZ is a region of mantle convergence, where plume material flows in from the south and ridge material (MORB) from the north. From larger datasets of the whole of Iceland, the strongest effect has been attributed to the variance in lithologies (tholeiite to picrite) (Chauvel and Hemond, 2000).
The high $^3He/^4He$ ratios of Kolbeinsey Ridge were explained by the model of Mertz et al. (1991) by the currents of mantle material along Kolbeinsey Ridge originating at another mantle plume further north, e.g. Jan Mayen. The revisited model of Chauvel and Hemond (2000) suggests an evolution of all lavas including Kolbeinsey Ridge by the icelandic mantle plume. The low values of Helium ratios dropping to a minimum in the Theistareykir picrites (Breddam et al., 2000) do not trivially support such a model (black curve in Fig. 81). Eiler et al. (2000) discovered that the composition of lava in the Theistareykir area expose strong contaminations by crustal material. Assuming this is also true for the Helium gases, the minimum in $^3He/^4He$ in the Theistareykir area indicates increasing influence of mantle plume fluids towards the south, whereas the increase towards the north might indicate lower input of crustal ^4He in thinner crusts. The slightly higher helium isotope ratios at Grimsey Hydrothermal Field is correlated to a 16 km thick crust (Darbyshire et al., 2000) in comparison to Iceland crust of ~30 km further south. This model can be expanded to the oceanic crust at Kolbeinsey Ridge, which is again thinner and thus less contaminated by crustal input and consequently exhibits even higher $^3He/^4He$ ratios. So it explains the difference between KHF and GHF, because KHF is already part of Kolbeinsey Ridge, whereas GHF is located above the thicker crust of the TFZ. Taking the crustal effect into account, the helium ratios data in the TFZ suit very well to the model of Chauvel and Hemond (2000).

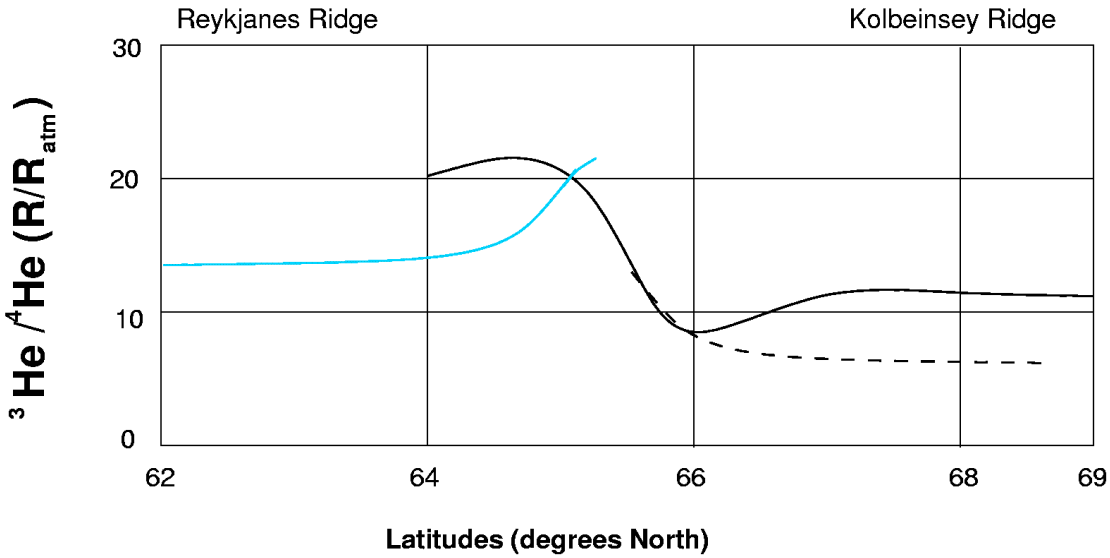

Figure 81: *Distribution of Helium ratios in Iceland (modified after Breddam et al., 2000). The grey curve represent the turned in southwestern Iceland, the black curve the trend from Grimsvötn to Kolbeinsey Ridge. From 66°N the curve diverges from a typical drop with rising distance to the mantle plume.*

The crustal effect cannot be found in the south of Iceland (grey curve in Fig. 81), so gradual thinning of crust is not connected to a minimum. The occurrence of a minimum rather implies a rapid decrease of crustal thickness north of 66° N.
The isotopic ratios show a decrease of plume influence towards the north of Iceland (Chauvel and Hemond, 2000; Breddam et al,. 2000). However, the helium ratios, in particular, are influenced by a strong crustal component in the TFZ which can be explained by this strong increase in crustal thickness towards Iceland and a thin crust in the TFZ.

	246	***248***	***249***	***323***	***328***	***380***	***382***	***386***
Carbon dioxide (nl/l)	83440	411636	10557	130880	378800	118579	335066	436156
Methane (nl/l)	243197	71666	163303	86905	46722	88806	77065	50311
$\delta^{13}C_{C1}$ (ppt PDB)	-26.1	-29.5	-29.4	-29.3	-26.8	-25.5	-21.5	-21
δD (ppt DDB)				-141.5	-142.6			
Ethane (nl/l)	3601	1280	2465	667	323	426	309	321
Propane (nl/l)	35	134	250	146	not detected	48	35	26
Butane (nl/l)	3	17	29	n.d.	n.d.	n.d.	n.d.	n.d.
Manganese (nMol/kg)		~155	~619					
Silica (g/l)		~0.8	~1.7					
$^3He/^4He$ (10^{-6})		13	13.6					

Table 4: *Composition of gas in Grimsey Hydrothermal Field.*

It should be noted that there appears to be a connection to deep reservoirs, followingly the decrease of $^3He/^4He$ from Kolbeinsey Ridge towards Iceland, which stems from the thickening of the crust. These reservoirs are connected to the crust-mantle boundary. They are filled by primitive magma very similar to that of the Theistareykir picrites and produce shallow igneous rocks of olivine-rich composition. There is no need for peridotites to explain possible serpentinization processes in the hydrothermal field, which is not heated up by a magma chamber from below, but covers an area which has been flooded by the picritic lavas from the close Manareyjar Ridge (representing the THE), the prolongation of the Theistareykir swarm into offshore regions.

4. Conclusions

4.1. A composite model of the Skjalfandi fault wedge basin

Summarizing the previous chapter, a dynamical model of Skjalfandi trough has to explain the following observations:

- The basic faults of the system is the Western Boundary Fault. It exhibits a dip of ~30° and can be interpreted as a basal, detached thrust fault.
- The basin was initially formed by the shear of the block east of the Basalt-Sediment boundary and the shear movement between BSB and WBF is continues in ongoing seismic activity. The extensional movement at the surface is mirrored in normal faults within the sediments of the basin.
- The tectonic situation of the subsurface is similar to fault-wedge basins, which are typical for continental transform faults and evolve between parallel lines of strike-slip shear.
- Volcanism and magmatism is confirmed by fresh basalts (McMaster et al., 1977), basement highs, high b-values and gravity highs at the western edge of the basin. Eruption do actually take place in the northwestern area only.
- A ridge, the THW, is imaged north of a hydrothermal field, which is not made up of basement material with the exception of the southernmost active tip. The ridge is lowering to the north and is covered by sediments in the northern part, i.e. this part of the ridge will mirror an earlier age in the evolution of the hydrothermal field.
- Shallow seismic activity is confined to the WBF and Grimsey Hydrothermal Field.
- Hydrocarbons rising from the hydrothermal field expose an abiogenic influence and helium ratios show the influence of a reservoir similar to the Theistareykir source, thus gases rise directly from a relatively shallow crust-mantle boundary at ~16 km.

The classical model of a fault-wedge basin (Woodcock and Fisher, 1986; Harding, 1985) can explain the tectonic features and accounts for the development of a geothermal field (Crowell, 1974). It is unable to explain the strong magmatic movements in the southwest of the basin. The driving force of fault-wedge basin dynamics would be two parallel lines of shear, but north of the Grimsey Lineament no such thing has been imaged up to now. Typically the hydrothermal field would be expected directly above the magmatic structure. East of the basin, however, no magma chamber was found. The isotopic composition of the fluids rising at GHF do hint on a thin crust as a heat source. In the TFZ, which is a region of hot spot-ridge interaction, the crust is thicker than oceanic crust (8-10 km) and considerably thinner than the crust of Iceland (20-30 km (Flovenz and Gunnarson, 1991; Darbyshire et al., 2000). So the thin crust could indeed be a driving force for geothermal activity.

Volcanism arises where void spaces open up in the subsurface. These are filled by low density, low viscosity fluids rising from the upper mantle. If the void spaces would have opened up by symmetric stress conditions, a symmetric distribution of magma along the edges of the basin would be expected. This is not the case. Thus, asymmetric conditions are essential for the formation of volcanic features in the west.
The thinning of crust towards the volcanic rift axes and from icelandic crust to oceanic crust could be responsible for the formation of a weakness zone which would produce

an asymmetric distribution of stress.
If shear force tears apart such a structure, extension near the thin crust will be faster (Fig. 82). This would lead to the observed magmatism and the formation of a basin. The highly active and thus permeable (Barton et al., 1995) faults in deeper locations will allow the rise of magma to even shallower depths, probably in the range of 8-10 km where most of the quakes vanish (Fig.58). Most of that will occur in the west of Skjalfandi basin and further north. The fluids may accumulate into magma chambers, where they are trapped beneath undisrupted layers., but in case, magma rises through faults, which are connected to shallow faults, they are found to rise towards the west of the basin and erupt from small isolated volcanic edifices, of which Grimsey itself may be the best example.
Along the rising magma, seawater heats up. It will rise along the most seismically active and thus permeable paths farther to the east, because the presence of liquid magma significantly lowers the permeabilities of faults in the west (Ingebritsen and Scholl, 1993). Thus, the aqueous solutions finally erupt in the hydrothermal field and carry the isotopic imprint of the mantle.

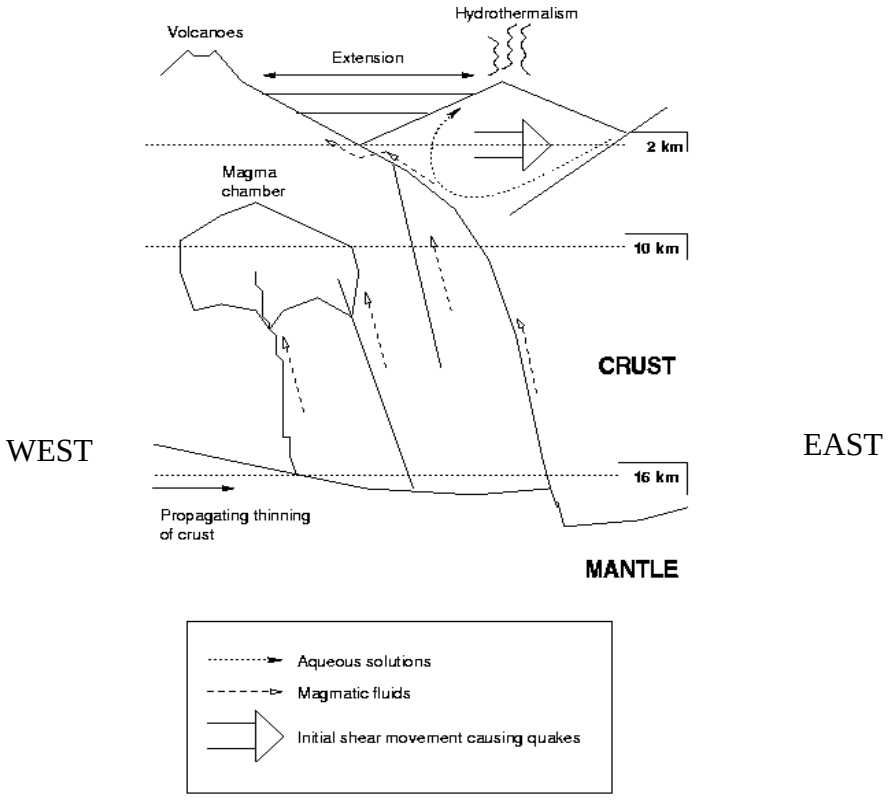

Figure 82: *The schematic interpretation of structural dynamics in Skjalfandi Trough shows a fault-wegde basin, where the western boundary is influenced by magma movements, along which on the hanging wall on the eastern side, water heats up and is relased into a hydrothermal field. Further extension to the east leads to progressional thinning of the crust by shearing.*

The ridge with its southern tip at GHF in the east of the basin must have evolved from continuous precipitation by the hydrothermal field, which was already suggested by Herzig (1999) from results of diving and sampling. It is a track of the hydrothermal field and consequently the relative track of the shallow permeable faults to the heat reservoir.

The shallow subsurface expanded above the detached WBF shear fault by tilting normal faults in east-west direction. The driving shear force however enforces a movement oblqiue to expansion, so the residual component of the oblique movement is mirrored in the formation of the ridge from north to south.
The offshore part of the Tjörnes Fracture Zone has not been geophysically investigated in detail before the presented survey, i.e. only selected features as active faults, gravity field or local magnetic anomalies were published. These features fit into a common model and the seafloor lithology map published in the Appendix is a first example to integrate the results. This map evolved from the reflectivity mapping and the subsequent detail analysis.
Loose sediments prevail in the fjord structures and in the northernmost bathymetric lows. This corresponds to high sedimentation rates of marine and terrigenous sediments that were derived for the area. On the other hand the geodynamic activity keeps ridges and isolated seamount (or rather submarine hills) nearly free from sedimentation. Compaction of sediments does foremost occur in tectonically relative quiet environment northeast of Skjalfandi Trough (see Fig. 83). The major tectonic features are indicated by the discontinuities in fault structures. All these geodynamic features are summarized in Fig. 83.

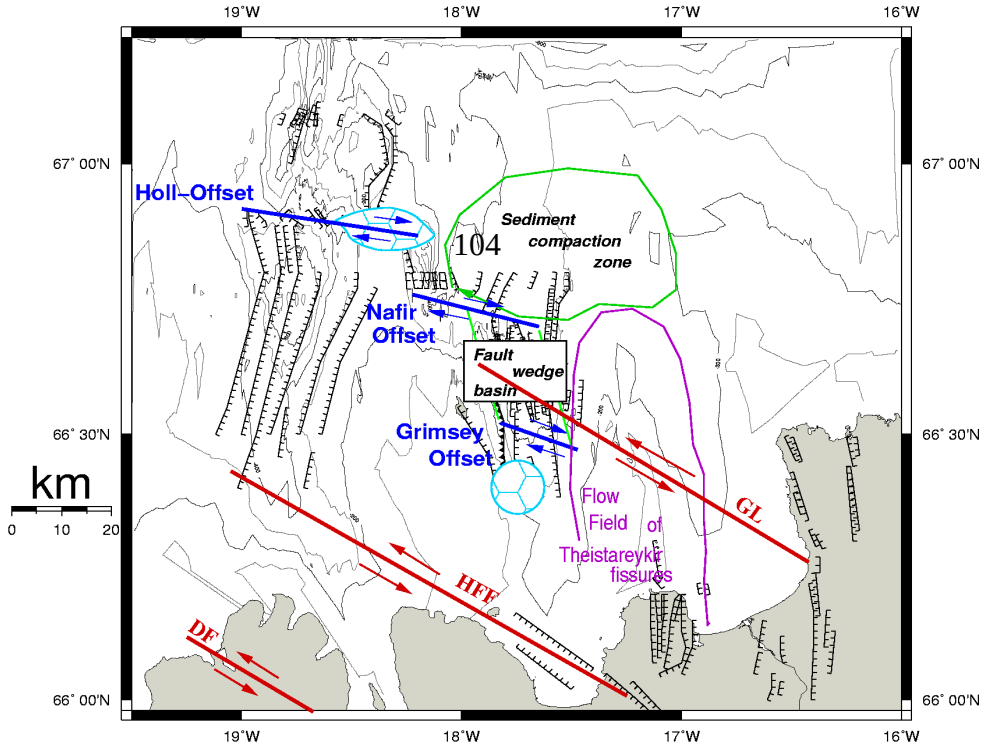

Figure 83: *The offshore part of the TFZ is composed of three main non-transform offsets (Grimsey, Holl, Nafir), which are driven by the stress build up along the Grimsey Lineament (GL), the Husavik-Flatey Fault (HFF) and Kolbeinsey Ridge. These tectonic units divide dynamic and quiet zones in the TFZ. Hexagonal patterns indicate potential magma chambers.*

4.2. The Self-Organizing Seafloor Mapping method and its perspectives

The comparison of stratigraphic and reflectivity analysis provided similar results, but whereas stratigraphic analysis can only separate discordances and differences in seismic transparence or style of reflection (seismic facies), the reflectivity can be used to infer

lithology semiautomatically. It could be used in an interpretation scheme to provide a first order model of the surface which compliments stratigraphic results gained pre-stack migrated recording or line-drawings. The surface is a mirror of the subsurface. It is used in standard way geological mapping. Self-organizing mapping could be used to extend this method to submarine mapping.
However, it will not possible to distinguish between rocks of similar physical properties. So, it will still be essential to sample rocks from the seafloor to provide unequivocal results. As a means to decide where basement rocks crop out in a sedimentary unit it is powerful tool. The variance of reflectivities within single rock classes may supply further physical properties of the surface which could refine the method in future investigations. Problems do occur where thin layers of hard rocks, i.e. precipitates or lava flows, overlie low impedance sediments. These layers cannot be distinguished from low impedance rock at the surface. Rough surfaces which are typically e.g. for outcropping basalt will produce unpredictable reflectivities that cannot beresolved by the method.
Thin layers can be resolved by high frequency sources, thus exploration companies use digitized echo-sounder signals or boomers for resolving thin loose sediment covers. A similar recording is essential for any seismic survey. Since echo sounders are installed on any ship and a single hydrophone can easily be controlled on a survey, there is no further recommendation for the equipment but to use it.
The neural network theory has not yet been exploited for the task of reflectivity mapping. By applying a back-propagating network to quality controlled data, it should be possible to map reflectivity trends onto physical properties, which can be used to determine porosity or permeability of subsurface structures. A detailed map of the subsurface even of the sediments could be developped if several cores were sampled and their physical properties were modelled. A best match to these modelled results might provide better results in a simpler way than any neural network. The best match criterion, which is stable for the Kohonen network should also be stable for a best match of typical lithologies.
In a wide range of roughnesses, the Self-Organizing Seafloor Mapping method delivered reasonable results that were used to determine the extents of a basin, a basaltic flow field overlain by conglomeratic rocks, a flow field of a ridge or thin sediment covers above young volcanoes. In the vicinity of an active spreading ridge or where rising gas from the seafloor blurs the signal, reflectivity is distributed in a chaotic way, that will not mirror the insitu lithology. This is an artifact of high roughness. The backscatter coefficient depends on roughness and reflectivity and it thus no wonder that the problem of fluctuating reflectivity classes is most severe where both values are high. Gas might have a similar effect as roughness is also a known phenomenon from optics. Where gas is rising the vision is often blurred, e.g. above rising flames or vapor rising from roads. The same happens when looking through glass windows consisting of ripples on the surface. Gas has a similar influence on optical waves as roughness. This might be analogous for seismic waves. The gas blur effect is temporary and might be used in terms of monitoring.

Appendix

A. Processing marine data from North Iceland

To arrive at the reflection seismic section presented during this thesis the following processing was performed:

1) **Band-pass filtering** (*Butterworth*), corner frequencies 10Hz-20Hz-125Hz-250Hz

2) **Prediction deconvolution:** length of filter from beginning of positive pulse to beginning of positive phase of bubble.

3) **Signal deconvolution:** length of filter from beginning of positive pulse of direct wave to beginning of phase of reflected wave.

4) **Band-pass filtering** (suited to application, high or low frequencies)

5) **Pre-stack depth migration** (Kirchhoff-*sukdmig2d*): model: 3 layers, sediments, transition zone, igneous crust.
   Information on velocities: Former surveys, NMO curves of the survey
   Important: Fitting the model so that no apparently continuous reflector is disrupted by the migration process !
   => Recursive process of migration by Seismic Unix:
      Pick prominent reflections
      Define Velocity-Depth model by pick points
      Loop:
      Raytrace model
      Stack information on all subsurface grid points
      Check for velocity information
      Check for disrupted reflectors
      Refine model, start loop until satisfied

6) **Display** with **Automatic Gain Control** (0.5 s) and Trace balancing !

This was not used for the true amplitude processing part, but only to those sections presented in the stratigraphic descriptions.

B. Automatic picking algorithm (*SUAVOPICK.C)*

Various methods for seafloor migration have been presented by other authors, the amplitudes are extracted here by simple geometrical considerations in order to estimate reflection angles.

Near-shot FRA amplitudes

Automatic picking was performed by detecting the FRA on the near-shot trace (single channel line). They can easily be identified in a moving time window centered on the last detected FRA and picking the closest maximum (Fig. B.1A). Where approriate a manual pick can stabilize this automatic picking algorithm in certain locations. The performance is fast and can be stabilized in interaction with the user in some minutes for some thousand CMPs.
Afterwards the zero crossings before the positive phase and after the negative phase of the FRA are determined and the time window inbetween is cut out for amplitude evaluation (Fig.B.1B/C). The rest of the time window up to a number of 2^j $(j \in \mathbb{N})$ samples is filled with zeroes. The number of 2^j values is essential for a DWPT analysis (chapter 2.5). Not necessarily better results could be obtained by using only the positive phase.
The direct wave amplitude is detected from the near-shot trace and stored in the header of the trace with location, slope and depth, which are calculated from geometrical considerations.

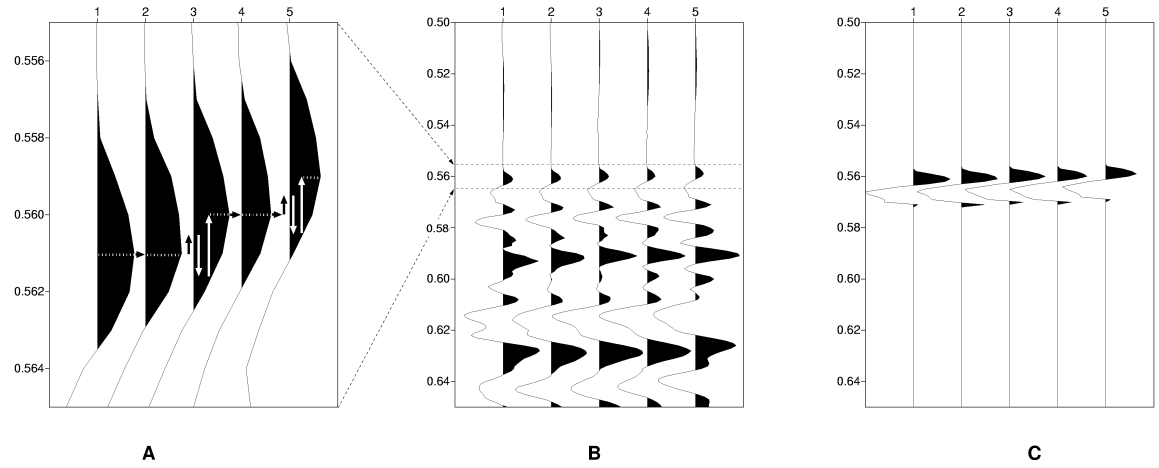

Figure B1: *The first reflected arrival (FRA) is picked by looking for the closest maximum on the same channel of the next shot point. A) Sample per sample of a trace is checked, first the previous sample and afterwards the following sample. Once a maximum value is found, one wavelength is cut out (see B) from zero crossing to zero crossing to arrive at figure C.*

Depth

The zero crossing at time t_{zero} just before the maximum of the FRA on the nearest offset x_n is a measure of depth *d*, where the sound speed in water v_{water} is known:

$$d = \sin(\arccos\frac{2x_n}{t_{zero} \cdot v_{water}}) \qquad \text{(B.1)}$$

Farther distance FRA amplitudes for flat surfaces

It can thus be used for modelling a reflection hyperbola t_{hype} along which the closest maxima

on other offsets x (= $\overline{SR}$ source-receiver distance) can be evaluated:

$$t_{hype} = \frac{4d^2 + x^2}{v_{water}^2} \qquad \text{(B.2)}$$

It can subsequently be used to determine an expectation value for the FRA amplitude on other traces and search the nearest maximum.Afterwards one wavelength was cut out just like in the near-shot trace.

Slope

After sorting the wavelets according to CMP, the approximate slope is determined by evaluating the apparent depths of the previous CMP d_{CMP-1} and the following CMP d_{CMP+1} and determining the gradient over double shot spacing x_S.

$$b = \left|\arctan\left(\frac{d_{CMP+1} - d_{CMP-1}}{2x_s}\right)\right|. \qquad \text{(B.3)}$$

What is the error made in this assumption ?

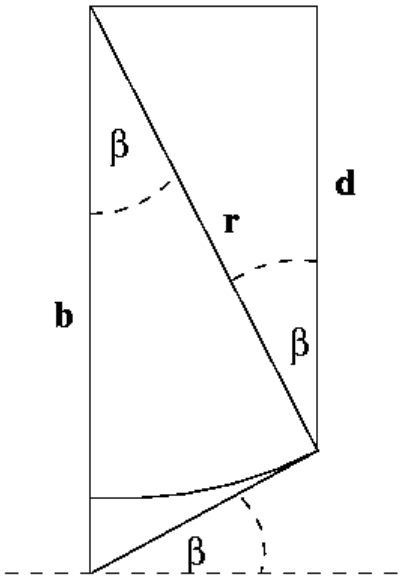

Figure B2:*shows a simple geometrical sketch of the apparent depth r determined from simple moveout analysis and the real depth d, if the sea floor dips at a slop**b**.*

From Fig. B2 it follows that the apparent depth which has to be used for reflectivity evaluation r is dependent on the real depth d as:

$$r = \frac{d}{\cos b}. \qquad \text{(B.4a)}$$

Thus the relative error made in depth is

$$\frac{r}{d} = \frac{1}{\cos b}. \qquad \text{(B.4b)}$$

Subsequently, if b and d shall not differ from each other within 4 samples (sample rate $Dt=1ms$) per trace, which is equivalent to a signal frequency band up to 125 Hz, a typical water depth of d=*400m* would result in (cf. equation (B.3)):

$$b = \arccos\left(\frac{d}{d + 4 \cdot 0.5 v_{water} \Delta t}\right) \approx 5°.$$

The slope angle β should not be steeper than 10° if the difference over the double distance is evaluated. Of course this decreases the lateral resolution of slopes, but since steep angles are not well approximated this does not restrict the method further.

***Figure B3**: For a slope of β on the sea-floor the reflection angle γ can be determined by geometrical considerations.*

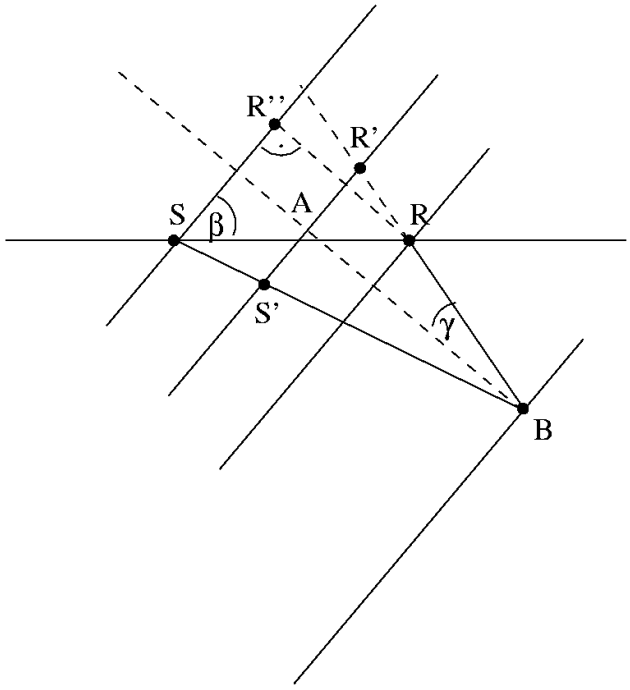

Reflection angle

Assuming the slope β is known and less than 9.5°, the theoretical reflection hyperbola and reflection angle can be calculated from Fig.A3.

The recorded travel time t_{hype} from source (S) to receiver (R) is equal to a two-way travel time (TWT) virtually recorded at a flat surface at half the vertical distance of R and S to the sea floor, i.e. a reflection at the CMP B finds its projection on a virtual sea surface crossing point A, where the virtual offset is $\overline{S'R'} = \overline{SR''}$

and thus $$\overline{SR''} = \frac{v_{water} t_{hype}}{2} \sin g \ . \qquad \text{(B.5a)}$$

On the other hand $\overline{SR''}$ can be calculated from the upper triangle as: $\overline{SR''} = x \cos b$. (B.5b)
The reflection angle without approximation in this last step is:

$$g = \arcsin\left(\frac{2x \cos b}{v_{water} t_{hype}}\right) . \qquad \text{(B.6)}$$

Farther distance FRA amplitude for sloping surface

The real moveout, i.e. the theoretical travel time, of this slope configuration follows as:

$$t_{hype} = \frac{2x \cos b \sin g}{v_{water}} . \qquad \text{(B.7)}$$

This again might serve as an expectation value for a maximum and the same time window procedure can be applied as above. In SU-Format the wavelets sorted after CMP and with the essential headers are output from the algorithm and further reflectivity calculations (frequency effects) are corrected in SURELEFF.C. If no improvement to the waveforms (frequency domain) shall be made, SUNORELEFF.C is capable of transforming the wavelets to reflectivity values.

C. The discrete wavelet transform, uncertainty principle and Heisenberg boxes

The discrete wavelet transform was developped as a special case for the continuous wavelet transform (CWT) (Hubbard, 1995):

$$CWT(a,b) = \int f(t)\,\psi(at+b)\,dt \quad , \qquad \text{(C.1)}$$

which evolves from $a=2^k$ and $b=l$, i.e. if a is used as a factor for *dyadic subsampling* and b means a shift of the time-series by the whole wavelet. This can be programmed as a pyramidal algorithm of quadrature mirror filters by using a matrix W acting on a line vector (time series) like the Daubechies 4 matrix (Press et al., 1992):

$$W_{D4} = \begin{bmatrix}
c0 & c1 & c2 & c3 & 0 & 0 & \dots & & \dots & \dots & \dots & \dots \\
c3 & -c2 & c1 & -c0 & 0 & 0 & \dots & \dots & \dots & \dots & & \dots \\
0 & 0 & c0 & c1 & c2 & c3 & \dots & \dots & \dots & & \dots & \dots \\
0 & 0 & c3 & -c2 & c1 & -c0 & \dots & \dots & \dots & \dots & \dots & \\
0 & 0 & 0 & \dots & \dots & \dots & \dots & \dots & 0 & 0 & 0 & \\
\dots & \dots & \dots & \dots & \dots & & 0 & 0 & c0 & c1 & c2 & c3 \\
\dots & \dots & \dots & \dots & & \dots & 0 & 0 & c3 & -c2 & c1 & -c0 \\
c2 & c3 & 0 & \dots & \dots & \dots & \dots & \dots & 0 & c0 & & c1 \\
c1 & -c0 & 0 & \dots & \dots & & \dots & \dots & & \dots & 0 & c3 & -c2
\end{bmatrix} \qquad \text{(C.2)}$$

The wavelet scaling filter is then defined as h=[c0,c1,c2,c3] and represents a moving average of the function, whereas its quadrature mirror filter g=[c3,-c2,c1,-c0] represents the rest of the time series, i.e. a detail function and these again represent the wavelet ψ(t):

$$\psi(t) = \sum g_k \sqrt{2}\,\varphi(2t-k) \quad \text{, where} \qquad \text{(C.3a)}$$

$$\varphi(t) = \sum h_k \sqrt{2}\,\psi(2t-k) \quad . \qquad \text{(C.3b)}$$

The c's can be calculated in various ways, which have to account for certain properties of the wavelets best explained in Strichartz (1993). The performance of such a wavelet transform is best explained in Press et al. (1992), Vidakovic and Müller (1991) and Strang (1993). It employs a matrix like (B2), which is used on the time series to its right and then permuted, so that the h-products and g-products are sorted, i.e. the "smooth" and the "detail" information. The lower right part of the matrix is then multiplied with the "smooth" part again. This process can be performed until the smooth part consists of only two samples. The result is a frequency-time partitioning of the time-series, which makes use of the uncertainty principle (see Chapter 2.5).

Although originally developped for quantum mechanics the uncertainty principle of the german nuclear physicist Heisenberg bears high importance for filtering techniques and time series. It states

$$\Delta p_x \Delta x \geq h\,, \qquad \text{(C.4)}$$

i.e. it impossible to determine both the location x of a particle and its impulse p_x precisely at the same time, the resolution is restricted to Δx and Δp_x. and their uncertainty is at least of the order of Planck's number h.

$\frac{\Delta p_x}{h}$ can be substituted by the reciprocal of the de Broglie wavelength $\Delta \frac{1}{l}$ or the wavenumber Δk. That was the original description by Heisenberg which he deducted for all waves and their wavenumbers. Since acoustic wavenumbers k lead directly to frequencies f, because the medium regulates their ratio via the acoustic medium velocity v by

$$v = \frac{f}{k}, \qquad \text{(C.5)}$$

the formulation

$$\Delta k \, \Delta x \geq 1 \qquad \text{(C.6)}$$

follows as

$$\frac{\Delta f}{v}(v\Delta t) \geq 1 \qquad \text{(C.7)}$$

or

$$\Delta f \, \Delta t \geq 1. \qquad \text{(C.8)}$$

The wavelet transform was first applied to geophysical time series and speech recognition tasks (Rioul and Vetterli, 1991), both acoustic tasks; so the area this product covers in the time-frequency plain was immediately identified with a *Heisenberg box*.

D. The Rayleigh approximation in C

The Rayleigh approximation (equation (1)) looks simple:

$$R(\theta) = \frac{z_p \sin^2 2\theta_s + z_s \cos^2 2\theta_s - z_{water}}{z_p \sin^2 2\theta_s + z_s \cos^2 2\theta_s + z_{water}} \quad , \qquad \text{(D.1)}$$

but it can only be solved for angles smaller than the critical angle. At the critical angles - there are two, one for p-wave and one for the s-wave - the adjacent impedances approach infinity. Above the critical angle, they acquire complex values and the complex sine function has to be evaluated by:

$$\sin \vartheta = \sin(\alpha + \beta i) = \sin\alpha + \cosh\beta + i(\cos\alpha + \sinh\beta). \qquad \text{(D.2)}$$

Hyperbolic cosine and sine function are part of the C libraries and can thus be calculated. This is not a difficult task, but it should not be forgotten. Once a function like (D.1) is displayed in MATLAB it is not clear whether the values can be complex !!! So when converting MATLAB functions, it is always worth thinking what values are part of the parameter space.

E. Roughness estimates for surface from airgun waves

Stanton (1985) approximates the term γ^{-1} for roughness, where:

$$\gamma^{-1} = \frac{1}{2\pi} k^4 h_{rms} \chi^2 I_{GC} \quad . \qquad \text{(E.1)}$$

I_{GC} is approximated as a correlation function in his Appendix and is denoted by two correlations lengths l_x and l_y for undulating surfaces as:

$$I_{GC} \simeq \frac{2}{3} l_x l_y \quad . \qquad \text{(E.2)}$$

Figure E.1*: The airgun beamwidth is assumed to be* π.

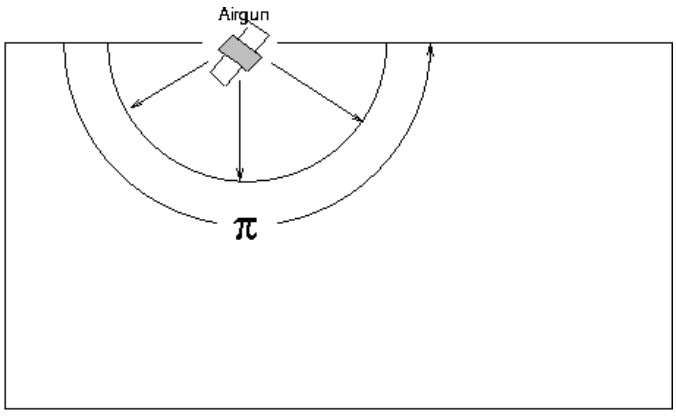

Acoustic wave number k is substituted by frequency and sound speed and χ is the full beamwidth, which is assumed to be π for airguns in a homogenous halfspace (Lerche and Hill, 1985), thus we arrive at:

$$\gamma^{-1} = \frac{\pi}{3} \left(\frac{2\pi f}{v_{water}}\right)^4 h_{rms}^2 l_x l_y \ , \qquad \text{(E.3)}$$

which is the formula printed as equation (6).

F. The reliability of the northern icelandic earthquake catalogue

The earthquake catalogue contains about ~120000 earthquakes from the SIL network (Rögnvaldsson, 1998) that were automatically picked since 1991. In the beginning of 1995, the mode of recording was altered and thus, it is not thought to be homogenous concerning the magnitudes. The SIL network uses the moment magnitude M_0 (Hanks and Kanamori, 1979) and the local magnitude M_l (Aki, 1966). The reliability of the data can be inferred from a summary plot of ZMAP (Wiemer and Zuniga, 1994) in Fig. F.1. The cumulative number of earthquakes increases with a constant slope since 1994, which increases only where strong earthquakes of magnitude 4 or higher occur (Fig. F2). The magnitude used for the catalogue is the moment magnitude M_0. The decisive information in the TFZ shrinks down to ~30000 quakes. The magnitude-frequency distribution can be considered linear from a magnitude of 1.5 up to 3.5, i.e. 2 scales which appears sufficient to determine the b-value. The lateral resolution since 1995 - i.e. of the large part of the data - is supposed to lie in the order of 10 m (Stefansson, 1999), which is similar to the GPS-NAV resolution of our seismic data, so they should be comparable. The lateral and vertical resolution decrease with rising distance to the SIL stations which are displayed in Fig. F1. The same applies to the vertical resolution of the data.

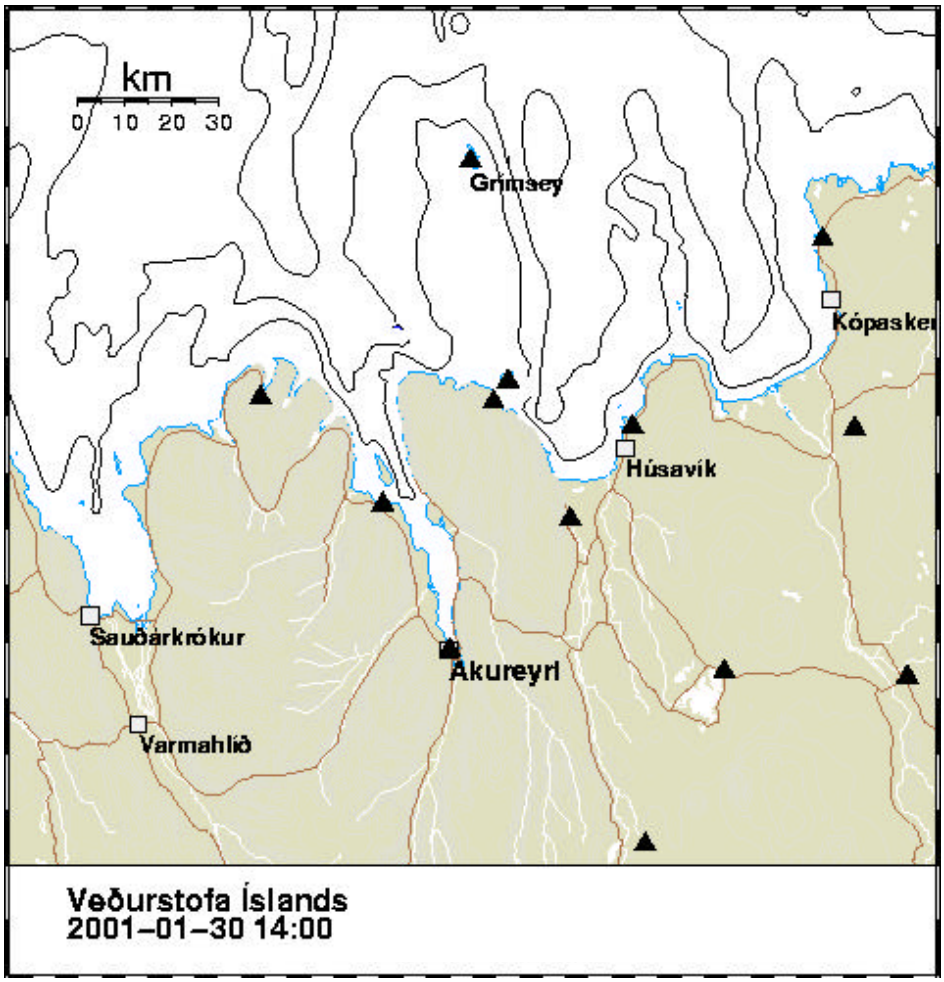

Figure F.1: *Graphics from Rögnvaldsson (1999). The SIL stations (black triangles) in the north cover the TFZ up to Grimsey, but were already used to determine dike intrusions up to 200 km from the is northernmost station (Riedel et al., 1999).*

In the TFZ, the hypocenters cease in a depth of 16-17 km which is similar to the crust-mantle boundaries discovered (Darbyshire et al., 2000) in Iceland, which is identical to the 1200°C

isotherm (Flovenz and Saemundsson, 1993) and not to the 800°C isotherm where earthquakes cease in oceanic environments (Bergman and Solomon, 1984).
These presented data were used to determine local b-values which include at least 100 quakes and span 2 magnitude orders (Wiemer and Zuniga, 1994) and to detect the 3D trend of fractures that were mapped outcropping on the seismic profiles, foremost between Grimsey, Kopasker (Melrakkasletta) and Husavik (Tjörnes), where five SIL stations are installed surrounding the region. Some of the results including the fault plane solutions were already published (Rögnvaldsson, 1998), the rest can be downloaded via Internet (http://hraun.vedur.is/cgi-bin/sellib).

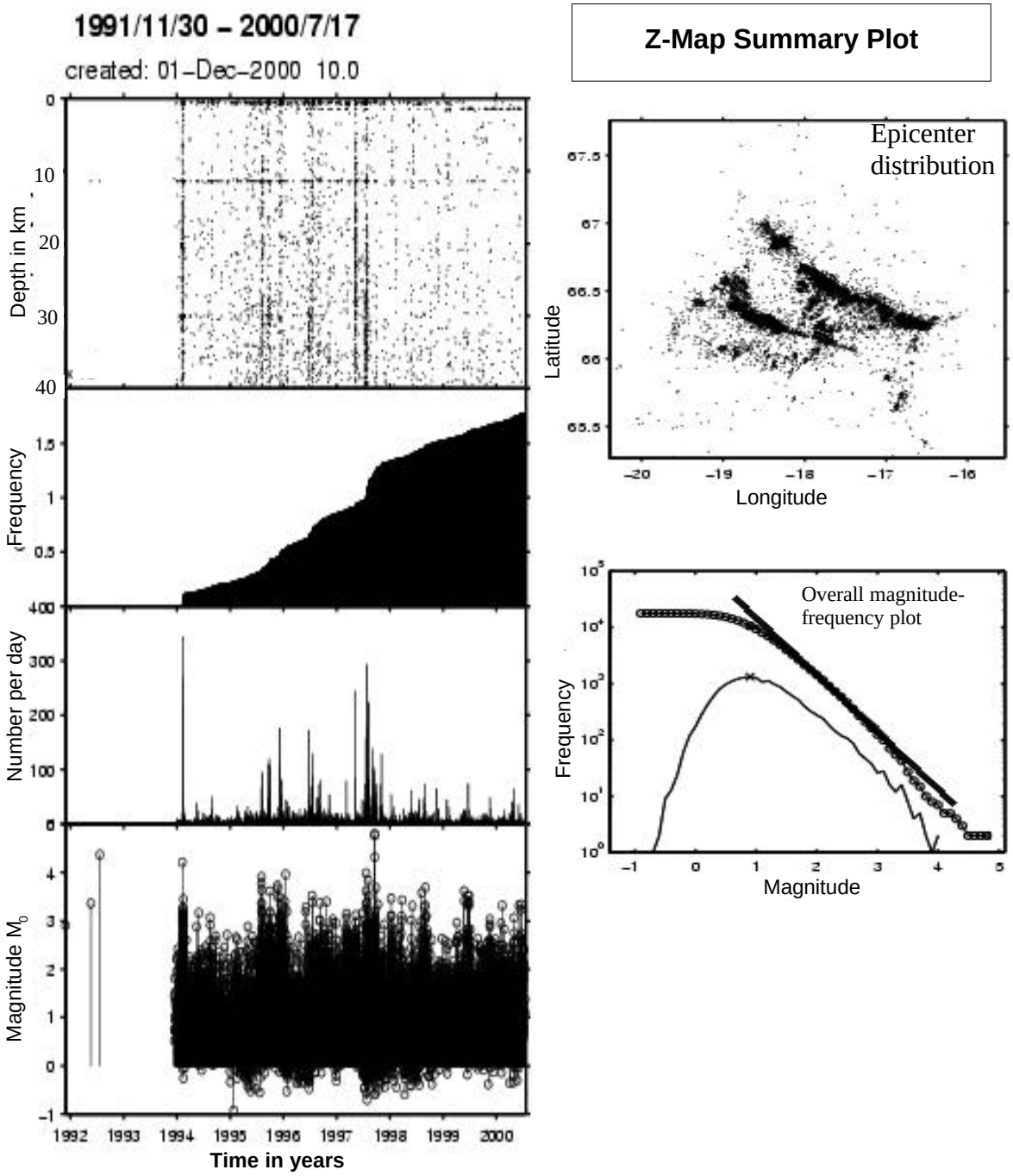

Figure F.2: *The cumulative number of earthquakes (here: frequency) increases constantly with time excluding periods when earthquakes of magnitude 4 or higher occur due to the number of aftershocks generated. The logarithmic magnitude-frequency plot shows a linear trend from magnitude 1.5 on, which is used in the b-value evaluation.*

G. The size of bubbles during collapse

When a bubble is rising from an external pressure p to a pressure of $p+dp$, the surface area A defined by angle q (Fig. G.1) will inflate to $A+dA$. The surface tension is defined by the tangential force dF and the offset ds of the surface A where it acts:

$$s = \frac{dF}{ds}. \qquad \text{(G.1)}$$

From an *actio=reactio* principle, it can be concluded for the pressure dp from inside the bubble:

$$dp = \frac{s}{dAds}. \qquad \text{(G.2)}$$

dA and ds can be derived from geometrical observations of a sector of a bubble of radius r (Fig. G1).

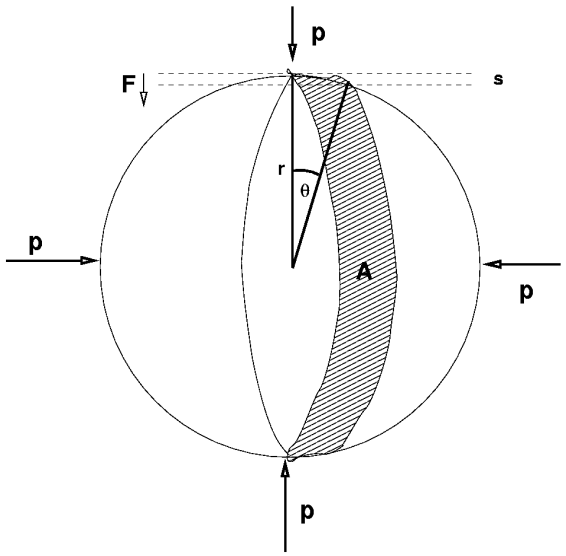

Figure G1*: Schematic plot of a bubble, where the external pressure p acts on the surface, resulting in a tangential force of F at an angle of q in every point of the surface, because p is always acting vertical to the bubble and thus the situation is circular symmetrical. For further analysis sectors of area A are evaluated.*

It can trivially be deducted:

$$s = r(1-\cos q), \qquad \text{(G.3)}$$

$$\text{i.e.} \quad \frac{ds}{dq} = r\sin q \quad \text{or} \quad ds = r\sin q dq. \qquad \text{(G.4)}$$

The surface A is evaluated as:

$$A = \frac{4pr^2}{q}, \qquad \text{(G.5)}$$

i.e. $$dA = A + dA - A = \frac{4p\,(r+dr)^2 - 4pr^2}{q}\,. \qquad \text{(G.6)}$$

This can be approximated as (assuming $rdr >> d^2r$):

$$dA = \frac{8prdr + 4pd^2r}{q} \approx \frac{8prdr}{q}\,. \qquad \text{(G.7)}$$

These results can be inserted into (F.2), resulting in:

$$dpr^2 dr \frac{\sin q dq}{q} = \frac{s}{8p}\,. \qquad \text{(G.8)}$$

Integrating from p_0 and r_0 to p and r and q along the circle from 0 to p follows as:

$$(p - p_0)\frac{1}{3}(r^3 - r_0^3)\int_0^p \frac{\sin q}{q} dq = \frac{s}{8p}\,. \qquad \text{(G.9)}$$

The remaining integral can only be solved numerically as (Bronstein, 1991):

$$\int_0^p \frac{\sin q}{q} dq = p - \frac{1}{18}p^3 + \frac{1}{600}p^5 - \frac{1}{5040}p^7 + \ldots \approx \frac{p}{2}\,. \qquad \text{(G.10)}$$

Thus, the radius of a rising bubble is given by:

$$r^3 = r_0^3 + \frac{3s}{4(p - p_0)}\,. \qquad \text{(G.11)}$$

The characteristic radius r_c is defined and calculated as the average radius of bubbles between the seafloor and the collapse depth here. The radius of bubbles at the sea floor was estimated to be ~1 *mm*, when they leave the hydrothermal vents (M. Schmidt, personal communication).

$$r_c^3 = \frac{1}{2MPa}\int_{2MPa}^{4MPa}(r_0^3 + \frac{3s}{4(p - p_0)})dp = \frac{1}{2MPa}\left[r_0^3 p + \frac{4}{3s}\ln\frac{3s}{4(p - p_0)}\right]_{2MPa}^{4MPa} = 2\ mm^3, \qquad \text{(G.12)}$$

i.e r_c=1.26 *mm.*

H. Modelling seismic data

Because the influence on the amplitude of the FRA is so manifold, there is need for modelling an idealized reflection. During the course of this thesis a finite-difference wave-field modelling algorithm created by Bohlen (1998) was applied. The algorithm can either be performed on 2D- or 3D-grids and allows elastic or viscoelastic modelling. These are 2 out of 3 commonly used models for the water-solid boundary at the sea floor:

- *acoustic:* only compressional waves propagate through water and the solid, i.e. the interface borders two domains which can be described by density ρ and compressional wave velocity v_p alone and thus no energy can be lost by converted shear waves of velocity v_s. This is usually valid for soft sediments where v_s->0.
- *elastic:* both media may be described by elastic properties of compression and shear. This is valid in case both media are solid. In case one of the domains does not allow shear (e.g. water) problems were reported for Finite-Difference algorithms.
- *viscoelastic:* both media are additionally described by absorption loss. In the case of a sea water-solid interface, Riedel (1998) showed there is a small influence on sediments. The amplitude I is further reduced by attenuation α of the wave energy in the water column in comparison to the source amplitude I_0. This is a frequency (f)-dependent effect, often expressed in terms of the quality factor Q and the wavelength l, which can be recalculated as frequency by applying the wave velocity v:

$$I=I_0 e^{-akt} \quad with \quad a=\frac{p}{Q\,l}=\frac{pf}{Qv}. \qquad (H.1)$$

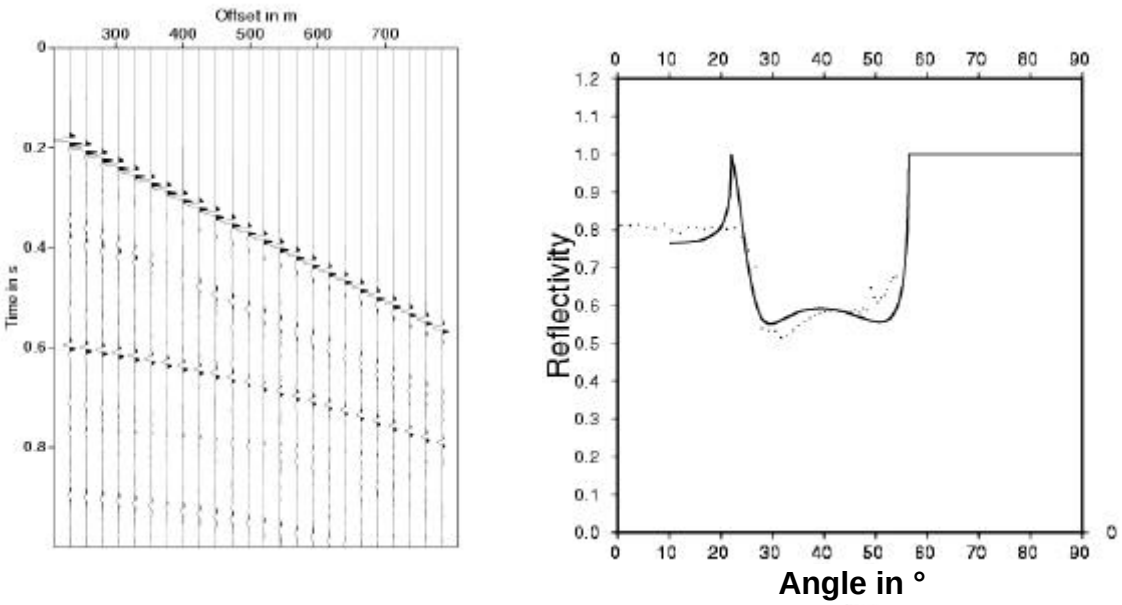

A ***B***

Figure H1: *Some typical CMP gathers (A) modelled at 50 Hz by the elastic FD-algorithm of Bohlen (1998) were picked (dots on B) and compared to the expected Zoeppritz reflectivities (line on B). They fit well in angles greater than 20°.*

The viscoelastic wave equation can be solved by assuming continuity of stress and dislocation, i.e. continuity of shear and pressure forces (Bohlen, 1998). An elastic 2D-algorithm was used on a flat seafloor in Fig. G1. Idealized boundary conditions of the survey in Iceland were used,

i.e. incidence angles ϑ in between 15° and 50°, a water depth of 400 m and a moderately hard anhydritic sea floor, i.e. v_p=4km/s, v_s=1.8km/s and ρ=2.8 km/s were used beneath the seawater column of v_p=1.473 km/s , v_s=0 km/s (no shear waves) and ρ=1.025kg/m^3. A CMP gather is displayed in Fig.H1A. In Fig. H1B the reflectivity versus angle gather from picking the second positive phase of the Ricker wavelet and the expected values calculated from the elastic Rayleigh approximation (Appendix D) are depicted. The dominant frequency was 50 Hz. The trend of the finite-difference algorithm is very similar to the Zoeppritz curve, but the critical angle could not be imaged.
The theory suggested that Zoeppritz might work well only in high frequencies, since ray theory is a high-frequency approximation of the wave-field. So, the same model was evaluated in higher frequencies. It turned out that the imaging of the first critical angle is improved by using a higher dominant frequency (Fig. H2). This result supports the findings of Cerveny (1967), that critical angles cannot be resolved in low frequencies. He observed that the modelling results do only approximate the results in the critical range of ray theory, if z/λ, i.e. the ratio of reflector depth to dominant wavelength, is high. That can be obtained by using high frequencies and/or large offsets. So, not only roughness estimates and thin layer resolution can be improved by using high frequencies, but even reflectivity is more characteristic of lithology in higher frequencies.

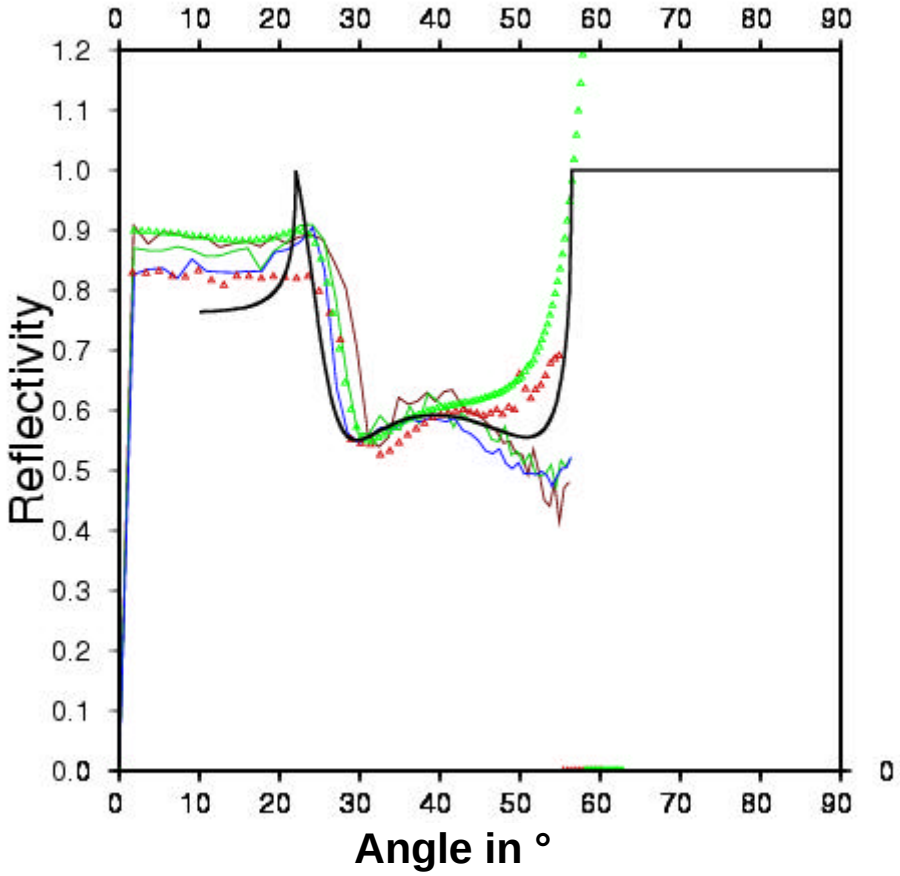

Figure H2: *Five curves show the modelled reflectivity from the main positive phase of a flat layer by MSEIS (at 50 Hz (red line), 100 Hz (green line) and 200 Hz (blue line) dominant frequency) and FD-Modelling (Bohlen, 1998) (at 50 Hz, red triangles and at 100 Hz, yellow triangles). None of them can fully resolve the first critical angle.*

I. Typical AVO gathers of the principal classes

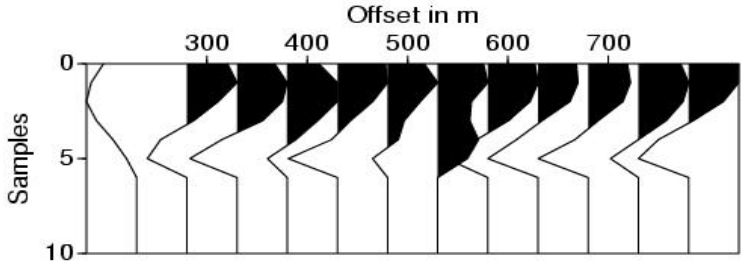

Red class: *Loose sediments, amplitude stays similar throughout.*

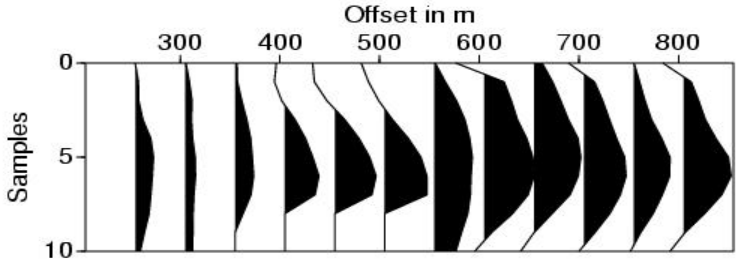

Yellow class: *Igneous rocks, amplitudes rise quickly and stay similar.*

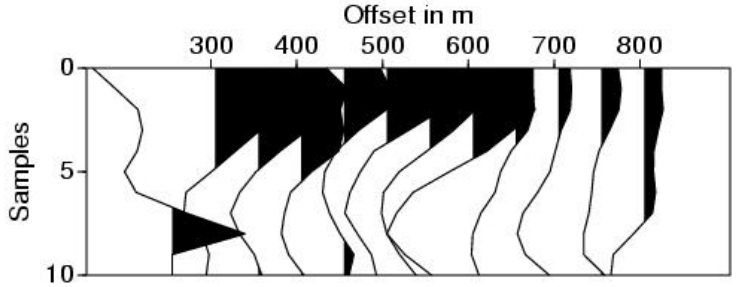

Cyan class: *Amplitudes is on a high level and falls towards higher offset, the signal is complex and cannot be picked in a reasonable way automatically.*

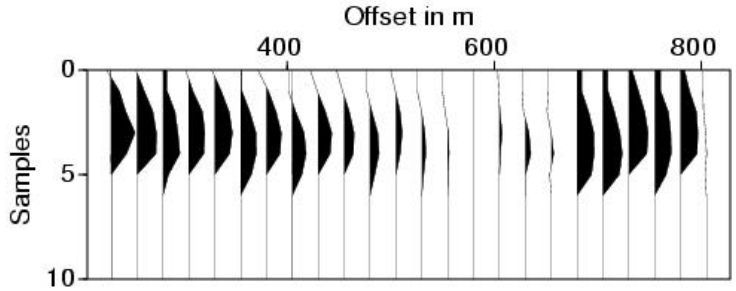

Orange class: *Ampliudes fall on a low level in mid-range offsets and rise again towards higher offset.*

Note: The blue class was represented in the text. CMPs include either 12 or 24 channels, depending on firing rate, but they cover the same offsets.

K. List of symbols (used in this thesis)

1. Small letters

a	proportionality constant of Gardner's rule
c_f	compressibility of water
d	damping constant of air
d	depth of reflector
d	internal spacing of hydrophones in group
ds	infinitesimal offset of force
dp	infinitesimal pressure
eff	streamer effect function
f	frequency
g,h	quadrature mirror filters of wavelet transform
h	thickness of thin layer
h_{rms}	roughness (root-mean-square deviation from planar surface)
i	impulse function
k	wave number
$k_{r,i}$	real and imaginary part of Young modulus of seawater
l_y,l_x	correlation lengths of undulations on a rough surface
m	arbitrary natural number
n	noise function
n	volume fraction of gas
o	output function of source
p	pressure
p	propagation function
p	momentum
p(x)	gridded reflectivity vector
r	reflectivity function
r	radius of bubble
r_c	characteristic bubble radius
r_{max}	maximum neighbour radius
r_i	maximum neighbour radius after i steps
s	recorded signal operator
sur	surface effect function
t	time
t_{zero}	time of first arrival at nearest offset
t_{hype}	time of first arrival at various offsets
v	wave velocity
v_p	P-wave velocity of seismic waves in some medium
v_s	S-wave velocity of seismic waves in some medium
v_{thin}	p-wave velocity in thin layer
v_{water}	acoustic wave velocity in water
w_i	weight vector of neural network
x_i	input vector of neural network
x,y,z	spatial coordinates
x	offset
x_n	nearest offset
y	raypath after scattering
z	acoustic impedance
z_p	p-wave impedance of seafloor
z_s	s-wave impedance of seafloor

z_{water} acoustic impedance of water

2. Capital letters

A area
CF coherence function
D number of grid angles of reflectivity vector
DWT discrete wavelet transform
DWPT discrete wavelet packet transform
dF infinitesimal tangential force
I amplitude
dI infinitesimal amplitude change
I_0 initial amplitude
I_{FRA} first reflected arrival amplitude
I_{DIR} direct wave amplitude
I_x first reflected arrival amplitude at offset x
<I> average amplitude
N number of hydrophone groups
O(x) output vector of neural network
P power spectrum
$P_{stacked}$ stack of power spectra of reflector signals
$P_{average}$ power spectrum of stacked reflector signals
Q quality factor
R reflectivity

3. Greek letters

α attenuation coefficient
β dip angle
γ term of coherence function
$\delta^{13}C$ isotopic ratio of $^{13}C/^{12}C$ in CH_4
κ_g young modulus of gas bubbles
ϑ incidence angle
ρ density
ρ_{floor} density of seafloor medium
ρ_{water} density of water
σ surface tension
ϕ phase of second reflection in contrast to first reflection
θ angle for polar coordinates of bubble
ζ angle close to 90°
λ wavelength of seismic wave
μ backscatter coefficient
ω_0 dominant or resonance (circular) frequency

L.Index of figures

Chapter 1

Chapter 2

Chapter 3

References:

E. Adam, G. Arnold, C. Beaudry, L. Matthews, B. Milkereit, G. Perron, R. Pineault, 1997, Seismic exploration for VMS deposits, in: A.G. Gubins, 1997, Proceedings of Exploration 97: Fourth Decennial International Conference on Mineral Exploration

K. Aki, 1966, Generation and propagation of G waves from the Niigata earthquake of June 16, 1964. Part 2. Estimation of earthquake moment, release of energy, and stress-strain drop from G wave spectrum: University of Tokyo, Earthquake Research Institute Bulletin, v. 44, pt. 1, p. 73-88.

K. Aki, P. Richards, 1980, Quantitative seismology, W.H. Freeman Co.

J. Árnarson, 1960, Islenskar Þjoðsögur og ævintyri (in icelandic), Vol. 4, 119

A. Ayres, F. Theilen, 1999, Relationship between P- and S-wave velocities and geological properties of near-surface sediments of the continental slope of the Barents Sea, Geological Prospecting, 47, 431-441

N.E. Bakke, B. Ursin, 1998, Thin-bed AVO effects, Geophysical Prospecting, 46, 6, 571-588

C.A. Barton, M.D. Zoback, D. Moos, 1995, Fluid flow along potentially active faults in crystalline rock, Geology, 23, 683-686

D. Beanouda, G. Wadge, R.B. Whitmarsh, I.G. Rothwell, C. MacLeod, 1999, Inferring the lithology of borehole rocks by applying a neural network classfier to downhole logs: an example from the Ocean Drilling Program, Geophys. Jour. Int., 136, 477-491

E.A. Bergman, S.C. Solomon, 1984, Source mechanisms of earthquakes near mid-ocean ridges from body waveform inversion; implications for the early evolution of oceanic lithosphere, J. Geophys. Res., 89, B13, 11415-11441

M.E. Berndt, D.E. Allen, W.E. Seyfried, 1996, Reduction of CO2 during serpentinization of olivine at 300°C and 500 bar, Geology, 24, 351-354

T. Bohlen, 1998, Viskoelastische FD-Modellierung seismischer Wellen zur Interpretation gemessener Seismogramme (in german), Dissertation, University of Kiel

H. Bougault, J.L. Charlou, Y. Fouquet, H.D. Needham, N. vaslet, P. Appriou, P.J. Baptiste, P.A. Rona, L. Dmitriev, S. Silantiev, Fast and slow spreading ridges: structure and hydrothermal activity, ultramafic topographic highs and CH_4 output, 1993, J. Geophys. Res., 98, B6, 9643-9651

R. Botz, G. Winckler, R. Bayer, M. Schmitt, M. Schmidt, D. Garbe-Schönberg, P. Stoffers, J.K. Kristjansson, 1999, Origin of trace gases in submarine hydrothermal vents of the Kolbeinsey Ridge, north Iceland, EPSL, 171, 83-93

K. Breddam, M.D. Kurz, M. Storey, 1999, Mapping out the conduit of the Iceland plume by with helium isotopes, Eart Plan. Sci. Lett., 176, 1, 45-55

H.-J. Brink, 1980, Das Gescgwindigkeits-, Reflexions- und Dämpfungsverhalten streuender elastischer Systeme anhand von Beispielen, Dissertation, University of Kiel

A. Broser, 2000, AVO-Untersuchungen des Meeresbodens nördlich von Island (in german), Diplomarbeit, University of Kiel

C.H. Bruce, 1973, Pressured shale and related sediment deformation, Am. Assoc. Pet. Geol. Bull., 57,878-886

B.A. Brunson, E.G. Mc Leroy, C.W. Holland, R.K. Hagg, 1985, Acoustic Sea Bottom Classification: A Requirement Analysisi, Planning Systems, Inc., Technical Report, 335313

P.J. Burt, W.W. Crouch, 1972, The logarithmic dependance of surface generated

ambient sea noise spectrum level on wind speed, J. Acoust. Soc. Am., 51, 1066-1072
D.A. Butterfield, 2000, Deep ocean hydrothermal vents, in EOV
C. Calderon-Macias, M.K. Sen, P.L. Stoffa, 2000, Artificial neural networks for parameter estimation in geophysics, Geophysical Prospecting, 48, 21-48
M. Cannat, C. Mével, M. Maia, 1995, Thin crust, ultramafic exposures and rugged faulting patterns at the Mid-Atlantic ridge (22°-24°N), Geology, 23, 49-52
R.S. Carmichael, 1982, Handbook of physical rock properties, CRC Press, Inc., Florida
J.P. Castagna, M. Backus, 1993, Offset-Dependent Reflectivity - Theory and practice of AVO analysis, SEG
V. Cerveny, 1967, The Amplitude-Distance curves for Waves reflected at a Plane Interface for Different Frequency Ranges, Geophys. J.R. Astron. Soc., 13, 187-196
R.D.Chapman, H.D. Scott, 1964, Backscattering Strength Measurements over an extended range of frequencies and grazing angles, J. Acoustic. Soc. Am., 36, 1735
C. Chauvel, C. Hemond, 2000, Melting of a complete section of recycled oceanic crust: Trace element and Pb isotopic evidence from Iceland, G-cubed, 1
W.B. Clarke, W.J. Jenkins, Z. Top, 1976, Determination of tritium by mass spectrometric measurement of ^{3}He (and atmospheric $^{3}He/^{4}He$ ratio), Inter. Jour. Of Appl. Rad. And Isotopes, 27, 515-522
J.K. Cohen, J.J.W. Stockwell, 1998, CWP/SU: Seismic Unix Release 32: a free package for seismic research and processing, Center for Wave Phenomena, Colorado School of Mines (1998)
J.C. Crowell, 1974, Sedimentation along the San Andreas Fault, California in: R.H. Dott, R.H. Shaver, Modern and ancient geosynchlinal sedimentation, Soc. Econ. Pal. Mineral. Spec. Pub., 22, 190-204
M.J. Daines, 2000, Migration of Melt in EOV
F.A. Darbyshire, K.F. Priestley, R.S. White, R. Stefansson, G.B. Gudmundsson, S.S. Jakobsdottir, 2000, Crustal structure of central and northern Iceland from analysis of teleseismic receiver functions, Geophys. J. Int. 143, 1, 163-184
I. Daubechies, 1988. Orthonormal bases of compactly supported wavelets, Communications on pure and applied mathematics, XLI:909-996
I. Daubechies, 1992, Ten Lectures on wavelets, Regional Conference Series in Applied Mathematics, SIAM Press, Philadelphia, 61
A.J. Deighan, 1997, PhD thesis, University of Glasgow
A.J. Deighan, D.R. Watts, C. Riedel, 1998, Wave swell noise suppression using a wavelet packet transform", Session 2-56, EAGE Extended Abstracts, 60 th Conference, Leipzig, 1998
R.S. Detrick, R.S. White, G.M. Purdy, 1993, Crustal structure of North Atlantic fracture zones, Rev. Geophys., 31, 439-457
C. Devey, M. Krienitz, F. Lichowski, H. Möller, J. Pracht, M. Zimmerer, 1997, Cruise report R/V Poseidon 229b
Devey, 1993, Structure and volcanism of the Mid-Atlantic Ridge within the Tjörnes Fracture Zone north of Iceland, Cruise report 185/3 b, R/V Poseidon
S.N. Domenico, 1982, Acoustic wave propagation in air-bubble curtains in water-Part I: history and theory, Geophysics, 47, 345-353
D. Donoho, I. Johnstone, G. Kerkyacharian, D. Picard, 1993, Density estimation by wavelet thresholding, Technical report, Department of Statistics, Stanford University
W.H. Dragoset, N. Hargreaves, K. Larner, 1986, Air gun source instability and shot-

by-shot signature deconvolution, Geophysics. 51, 858-859
W.H. Dragoset, 1990, Air-gun array specs: A tutorial, The leading edge, 24-32
A.D. Dunsiger, N.A. Cochrane, W.J. Vetter, 1981, Seabed characterization from Broad-Band Acoustic Echosounding with Scattering Models, IEEE J. Ocean. Eng., 6, 94-106
C. Eckart, 1953, The scattering of sound from the sea surface, J. Acoust. Soc. Am., 25, 566-570
J.M. Eiler, K. Grönvold, N. Kitchen, 2000, Oxygen isotope evidence for the origin of chemical variations in lavas from Theistareykir volcano in Iceland's northern volcanic zone, Earth Planet. Sci. Lett. 184, 269-286
P. Einarsson, 1976, Relative location of earthquakes in the Tjörnes Fracture Zone, Soc. Sci. Iceland, 32, 1-79
J. Eiríksson, A. Gudmundsson, L. Kristjánsson, K. Gunnarsson, 1990, Palaeomagnetism of Pliocene-Pleistocene sediments and lava flows on Tjörnes and Flatey, North Iceland, Boreas, 19, 39-55
EOV: H. Sigurdsson, B. Houghton, S.R. McNutt, H. Rymer, J. Styx, 2000, Encyclopedia of Volcanoes, Academic Press
Fan, 1990
K. Fjäder, A. Gudmundsson, T. Forslund, 1994, Dikes, minor faults and mineral veins associated with a transform fault in North Iceland, Jour. Struct. Geol. , 16, 1, 109-119
Ó.G. Flóvenz, K. Gunnarson, 1991, Seismic crustal structure in Iceland and surrounding area, Tectonophysics, 189, 1-17
Ó.G. Flóvenz, K. Saemundsson, 1993, Heat flow and geothermal processes in Iceland, Tectonophysics, 225, 123-138
G.H.F. Gardner, L.W. Gardner, A.R. Gregory, 1974, Formation velocity and density - the diagnostic basis for stratigraphic traps, Geophysics, 39, 770-780
C.R. German, J. Briem, C. Chin, M. Danielsen, S. Holland, R. James, A. Jonsdottir, E. Ludford, C. Moser, J. Olafsson, M.R. Palmer, M.D. Rudnicki, 1994, Hydrothermal activity on the Reykjanes Ridge; the Steinaholl vent-field at 63 degrees 06'N, Earth. Planet. Sci. Let., 121, 647-654
D.W. Graham et al., 1998, Helium isotope composition of the early Iceland mantle plume inferred from the Tertiary picrites of West Greenland, Earth Planet. Sci. Lett. 160, 3-4, 241-255
H.J. Grubb, A.T. Walden, 1997, Characterizing seismic time series using the discrete wavelet transform, Geophysical Prospecting, 45, 183-205
T. Gudjonsson, 1999, The Parliament Plains of Iceland, Reykjavík
A. Gudmundsson, S. Brynjolfsson, M.T. Jonsson, 1993, Structural analysis of a transform fault-rift zone junction in North Iceland, Tectonophysics, 220, 205-221
K. Gunnarsson, M. Kjartansdóttir, J. Eiríkson, L. Símonarsson, 1984, Rannsóknarborunn í Flatey á Skjálfanda (in icelandic), Orkostofnun, Reykjavík, OS-84052/JHD-10
D. Halliday, R. Resnick, 1977, Physics I, 3rd edition, Wiley & Sons, New York
D. Halliday, R. Resnick, 1986, Physics II, 3rd edition, Wiley & Sons, New York
Hampson-Russell Software, 1997, Amplitude Versus Offset Analysis, Manual
T.C. Hanks, H. Kanamori, 1979, A moment magnitude scale: Journal of Geophysical Research, v. 84, no. BS, p. 2348-2350.
M. Hannington, P. Herzig, P. Stoffers, J. Scholten, D. Garbe-Schönberg, I.R. Jonasson, W. Roest and the Shipboard Scientific Party, First High-Temperature

submarine hydrothermal vents and massive anhydrite deposits off the north coast of Iceland, submitted to Marine Geology
J.J. Hanrahan, 1980, A perspective on bottom reflectivity and backscattering, in: Kuperman and Jensen, Bottom interacting ocean acoustics, NATO conference series: IV, Marine Sciences, 5
W. Hansen, 1985, Asgard (in german), Bastei-Lübbe, Bergisch-Gladbach
T.P. Harding, 1985, Seismic characteristics of negative flower structures, positive flower structures and positive structural inversion, Bull. Am. Assoc. Petrol. Geol., 69, 582-600
O.F. Hastrup, 1980, Some bottom-reflection loss anomalies near grazing and their effect on propgation in shallow water, in: Kuperman and Jensen, Bottom interacting ocean acoustics, NATO conference series: IV, Marine Sciences, 5
L. Hatton, 1986, Weather and the 3-microbar limit on the North-West European continental shelf, First Break, 8, 1986
G.C. Herman, B. Blonk, 1990, Influence of Small-Scale Interface Roughness in the Estimation of lithologic parameters from reflection coefficients, SEG Expanded Abstracts, 1475-1478
P. Herzig, Hydrothernalismus am Kolbeinseyrücken, Antrag auf BmBF-Förderung, 1999
B.B. Hubbard, 1995, Ondes et Ondelettes (in french), Pour la science, Paris
S.E. Ingebritsen, W.E. Sanford, 1998, Groundwater in geologic processes, Cambridge University Press
S.E. Ingebritsen, M.A. Scholl, 1993, The hydrogeology of Kilauea volcano, Geothermics, 222, 255-270
D.R. Jackson, D.P. Winebrenner, A. Ishimaru, 1986, Application of the composite roughness model to high-frequency bottom backscattering, Journ. Acoust. Soc. Am., 79, 5, 1410-1422
H. Johannesson, K. Saemundsson, 1998, Geological Map of Iceland, Bedrock Geology, Icelandic Institute of Natural History, Reykjavik
P. Johnson, Magnetic surveys of Iceland, Tectonophysics, 189 (1991) 246-263
P. Keary, F.J. Vine, 1996, Global tectonics, 2nd edition, Blackwell Science
T. Kohonen, 1997, Self-Organizing Maps, Springer, Berlin
T. Kohonen, 1982, Self-organized formation of topologically correct feature maps. Biological Cybernetics, 43, 59-69.
M.D. Kurz, P.S. Meyer, H. Sigurdsson, 1985, Helium Isotope systematics within the neovolcanic zone of Iceland, Earth Plan. Sci. Lett., 74, 291-305
K.S. Lakschewitz, H.J. Wallrabe-Adams, 1991, Composition and origin of sediments on the mid-oceanic Kolbeinsey Ridge, north of Iceland, Marine Geology, 1001, 71-82
D.N. Lambert, 1988, An evaluation of the Honeywell ELAC Computerized Sediment Classification System, Naval and Ocean Research and Develeopment Activity, 169
B.O. Långbacka, A. Gudmundsson, 1995, Extensional tectonics in the vicinity of a transform fault in north Iceland, Tectonics, 14, 2, 294-306
K. Larner, R. Chambers, M. Yang, W. Lynn, W. Wai, 1986, Coherent noise in marine seismic data, geophysics, 48, 854-886
I. Lerche, N.R. Hill, 1985, A mean-field solution of the reflection of a spherical acoustic wave from a rough interface, J. Math. Phys. 26, 1420-1427
Y. Linde, A. Buzo, R.M. Gray, 1980, An algorithm for vector quantizer design, IEEE Transactions on Communications, 28, 84-95

L. Lin, R. Phair, 1993, AVO tuning, SEG Expanded Abstracts, 727-730
J. Ludwig, J. Nafe, C. Drake, 1971, Seismic refraction in: A.E. Maxwell, The sea, 4, Wiley, New York, 53-84
R.J. Ludwig, G.J. Iturrino, P.A. Rona, 1998, Velocity-Porosity-relationship of Sulfate, Sulfide and Basalt samples from the TAG Hydrothermal Mound, in: P.M. Herzig, S.E. Humphris, D.J. Miller, R.A. Zierenberg, Proceedings of the Ocean Drilling Program, Scientific results, 158, 313-327
K.C. Macdonald, D.A. Castillo, S.P. Miller, P.J. Fox, K.A. Kastens, E.Bonatti, 1986, Deep-tow studies of the Vema fracture zone; 1, Tectonics of a major slow slipping transform fault and its intersection with the Mid-Atlantic Ridge, J. Geophys. Res., 91, 3334-3354
N. Maercklin, 1999, Polarisationsanalyse refraktionsseismischer Daten vom Vulkan Merapi, Indonesien (in german), Diploma Thesis, University of Kiel
S. Mallat, 1989, A theory for Multiresolution Signal Decomposition: the wavelet representation, IEEE Transactions on pattern analysis and machine intelligence, 11, 7
W.S. McCulloch, W. Pitts, 1943, A logical calculus of the ideas immanent in nervous activity, Bull. Math. Biophys., 5, 115-133
Malmis, 1990, Gold Occurences in Iceland, http://www.tv.is/melmi/occur.html
R L. McMaster, J.-G.E. Schilling, P.R. Pinet, 1977, Plate boundary within Tjörnes Fracture Zone on northern Iceland's insular margin, Nature, 269, 663-667
R. Meißner, L. Stegena, 1977, Praxis der seismischen Feldmessung (in german), Studienhefte zur angewandten Geophysik, 1, Budapest
D.F. Mertz , C.Devey, W. todt, P. Stoffers, A.W. Hofmann, 1991, Sr-Nd-Pb isotope evidence against plume-asthenosphere mixing north of Iceland, Earth. Planet. Sci. Let., 107, 243-255
O. Meyer, D. Voppel, U. Fleischer, H. Closs, K. Gerke, 1972, Results of bathymetric, magnetic and gravimetric measurements between Iceland and 70°N, Deutsche Hydrograph. Zeit., 25, 193-201
P.J. Michael, W.C. Cornell, 1998, Influence of spreading rate and magma supply on crystallization and assimilation beneath mid-ocean ridges: Evidence from chlorine and major element chemistry of mid-ocean ridge basalts, J. Geophys. Res., 103, 18325-18356
M. Mochizuki, S. Kodaira, H. Shiobara, H. Shiamura, B. Brandsdottir, E. Sturkell, G. Gudmundsson, R. Stefansson, 1995, Seismicity in the Tjörnes Fracture Zone off North Iceland, Derived from an OBS observation (in japanese)
R. Muckelmann, 1985, Theoretische und experimentelle Untersuchungen von P- und
C. Müller, W. Jokat, 2000. Seismic evidence for volcanic activity discovered in central Arctic, EOS Transactions, 265-269
S-Wellen in Sanden unter besonderer Berücksichtigung ihrer Dämpfungseigenschaften (in german), PhD Thesis, Universität Kiel
S. Neben, 1992, Der Aufbau des südlichen Kolbeinseyrückens (in german), Dissertation, University of Kiel
M. Nettles, G. Ekström, 1998, Faulting mechanisms of anomalous earhtquakes beneath Bardarbunga Volcano, Iceland, J. Geophys. Res., 103, 17973-17983
C.L. Nicholson, L. Steeber, P. Williams, L.R. Sykes, 1986, Seismicity and fault kinematics through the Eastern Transverse Ranges, southern California: block rotation, strike-slip faulting and low-angle thrusts, J. Geophys. Res., 81, 4891-4908
R. Oehmig, H.J. Wallrabe, 1993, Hydrodynamic properties and grain-size

characteristics of volcaniclastic deposits on the Mid-Atlantic Ridge north of Iceland (Kolbeinsey Ridge), Jour. Sed. Petrol., 63, 140-151
J. Olafsson, K. Thors, U. Stefansson, S.P. Jakobsson, W.J. Jenkins, G. Thompson, S. Honjo, F.T. Manheim, R.F. Commeau, R.R. Jones, 1990, Geochemical observations from a boiling hydrothermal site on the Kolbeinsey Ridge, EOS 71, 1650
G. Parkes, L. Hatton, 1986, The marine seismic source, D. Reidel Publishing
G. Pálmason, 1974, Insular margins of Iceland, In: Eds. C.A. Burke, C.L. Drake, Geology of Continental Margins, Springer, New York, 375-379
M.R. Perfit et al., 1996, Recent volcanism in the Siqueiros transform fault: picritic basalts and implications for MORB magma genesis, Earth Planet. Sci. Lett. 14, 91-108
M.R. Perfit, J.P. Davidson, 2000, Plate tectonics and volcanism, in: EOV
T. Petersen, 2000, Anzeichen für eine Magmakammer nördlich von Island, Diploma Thesis, University of Kiel
H. Péturss, 1959, The earthquakes in northern Iceland and the gology of Iceland (in icelandic), In: Ed. V.Þ. Gíslason, Ferðabók, Reykjavík, 221-222
C.L. Piggott, 1964, Ambient sea noise in low frequencies in shallow water of the Scotian Shelf, J. Acoust. Soc. Am., 36, 2152-2163
R.J. Poreda, H. Craig, S. Arnorsson, J.A. Welhan, 1992, Helium isotopes in Icelandic geothermal systems, I, ^{3}He, gas geochemistry and ^{13}C relations, Geochim. Cosmochim. Acta, 56, 4221-4228
R. Poreda, H. Craig, J.G. Schilling, 1986, Helium and hydrogen isotopes in ocean ridge basalts north and south of Iceland, EPSL, 78, 1, 1-17
W.H. Press, S.A. Teukolsky, W.T. Vetterling, B.P. Flannery, 1992, Numerical recipes in C, 2nd edition, Cambridge University Press, Cambridge
G.W. Purnell, Y. Shin, G. Hampson, J.A. McDonald, 1990, Effects of Interface roughness on wave propagation, SEG Expanded Abstracts, 1561-1564
C.B. Raleigh, J.H. Healy, J.D. Bredehoeft, 1976, An experiment in earthquake control at Rangely, Colorado, Science, 191, 1230-1236
Lord Rayleigh, 1886, The Theory of Sound, 2nd ed., Macmillan, London
C. Reimers, K.S. Lakschewitz, C. Stolte, H.J. Wallrabe-Adams, 1989, Morphologie, Struktur und Sedimentverteilung (in german) in: Cruise report R/V Poseidon 175, GEOMAR, 11
M. Riedel, 1998, AVO/AVA-Untersuchungen an flachmarinen Sedimenten, Diploma Thesis, University of Kiel
C. Riedel, F. Theilen, 2000, BmBF Abschlußbericht zum Projekt "Hydrother-malismus am Kolbeinseyrücken"
C. Riedel, Vedurstofa Islands, Kolbeinsey Ridge: Submarine eruption or dike intrusion south of the Spar Fracture Zone, Bull. Global Volc. Network, 24
C. Riedel, F. Theilen, A. Broser, T. Petersen, M. Schmidt, 2000, Constraining seismic data by geological boundary conditions in a hydrothermal environment, AGU Fall Metting 99, EOS Transactions
O. Rioul, M. Vetterli, 1991, Wavelets and signal processing, IEEE SP Magazine, 14-37
R. Rojas, 1995, Theorie der neuronalen Netze, Springer Verlag, Berlin
D. Ross, 1976, Mechanics of underwater noise, Pergamon Press
S.T. Rögnvaldsson, 1998, Seismotectonic analysis of the Tjörnes Fracture Zone, an active transform fault in north Iceland, JGR, 103, B12, 30117-30129
S.T. Rögnvaldsson, 1999, http://hraun.vedur.is

W.W. Rubey, M.K. Huppert, 1959, Role of fluid pressure in mechanics of overthrust faulting. II. Overthrust belt in geosynclinal area of western Wyoming in light of fluid-pressure hypothesis, Geol. Soc. Am. Bull., 70, 167-206
A.D. Saunders, H.C. Larsen, J.G. Fitton, 1998, Magmatic development of the southeast Greenland Margin and evolution of the Iceland Plume: geochemical constraints from Leg 152, pp. 479-502 in: Saunders, A.D., Larsen, H.C., and Wise, S.W., Jr. (Eds.), 1998. Proc. ODP, Sci. Results,152: College Station, TX (Ocean Drilling Program).
K. Saemundsson, 1974, Evolution of the Axial Rifting Zone in Northern Iceland and the Tjörnes Fracture Zone, GSA Bulletin, 85, 495-504
K. Saemundsson, Á. Hjartarson, 1994, Geology and erosion of Kolbeinsey North Iceland, In: Proceedings of the Hornafjördur International Coastal Symposium, Ed. Gísli Viggóson, Reykjavík
M.H. Salisbury, B. Milkereit, W. Bleeker, 1996, Seismic Imaging of Massive Sulphide Deposits: Part I. Rock Properties, Economic Geology, 91, 821-828
D.T. Sandwell, W.H.F. Smith, S.M. Smith, C. Small, 1997, Measured and estimated sea floor topography, http://topex.ucsd.edu
D.T. Sandwell, W. H. F. Smith, 1998, Marine gravity anomaly from Geosat and ERS 1 satellite altimetry, Journal of Geophysical Research, 102, 10039-10054
J.G. Schilling, R. Kingsley, D. Fontignie, R. Poreda, S. Xue, 1999, Dispersion of the Jan Mayen and Iceland mantle plumes in the Arctic: a He-Pd-Nd-Sr isotope tracer study of basalt from the Kolbeinsey, Mohns and Knipovich ridges, Jour. Geophys. Res., 104, 5, 10543-10569, 1999
J. Scholten, F. Theilen, P. Herzig, M. Schmidt, Shipboard Scientific Party, 1999, Hydrothermal activity along the Tjoernes Fracture Zone, north of Iceland: Initial results of R/V Poseidon cruises 252 and 253, Interridge News 8, v.2, 28-31
H.U. Schmincke, 1999, Vulkanismus, Verlag
M.I. Scranton, P.G. Brewer, 1978, Consumption of dissolved methane in the deep ocean, Limnology and Oceanography, 23, 1207-1213
R.E. Sheriff, 1975, Factors affecting seismic amplitudes, Geophysical Prospecting, 13, 125-138
Shell, 2000, http://www.smds.shell.nl/smds/6.html
R.T. Shuey, 1985, A simplification of the Zoeppritz equations, Geophysics, 50, No.4
H. Sigurdsson, G.M. Brown, 1970, An unusual enstatite-forsterite basalt from Kolbeinsey island, north of Iceland, Journal of Petrology, 11, 205-220
T.K. Stanton, 1985, Echo fluctuations from the rough seafloor: Predictions based on acoustically measured microrelief propertied, Jour. Acoust. Soc. Am., 78, 2, 715-721
R. Staples, R. White, B. Brandsdottir, W. Menke, P. Maguire, J. McBride, J. Smallwood, 1997, Faeroe-Iceland Ridge Experiment -- I. The crustal structure of north-eastern Iceland, J. Geophys. Res. 102, 7849-7866
R. Stefánsson, F. Bergerat, M. Bonafede, R. Böðvarsson, S. Crampin, K.L. Feigl, F. Roth, F. Sigmundsson, R. Slunga, 1999, Earthquake prediction research in a natural laboratory, PRENLAB I/II final report
P. Stoffers, R. Botz, D. Garbe-Schönberg, M. Hannington, B. Hauzel, P. Herzig, K. Hissmann, R. Huber, J.K. Kristjansson, S.K. Petursdottir, J. Schauer, M. Schmitt, M. Zimmerer, 1997, Cruise Report Poseidon 229a, Kolbeinsey Ridge, Geologisch-Paläontologisches Institut, Kiel
G. Strang, 1993, Wavelet transforms vs. Fourier transforms, Bull. Am. Math. Soc., 28,

288-304
F. Strauch, 1963, Zur Geologie von Tjörnes, Nord-Island, Köln Univ. Geol. Inst. Sonderveröffentlichung No. 7, 122
R.S. Strichartz, 1993, How to make wavelets, Am. Math. Monthly, 100, 539-566
K. Strobach, 1991, Unser Planet Erde (in german), Gebrüder Borntraeger
L.R. Sykes, 1967, Mechanism of earthquakes and nature of faulting on the mid-ocean ridges, JGR, 72, 2132-2153
B. Taylor, K. Crook, J. Sinton, 1994, Extensional transform zones and oblique spreading centers, J. Geophys. Res., 99, 19707-19718
W.M. Telford, L.P. Geldart, R.E. Sheriff, 1990, Applied Geophysics, 2nd ed., Cambridge University Press, Cambridge
F. Theilen, J. Scholten, 2000, Cruise report R/V Poseidon 252/253 (1999), Institut für Geowissenschaften, University of Kiel
G. Thompson, W.G. Melson, 1972, The petrology of oceanic crust across fracture zones in the Atlantic Ocean: evidence of a new kind of sea-floor spreading, J. Geol., 80, 526-538
Þ. Thoroddsen, 1925, Geschichte der isländischen Vulkane (in german), Copenhagen, Danske Vidensk. Selsk. Skr., Naturv. Og Mathem., ser. 8, 9, 1-458
K. Thors, 1982, Shallow seismic stratigraphy and structure of the southernmost part of the Tjörnes Fracture Zone, Jökull, 32, 107-112
H. Trappe, C. Hellmich, 2000, Using neural networks to predict porosity thickness from 3D seismic data, First Break, 18, 9, 385-391
E. Tryggvason, 1959, Seismicity of Iceland and surrounding areas (in icelandic with english summary), Náttúrufræðingurinn, 26, 194-197
E. Tryggvason, 1973, Seismicity, earthquake swarms and plate boundaries in the Iceland region, Bull. Seis. Soc. Am., 63, 1327-1348
B. Ursin, B. Ekren, 1995, Robust AVO analysis, Geophysics, 60, 317-326
R.J. Varga, J.S. Gee, L. Bettison-Varga, R.S. Anderson, C.L. Johnson, 1999, Early establishment of seafloor hydrothermal systems during structural extension: paleomagnetic evidence from the Troodos ophiolite, Cyprus, Earth Planet. Sci. Let., 221-235
Veðurstofa, 2000, South Iceland Lowland (SIL) network database, http://www.vedur.is/cgi-bin/sellib
B. Vidakovic, P. Müller, 1991, Wavelets for Kids, Duke University report
P.R. Vogt, G.L. Johnson, L. Kristjansson, 1980, Morphology and magnetic anomalies north of Iceland, J. Geophys., 47, 67-80
P. Wallace, A.T. Anderson, 2000, Volatiles in magma, in: EOV
P.L. Ward, 1971, New interpretation of the geology of Iceland, Geol. Soc. Am. Bulletin, 82, 2991-3012
D.R. Watts, A.J. Deighan, C. Riedel, 1999, Attenuation of marine wave swell noise by stacking in the wavelet packet domain, SEG Expanded Abstracts, Houston, 1999
J. Weiner, 1986, Planet Earth, Metropolitan Pittsburgh Public Broadcasting
Þ. Þorláksson, 1668, Delineatio Gronlandiae Theodori Thorlacii, Anno 1668
U. Wegler, 1999, Doktorarbeit, Universität Potsdam
J.A. Welhan, 1988, Origin of methane in hydrothermal systems, Chemical Geology, 71, 183-198
P. Wessel, W.H.F. Smith, 1991, Free software helps map and display data, EOS Transactions, 72, 441

N.C. White, R.J.Herrington, 2000, Mineral deposits associated with volcanism, in EOV
M. Wickerhauser, 1993, Wavelets, adapted waveforms and denoising, EEG Symposium on Continuous Waveform Analysis, New Orleans
M. Widess, 1973, How thin is a thin bed ?, Geophysics, 38, 1176-1180
S. Wiemer, S. McNutt, 1997, Variations in the magnitude-frequency distribution in two volcanic regions: Mt St Helens (Washington) and Mt Spurr (Alaska), GRL, 24, 189-192
S. Wiemer, R.F. Zuniga, 1994, ZMAP - a software package to analyze seismicity, EOS Transactions, Fall Meeting, AGU, 75, 456
G. Winckler, 1998
J.R. Wood, T.A. Hewett, 1984, Reservoir diagenesis and convective fluid flow, In: D.A. McDonald, R.C. Surdam, Clastic Diagenesis, AAPG Mem., 37, 99-110
N.H. Woodcock, M. Fisher, 1986, Strike-slip duplexes, J. Struct. Geol.,8, 725-35
M. Wyss, K. Shimazaki ,S. Wiemer, 1997, Mapping active magma chambers by b values beneath the off-Ito Volcano, Japan, J. Geophys. Res, 102, 20413-42022
T. Yoshida, K. Nishizawa, M. Tabata, H. Abe, T. Kodama, M. Tsuji, Y. Tamaura, 1993, Methanation of CO_2 with H_2-reduced magnetite, Jour. Material Sci., 28, 1220-1226
G. Zhao, H. Chen, S. Ma, D. Zhang, 1995, Research on earthquakes induced by water injection in China, Pure and Appl. Geophysics, 145, 60-68
R.A. Zierenberg, Y. Fouquet, D.J. Miller, J.M. Bahr, P.A. Baker, T. Bjerkgård, C.A. Brunner, R.C. Duckworth, R. Gable, J. Gieskes, W.D. Goodfellow, H.M. Gröschel-becker, G. Guèrin, J. Ishibashi, G. Iturrino, R.H. James, K.S. Lakschewitz, L.L. Marquez, P. Nehlig, J.M. Peter, C.A. Rigsby, P. Schultheiss, W.C. Shanks III, B.R.T. Simoneit, M. Summit, D.A.H. Teagle, M. Urbat, G.G. Zuffa, 1994, The deep structure of a sea-floor hydrothermal deposit, Nature, 392, 485-488
M.D. Zoback, J.H. Healy, 1984, Friction, faulting, and in situ stress, Annales Geophysicae, 2, 689-698

Acknowledgements

I would like to thank the Bundesministerium für Bildung und Forschung (BmBF), the Deutsche Forschungsgemeinschaft (DFG), the Arbeitsamt and Total Fina Elf for sponsoring the work presented in the thesis, which evolved in a couple of projects including work at location in Glasgow/Scotland, Yogyakarta/Indonesia, Iceland and last but not least the nice city of Kiel in Schleswig-Holstein. I would also like to thank my professor B. Milkereit and my project coordinator F. Theilen for supporting the work of this thesis. Further important informational input sprang from discussions with the geological division of the department, foremost M. Schmidt and R. Botz and two diploma students A. Broser and T. Petersen, who studied the same area in Iceland for a while. Sometimes even more fruitful were discussions with other people from the department, including C. Papenberg, W.Rabbel, T. Bohlen, both C. Müllers, S. Bussat, S. Kugler, N. Maercklin, S. Kroll, J. Ebbing, S. Werner, M. Budweg, H. Busche and T. Beilecke. Of course, there were people from other parts of the world like B. Lühr, D. Watts, R. Blakeman and some people at the AGU Fall Meeting 1999 who I would like to thank for discussions.
But last but not least, there needs to another big thanks for people like all the Riedels of Nordhorn, S. Martens, I. Wölbern, P. Liersch, N. Gesche, M. Strehl, A. Rogatchevski, J.M. Torrealba, H. Muray, W. Wolts etc. for getting insight into meaning of life...(of course some of the persons mentioned earlier would have to be included, but, hey, this is to cut it short...!)
Well, I hope I forgot nobody, but that hope is subject to fail once in a while, the world is just too big to remember everything in the right moment.

Carsten Riedel

Geological Map of the Tjörnes Fracture Zone

Seafloor Lithology

Igneous Rocks

- Lava flows or dike intrusions
- Ridge area

Sediments

Altered

- Volcaniclastic
- Hydrothermal

Marine or terrigenous input

- Conglomerate intercalated by lavas (?)
- Compacted sediment (Sandstone, etc.)
- Mud or Ooze

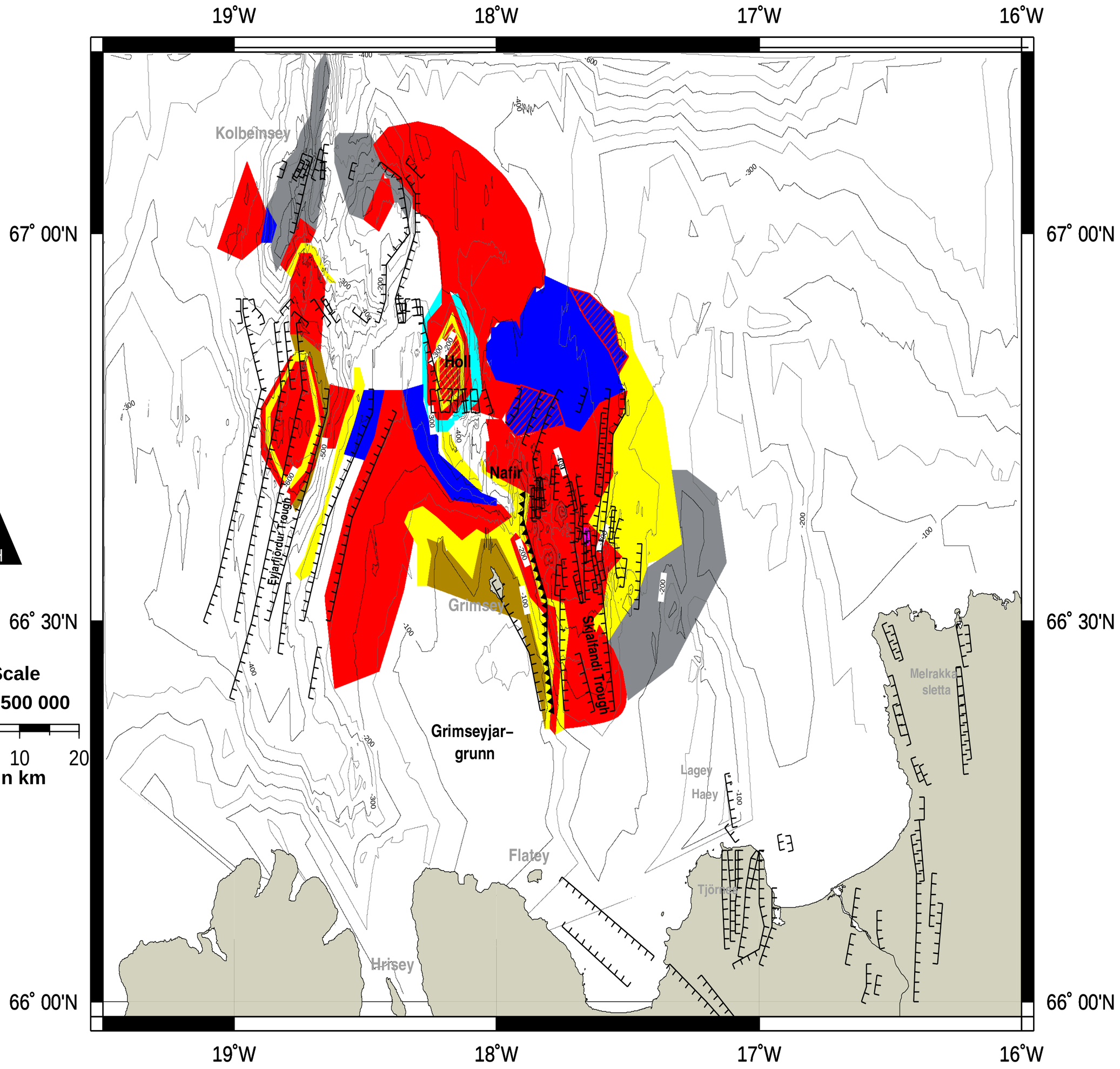

geographic NORTH

Universal Transverse Mercator Projection

Base coordinates:
18° W for projection
66° N for scale

Scale
1 : 500 000

0 10 20
in km

Symbols

Holl	submarine location
Grimsey	subaerial location
	Fault (unspecified / Thrust)
	Bathymetry contours

Geologische Karte der Tjörnes Fracture Zone * Jardfraedikort Tjörnes Brotabeltinu